Development and Investigation of Gas-Diffusion Electrodes for the Electrochemical Reduction of CO_2

Von der Fakultät Energie- Verfahrens- und Biotechnik
der Universität Stuttgart
zur Erlangung der Würde eines Doktors der
Ingenieurswissenschaften (Dr.-Ing.) genehmigte Abhandlung

vorgelegt von

Dennis Kopljar
aus Heilbronn

Hauptberichter: Prof. Dr. Elias Klemm
Mitberichter: Prof. Dr. Kaspar Andreas Friedrich
Prüfungsvorsitzender: Prof. Dr. Joachim Groß

Tag der mündlichen Prüfung: 30.01.2023

Institut für Technische Chemie
2023

Acknowledgements

Haste makes waste is the English expression for the German saying “*Gut Ding will Weile haben*”. Being honest, however, in this context it is merely a silly euphemism for the seemingly never-ending process of finalizing my thesis which made the people involved quite desperate and head-shaking at times. I was very lucky that I could count on the steady support from Professor Klemm who was mildly but permanently pushing and building up a network of people from my new institution doing the same thing. Thankfully, everyone was very understanding that handling the multiple obligations, most importantly the kids and the new job, plus the Corona-crisis which came on top, made it quite difficult to invest the required time and engage consistently over such a long period of time and the extended unavoidable breaks in between. The new-found passion for my role as a battery researcher surely didn’t help to focus on my past work.

Anyways, the most important thing is: I finally made it. At this point I want to thank the people who supported me throughout my career, the experimental work at the institute and during the writing of the thesis. First, I want to start with my wife who always had my back, pushed me and facilitated that I take the spare time for writing. My family who supported me throughout my life and made all of this possible in the first place. My mentor, Professor Klemm, who allowed me to work on this fascinating topic, gave me the freedom to own the project and thereby facilitated my growth as researcher. The colleagues, namely, Heike, Barbara, Christoph and Mrs. Favaro (who always had a smile confronted with my chaos) and students – Katja, Fabian, Paul, Michael and Max – who contributed to this work and provided the essential pieces to the puzzle. Finally, all the colleagues and friends who made the time at the institute an incredibly entertaining journey: Moritz², Feierlein, Traudy, Paul, Niffler, Thomas, Sandra, Fabi, Ümit, Nagme, Doro and many others. I hope I didn’t forget anyone. But whoever knows me, also knows that chances are high and that one shouldn’t be mad at me :)

For every complex problem there is an answer
that is clear, simple, and wrong.

- *H.L. Mencken*

Abstract

For the chemical industry, the transformation towards a climate-neutral society demands for the implementation of novel production technologies based on non-fossil resources. An attractive solution to produce carbon-based chemicals is to utilize CO_2 as raw material and renewable electricity as energy source for its activation. One such process which is investigated in this work is the electrochemical reduction of CO_2 (CO2RR) into formate salts. The scope of this work is to develop and investigate the gas-diffusion electrode (GDE) for this reaction with the aim of deriving a better understanding of the complex interplay of the GDE production parameters, the resulting properties and its electrochemical behavior.

The GDEs are produced using a dry deposition technique. A carbon black supplies the porous matrix and skeleton of the GDE. It is covered by tin oxide as electrocatalyst – mechanically mixed or finely dispersed *via* a homogeneous precipitation method. The hydrophobic PTFE (10 to 50 wt.-%) is used as binding agent and supplies mechanical integrity. A thermal treatment step at 340 °C ensures its homogeneous distribution over the carbon matrix as physical characterization of the electrode texture shows. The tin-based GDEs favor formate production with a Faradaic Efficiency > 80% over the whole potential region studied with lower polarization slightly shifting the product distribution towards CO (< 20%). Hydrogen evolution (HER) is largely suppressed but becomes dominating at high current densities when mass transport limitation sets in. Optimizing reaction conditions and production parameters of the GDE, this type of electrode facilitates current densities up to 500 mA/cm² before HER takes over.

The achievable current density is strongly affected by wettability and structure of the GDE. Comprehensive characterization of the latter shows the characteristic bimodal electrode structure that is attributed to a primary and secondary pore system that forms *inside* and *between* the carbon agglomerates, respectively. Whereas the primary porosity is largely determined by the type of carbon, the secondary pore system is a result of the manufacturing method, thus, affected by PTFE and compacting pressure. Correlating electrochemical behavior with electrode properties showed the importance of an open primary porosity which is why the highly macroporous Acetylene Black (AB) has been determined to be the most suitable substrate for maximizing current density. Essential for the operation of the GDE, the wetting of the hydrophobic pore system by the aqueous $KHCO_3$ electrolyte is thoroughly investigated. It is initiated by polarization of the electrode, a process called electro-wetting that leads to penetration of the electrolyte into the carbon agglomerates by capillary forces. A combination of *post-mortem* element mapping and cyclic voltammetry revealed that during electrolysis an electrolyte front traverses the GDE. Inside the macroscopically wetted volume, only a small portion of the electrode surface is in contact with electrolyte (~20% for AB at 500 mA/cm²) due to the high hydrophobicity of the studied carbon blacks. While the activity is directly correlated to the wetted catalyst surface, the pronounced hydrophobicity was shown to be essential for facilitating efficient gas supply to the triple-phase boundary throughout the electrode volume. Accordingly, oxidizing the carbon substrate to increase wettability leads to a decrease of the limiting current density. The benefits of the macroporous primary porosity together with the negative effect of pore forming agents (increase of tortuosity for liquid-phase diffusion) and the influence of the operating mode (CSTR vs. semi-batch, which affects the degree of product accumulation) points towards a limitation by product diffusion. This hypothesis, however, could not be unambiguously validated as the actual electrode behavior is heavily masked by catalyst degradation. In all experiments, a constantly rising HER can be observed. *Post-mortem* analysis of the GDE points towards a reductive dissolution of the tin oxide and partial redeposition of metallic tin favoring HER over CO2RR. This loss of active catalyst phase is caused by the high alkalinity (OH^- accumulation) adjacent to the active sites and the highly negative electrode potentials. This suggests that in this system, tin oxide is not a suitable catalyst in contrary to what is commonly proposed in literature. Evidently, this observation becomes apparent when working at industrially-relevant conditions as done in this work.

Finally, an analysis on the effect of the operating point on total electrolysis cost is performed to derive performance targets for formic acid production. Using an alkaline electrolyzer as basis for a rough cost estimation, it can be clearly shown that current densities on the order of 100 mA/cm² and, thus, the use of optimized GDEs as developed in this work are essential to minimize the contribution of the investment cost to the electrolyzer stack. This is because for the same amount of product, the electrolyzer can be build more compact. However, beyond a certain threshold, the beneficial effect of increasing current density becomes marginal. In contrary when a realistic U-I curve is assumed, the curve undergoes an optimum – with the assumptions used herein at 200-300 mA/cm² – and higher currents lead to the operating cost to dominate due to the ohmic losses which scale linearly with current density. Production cost then rises almost linearly.

Kurzfassung

Für die chemische Industrie erfordert die Transformation der Gesellschaft hin zu Klimaneutralität die Entwicklung und großflächige Einführung neuartiger Produktionstechnologien auf der Grundlage nicht-fossiler Ressourcen. Eine attraktive Lösung für die Herstellung kohlenstoffbasierter Chemikalien ist die Nutzung von CO_2 als Rohstoff und erneuerbarem Strom als Energiequelle. Ein solcher Prozess, der in dieser Arbeit untersucht wird, ist die elektrochemische Reduktion von CO_2 (CO2RR) zu Formiatsalzen. Die vorliegende Arbeit befasst sich mit der Entwicklung der Gasdiffusionselektrode (GDE) und deren tiefgehende Untersuchung für diese Reaktion, mit dem Ziel ein besseres Verständnis des komplexen Zusammenspiels der Herstellungsparameter, der resultierenden Eigenschaften und des elektrochemischen Verhaltens der GDE zu erhalten.

Die GDEs werden mit Hilfe eines Trockenabscheidungsverfahrens hergestellt. Ein Ruß bildet die poröse Matrix und das Gerüst der GDE. Dieser wird mit Zinnoxid als Elektrokatalysator beladen – mechanisch vermischt oder fein dispergiert über eine homogene Fällungsmethode. Das hydrophobe PTFE (10 bis 50 Gew.-%) dient als Bindemittel und sorgt für mechanische Stabilität. Ein thermischer Behandlungsschritt bei 340 °C sorgt für eine homogene Verteilung über der Kohlenstoffmatrix, wie die physikalische Charakterisierung der Elektrodenstruktur zeigt. Die auf Zinn basierenden GDEs begünstigen die Formiatproduktion mit einer Faraday-Effizienz von > 80% über den gesamten untersuchten Potenzialbereich, wobei sich die Produktverteilung bei geringerer Polarisierung leicht in Richtung CO (< 20%) verschiebt. Die Wasserstoffentwicklung (HER) ist weitgehend unterdrückt, dominiert jedoch bei hohen Stromdichten sobald Stofftransportlimitierung einsetzt. Durch Optimierung der Reaktionsbedingungen und der Produktionsparameter der GDE können Stromdichten bis zu 500 mA/cm² erreicht werden, bevor es vermehrt zu HER kommt.

Die erreichbare Stromdichte wird stark von der Benetzbarkeit und der Struktur der GDE beeinflusst. Eine umfassende Charakterisierung zeigt die charakteristische bimodale Elektrodenstruktur, die auf ein primäres und sekundäres Porensystem zurückzuführen ist, das sich innerhalb bzw. zwischen den Kohlenstoffagglomeraten bildet. Während die primäre Porosität weitgehend von der Art des Kohlenstoffs bestimmt wird, ist das sekundäre Porensystem ein Ergebnis des Herstellungsverfahrens und wird somit von PTFE und dem Verdichtungsdruck bei der Herstellung beeinflusst. Die Korrelation des elektrochemischen Verhaltens mit den Elektrodeneigenschaften demonstriert die Bedeutung einer offenen Primärporosität. Dies erklärt neben der hohen Hydrophobizität, weshalb das makroporöse Acetylene Black (AB) als das am besten geeignete Substrat zur Maximierung der Stromdichte ermittelt wurde. Die Benetzung des hydrophoben Porensystems durch den wässrigen $KHCO_3$-Elektrolyten ist für den Betrieb der GDE von entscheidender Bedeutung und wird umfassend untersucht. Eine Kombination aus *post-mortem* Element-Mapping und zyklischer Voltammetrie zeigt, dass während der Elektrolyse eine Elektrolytfront die GDE durchquert. Innerhalb des makroskopisch benetzten Volumens ist aufgrund der hohen Hydrophobizität der untersuchten Ruße nur ein kleiner Teil der Elektrodenoberfläche in Kontakt mit dem Elektrolyten (~20% für AB bei 500 mA/cm²). Während die Aktivität direkt mit der benetzten Katalysatoroberfläche korreliert, ist die ausgeprägte Hydrophobizität der GDE essentiell für die effizienten Gaszufuhr zur Dreiphasengrenze entlang des gesamten Elektrodenvolumen. Dementsprechend führt die Oxidation des Kohlenstoffsubstrats zwar zur Erhöhung der Benetzbarkeit aber zu einer Verringerung der Grenzstromdichte. Die Vorteile der makroporösen Primärporosität zusammen mit dem negativen Effekt der Porenbildner (Erhöhung der Tortuosität für die Flüssigphasendiffusion) und dem Einfluss der Betriebsweise (CSTR vs. Semi-Batch, was Ausmaß der Produktakkumulation im Porensystem beeinflusst) deuten auf eine Begrenzung durch Produktdiffusion hin. Diese Hypothese konnte jedoch nicht eindeutig validiert werden, da das tatsächliche Elektrodenverhalten durch die Degradation des Katalysators überlagert ist: in allen Experimenten ist ein konstant steigende HER zu beobachten. *Post-mortem* Analyse d deutet auf eine reduktive Auflösung des Zinnoxids und eine teilweise Wiederabscheidung von metallischem Zinn hin, was HER gegenüber CO2RR begünstigt. Dieser Prozess wird durch den hohen pH (OH^- Akkumulation) an der Dreiphasengrenze und die stark negativen Elektrodenpotentiale verursacht. Dies deutet darauf hin, dass Zinnoxid in diesem System kein geeigneter Katalysator ist, was im Gegensatz zur wissenschaftlichen Literatur steht. Die Diskrepanz lässt sich höchstwahrscheinlich mit den hier vorhandenen industriell-relevanten Bedingungen erklären, welche diesen Effekt deutlich verstärken.

Schließlich wird anhand der Kennzahlen und wirtschaftlichen Abschätzungen eines alkalischen Elektrolyseurs der Einfluss des Betriebspunktes auf die Gesamtelektrolysekosten untersucht, um Zielgrößen für die Ameisensäureproduktion zu ermitteln. Durch eine grobe Kostenabschätzung kann gezeigt werden, dass Stromdichten in der Größenordnung von 100 mA/cm² und damit die Verwendung optimierter GDEs, wie sie in dieser Arbeit entwickelt wurden, notwendig sind, um den Anteil der Investitionskosten am Elektrolyseur-Stack zu minimieren. Der Elektrolyseur kann dadurch bei gleicher Produktmenge kompakter gebaut werden. Jenseits eines bestimmten Schwellenwerts wird dieser Effekt jedoch marginal und eine weitere Erhöhung der Stromdichte führt zu steigenden Kosten: sofern eine realistische U-I-Kurve angenommen wird, durchläuft die Kostenkurve ein Minimum - bei den hier verwendeten Annahmen bei 200-300 mA/cm². Höhere Ströme führen dann dazu, dass die Betriebskosten aufgrund der ohmschen Verluste, die linear mit der Stromdichte skalieren, dominieren und die Elektrolysekosten in die Höhe treiben.

Table of Content

List of abbreviations

AB	Acetylene Black (carbon material)
AB35	gas-diffusion electrode based on Acetylene Black with 35% PTFE content, analogous for electrodes with other composition
AEL	alkaline electrolysis
AFC	alkaline fuel cell
BET	Brunner-Emmet-Teller (model for surface area determination)
BJH	Barrett-Joyner-Halenda (model for pore size distribution analysis)
BP	Black Pearls (carbon material)
CD	current density
CL	catalytic layer
CNT	carbon nanotube
CO2EL	carbon dioxide electrolysis
CO2RR	carbon dioxide reduction reaction
CSTR	continuously-stirred tank reactor
CT	computer tomography
CV	cyclic voltammetry
DFT	density functional theory
ECSA	electrochemically active surface area
EDX	energy dispersive X-ray spectroscopy
EE	energetic efficiency
ENS	Ensaco (carbon material)
FE	Faradaic efficiency
GDE	gas-diffusion electrode
GDL	gas-diffusion layer
GHG	greenhouse gas emission
$HCOO^-$	formate
HER	hydrogen evolution reaction
HPLC	high performance liquid chromatography
ICP-OES	inductively coupled plasma - optical emission spectroscopy
IPCC	Intergovernmental Panel on Climate Change
KB	Ketjen Black (carbon material)
LSV	linear sweep voltammetry
MPL	microporous layer
NOR	Norit (carbon material)
OCV	open-circuit voltage

ODC	oxygen-depolarized cathode
OER	oxygen evolution reaction
ORR	oxygen reduction reaction
PAFC	phosphorous acid fuel cell
PEM	polymer electrolyte membrane
PSD	pore size distribution
PTFE	polytetrafluoroethylene
pzc	Point of zero charge
RDS	rate-determining step
RHE	reversible hydrogen electrode
SEM	scanning electron microscopy
SHE	standard hydrogen electrode
TEM	transmission electron microscopy
TGA	thermogravimetric analysis
VXC	Vulcan (carbon material)
XPS	X-ray photoelectron spectroscopy
XRD	X-ray diffraction

List of symbols

a_i	activity
C	capacitance
C_{DL}	electrochemical double-layer capacitance
c_i	concentration of species i
d_p	pore diameter
d	distance
D_i	diffusion coefficient
$D_{i,eff}$	effective diffusion coefficient
e	charge of electron
E^0	standard electrode potential
EE	energetic efficiency
F	Faraday constant
FE	Faradaic Efficiency
I	current
i	current density
i_0	exchange current density

i_L	limiting current density
n	amount of substance
$\dot{n}$	molar flux
N_A	Avogadro constant
p	pressure
Q	charge
R	resistance
r_i	reaction rate
r_p	pore radius
t	time
T	temperature
U_{cell}	cell voltage
V	volume
$\dot{V}$	flow rate
V_P	pore volume
V_R	reactor volume
ΔH	enthalpy change of reaction
ΔS	entropy change of reaction
ΔG	Gibbs free energy

Greek symbols

α	symmetry factor (Butler-Vollmer)
γ	surface tension
δ	diffusion layer thickness
ε	porosity
η	overpotential
θ	contact angle
κ	specific conductivity
μ	chemical potential
μ^*	electrochemical potential
ν	stoichiometric coefficient
τ	tortuosity
φ	Galvani potential

Chapter 1

Introduction

1.1 Motivation

The availability of abundant and inexpensive fossil resources has ensured a seemingly never-ending source of cheap energy and versatile feedstock for the production of a variety of carbon-based chemicals. Thereby, it enabled the enormous growth of the worldwide economy and standard of living witnessed over the last century, particularly in the nowadays wealthy industrialized countries. However, in light of the climate crisis induced by anthropogenic greenhouse-gas emissions (GHG, mainly CO_2, CH_4 and N_2O) and environmental breakdown that parallel this development, it has become increasingly evident that this reliance comes with a high price for the environment, public health and could threaten modern civilization if no effective counteractive measures are initiated [1,2]. As this problem has been discerned, the international community has pledged to increase their efforts to drastically reduce GHG emissions under the frame of the Paris Agreement in order to mitigate the most severe outcomes and to stabilize the global temperature increase in 2100 to *well below 2 °C* with regard to the pre-industrial baseline [3]. To achieve that, according to the most recent scenarios by the Intergovernmental Panel on Climate Change (IPCC) and estimated carbon budgets, GHG emissions have to fall drastically in the upcoming decades [4]. Figure 1.1 depicts the allocation of greenhouse gas emissions (in CO_2 equivalents) to the specific sectors and according to their end use, in a so-called Sankey chart. Since more than 70% of the worldwide GHG emissions (85% in Germany [5]) are energy-induced, *i.e.* directly coupled to the combustion of fossil resources, the development of alternatives and subsequent large-scale deployment is of utmost importance. The chemical sector in particular accounts for around 6% of greenhouse gas emissions associated with the use of fossil resources for the supply of energy, heat and as chemical feedstock [6]. Without paradigm shift, this share is expected to rise in case decarbonization of electricity generation and transport prevails as expected. It is commonly suggested that electrification will become a key element for the defossilation of chemical production processes facilitating the integration of renewable electricity to drive chemical conversion [7]. This can be done either directly or indirectly, the latter *via* the use of green hydrogen (derived from water electrolysis) as reactant in chemical processes. In contrary, simply relying on process improvements and the energy transition in the energy sector will only result in a moderate decrease of GHG emissions, as *e.g.* shown by the German association of the chemical industry (VCI) in the recently published *Roadmap Chemie 2050* [8].

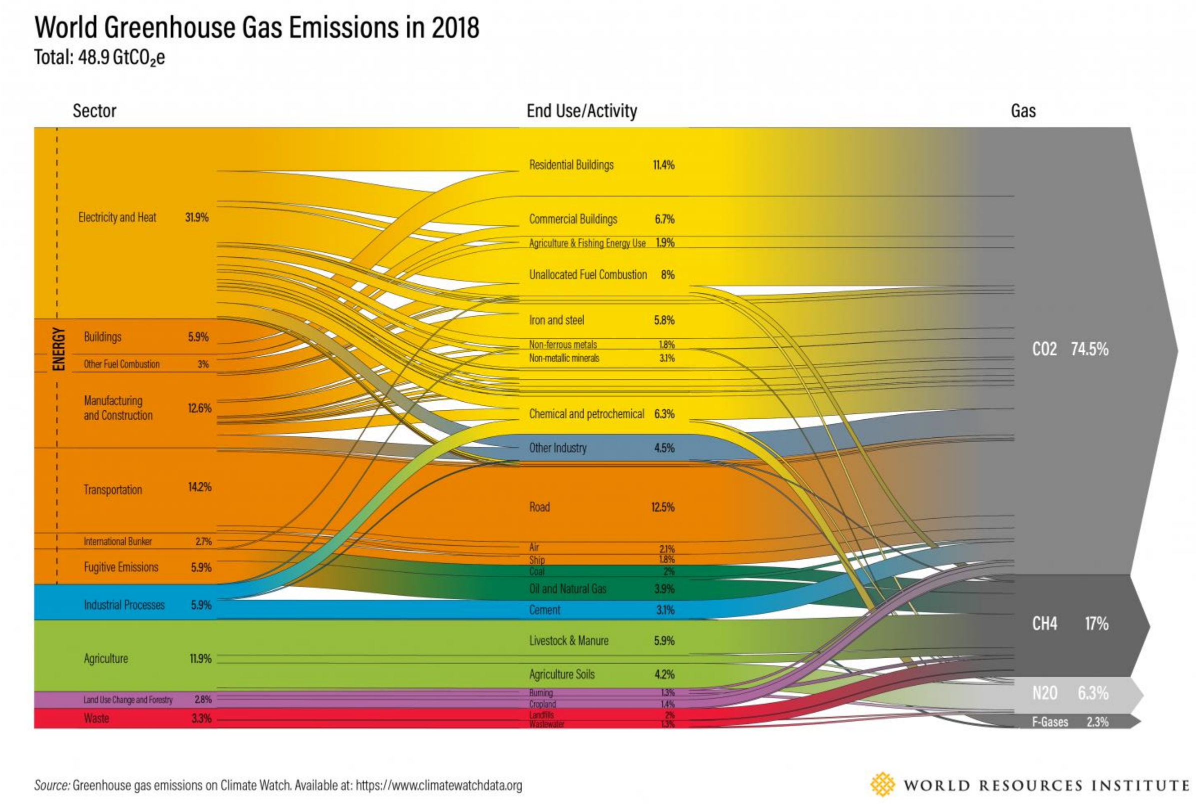
World Greenhouse Gas Emissions in 2018
Total: 48.9 $GtCO_2e$

Source: Greenhouse gas emissions on Climate Watch. Available at: https://www.climatewatchdata.org

Figure 1.1. Sankey chart of worldwide greenhouse gas emissions in 2016 divided by sectors, end use and type of GHG [9]

Substituting fossil feedstock is challenging as the supply chain has been specialized over decades around an array of platform chemicals that are mostly derived from petroleum, natural gas and coal. In 2013, this share constituted 87%, the remainder being mostly biomass [10]. Only very recently, this distribution is slowly shifting. Efforts to valorize CO_2 as chemical feedstock are steadily increasing, both in academia and in industry [11,12]. Its use is largely inevitable in the long-term as, besides biomass, it is the only viable, non-fossil carbon source for the production of carbon-based chemicals. CO_2 can be derived from waste streams in conventional power plants and chemical production sites such as in ammonia or ethylene oxide synthesis, thereby aiding in decreasing the carbon footprint of existing facilities. In a fully decarbonized world, CO_2 can be derived *e.g.* from highly integrated bio-refineries where it is produced as by-product in fermentation and other biotechnological processes or from direct air capture (DAC) [13].

Coupling both developments – electrification and feedstock change –, the direct electrochemical reduction of CO_2 on the cathode of an electrochemical cell, has emerged as highly promising solution for direct integration of renewable electricity into chemical production and utilization of CO_2. Despite the significant advances that have been made in recent years with regard to improving and understanding the reaction, commercialization of this process is still elusive as simultaneous demonstration of high current densities, high enough energetic efficiency and long-term stability has not been achieved so far

[14–16]. Accordingly, the scientific community has only recently begun to close the gap between fundamental, mostly catalyst-related investigations of the reaction, and more applied studies [17,18]. Besides the design and investigation of flow-cell configuration and optimization of reaction conditions, the latter comprises most importantly the development and investigation of electrode systems that are capable of fulfilling the requirements for technical processes [19]. Amongst others, this entails their production *via* industrially scalable methods and the ability of working at industrially relevant current densities on the order of several 100 mA/cm². For this purpose, the use of so-called gas-diffusion electrodes (GDEs) is suggested to be inevitable. Such porous electrodes partially wetted by electrolyte allow for the use of gaseous CO_2, thereby shifting transport limitations induced by the low solubility of CO_2 in aqueous electrolyte to significantly higher current densities [20]. To allow for a thorough understanding of how the manufacturing process determines the electrode properties and how the properties influence the electrochemical performance – that is activity, product distribution and stability – elaborate and systematic studies are needed. However, at the time this study has been commenced, such electrodes were mostly regarded as black box in this specific reaction with only a few studies particularly devoted towards understanding and optimization of the GDE itself. Only in recent years more profound studies were conducted in order to shed light into how such electrodes operate, what limits their performance and how they can be further optimized to step towards technical implementation [21–23]. The work at hand is part of these efforts, ultimately, aiming at establishing the relationship between GDE preparation, properties and electrochemical performance.

1.2 Scope and Aim of Research

The lack of systematic and elaborate studies on GDE development as well its targeted optimization is the starting point of the study at hand. In the frame of this work, it became increasingly evident that treating the GDE as “black-box” that can be optimized simply according to the variables employed in its preparation, *might* yield satisfactory results with regard to an improvement in their performance. However, it will necessarily fail to generate a more detailed understanding of the phenomena involved in the reaction and the complex interplay between preparation parameters, electrode properties and electrochemical performance. Thus, in order to establish a solid basis for the continuing work in this field and to allow for a more targeted optimization in the future, the goal was to derive a clear understanding on the governing parameters for the electrochemical performance of the GDE. To this end, the objective entails the following steps:

i) to thoroughly examine the properties of the GDE as function of preparation conditions and its composition,

ii) reveal, how the GDE works and what the governing properties are to achieve the desired performance,

iii) establish the relationship between preparation, properties and performance by separately evaluating the influence of the different contributions and to

iv) ultimately, evolve from an empirical trial-and-error approach to a more sophisticated and knowledge based optimization strategy for the GDE.

It is important to note, that throughout this work, high priority was placed on maintaining within the boundaries of an industrial environment. This includes, amongst others, the choice of ambient temperature and pressure, the use of an aqueous electrolyte and inexpensive conductive salt, the development of a simple and scalable electrode preparation as well as the use of tin as an inexpensive and abundant electrocatalyst produced by a simple synthesis method.

Finally, assessing the relationship between the achievable key performance indicators of the electrolysis and the resulting electrolysis cost was aimed for. To this end, a cost model was implemented which describes the interplay between the electrolysis parameters, namely, cell voltage and current density, and cost of formate production from CO2RR which is comprised of the investment and operating cost of the electrolyzer. As current density and energetic efficiency at which the electrolysis is operated is directly reflected in the above, the model can be employed to derive a rational and quantitative evaluation of how the electrode development should be advanced in the future to achieve the most efficient outcome for technical application.

Chapter 2

Basics of Electrochemical Engineering

The interest in the development and technical realization of novel electrochemical processes has gained increased attention in the last decades, since their use allows the interconversion of electrical into chemical energy (electrolysis cell), and vice versa (galvanic cell), as well as integration of renewable electricity into chemical production. Such processes can thereby be used to utilize excess electricity to drive "non-spontaneous" reactions or in other cases store and provide electricity. Besides that, many electrochemical processes have certain advantages over classic thermochemical and thermocatalytic reactions, that can (but do not necessarily) include mild reaction conditions (often at ambient pressure and slightly elevated temperatures), more direct production of the desired product (*i.e.* less involved reactants, auxiliary substances and solvent) and less side reactions. This commonly leads to less environmental impact and higher energetic efficiency. In principle, it is therefore often considered a green alternative to conventional means of production [24]; an appraisal that obviously only holds true, when the electricity is derived from renewable energy. On the other hand, electrons are considered rather expensive reactants, which is why minimizing specific electrical power input is one of the key aspects for technical realization of an electrochemical process.

In the following the basics of electrochemistry are described, from general terminology to thermodynamics and the situation under electrical current, to the aim of designing an electrochemical cell with its various components. The description is mostly based on [25–27]. Due to its relevance in this work, the last section will deal with the gas-diffusion electrode in more detail.

2.1 General

In an electrochemical cell, reduction and oxidation reaction of two species takes place spatially separated on two electrodes, commonly immersed in a solution, with the electrons traveling through an external circuit from one electrode to the other. The electrode where the reduction proceeds, *i.e.* where electrons are passed from the electrode over the electrode/electrolyte interface to the species being reduced, is termed the cathode while on the anode another species is oxidized supplying electrons for the reduction in the other half-cell. To compensate for the external flux of electrons and to close the electrical circuit, ions have to transport the charge inside of the cell, as shown in Figure 2.1 along a sketch of the cell and the important terminology.

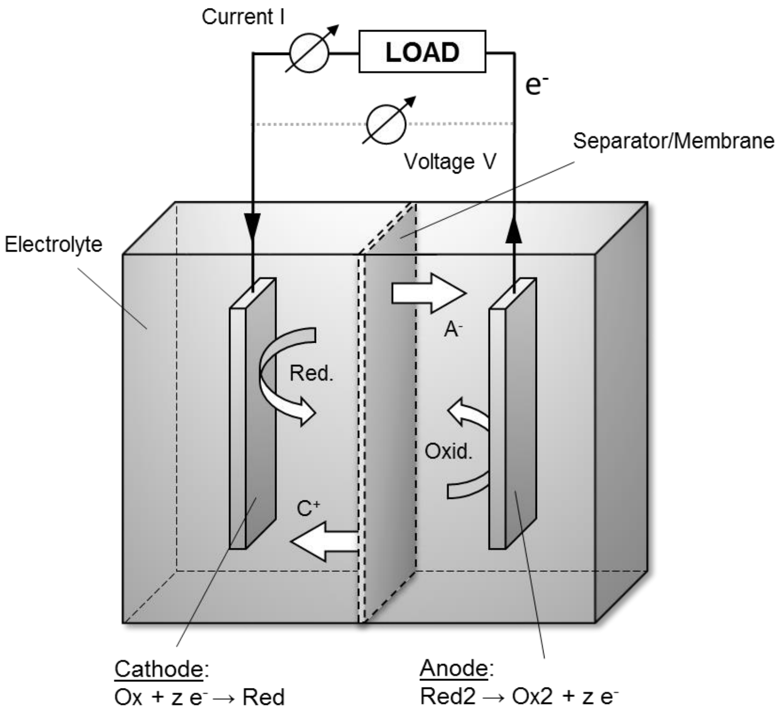

Figure 2.1. Sketch of an electrochemical cell with its various components (A^- anions, C^+ cations)

Whereas in a galvanic element, such as a battery or a fuel cell, the reaction proceeds spontaneously with net generation of electrical energy, electric work has to be supplied from an external source in an electrolysis process to drive the conversion of substrates. In the first case, chemical energy is converted into electrical energy and vice versa in the latter. The direction of the overall reaction depends on the change of the Gibb's free energy ΔG of the reaction and is determined by thermodynamics as it will be discussed in the next chapter [26].

The basis for the discussion of electrochemical reactions is the *Faraday Law* which relates the turnover of an electrochemical reaction and the charge Q passed for the conversion, in case of current flow and when the system is not in equilibrium. Introducing the Faraday constant F as proportionality factor for this relation together with the valence number z, the number of electrons per turnover of one molecule, it is one of the most important equations in electrochemistry and is summarized in the form of

$$Q = n \cdot z \cdot F. \qquad 2.1$$

F can be regarded as comprising the charge of one mole of electrons according to $F = e \cdot N_A$., with e being the charge of an electron and N_A the Avogadro constant. Thereby, the current, *i.e.* the charge per time ($I = Q/t$) or the current density, *i.e.* current normalized on the geometric area of the electrode ($i = I/A$), is defined as the electrochemical reaction rate r_i :

$$\frac{dn_i}{dt} = r_i = \frac{I}{z \cdot F} \qquad 2.2$$

In case that more than one product is formed on the electrode, it further introduces an important key figure for the evaluation of efficiency and the yield of an electrochemical cell: the Faradaic Efficiency (FE), which can be regarded as the current selectivity. In contrast to the conventional selectivity of a chemical reaction it is normalized to charge instead of converted reactant, according to:

$$FE_i = \frac{n_i \cdot z \cdot F}{I \cdot t} \qquad 2.3$$

2.2 Electrochemistry and Thermodynamics

When no current is passed through an external circuit and no net turnover of substance is observed, the electrochemical cell is in equilibrium and the reversible cell voltage U_0 is established between the electrodes (see [25,26] for a more detailed derivations of the following explanations). This voltage is determined by the potential differences of the electrode reactions, the concentrations of involved species and the external variables temperature and pressure. It is related to the thermodynamic quantity, the Gibbs free reaction energy ΔG of the overall reaction, according to

$$U = -\frac{\Delta G}{z\,F} \qquad 2.4$$

For an exergonic reaction in which $\Delta G < 0$, the reaction proceeds spontaneously under generation of electrical energy under given pressure and temperature. The maximum work (that decreases with the current, as will be discussed in 2.3) that can be drawn from such a cell is equal to $\Delta G = \Delta H - T\Delta S$. In an electrolysis cell for which $\Delta G > 0$, in contrary to the galvani element before, the minimum work equal to ΔG has to be delivered externally to drive the reaction.

The reversible cell voltage can be derived by establishing the equilibrium conditions between the phase boundaries and the involved species. In chemical equilibrium between two phases I and II in direct contact, the condition for phase equilibrium must be fulfilled for all involved species *i*, which means that the chemical potentials μ_i must be equal in both phases for all *i*.

$$\mu_i\,(I) = \mu_i\,(II) \qquad 2.5$$

Depending on the type of electrochemical system, involved species can for example mean ions in solution and the corresponding species deposited on the surface of the electrode in the case of metal electrodes in a solution of metal cations (equation 2.6). For redox reactions (equation 2.7) on the other hand, for which the electrode species is not directly involved but responsible for the passage of charge, electrons instead of ions are exchanged between electrode and a redox-couple dissolved in the electrolyte.

$$\mathrm{Me} \rightleftharpoons \mathrm{Me}^{z+} + z\,\mathrm{e}^- \qquad 2.6$$

$$S_{ox} \rightleftharpoons S_{red} + z\,e^- \qquad 2.7$$

In either case, for an electrode immersed in a solution, this means that on the interface between surface and solution, the phase boundary, chemical reactions involving the exchange of species and/or electrons from both phases takes place which leads to the establishment of the electrolytic double layer and the orientation of the charge carriers and reactants according to the energetic conditions. During this course, the electrode becomes either negatively or positively charged, depending on the direction of the chemical reaction and the passage of current over the electrode/electrolyte interface. This is again determined by the energetics of the system, leaving either an excess or shortage of electrons on the surface. This process continues until equilibrium conditions are met. Because the force equilibrium between the two phases in this case now also involves an electrostatic contribution, due to the arrangement of the electrons on the electrode surface and ions in the double layer, the electrostatic potential difference has to be included into the equilibrium condition in addition to the chemical potential.

$$\mu_i\,(I) + z_i F \varphi(I) = \mu_i\,(II) + z_i F \varphi(II) \qquad 2.8$$

Both terms on each side together constitute the electrochemical potential μ_i^* of the respective phase, where φ is the so-called electric Galvani potential of each phase and a_i the activity of the species in the corresponding phase. For standard conditions it follows:

$$\mu_i^* = \mu_i + z_i F \varphi = \mu_i^0 + RT \ln a_i + z_i F \varphi \qquad 2.9$$

Accordingly, for the difference of the Galvani potential between electrode (I) and solution (II), it is

$$\Delta\varphi = \varphi(I) - \varphi(II) = \frac{\mu_i^0(II) - \mu_i^0(I)}{z\,F} + \frac{RT}{z\,F} \ln \frac{a_i(II)}{a_i(I)} \qquad 2.10$$

Abbreviating the first term on the right side as $\Delta\varphi_0$ which corresponds to the standard potential difference of species *i* between both phases (electrode and electrolyte) for $a_i(I) = a_i(II) = 1$, gives the influence of the activity on the electrochemical potential known as the *Nernst equation*. Similarly, for a redox reaction the potential of the *electron* in both phases is decisive and the activity of the reduced and oxidized species has to be accounted for. In this case, the Nernst equation at standard conditions is defined as

$$\Delta\varphi = \Delta\varphi_0 + \frac{RT}{z\,F} \ln \frac{a_{ox}}{a_{red}} \qquad 2.11$$

Ultimately, at standard conditions, the equilibrium cell voltage U_0 can be calculated by the difference of the Galvani potentials of the half-cell reactions 1 and 2 according to

$$U_{0,cell} = \Delta\varphi_0(1) - \Delta\varphi_0(2) \qquad 2.12$$

When both electrodes are immersed in the same solution, the potential difference of the electrolytes is zero and the equation reduces to the difference of the standard electrode potentials, usually presented as E^0.

$$U_{0,cell} = E^0(1) - E^0(2) \tag{2.13}$$

If electrolytes of different composition or activity are used (e.g. separated by a membrane or diaphragm), an additional phase-boundary and potential difference is created between the electrolytes, which has to be accounted for. As the Galvani potential at a phase-boundary, and by that, also the standard electrode potential of a given half-cell reaction, is experimentally not accessible (as absolute value), it is measured against a common reference electrode, which is usually the standard hydrogen electrode (SHE, defined as zero reference point $E^0(SHE) = 0\ V$) and tabulated for many half-cell reactions. Besides SHE, many different reference electrodes with constant electrode potential exist which are used to measure the electrode potential (in equilibrium or away from it) in a three-electrode configuration.

2.3 Electrochemical Kinetics and Electrocatalysis

The kinetics of an electrochemical reaction describe the turnover of the electrochemically active substance on the electrode/electrolyte interface and the according current flow as a function of the electrode potential. Besides the simple charge-transfer steps, the kinetics of the reaction are governed by all the other precedent and subsequent steps such as chemical reactions, the involved chemical equilibria, adsorption as well as transport to and from the electrode surface, as depicted in Figure 2.2.

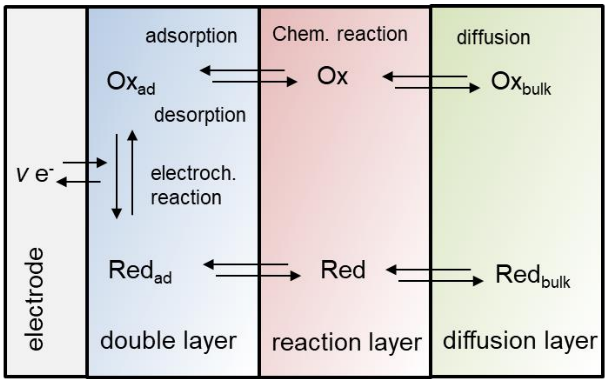

Figure 2.2 Steps involved in electrolyte and on electrode surface before and after electrochemical reaction (adapted from [27])

As in classical catalysis, the slowest step, which depends on the reaction conditions, the electrode polarization and the involved materials, determines the macroscopically observable reaction rate. If a comprehensive description of the kinetics is required, the contribution of each part of the reaction sequence to the current-potential relation has to be included into the overall rate expression. The finite velocity of these elementary steps entails the polarization of the electrode surface beyond the equilibrium value of the reaction as driving force to overcome the reaction-specific resistances and to initiate a net flux of electrons over the solid/liquid interface. As an important parameter in electrochemistry, the difference between the electrode potential under current flow and its equilibrium value is termed the overpotential

η which is a function of the involved species of the reaction, reaction conditions and the electrode material:

$$\eta(i) = E(i) - E^0 \tag{2.14}$$

It depends on the current density (as compared to the ohmic resistance which is independent of the current) and can be separated into different contributions, which will be introduced in the following.

In many cases, at low polarization, the overpotential is mostly governed by the electron transfer of the rate-determining elementary step, and the kinetic inhibition or activation barrier of this step. It is attributed to the finite velocity of the charge-transfer over the electrode/electrolyte interface to or from the redox species. When the rate-determining step of the reaction is a one-electron transfer and other contributions are negligible (*e.g.* for $\eta \rightarrow 0$), the current-voltage curve can be described by the so-called *Butler-Volmer equation* which is a phenomenological equation of pivotal importance in electrochemical kinetics. It describes the magnitude of the oxidative and reductive charge-transfer reaction ($i_{ct,ox}$ and $i_{ct,red}$), as for example given in the reaction equation 2.7, and, the according net flux of electrons over the electrode surface as function of the charge-transfer overpotential η_{ct}, *i.e.* the polarization solely attributed to the charge-transfer. It can be derived from the theory of the activated complex in which the change of the Gibbs free energy along the reaction coordinate for the forward and backward reaction is examined. It goes through a maximum when the so-called *activated complex* (the transition state between reactant and product, according to the theory) is formed. For an electrochemical reaction, the change in the energetic situation for forward and backward reaction is accounted for, as the potential difference between electrode and electrolyte is changed when the electrode is polarized. As a result, the change of the Gibbs free energy of forward and backward reaction is affected to different degrees and, thus, either one of the directions is favored or impeded (negative polarization favors reduction, and vice versa) [26]. For a derivation and treatment, it is referred to [28] as a profound discussion on the theory behind this equation would go beyond the scope of this work. This derivation gives

$$\begin{aligned} i_{ct}(\eta_{ct}) &= i_{ct,ox}(\eta_{ct}) + i_{ct,red}(\eta_{ct}) \\ &= i_0 \left\{ exp\left(\frac{\alpha \cdot z \cdot F}{RT} \eta_{ct}\right) - exp\left(-\frac{(1-\alpha) \cdot z \cdot F}{RT} \eta_{ct}\right) \right\} \end{aligned} \tag{2.15}$$

In this equation, important variables of electrochemical kinetics are introduced: the exchange current density i_0 is a measure of the current density of the material at the equilibrium potential ($\eta = 0$) and is thus, a (palpable) property of the electrocatalyst while charge transfer coefficient or symmetry factor α ($0 > \alpha < 1$) is derived from quantum mechanics [25] and expresses how strongly the galvani-potential difference between electrode and electrolyte (see above) impacts the activation energy change; thus, how severe polarization of the electrode affects the reaction in either direction.

When the magnitude of η_{ct} is sufficiently high, *i.e.* $|\eta_{ct}| >> RT/zF$ (= $25.6/z$ mV at T=298 K), in the cathodic case the oxidative current can be neglected, and *vice versa*, and the relationship becomes a simple exponential relationship. Rearranging the equation (including $ln \rightarrow log$) and solving for η the gives the so-called *Tafel equation* with the Tafel slope *b* (given in mV/decade) and the constant *a*, which includes i_0, according to

$$\eta_{ct} = \frac{2.303\ RT}{(1-\alpha)\ zF} \log i_0 - \frac{2.303\ RT}{(1-\alpha)\ zF} \log i_{ct} \ = a - b \log i_{ct}\ . \qquad 2.16$$

Plotting the overpotential of this semi-logarithmic relation over the logarithm of the current density yields the *Tafel-plot*, a common form to compare different electrocatalysts and assess their macroscopic activity as well as to derive information on the rate-determining step and how it changes with potential. The latter can be observed for example by a change of the Tafel-slope at given overpotential or as function of the reaction conditions and catalyst.

When the reaction is fast and the transport of the electroactive species to and from the electrode surface cannot keep up with their consumption/generation, the reactants start to be depleted and product accumulates in the double layer. As a consequence, the actual concentration c_{surf} deviates from the initial concentration c_0 to which E^0 corresponds to and a concentration gradient develops between bulk electrolyte and the surface. This necessitates that the difference in the concentration has to be accounted for in the electrode potential. It is described by the concentration overpotential η_{conc}. Accounting for the concentration dependence of the standard potential according to the Nernst equation (eq 2.11) gives

$$i_{red}(\eta) = -i_0 \frac{c_{surf}}{c_0} exp\left(-\frac{(1-\alpha)\cdot z\cdot F}{RT}\ \eta\right), \qquad 2.17$$

for the cathodic current at moderate to high overpotential (neglecting oxidative contribution). Solving for the overpotential and comparing with eq. 2.16 gives

$$\eta_{conc} = -\ \frac{RT}{(1-\alpha)\ zF} \ln \frac{c_{surf}}{c_0} \qquad 2.18$$

for the concentration overpotential.

Especially in technical electrode systems, where high current densities are targeted, the different contributions of mass transport and limitations induced by it play an important role. On the one hand, such concentration gradients amount to a significant electrode polarization at high conversion and entail the presence of a limiting current density i_L beyond which further polarization does not result in a further increase of reaction rate anymore. Furthermore, for certain situations, where different reactions are competing for active sites which are affected by transport limitations to different degrees, even before this limiting current is achieved, a shift of the product distribution to undesired by-products such as the decomposition of the electrolyte *(e.g.* yielding hydrogen in aqueous CO_2 reduction) can be provoked. Also for other kinetic phenomena mathematical descriptions can be derived quantifying the extent of their inhibition and their share to the total overpotential, such as the reaction overpotential when the reaction is limited by the rate of preceding or subsequent coupled chemical reactions or by ad-/desorption. For a more profound discussion it is again referred to the above mentioned textbooks.

Electrocatalysis

The type and morphology (*e.g.* crystal facet, presence of steps, kinks or defects on the surface) of the electrode material strongly affect the activation energy of the elementary steps which is governed by the strength of interaction between the electrode surface and the reaction intermediates. It thereby determines the extent of kinetic inhibition of a reaction, the magnitude of the charge-transfer overpotential and, ultimately, the intrinsic activity of the material. Furthermore, the electrode material can favor certain reaction pathways while suppressing or inhibiting others, thereby, guiding the reaction towards the desired product while minimizing side reactions.

For simple reactions, the activity of a catalyst can often be described by such properties as the binding energy towards the intermediate involved in the rate-determining step which, in turn, can be correlated fairly well with the reaction-rate. Two important examples are the hydrogen- or oxygen-metal bond strength ΔG_H for the hydrogen evolution reaction (HER) or ΔG_O for the oxygen reduction reaction (ORR), respectively. Also for CO_2 reduction such activity descriptors have been established as will be discussed in 3.2. Plotting the experimental reaction rate over the values calculated from first principles (*e.g.* DFT) for different metals yields so-called Volcano plots which render the catalyst with optimum properties at the top, in agreement with the Sabatier principle [29,30]. An example of this is shown in Figure 2.3 for HER and ORR:

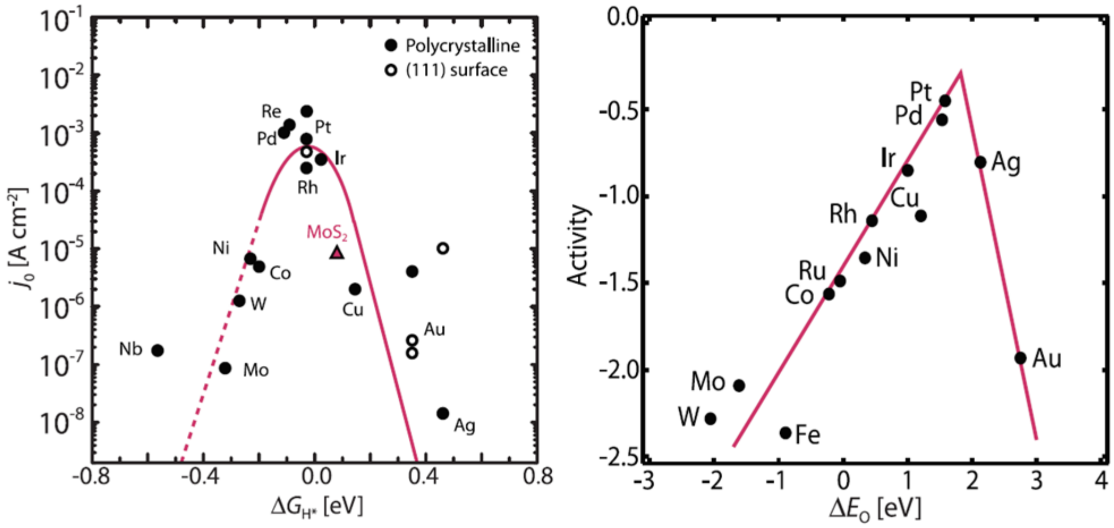

Figure 2.3 Volcano plots of HER (left) and ORR (right) describing activity of different metals as function of metal-hydrogen and -oxygen bond strength [29].

Increasing the activity of an electrocatalyst can either be approached by tuning the intrinsic activity of the catalyst or by maximizing the number of active sites at which the reaction is performed. The first comprises *e.g.* the derivation of novel catalysts, alloying, deposition of supported particles with high share of undercoordinated kink or step atoms, grain boundaries or core-shell particles while the latter can be achieved by nanostructuring, deposition of highly dispersed nanoparticles on a high surface area support or the use of three-dimensional electrode systems [29]. Ultimately, the goal of minimizing overpotentials is supplemented by the requirement of high stability under reaction conditions, which are often highly corrosive, and economic viability, *i.e.* the use of abundant and inexpensive materials if possible.

2.4 The Electrochemical Cell

Besides the thermodynamically determined reversible cell voltage and the reaction specific overpotentials, additional reactor dependent ohmic resistances have to be overcome which lead to ohmic voltage losses, *i.e.* following Ohm's Law ($\Delta U = R \cdot I$). These losses require additional input of electrical energy into the system which is dissipated into heat. The significance of the different barriers and resistances depends on the reaction, the cell geometry, reactor design and electrolyte properties but can basically be found in every system and be classified in three categories [24]:

1) Electrical resistances:
    - Contact and wiring resistances in the electrical circuit,
    - limited electrical conductivity of the electrode material and interfacial contact resistances between the different components (current collector, electrode layers).

2) Transport-related resistances:
    - Limited ionic conductivity in electrolyte,
    - ionic conductivity of separator or membrane, and,
    - if applicable, formation of gas bubbles between electrodes, displacing electrolyte and decreasing its conductivity.

3) Overpotentials η directly related to electrochemical reaction (see above):
    - Kinetic barriers of electrode reactions (activation polarization) and
    - mass transport resistances.

Accordingly, the actual cell voltage to achieve a desirable current density is given by

$$E_{cell} = E^0_{anode} - E^0_{cathode} + \eta_{ct,i} + \eta_{conc,i} + \eta_{ohm} , \qquad 2.20$$

with $\eta_{ohm} = i \cdot R_{cell}$ and R_{cell} the sum of all the above mentioned ohmic resistances encountered in the employed cell. Compared to the overpotentials, the ohmic resistances are independent of the current density. The different contributions are illustrated in Figure 2.4 in the form of an equivalent circuit diagram. Here, R_{el}, R_{sep} and R_{ct} represent the resistances of the electrolyte, the separator and of the respective electrodes, respectively, C_{dl} denotes the double layer capacitance.

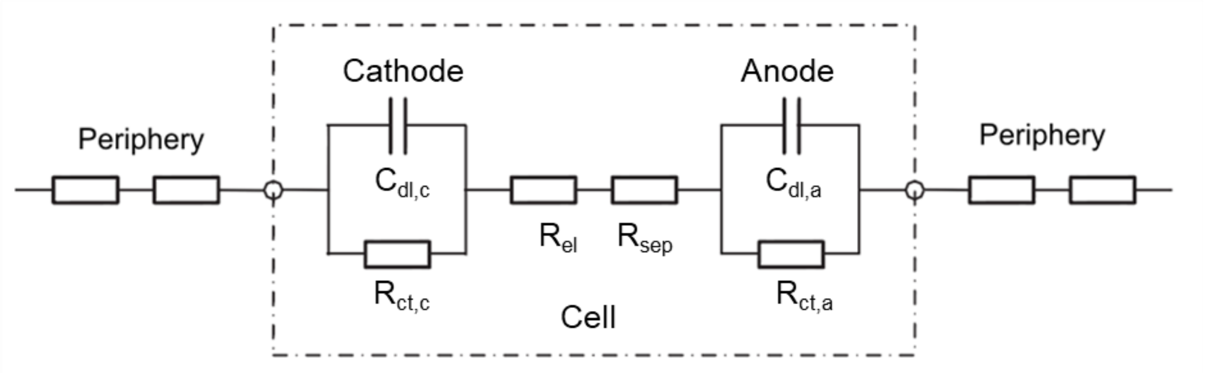

Figure 2.4. Electronic equivalent circuit diagram of an electrochemical cell describing the different resistances contributing to the reactor voltage (from [24], naming of variables adjusted for consistency).

Clearly, in order to optimize an electrochemical process, the scope of the engineer or chemist is to separate, understand and determine the different contributions, and eventually target and minimize them as much as possible. This is because their magnitude (reflected in the cell voltage U_{cell}) directly affects the energetic efficiency according to

$$\varepsilon = \frac{\left(E^0_{anode} - E^0_{cathode}\right)}{U_{cell,measured}} \cdot 100\ \%. \qquad 2.21$$

From the above resistances, particularly the ohmic contributions by the electrolyte and the electrode, for the latter, particularly, contact resistances between its components (current collector, gas diffusion and catalytic layer, see below), play an important role. To ensure a sufficiently low resistance towards electron conduction, often a highly conductive carbon black or metal matrix is used, and a current collector applied to the back of the electrode. The resistance of the electrolyte is determined by its specific conductivity κ, which in turn depends on type and concentration of the conducting salt, and the dimensions of the gap *d* between anode and cathode, according to

$$R_{el} = \frac{1}{\kappa \cdot d}. \qquad 2.22$$

However, the choice of the electrolyte is not an independent variable, as it is directly involved in the electrochemical reaction, by i) dissolving the reactants and products, ii) influencing the transport to and from the electrode surface, iii) constituting the location for preceding or subsequent elementary steps and iv) stabilization of reaction intermediates [25]. Furthermore, besides having high conductivity, reaction-dependent requirements are posed on the electrolyte such as the electrochemical and chemical stability, adequate solubility for the reactants and low viscosity. To avoid interference of species involved in the respective counter reaction, anode and cathode chamber are often divided by a separator or a selectively permeable membrane which has to be conductive to the available charge carriers to maintain the charge balance between both chambers during reaction. Analogous to equation 2.22, high conductivity and low thickness of few µm have to be aimed for as well as sufficient stability and low cost.

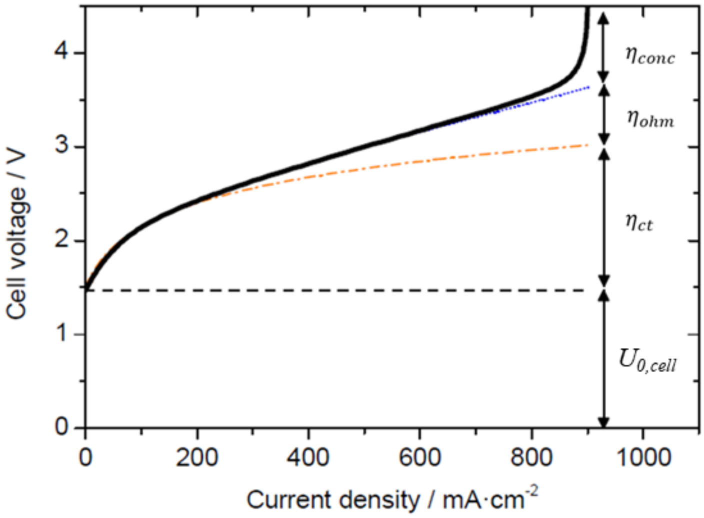

Figure 2.5 Current-voltage curve of electrolyzer with corresponding contribution towards cell voltage, (from [20], naming of variables adjusted for consistency)

A typical current-voltage curve of an electrolyzer looks like the one shown in Figure 2.5. Therein one can distinguish the different contributions, each being significant at specific operating conditions. At low current, the reactor voltage is mainly determined by the thermodynamics and the charge-transfer overpotential of the reactions. As the relation between current density and polarization is exponential, its relative share becomes smaller in favor of the ohmic voltage losses which rise linearly with current and lead to a largely linear slope in the current-voltage curve at intermediate to high current densities. Finally, at high cell voltage characteristic of high conversion of reactants, transport-related overpotentials become pronounced and the curve reaches the limiting current density, beyond which further polarization does not yield additional turnover of substance [24].

2.5 Gas-diffusion electrodes

The electrodes, as location where the reaction takes place determine the *non-ohmic* share of the current-voltage relationship. As discussed above, the optimization of the electrocatalyst is the key to minimize the kinetic overpotentials while the electrode structure governs the degree of transport limitations and availability of active sites. The design of efficient electrode systems and their targeted optimization is one of the key steps in the development of an electrochemical process.

An important type of electrode structure which is used to overcome transport limitations in multi-phase reactions is the so-called gas-diffusion electrode (GDE). GDEs are commonly used in electrochemical reactions where gas phase reactants are converted, and limited solubility of these species in the electrolyte entail the need for an intensification of mass transport to achieve desired reaction rates [31]. Typical examples from industrial application are hydrogen oxidation and oxygen reduction reaction in the different type of fuel cells [31], the latter also in metal-air batteries [32] or the chlor-alkali synthesis when oxygen-depolarized cathodes (ODC) are employed [33]. In this chapter, a short description of the important features of the GDE and their preparation is given with an emphasis on the similarities of the GDE in these reactions without going in too much detail on the specific requirements for each application. A more profound discussion on the use of GDEs for CO2RR is given in chapter 3.4.2.

2.5.1 Properties and Types of GDEs

A gas-diffusion electrode is a porous electrode which is typically comprised of a high surface area matrix of an electrode support (often carbon material) and an organic binding agent into which the electrocatalyst is dispersed. The matrix can also be made up of the active material itself, such as porous silver or N-doped carbon acting as both support and catalyst for ORR. The partial penetration of electrolyte into the pore system allows the interfacial area between electrolyte and gas phase to be formed within the material of the electrode and, thus, the triple-phase boundary (TPB) of gas, electrolyte and catalyst where the reaction takes place is significantly enhanced. The electrolyte in this case does not necessarily have to be a liquid but can also be an ionomer as in polymer electrolyte membrane fuel cells (PEMFC). In both cases, solubility issues are reduced since the gas molecules only have to diffuse through a thin layer of electrolyte in order to reach the active site. As the effective reaction zone is much larger than the geometric area, the observable reaction rates are usually one or two orders of magnitude higher than on conventional flat electrodes [20,34].

Over the decades, many different types of GDEs have been developed and optimized with regard to the requirements of the respective reactions. Whereas, for example, for the development of PEMFC electrodes, high priority is assigned to the maximization of catalyst utilization to decrease the use of precious metal loading, the GDE-assembly also has to perpetuate water management on the cathode side (ORR) where water is generated as product [35]. On the anode side, this does not constitute a challenge and the requirements are less severe. In metal-air batteries, the GDE is designed as bifunctional electrode for both OER and ORR necessitating the use of one bifunctional or two complementing catalysts. Besides, facilitating gas evolution and its reduction, the electrode structure requires high stability in the highly corrosive environment of OER [36]. In non-aqueous metal-air batteries, the generation of insoluble reaction product, further complicates operation as micropores are quickly clogged during discharge leading to an abrupt end of lifetime [37]. Evidently, requirements and optimization targets of GDEs can be substantially different with regard to the applications what makes a general discussion circumstantial. On the other hand, drawing parallels and finding similarities is valuable, especially, since one has access to decades of knowledge and experience concerning the optimization and understanding of GDEs. Thus, it is possible to benefit from research in these applications that are already commercialized, thoroughly studied and optimized. Having a liquid electrolyte and gaseous reactant, out of the above examples especially the alkaline fuel cell (AFC) [31] and early work on fuel cells with acidic liquid electrolyte (e.g. phosphoric acid fuel cells (PAFC) [38,39]) are of interest for CO_2 reduction, because the reaction proceeds in a similar manner.

In any case, the resistance towards transport of all reactants should be as low as possible, while the concentration of gas dissolving sites and the surface area of active sites in the reaction zone needs to be maximized. In many applications, it is deemed beneficial to choose a dual-layer approach, comprising the catalytic layer and a gas diffusion backing, each with distinct function [31]. The catalytic layer contains the active material, preferably at high dispersion and tailored according to established structure-activity relationship so that both intrinsic activity and the number of active sites are high at reasonable loading and manufacturing cost. Of particular importance when expensive materials are used, is that catalyst utilization is close to 100% which introduces the target to deposit the catalyst where the reaction takes place, *i.e*. in ionic and electronic contact [38,40]. The gas diffusion layer (GDL) often consists of a macroporous substrate (*e.g*. carbon paper or fiber), and a so-called microporous layer (MPL), commonly made up of polytetrafluoroethylene (PTFE) and carbon black. Besides decreasing contact resistance between catalyst layer (CL) and the macroporous substrate which is optimized for high gas permeability and homogeneous delivery of reactant to the TPB, the main purpose of the water-repellent MPL is to separate the wetted CL from the gas-phase by exhibiting tailored hydrophobicity while facilitating high flux of gases. In ORR in PEMFC, the GDL assembly is of pivotal importance as it is also responsible for draining the catalyst layer from produced water while avoiding its condensation in the pores which would lead to additional transport resistance [35,41]. Using this multi-layer approach allows the separate optimization of their composition according to their function and the respective requirements.

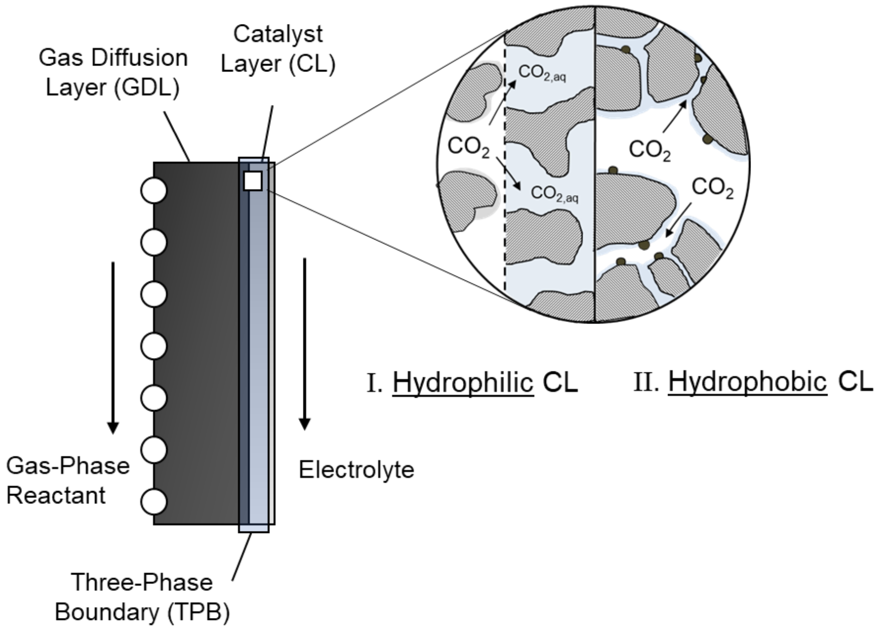

Figure 2.6 Sketch of the GDE assembly and schematic drawing of the two different types of catalytic layers and how the TPB is constituted

In general, two different state-of-the-art catalyst layer types have emerged over time, which are mainly distinguished by the kind of binding agent and resulting water uptake:

i) Hydrophilic thin-film catalytic layers:

In acidic electrolyte which is nowadays almost exclusively employed in the form of an acidic polymer-electrolyte such as Nafion, a thin film of ionomer-bonded catalytic layer, is deposited on a hydrophobic substrate. The use of Nafion as ionomer ensures the wetting of the whole catalyst layer due to its high water uptake in case a liquid electrolyte is used, (e.g. in PAFC or in direct liquid fuel cells where accessibility of the liquid fuel is essential [42]). Its primary function as ionomer is to provide proton-conduction in polymer-electrolyte systems, thereby extending the triple-phase boundary from the membrane into the CL. Similarly, the same approach is also investigated for alkaline conditions in which hydroxyl-conducting ionomers are used for the same purpose [43]. The deposition of a very thin film of a few µm is pivotal in both cases for fully-wetted layers, as only catalyst close to the gas-liquid interface participates in the reaction at high current densities where diffusion of the dissolved species becomes rate-determining.

ii) Hydrophobic GDEs:

Partial hydrophobicity of the CL, in turn, allows the extension of the TPB throughout the whole catalyst layer, instead of limitation of the reaction zone to a thin film close to CL/GDL interface as above. As binding agent hydrophobic PTFE is used to form hydrophobic channels for gas passage while other parts of the pore system are in contact with electrolyte wetted by capillary forces. This approach is more common in alkaline systems where proton-conduction by Nafion is not required [31,44] owing to the presence of liquid electrolyte. This is the case in in PAFC, AFC or in aqueous metal-air batteries [44,45]. Besides carbon-based GDEs, also carbon-free GDEs have been developed with a hydrophobic pore system, such as those based on porous Raney-Silver [46] for AFC or with Ag in oxygen-depolarized cathodes [47].

Naturally, also alternatives, modifications and combinations of these exist. The discussion in the following will focus on hydrophobic GDEs with liquid electrolyte as it is the approach chosen in this work. A comparison between both strategies for CO2RR is discussed in chapter 3.4.2 in which the literature is reviewed.

2.5.2 Properties and way of operation of carbon black-based GDEs

The effectiveness of a hydrophobic carbon black-based GDE in triple-phase reactions can be attributed to its bimodal pore structure which is governed by the structure of the employed carbon material, the carbon particle size and agglomerate morphology, as well as the preparation method. On the smallest scale, carbon black is composed of crystalline domains of aromatic systems which resemble the graphene planes found in graphite but with low spatial extension [48]. These domains are connected in an unsystematically ordered layered arrangement to the near-spherical particles, illustrated in the center of the Figure 2.7. A transmission electron microscopy (TEM) image of a carbon black aggregate is depicted on the left, showing how the near-spherical primary particles of the carbon black coalesce or fuse together during their synthesis (pyrolysis or incomplete combustion of hydrocarbons) to small and rigid, colloidal aggregates, the smallest dispersible unit in the carbon black [31,49]. In turn, these aggregates build agglomerates, as schematically drawn on the right, spanning a large three-dimensional network. This is essential for the effectiveness of the carbon black as support in the GDE as it constitutes the skeleton of the structure. Depending on the type, the carbon black is composed of more than 98% of carbon, with oxygen and hydrogen containing functional groups, exemplary shown in the background of the figure, determining the surface chemistry and thereby hydrophobicity of the material [48,49]. As a model for describing how carbon black-based GDEs operate, their pore system is commonly described in literature [31,50–52] to be made up of the so-called *primary* and *secondary* pore system.

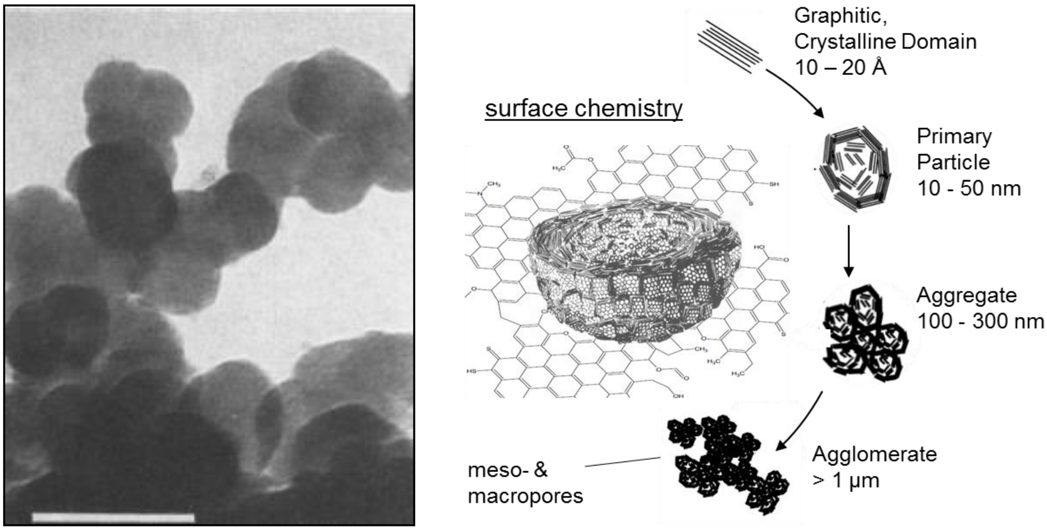

Figure 2.7. left: TEM-image of Vulcan XC72-R (bar implies 0.1 µm) [52], center: structure and assembly of primary particle with graphitic planes [48], background: exemplary chemical composition of surface with defect chemistry [53], right: Schematic drawing of the typical assembly of the primary particles formed by graphitic planes of aromatic systems to large three-dimensional powder agglomerates forming the porous backbone in the electrode structure [54]

Although this model which will be elaborated in the following is very helpful to get a better idea of the GDE assembly and its mode of operation, naturally, it is a simplification of the highly complex nature of the GDE with its continuous, three-dimensional pore network, heterogeneous surface chemistry and wetting properties. According to the model perception, the primary pore structure is formed inside of the carbon agglomerates, between the aggregates and, if porous, within the primary particles. The space *between* the agglomerates constitutes the secondary pore system forming the skeleton of the matrix. During the electrode manufacturing process, the secondary pores are coated by a PTFE-film or filaments which renders the GDE with mechanical stability. Also, it gives additional hydrophobicity to the pore system and prevents the excessive flooding with electrolyte. The structure can be adjusted during electrode preparation, *e.g.* by the PTFE/carbon ratio. In contrast, the primary pore system – or "agglomerate-porosity" as it is often called – is directly linked to the employed carbon material and its manufacturing process. As the primary porosity in the GDE is still hydrophilic to a certain degree or can be wetted when a potential is applied and surface tension decreased sufficiently (see *electrowetting* below), the pores are penetrated by the liquid electrolyte *via* capillary forces [31,55]. According to this model perception, when reaching the wetted agglomerates, the gas molecules are dissolved and transported by diffusion to the active sites. Especially at high reaction rates the diffusion of the dissolved reactant to the catalyst as well as the products out of the pore system become the limiting factors [31,56]. Hence, the design of an optimal porous structure and the area where the gas can dissolve into the electrolyte is the crucial target to enhance the electrode performance [51]. In order to minimize diffusion length through the electrolyte layer to the catalytic particles the carbon needs to facilitate a high dispersion of the catalyst. The important properties of the employed carbon type which have to be evaluated and balanced for the respective reaction and process conditions are surface area, pore size distribution and electric conductivity [36]. At this point it should be noted that while the primary porosity is often referred to as "agglomerate porosity", this is not ideal and unambiguous as in the final electrode structure distinguishing between agglomerates and aggregates is not possible anymore. Similarly, the notion that the secondary porosity resides between these agglomerates is only meaningful if one is referring to the agglomerates in the powder form before the manufacturing process and assumes they remain largely intact when the GDE is produced. The balance between hydrophobic and hydrophilic nature of the pore system plays an important role in maintaining a stable and extended triple-phase zone, facilitating the wetting of electrocatalyst, without flooding the pore system extensively. On the pore-level, this balance is determined by the force equilibrium acting on the gas-liquid interface inside the pore at the TPB, as shown in Figure 2.8. At stationary conditions, the capillary pressure P_C equals the difference between gas and liquid pressure, P_G and P_L:

$$P_C = P_G - P_L. \tag{2.23}$$

The capillary pressure over the interface as function of the surface tension γ between the phases is described by the Young-Laplace equation which accounts for contact angle θ between pore wall and fluid, and the pore radius r according to equation 2.24 for a cylindrical pore and meniscus of spherical shape [57].

$$P_C = \frac{2 \cdot \gamma \cdot cos\theta}{r}. \tag{2.24}$$

The surface tension and contact angle depend on the hydrophobicity of the material, *i.e.* the interaction between the electrolyte and the functional groups on the pore surface. It is further influenced by the temperature and electrode potential, the latter effect described in more detail in chapter 5.2. The magnitude of the above contributions decides if pores are wetted by the liquid electrolyte or not and up to which pore radius wetting proceeds. Thus, the fine-tuning of this complex relationship either by tailoring the surface chemistry of the support or by the type and concentration of binding agent, plays an essential role in the optimization of the electrode [36,39].

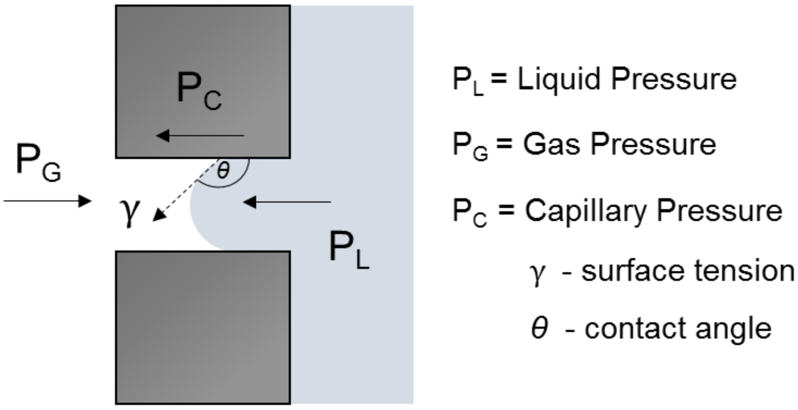

Figure 2.8. Pressure equilibrium between pore wall, gas- and liquid-phase for a hydrophobic pore ($\theta > 90°$)

Chapter 3

Literature Overview on the Electrochemical Reduction of CO_2

3.1 General description of Electrochemical CO_2 Reduction

Over the years, a remarkable amount of literature has been published on the electrochemical CO_2 reduction (CO2RR). Figure 3.1 shows the exponential growth of published literature for CO_2 utilization in general and CO2RR in particular, which can be found searching for the according phrases in the *Web-Of-Science* database (see figure caption). Since naturally such a graph could be constructed with almost any topic due to the substantial increase of scientific output in the last decades, it is necessary to normalize the data on total scientific output to be able to assess real research trends. Normalizing on the number of publications with the phrase 'chemistry/chemical' found at the same source, however, gives a similar picture as illustrated in Figure 3.1 on the right. Accordingly, it is evident that the recent trend is real, however, the uptick of research on CO_2-related technology in the middle of the 1980's, most probably a result of the two oil crises in the 1970's is also remarkable. As will later be shown, in this time a lot of the pioneering work on CO2RR has been conducted.

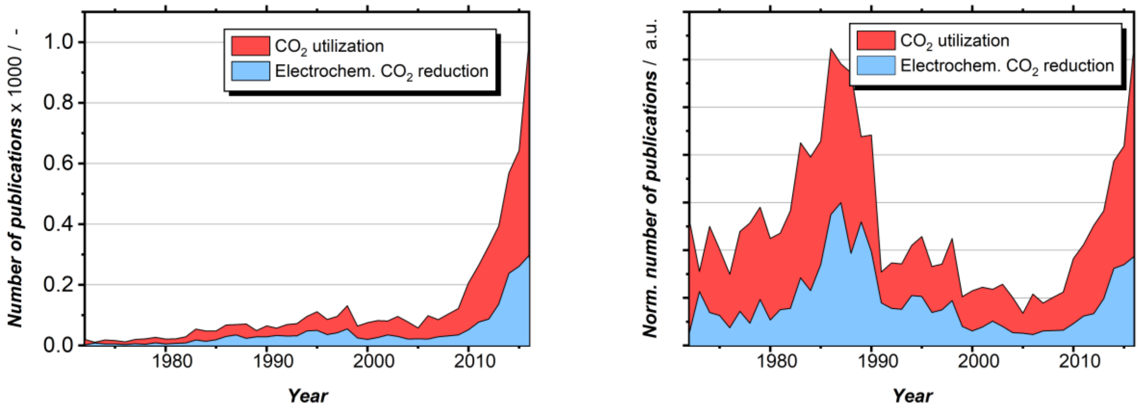

Figure 3.1. Literature survey in *Web of Science* database for the number of publications / year containing "CO2/carbon dioxide" plus "electroc*/electrolysis/electroreduction" (blue) and "CO_2 /carbon dioxide" plus "conversion/utilization/reduction/valorization" (red) in the title.

The reduction of CO_2 on the cathode of an electrochemical cell is known since as early as 1870 [58]. This is because the reaction is easily conducted by simply applying a high enough voltage in a CO_2

saturated electrolyte between metal electrodes. Depending on the electrode material and the reaction conditions (*e.g.* electrolyte, potential, pressure) different products can be obtained, starting from the rather easily accessible C_1-products formic acid (in the following, denoted as formate as the reaction is mostly conducted in neutral to basic conditions where the equilibrium is strongly on the deprotonated side, $pK_a = 3.77$), CO and methane, to more advanced higher hydrocarbons with ethylene, methanol or ethanol obtained in moderate quantities while a huge variety of other C_{2+} products such as oxalate, propanol or acetate were reported, yet, with very low efficiency to traces [59]. The most prevalent reactions encountered are given in equation 3.1 to 3.6 together with the standard potential of the reaction at standard conditions versus SHE and at pH=7, calculated with the data given in *Bard – Standard Potentials in Aqueous Solution* [60]:

$$CO_2 + H_2O + 2\,e^- \rightleftharpoons HCOO^- + OH^- \qquad E^0 = -0.51\ V \tag{3.1}$$

$$CO_2 + H_2O + 2\,e^- \rightleftharpoons CO + 2\,OH^- \qquad E^0 = -0.52\ V \tag{3.2}$$

$$CO_2 + 5\,H_2O + 6\,e^- \rightleftharpoons CH_3OH + 6\,OH^- \qquad E^0 = -0.40\ V \tag{3.3}$$

$$CO_2 + 6\,H_2O + 8\,e^- \rightleftharpoons CH_4 + 8\,OH^- \qquad E^0 = -0.25\ V \tag{3.4}$$

$$2\,CO_2 + 8\,H_2O + 12\,e^- \rightleftharpoons C_2H_4 + 12\,OH^- \qquad E^0 = -0.34\ V \tag{3.5}$$

$$2\,H_2O + 2\,e^- \rightleftharpoons H_2 + 2\,OH^- \qquad E^0 = -0.41\ V \tag{3.6}$$

In aqueous environment, the reduction of CO_2 competes with the cathodic hydrogen evolution (HER, eq. 3.6) which proceeds in the same potential range and can be catalyzed by almost every metal and metal oxide at high enough electrode polarization in the absence of other electrochemically active species. Compared to CO_2 reduction which is kinetically challenging on most electrode materials, HER is kinetically a rather favorable reaction comprising only two or three elementary steps, depending on the catalyst [61]. That is why for CO2RR to proceed in aqueous electrolyte, catalysts which show a high overpotential towards HER are necessary to suppress this undesired cathodic decomposition of the electrolyte. Most employed catalysts for CO_2 reduction are thus on the left side of the respective HER-Volcano-plot with too low binding strength for H-atoms on their surface to be good catalysts for HER. This reasoning is used in various processes to increase the working potential window and to allow for other cathode reactions to proceed. Important examples are the use of lead in lead-acid batteries or Hg-electrodes in the amalgam process in chlor-alkali synthesis [27].

Pioneering work to get a general understanding of the reaction and for establishing a systematic classification of bulk metal electrodes according to their product spectrum was done by Hori et al. in the late 80s and early 90s [62–66]. The obtained knowledge was substantiated and extended over time by the investigation of a huge amount of materials, also beyond the classical metal electrodes. Typical electrode materials known from literature are summarized in Table 3.1 according to the common main product, a classification from early studies [67] which was recently re-evaluated and underpinned with new findings [68]. It is noteworthy, however, that tailoring the process conditions or catalyst properties can substantially shift the product spectrum, as shown for Cu-based catalyst as a function of electrolyte and pH value [69], morphology [70,71] or for carbon-based electrodes which can give substantially different products depending on the type of carbon [72], heteroatom doping [73–75] or use of a co-catalyst [76], respectively.

Table 3.1 Commonly employed materials in literature and corresponding main product in aqueous electrolyte.

Materials	**Products**
Sn, Pb, In, Co, Bi, Pd	$HCOOH/HCOO^-$
Ag, Au, Zn	CO
Cu-based	CH_4, C_2H_4, CH_3OH, etc.
Fe, Ni, Pt	H_2

3.2 Mechanistic Considerations

Formate producing catalyst such as Sn, Pb or Hg seemingly reduce CO_2 over a similar mechanism in which the carbon-oxygen bonds stay intact. On other electrode materials CO_2 reduction involves the cleavage of one such bond, yielding pre-dominantly CO, whereas for metals with high binding energy of CO such as Ni and Pt, the active sites capable of this reaction are quickly poisoned, leading to exclusive generation of hydrogen. On the other hand, Au, Ag and Zn for which CO adsorption equilibrium is largely on the desorption side readily produce CO at high rates. Ag is the most widely studied in literature as it is argued to be the most promising for this reaction due to its low price, high selectivity and low overpotentials [77,78]. Cu is particularly interesting as first discovered by Hori et al. in 1985 [65] as it seems to be one of the few materials which have an optimum CO binding strength which is high enough for its further reduction without binding it too strongly. This ranks it on top of the volcano-plot for further reduction of adsorbed CO to a variety of different products and a typical example displaying the Sabatier principle. Only a few further examples of other catalysts which are capable of producing hydrocarbons have been reported in literature [79–81].

Besides determining the obtainable products, the use of an appropriate electrocatalyst for CO_2 reduction is particularly important because although the standard potential – which only reflects the minimum driving force to enable the reaction – is not very negative, CO2RR is kinetically challenging due to a high activation barrier of the intermediate elementary steps. It was historically agreed upon that on most metal electrode materials reaction proceeds through a first electron transfer to an adsorbed CO_2 molecule forming CO_2^-. The generation of this intermediate has a very high activation barrier as stabilization of the negatively charged radical on the negative electrode is not favored. Quoting an early DFT study on the reaction, a theoretically calculated standard potential of – 1.9 vs. SHE for the generation of this intermediate has been consistently invoked in literature to explain the high overpotentials despite low standard potentials of the corresponding products [82]. Accounting for the enormous progress of the last years, this consent has been questioned by recent investigations using more sophisticated and advanced methods, described below. It is evident that in most system the actual mechanism is often far more complex and the sequence of reaction steps comprises a series of proton-coupled or single electron-transfer steps for which the rate-determining step depends on actual process conditions, such as electrolyte, pH, potential and particularly the state of the electrode surface, morphology and preparation method.

In recent years, insight into mechanistic questions and the governing parameters for activity has been massively increased by the combination of computational approaches [83], electro-kinetic analysis and *in situ/operando* methods [84] as well as the testing of a vast variety of different materials with different electronic properties and morphologies. In general, the activation of CO_2 can proceed *via* two main reaction pathways, which are characterized by the key intermediate adsorbed on the surface after an electron and proton transfer, according to Figure 3.2. This includes either a carboxylate intermediate *COOH or a formate intermediate *OCHO which are distinguished by the type of adsorption to the surface, namely binding over the carbon or the oxygen atom, respectively. Consequently, via additional electron and proton transfer, from *COOH, CO can be produced via dehydration or formate via a C-H binding step. On the other hand, *OCHO with its already protonated carbon atom exclusively yields formate as product. CO is not accessible following this route. As important side-reaction also the electrochemical activation of water yielding an adsorbed hydrogen atom after a one-electron transfer is an important elementary step to consider. After thermochemical coupling with CO_2 the same surface adsorbates can be obtained as above starting from *H [85]. While in the past there was debate in literature on the actual electroactive species which is reduced on the surface, it is nowadays accepted that it is dissolved free CO_2 (not carbonate). This is supported by recent experimental findings [86,87].

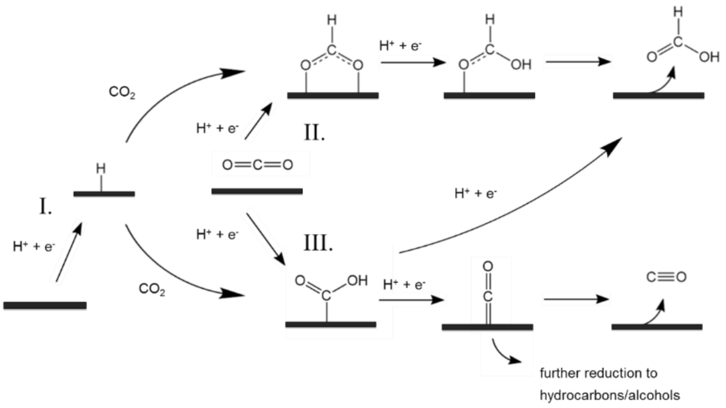

Figure 3.2 Proposed reaction mechanism of CO2RR on metal surfaces (based on [88] and [85]).

As mentioned above, when the surface exhibits the right binding energy towards CO, its further reduction can proceed via a complex series of different possible pathways including both electrochemical and chemical reaction steps and the stepwise addition of multiple electron and protons and C-C coupling reactions [89,90]. Confinement effects further enhance the C-C coupling probability due to intermediate accumulation in confined spaces [91].

Depending on the affinity of the surface towards the binding of the different intermediates, different pathways and product distribution prevails. Computational analysis of the binding energy of the intermediates can help to understand selectivity trends for certain metal surfaces. In a combined computational and experimental effort, the group of Jaramillo and Norskov established activity descriptors from first principle DFT calculations that can describe the behavior of different metals in their ability to reduce CO_2 to formate or CO [88]. Using the binding energy of both key intermediates and the measured partial current density at -0.9 V vs. RHE, volcano-type plots could be deduced which are shown in Figure 3.3. It is evident, that the Sabatier principle holds true for this reaction with an optimum binding energy resulting in maximum intrinsic activity placing the respective metals known to be the most selective – Sn and In for $HCOO^-$, Au and Ag for CO – on top. This further suggests that the corresponding intermediates are the actual intermediates for the respective products on the metals. It particularly indicates that formate production goes through the *OCHO intermediate on tin instead of *COOH. For the other metals which are on neither graph close to the top, the discussion becomes more complex [68]. Yet, the actual behavior can still be explained with the obtained results.

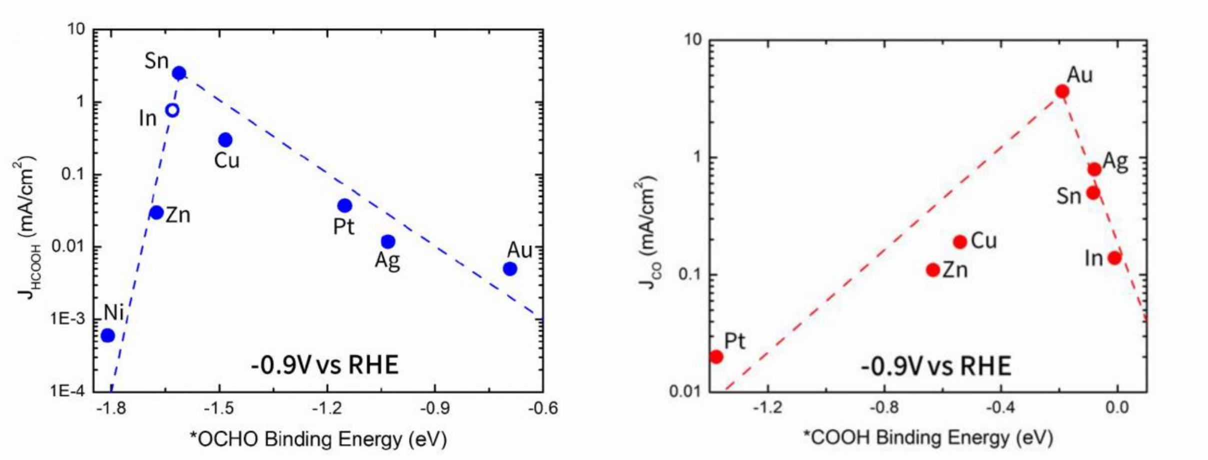

Figure 3.3 Volcano plots for CO_2 reduction to HCOOH and CO, plotting partial current density over binding energy of the suggested key intermediate as activity descriptor (*OCHO for HCOOH and *COOH for CO) [88].

3.3 CO_2 Reduction on SnO_x Surfaces

The further discussion will focus on the generation of formate on tin-based surfaces. It is important to note, that despite the relatively simple nature of the reaction only comprising two electron transfers and one proton transfer to reduce CO_2 to formate, there is still some debate and no clear and concluding consensus reached in literature on the exact reaction sequence and the rate-determining step. Nevertheless, a summary and assessment of the recent findings will be discussed. A well-crafted review on this topic with focus on formate production on tin surfaces and the corresponding mechanistic aspects is given in [85].

Tin is the most prevalently used material for formate generation as it is rather inexpensive and low in toxicity compared to the other formate producing metals Pb, Hg, Cd and In while showing moderate overpotential for the reaction. When comparing the broad range of reported results for tin electrodes in experimental studies, with Faradaic efficiencies (FE) ranging between 10% and 90%, it is evident that the reaction must be highly sensitive to the preparation of the tin surface, its chemical state and the exact reaction conditions (*i.e.* potential, electrolyte and pH). Early studies such as the ones from Hori et al. [65,92] or Ito [67] already showed the ability of tin to reduce CO_2 to formate at FE at 88%, 65-80% and 63%, respectively. In these studies, in which the product spectrum of a variety of different metals under same conditions has been evaluated, bare metal plates in CO_2 saturated $KHCO_3$ electrolyte were used, with current densities around 5 mA/cm² and potentials between -1.4 and -1.5 V vs. SHE. In other studies which used the bare metal foil as benchmark, in parts much lower FE were reported, e.g. 50% in [93] or even below 20% in [94]. In studies in which the performance over a wider potential range was evaluated, it can be observed that starting from the on-set potential of CO2RR (around -1 V vs. SHE), the FE linearly increases from 20% up to 80% at around -1.6 V [95–97]. Furthermore, in [98] it was shown that by intentional oxidation of the tin surface, the potential window in which FE is above >50% can be largely enhanced and that the FE actually scales linearly with the oxygen content on the surface. It is suggested here, that the latter, together with the strong influence of the potential, is the cause for the strong variation of reported figures in literature which is further augmented by the use of different electrolytes and pH values.

For a long time, it was consensus and not questioned that metallic tin is the electrochemically active state of tin electrodes. It was only in 2012 when it was first discovered by the group of Kanan [94] that the activity of bare tin electrodes is highly dependent on the existence of a thin oxide layer formed rapidly when exposed to air. This metastable oxide layer supposedly remains during the experiment despite the negative potential exceeding the redox potential between Sn^0 and the respective oxides. Kanan could show that by etching the oxide layer with HBr and directly utilizing the electrode mainly comprised of Sn^0, the FE towards formate decreased from 19% (at -1.1 V, see above) to only 1% as compared to the native untreated Sn foil. Furthermore, in-situ electrodeposition of a Sn^0/SnO_x composite (surface ratio 93:7) enhanced CO_2 reduction to 85% which was ascribed to the intimate contact between both phases and the important contribution of the oxide. Tafel plot analysis led to the suggestion that stabilization of the CO_2^- radical anion created after a first reversible transfer of one electron to adsorbed CO_2 proceeds prior to a rate-determining chemical step for this catalyst which could be the protonation of the radical. The same observation has been made for Indium which also produced mainly formate [98], whereas Bismuth is fully reduced under working conditions and for Lead although it exhibits a metastable surface oxide [99] metallic active sites are responsible for CO_2 reduction [84]. In a more fundamental electrochemical study of the tin/tin oxide interface, it was pointed out that the capability of performing HER decreases with the extent of the oxide layer grown on the tin surface (in the absence of CO_2) [100] which is consistent with the observation that etching the oxide substantially favors hydrogen production over CO2RR. Following the findings of Kanan, further studies were conducted to gain insight into the reaction mechanism and to identify key surface species. In-situ spectroscopic investigations have been demonstrated to be powerful tools for this purpose. Baruch et al. showed further evidence of the surface oxides being the key factor in activating CO_2 [97]. Using attenuated total reflectance IR-spectroscopy they proposed a mechanism which involves a spectroscopically observable metal-carbonate species for both tin and indium. Accordingly, for the oxide surface to be catalytically active in the reaction, it first has to undergo an electrochemically reduction to form a Sn^{II} oxyhydroxide species in a preceding step as shown in Figure 3.4. For subsequent CO2RR, a surface-bound carbonate species is formed in an equilibrated chemical step with CO_2 which is then further reduced *via* the transfer of two electrons and one proton. This finding is supported by DFT calculations [83] suggesting the formation of hydroxyl groups on the oxide layer by a reduction of a proton or dissociation of water as a first electrochemical step. A consequent protonation of an H* adatom yielding H_2 is not favored as the surface hydroxyl is more stable which explains low FE to HER on this surface. CO_2 is embedded as bicarbonate species on the hydroxyl group which is then further reduced electrochemically. The study further showed that adsorption and conversion of CO_2 on the bare metal surface is energetically highly unlikely which is in agreement to the results of Kanan.

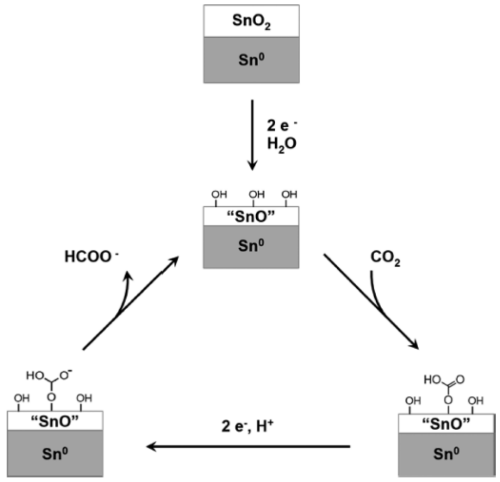

[a]Here "SnO" denotes a Sn^{II} oxyhydroxide species.

Figure 3.4 Proposed reaction mechanism of CO_2 reduction to formate on Sn/SnOx surface [97]

In a further study [101], these results were refined by monitoring the chemical state of the surface by Raman spectroscopy in-operando under varying reaction conditions, namely different electrolyte pH and applied potential. It could be shown that the oxide layer undergoes progressive reduction as the potential is made more negative and that the reduction happens with significant overpotential compared to what is expected from thermodynamics. Furthermore, the chemical state could be reasonably correlated with the FE towards formate showing that maintaining the metastable oxide layer is crucial for CO_2 reduction. It is further argued that the reason for enhanced performance in alkaline media is due to the stability of the surface oxide as function of the pH value which is determined by the Pourbaix diagram. This is consistent with literature data in which CO2RR has mostly been conducted in neutral to basic solution. On the other hand, there are two exceptions to this, which demonstrated that formate/formic acid can also be produced in acidic conditions on tin without compromising the performance strongly. Accordingly, 80% was achieved at pH 4 with KCl (vs. 60% at pH 10) [102] and 60% at pH 2 and $NaSO_4$ as electrolyte (both using gas-diffusion electrodes) [103], rendering that there is still need for further investigation of the complex interplay between the effect of electrolyte and the pH value, together with their influence on the catalyst state. It should be noted herein, that actual pH value during reaction can be much higher than in the bulk due to the generation of OH^- during the reaction, explaining the latter seemingly deviating results [104].

3.4 Catalyst and Electrode Structures

As discussed above, the electrode material determines the range of accessible products and is crucial to overcome high activation barriers of the reaction which are still two of the most important challenges for the reaction. In this light, it is not surprising that the majority of literature published is concerned with this topic, as summarized in various review articles on the design of electrocatalysts [105–107] or the theoretical understanding of activity descriptors [108].

3.4.1 Electrocatalyst design

Over the years, for the various products, distinct materials and their derivatives have been pointed out to be the most promising and therefore most prevalently used, that are tin/tin oxide for formate production, Au and Ag for CO and Cu-based for the generation of hydrocarbons. However, the observable overpotentials are still moderate, leaving room for further development. For example, Perez-Ramirez et al. suggest a target of ~400 mV as maximum overpotential at 1000 mA/cm² for CO2RR to be economically competitive with water electrolysis. This would amount to an electrode potential more positive than -1 V vs. SHE. Although on set potentials close to the equilibrium value have been reported [109,110], achieving low overpotential *and* high current density simultaneously to a satisfactorily degree have not been demonstrated so far. Nanostructuring of electrocatalysts is one promising pathway to decrease activation barriers, increase availability of active sites and tune selectivity. Sophisticated design of such nanostructures, i.e. geometries and morphologies in the nanometer range, has been shown to allow for a significant improvement in the performance of catalysts, potentially decreasing on set potential, while increasing current densities and selectivity at given electrode potentials. On the one hand, the improved activity over polycrystalline bulk electrodes is ascribed to an increased electrochemical surface area displaying more active sites per geometric electrode area with improved accessibility.

On the other hand, nanostructures can exhibit high amount of undercoordinated corner, edge and kink atoms which show improved intrinsic activity over flat surfaces [71].

Notable examples for formate generation on nanostructures, range from simple synthesis of carbon-supported nanoparticles (with optimum size at 5 nm [96] with 90% selectivity compared to 25% on bulk electrodes) to porous tin structures and more advanced geometries including nanowires and dendrites [98,111,112]. Won et al. demonstrated such hierarchical dendrite architecture with enhanced ratio of subsurface oxygen. Besides showing increased performance of 35 mA/cm² at 70% FE as compared to 50% and 5 mA/cm² on bare tin foil (ascribed to surface area, undercoordinated active sites, thermal treatment enriching oxygen content), a direct correlation between this oxygen content on the surface and FE to formate could be drawn [98]. The use of hierarchical SnO_2 nanosheets deposited on conductive carbon cloth yielding current densities up to 45 mA/cm² at 90% formate is to the knowledge of the author the highest reported value of non-GDE electrode structures at ambient pressure [95]. It is associated with the high surface area and good accessibility of the active sites due to the porous interconnected pore structure in the mesopore range. Kanan et al. could demonstrate the importance of defect sites and were able to directly correlate the grain boundary density of chemical-vapor deposited Au-NPs on carbon-nanotubes with the surface-area normalized current density for both CO_2 [113] and CO reduction [114]. This finding was qualitatively confirmed for SnOx nanowires demonstrating ten times increased current density for formate production at porous nanowires with grain boundaries as compared to nanowires without such defects [111]. The breakage of the local spatial symmetry is suggested to facilitate the binding of CO_2 and its intermediates based on DFT calculations. The benefit of employing synthetic strategies to develop well controlled structures and chemical composition down to the atomic scale is further demonstrated in the study of Gao et al. [115] who showed that the mostly inactive bulk cobalt oxide can be tuned into one of the best performing catalysts for formate production (10 mA/cm², 90% FE at 240 mV overpotential, on set after 70 mV) by designing four-atom-thick partially oxidized layers of Co_2O_3.

3.4.2 From catalyst to technical electrode systems

When the work at hand started, there was a substantial lack of systematic studies on preparation and optimization of technical electrode systems which facilitate conversion of CO_2 at industrially relevant rates, *i.e.* on the order of several 100 mA/cm². This only changed recently showing that the field is approaching more mature levels and coming closer to commercialization. Before that, in most studies CO_2-saturated electrolyte and planar electrodes have been employed in which, depending on the surface roughness of the electrode, hardly above 10 mA/cm² are reached. This is due to the low solubility of CO_2 in the aqueous electrolyte because of which the diffusion of dissolved CO_2 through the diffusion layer to the active site becomes rate-determining already at very low rates. Driving the reaction beyond this limiting current density (by applying higher electrode polarization) only leads to an increase of HER as transport limitation sets in. The according limiting current density can be approximated together with the solubility of CO_2 in water and its mass transfer coefficient according to

$$i_L = zFD_{CO2,aq}\frac{c_{CO2}}{\delta} \qquad 3.7$$

With the diffusion coefficient D_{CO2}=1.94·10^{-5} m/s [116], a diffusion layer thickness of 0.1 mm and C_{CO2} = 33 mmol/L in saturated 0.1 M $KHCO_3$ [87], the electrolyte most often employed, a value of ~13 mA·cm^{-2} can be obtained which is close to typical experimental literature values using polycrystalline planar electrodes. Different approaches have been employed to shift the achievable current density to higher values. As discussed above, nanostructuring with the aim of producing three-dimensional catalyst networks allows to increase achievable current densities beyond the 10 mA/cm² by offering an enlarged surface area for reaction. While the improvement over reference systems with flat electrodes is significant, reported current densities are still far below targeted values. By the knowledge of the author, the highest achieved CD for formate production was obtained by the use of depositing hierarchical porous nanosheets described above [95]. Thereby, production of formate with 45 mA/cm² was facilitated while for CO generation 25 mA/cm² has been demonstrated on porous thin-layer silver electrodes [117]. Although by tuning the reaction parameters, such as pressure [118] and the use of organic electrolytes or ionic liquids, much higher current densities are possible, this effect cannot be ascribed to the electrode itself and makes the process more complicated. Furthermore, the use of different types of three-dimensional electrode concepts has been suggested and evaluated. Specifically, Oloman et al. developed a three-dimensional trickle-bed reactor with tin granules and co-current gas and liquid flow to intensify mass transport and supply high surface area electrode for the reaction. In their promising set of studies, they could accomplish current density as high as 310 mA/cm² at 65% FE for formate which was at the time published by far the highest value obtained for CO2RR in continuous mode of operation and is still significant [119]. From a technical point of view, despite improvements in mass transport, however, such reactor concepts – particularly when scaled-up – commonly suffer from difficulty of maintaining a uniform gas-liquid distribution and resulting current/potential distribution which could be a reason why this concept was not further pursued [120]. Other successfully employed approaches are the use of a fixed-bed reactor with CO_2 saturated electrolyte [121] and flow-through electrode from electrodeposited Sn on carbon fibers [122], through which gaseous CO_2 is forced to flow into the liquid catholyte. Using these approaches, only small current density of 5 mA/cm² and 40 mA/cm² have been achieved, respectively.

3.4.3 Use of gas-diffusion electrodes in CO2RR

In light of the above, it is now mostly agreed that desired rates at ambient pressure and in aqueous electrolyte can only be achieved when gas-diffusion electrodes are employed (see chapter 2.5 for general description of GDEs). As they also have to prove cost-efficient, suitability of complex and expensive synthesis routes to produce efficient but exotic catalysts is questionable. This as well accounts for complex nanostructures that would need to be integrated into such electrode structures. Albeit the use of GDEs has been shown to allow for the targeted current densities and their use in research becomes increasingly prevalent, a systematic and detailed investigation on the complex interplay between preparation method, properties and electrochemical performance has only partially been conducted for this reaction.

Mahmood et al. were the first using a GDE for CO2RR already in 1987 [103]. The method based on the deposition of several layers of a thick paste from carbon, catalyst, PTFE and solvent using a paint-brush with intermediate drying and a final pressing step was relatively common at the early stage. This is because it does not require very sophisticated equipment and is relatively simple to perform on the lab-scale. It is basically an early form of the air-brushing technique used nowadays and was employed in a similar manner by the group of Sammels et al. [123,124] and Delacourt et al. [125]. Interestingly, already at this early stage current densities of as high as 115 mA/cm² were achieved with almost quantitative yield of formic acid (pH<2) using lead as catalyst. In the following, many studies were published in which GDEs were used according to this preparation method, all showing very high achievable current densities around 100 mA/cm², e.g. cumulative alcohol CD of 70 mA/cm² using Cu-containing perovskite-based electrodes, 80 mA/cm² towards formate with an Ru-Pd alloy [126] and partial CD towards methane and ethylene as high as 400 mA/cm² on copper-loaded GDEs [124]. Besides the work of Mahmood at al., who examined the influence of PTFE content, metal loading and curing temperature, none of these publications describe a more profound optimization of the GDE composition or properties. Despite the promising results of these early studies, with the emergence of more mature and technologically advanced PEMFC electrode preparation techniques, the approach described above (hand-painting with PTFE as binder) was not continued when in the late 2000s interest in CO2RR was revived. Accordingly, hand-painting which suffers from low reproducibility and questionable transfer into industrial environment was replaced by state-of-the-art techniques used in similar applications, such as air-brushing or electrodeposition and instead of PTFE producing hydrophobic GDEs, Nafion is almost exclusively used as binder (see below).

Although the electrode preparation method substantially influences the properties of the GDE and is an important factor for technical realization, studies examining the influence of the applied technique or comparing different methods are scarce. A comparison of different preparation methods is to the knowledge of the author only presented by Kenis et al. who evaluated an air-brushing and hand-painting method regarding homogeneity of the catalyst layer for CO2RR to CO using micro-computed X-ray tomography [127]. As expected, the automated air-brushing significantly improves reproducibility, uniformity of and material distribution in the catalyst layer at reduced agglomeration. This improvement directly translates to an increase of CO FE and illustrates the importance of choosing an appropriate and state-of-the-art deposition method.

GDE architecture and properties

In contrary to earlier studies in which PTFE was employed in hydrophobically rendered GDEs, nowadays Nafion solution is used in almost any case to serve as binder in the catalytic layer (CL) of the GDE. The technology and the composition of the ink formulation is inspired by PEM fuel cell and water electrolysis electrode manufacturing. Despite different requirements for the reactions this allows leveraging the experience of a highly optimized and state-of-the-art preparation procedure. For fuel cells, the use of the proton-conducting ionomer Nafion as binder, which was developed as ionomer in acidic media [128], is essential and serves the purpose to extent the triple-phase boundary, *i.e.* proton transport, from the polymer-electrolyte membrane interface into the CL. In contrast, in the case of CO2RR, the proton source for the reduction is water from the liquid electrolyte, thus, this necessity does not apply. Most importantly, the rational of Nafion completely replacing PTFE as binder of choice in acidic fuel cells was largely driven by the aim to reach 100% Pt-utilization as number one priority to minimize its loading and cost. The disadvantage of hydrophobic electrodes in this respect, is that a significant part of the electrode structure, which comprises both wetted and non-wetted hydrophobic PTFE-coated regions, does not participate in the reaction. Thus, catalyst dispersed in these channels is not in contact with electrolyte and therefore lost. In alkaline media on the other hand, the effect of using the expensive Nafion is merely limited to improving water uptake due to its hydrophilicity which can be an important property when, as in the case of PEMFC, expensive catalysts are used and a fully wetted electrode architecture is desired [129]. On the other hand, certain hydrophobicity has been demonstrated to be an important feature of GDEs in alkaline media, to achieve distribution of gas and liquid phase throughout the active layer which can significantly increase TPB as gas-phase diffusion is known to be orders of magnitude faster as that of species in dissolved state [31]. In addition, extensive use of Nafion leads to high proton concentration which is suggested to be problematic for CO2RR where the reduction of CO_2 competes with HER [62]. However, as promising results have been achieved with Nafion-bound GDEs in this reaction, this evidently does not seem to constitute a severe problem. The question is rather, if a hydrophobic or hydrophilic catalytic layer is aimed for and which approach serves the requirements of the reaction better. In this light, also the use and optimization of the gas diffusion layer as backing substrate of the CL has to be discussed. The rationale in the development of multi-layered electrodes consisting of catalytic, gas diffusion and microporous layer was the ability to tailor each layer according to its requirements. This means the catalytic layer can be optimized according to desired wetting degree and catalyst loading while the GDL for high gas permeability and hydrophobicity to prevent flooding of the gas transport channels. Whereas in PEMFC an important aspect is the water management of this layer, i.e. removal of formed water in the CL cathode (ORR), this does not apply for CO2RR where it mainly serves as separator between electrolyte-wetted catalytic layer and the gas-phase as well as efficient delivery of CO_2 to the reaction zone. An additional benefit of the microporous layer (MPL) is a decrease of contact resistance between the macroscopic GDL substrate and the more dense catalytic layer [130]. Accordingly, so far only Kenis et al. have examined its influence on CO2RR and developed their own design, based on the above-mentioned automated air-brushing method whereas in most literature studies commercial type of GDLs were used. In the work of Kenis, it was shown that deposition of the CL directly on the macroporous fiber substrate GDL substantially deteriorates achievable current densities to below 30 mA/cm² compared to almost 300 mA/cm² when an appropriate wet-proofed MPL is used. The latter physically separates electrolyte from the diffusion layer and allows homogeneous and uniform distribution of the CL. They further investigated the important interplay between wet-proofing, gas permeability, electrical resistance and the performance of the GDE assembly. In an array of additional studies on GDE optimization for CO2RR, also the influence of the support (Titania [131], carbon foam [132], carbon nanotubes (CNT) [133]) and the electrocatalyst [134,135] was evaluated. At the time this work herein was concluded, the highest achieved current density are 160 mA/cm² at 80% FE [102] and as high as 350 mA/cm² with FE close to 100% [133], for formate (Sn-GDE) and CO (Ag/CNT-GDE) production, respectively. The same approach of spraying a formulated ink as thin and fully-flooded layer on a GDL is used by the group of Irabien et al., which progressively optimized their preparation procedure with respect to metal-loading and tin particle size, reporting the production of formate at 150 mA/cm² and 70% FE in a full and continuously operated cell [136]. Using unsupported tin nanoparticles gave a very thin but dense catalytic layer impeding transport of CO_2 throughout the layer, rendering carbon-supported particles and a more porous layer more efficient (thickness 50 µm). High loadings on the other hand, translated in severe thickening of the layer without increase of actual reaction zone as diffusion of dissolved CO_2 through the flooded layer becomes the limiting factor. At high current density, the TPB shrinks to the region close to the GDL/CL interface, thereby, severely minimizing catalyst utilization which was also observed by Wu et al [137]. This is analogous to the case of a low effectiveness factor in heterogeneous catalysis where reaction is limited to the outer layer of the catalyst particle when reaction rates is much higher than diffusion. As a result, an important requirement for such type of GDEs is to obtain very thin catalytic layers, as exemplary depicted in Figure 3.5.

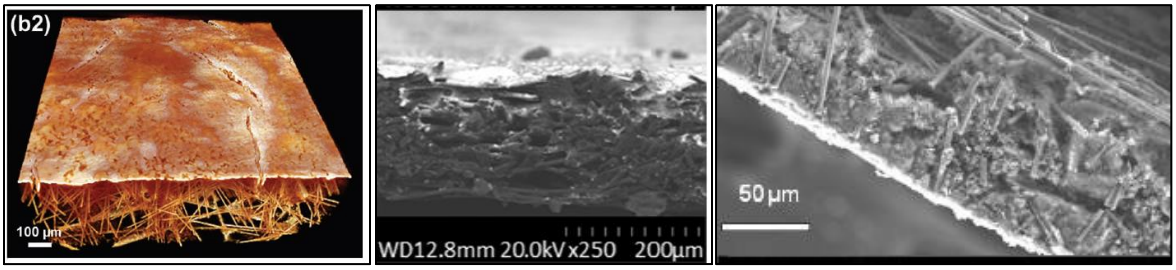

Figure 3.5 Images of thin-film catalytic layer-based GDEs employed in CO2RR ([127,136,138] from left to right)

This can be avoided when gas channels are implemented into the CL as it is the case in PTFE-bound GDEs with hydrophobic dedicated channels for gas transport distributed throughout the CL. In alkaline fuel cells with liquid electrolyte and non-noble metals (for which minimization of loading is not high priority), hydrophobic GDEs with PTFE as binder are still favored to maximize the triple-phase area and to achieve distribution of gas channels throughout the active layer [31]. The only more recent work for CO2RR-GDEs applying PTFE in the CL are the studies of Delacourt et al. [125] and Wang et al. [139]. Delacourt et al. prepared catalyst-coated ion-exchange membranes and PTFE-bound GDEs via hand-painting of a catalyst dispersion onto a support followed by hot-pressing. They further experimentally compared GDEs with different composition (two different carbon materials, PTFE addition, carbon loading) without going too much into detail on the relationship between the performance of these electrodes and their properties. At optimized conditions, the highest achieved current density towards CO was 30 mA/cm² [125]. Also, the reported maximum in [139] was relatively low with 25 mA/cm² and 90% formate selectivity. However, they reported the beneficial effect of supplying PTFE into the Nafion-bound electrodes which was ascribed to the formation of hydrophobic non-wetted gas channels increasing access of CO_2 throughout the electrode structure. The electrodes were prepared via spraying the CL onto a roll-pressed self-made GDL/MPL assembly. Obviously, comparing these more recent results with those from earlier work with much higher current densities, shows that there is definite promise and room for improvement for the use of such GDE structures which has not been realized so far.

3.4.4 Summary

Electrochemical CO_2 reduction is steadily approaching technical realization which is evidenced by the fact that it has left the realm of academic research and intruded industrial research facilities. Still, as discussed in the preceding chapters, there is the need for further improvement of the process, particularly, aiming at the technological advancement of electrode manufacturing, cell design and the demonstration of technical feasibility including long-term stability and technical upscaling as required for an economically viable process [20,21,140]. Ultimately, all the above studies show the potential of using and optimizing GDE structures. However, so far, the complex interplay between the electrode properties, the physico-chemical phenomena occurring during reaction and the electrochemical, macroscopically observable performance is barely understood. Systematic investigation including advanced multiscale modelling will aid in enhancing performance by facilitating sophisticated and rational design of electrode structures, their preparation and the choice of appropriate process conditions. The work conducted in herein is supposed to contribute towards this goal.

Chapter 4

Experimental Techniques and Cost Analysis

4.1 Electrode and Catalyst Preparation

Materials

The employed materials are listed in Table 4.1 together with the respective supplier and further information such as particle size or purity, when available.

Table 4.1 Information regarding employed materials.

Electrode Components	**Abbr.**	**Supplier**	**Additional Information**
Acetylene Black	AB	Alfa-Aesar	>99% Purity, 100% compressed
Vulcan XC72-R	VXC	Cabot	in granular form, milled before use
Ensaco 250	ENS	Imerys	
BlackPearls 2000	BP	Cabot	
KetjenBlack EC600JD	KB	AkzoNobel	
Norit GSX CAT	NOR	Cabot	
Pyrolyzed Wood 700°C	PW7	-	self-synthesis [141]
Pyrolyzed Wood 900°C	PW9	-	self-synthesis [141]
Polytetrafluorethylene	PTFE	Dyneon	TF 92070Z, agglomerate and primary particle size: 4 µm and 120 nm
Tin nanopowder	Sn	Sigma-Aldrich	particle size <150 nm, >99% trace metal basis
Sigracet GDL 39AA		SGL	Gas diffusion layer
Catalyst preparation and carbon modification			
Urea	CH_4N_2O	Carl Roth	>99.5% purity
Tin (IV) chloride	$SnCl_4 \cdot 5H_2O$	ACROS org.	>98% purity
Hydrogen peroxide solution	H_2O_2	Sigma-Aldrich	30 wt.-% in water
concentrated nitric acid	HNO_3	Sigma-Aldrich	68 wt.-% in water
Electrolysis			
Carbon dioxide	CO_2	Westfalen	4.5
Water	H_2O	Carl Roth	HPLC grade
Potassium bicarbonate	KHCO3	Sigma-Aldrich	99.99% trace metal basis

Potassium hydroxide	KOH	Sigma-Aldrich	Pellets, puriss, p.a., >85%
Potassium formate	HCOOK	Carl Roth	>98%, syn.
Analytics			
Helium	He	Westfalen	4.6
Nitrogen	N_2	Westfalen	5.0
Sulfuric acid	H_2SO_4	Sigma-Aldrich	
Water	H_2O	Carl Roth	HPLC grade

Preparation of gas-diffusion electrodes

GDEs have been prepared *via* a simple dry pressing method. The powder components are thoroughly mixed in a knife mill (IKA, M20 Universal mill) in predetermined intervals to obtain a homogeneous and reproducible mixture. Intermediate pause periods are implemented to prevent excessive heating of the powder mixture. The GDEs are typically comprised of a carbon black or an activated carbon type, Polytetrafluorethylene (PTFE) powder and tin / tin oxide as electrocatalyst (in the following denoted SnO_x). The latter is either mechanically mixed using commercial nanoparticulate tin powder or supported on the carbon black beforehand. For the reference GDE with 1 mg/cm² SnO_x, a carbon:PTFE ratio of 65:35 was chosen and the mass loading of the powder mixture was set to 33.7 mg/cm². When different metal loadings were examined, the mass of carbon and PTFE, *i.e.* the porous electrode matrix, was fixed (not the overall mass which changed due to the loading variation). For different PTFE contents, the carbon and SnO_x mass was set constant, to maintain both a fixed SnOx loading on the GDE and constant carbon:SnOx ratio. The powder mixture is put in a cylindrical mask of 4 cm diameter and compacted with a hydraulic press at 11 kN/m² if not otherwise mentioned. Finally, the GDE was sintered in an oven at 340 °C, slightly above the melting point of PTFE for 10 min in N_2 atmosphere. For practical reasons, a gas diffusion layer (GDL, Sigracet GDL 39AA, SGL) is placed on the backside of the GDE. Due to the location of the triple-phase boundary inside of the thick single-layer GDE relatively close to the electrolyte side (see chapter 6.3) and the duration of the electrolysis tests, the GDL does not have effect on electrochemical performance as demonstrated in preliminary studies not shown herein. This is in contrary to thin catalytic layers which use the GDL as gas distribution and which utilize the full thickness of the catalyzed layer. A stainless-steel net is incorporated into the half-cell set-up for contacting the GDL. For later technical realization, the stainless-steel net can be incorporated into the GDE as current collector without changing the preparation method or the performance of the electrode.

Preparation of carbon-supported tin oxide

The SnO_x electrocatalyst is synthesized by a homogenous precipitation method, based on [142]. $SnCl_4$ is dispersed in aqueous urea solution (0.5M in double-distilled water), carbon black is added in an amount depending on the desired catalyst loading and sonicated for one hour to deagglomerate the carbon agglomerates and facilitate thorough wetting. After that, the solution is mixed for further 4 hours at vigorous stirring with a magnetic stirrer. The last point is essential to ensure a homogeneous dispersion of the catalyst over the carbon surface. The slurry was then refluxed at 90 °C for 4 h through which urea slowly decomposes. As a result, the pH value is homogenously increased resulting in precipitation of tin oxide on the carbon surface. Actual tin mass has been quantified by burning off the carbon at 1000 °C and weighing the tin oxide leftover. The metal loading is always referred to tin metal content independent on oxidation state to allow for a comparison between the synthesized tin oxide nanoparticles and the metallic tin powder (with thin native oxide layer) used as starting point in this work.

Modification of carbon black to increase hydrophobicity

The carbon black types VXC and AB were oxidized using two different methods to increase their hydrophilicity and respective wettability. Moderately strong oxidation was conducted by heating 3 g of the carbon black in 250 ml of concentrated HNO_3 (68 wt.-%) to 70 °C for 2 hours [143]. The temperature was then reduced to 35°C for 24 hours. Mild oxidation was conducted by suspending the same amount of carbon black in 30 wt.-% H_2O_2 solution at 30 °C for 2 hours [144]. In both cases, the carbon black was finally washed and dried at 60 °C over night.

4.2 Experimental procedure

Half-cell experiments

Semi-batch experiments were conducted in a custom-made half-cell designed by the German Aerospace Center (DLR) and fabricated from polymethylmethacrylate (PMMA). The cell consists of cathode and anode chamber separated by a proton-conducting membrane (Nafion® 117, DuPont). A scheme of the set up is given in Figure 4.1. 8 mL of catholyte and 20 mL of anolyte were filled into the respective chambers before the experiment. For isothermal conditions (see below), the catholyte chamber was increased to 30 mL to accommodate the additional periphery. During the experiments K^+ ions are transported through the membrane from anode to cathode chamber to maintain charge neutrality, resulting in depletion of conducting salt on the anode side. High enough salt concentration is therefore necessary for prolonged electrolysis at high current densities conducted in this work. 2 M $KHCO_3$ was chosen for this purpose. Both chambers were agitated throughout the experiment using a magnetic stirring bar. CO_2 was fed from the back of the GDE (geometric area 1 cm²) with a mass-flow-controller MFC, Bronckhorst), with the unreacted CO_2 and the gaseous products being passed to a gas-chromatograph (see Analytics) for product quantification. Depending on the set current density, the flow-rate was adjusted between 5 and 15 nmL/min such that conversion was always <10% to ensure excess of CO_2 in the gas-phase, *i.e.* prevent limitation by CO_2 supply from the gas chamber, as it was noticed in preliminary experiments to have an effect. To ensure reproducible conditions, the system was always allowed to equilibrate for 10 min under CO_2 flow, before the experiments were started, as especially in the first minutes large quantities of CO_2 are dissolved into the electrolyte. The experiments were conducted using a potentiostat

(Gamry Reference 3000), a Pt-foil counter electrode and a Hg|HgO reference electrode filled with 1M KOH (E = 98 mV vs. SHE at pH 14 and 25 °C). Preliminary experiments were conducted without cooling of the cell but at room temperature. Already at moderate current densities, the heating of the cell became considerable, as described in chapter 6.3.1. Therefore, the set-up was modified to include cooling and ensure isothermal conditions. This was done by pumping the electrolyte through an external cryostat. The temperature was monitored during the experiments via a Type-K thermocouple inside the cell and recirculation speed of the electrolyte adjusted such that a temperature of ~25 °C was maintained. It is mentioned in the text if isothermal conditions were ensured or not.

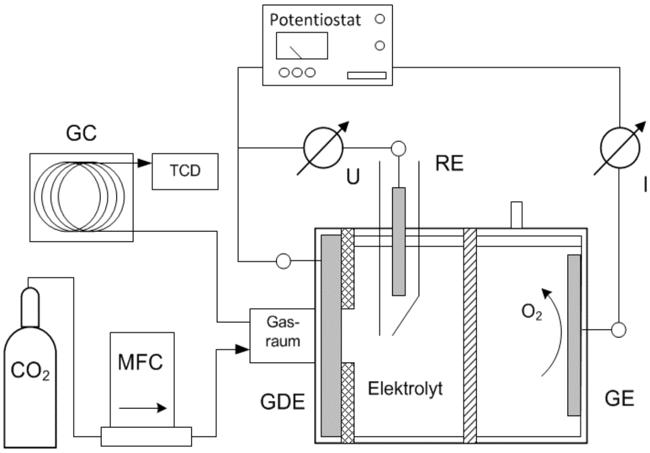

Figure 4.1 Sketch and process flow-chart of experimental set-up

Analytics

The amount of formate produced was quantified using high performance liquid chromatography (HPLC) with an Agilent Technology type 1200 equipped with a Nucleogel Sugar 810H column (Macherey–Nagel) and an refractive index detector. The eluent consists of a 5 mmol/L aqueous solution of H_2SO_4 as suggested from the manufacturer. To evaluate gas phase composition, an Agilent Technologies 7890 gas chromatograph was employed. Samples were injected on a separation column combination of Poropak Q and Molsieve 5A connected to the thermal conductivity detector. Combining both GC and HPLC, the current balance could be closed in between 5% for all experiments. Furthermore, for selected and exemplary experiments covering the whole range of experimental conditions, the carbon balance was quantified, including dissolved CO_2 and generated bicarbonate. For all conditions, it could be closed within 10%.

4.3 Characterization Techniques

4.3.1 Nitrogen physisorption

For nitrogen physisorption measurements liquid nitrogen at 77 K is dosed in known volume intervals to an evacuated and degassed sample and the amount of adsorbed nitrogen measured at the respective equilibrium partial pressure. Point by point this yields an adsorption isotherm for which information can be extracted regarding the porosity of the studied sample. Adsorption isotherms were collected with a Quantachrome Autosorb 3B and liquid nitrogen at 77 K, the samples were degassed at 120 °C for 16 h. The linear range employed for BET-method was chosen between $p/p0 = 0.05$ and 0.3. For the pore size distribution in the mesopore range, the BJH-method was chosen to give a qualitative assessment. To exclude pore network effects, the adsorption branch was used for evaluation which is recommended for disordered, connected pores [145]. Microporosity is assessed by the t-plot method using carbon black as reference material to obtain the statistical thickness

4.3.2 Mercury porosimetry

In Hg-porosimetry measurement the non-wetting mercury is forcefully penetrated with pressure against its surface tension into the pores of a porous sample while the volume change of the liquid, which equals the wetted pore volume, is plotted over the applied pressure. Using the Laplace-Washburn equation with the surface tension γ (0.48 N/m for Hg) and contact angle between liquid and sample (140° for Hg), the employed equilibrium pressure can be converted into the corresponding pore diameter d_{pore} which is just wetted at the respective pressure.

$$\Delta p = 4\,\gamma \cdot \cos\theta \;/\; d_{pore} \tag{4.1}$$

Thereby, a pore size distribution as a function of pore diameter can be constructed. Due to an overlap with the distribution obtained from physisorption in the mesopore-range, both methods can be checked for consistency. The porosimetry hysteresis has been recorded via a Pascal 140 porosimeter (Porotec) at the DLR by Gudrun Steinhilber and Noriko Sata. The apparatus allows the application of pressures up to 200 MPa in order to assess pore diameters down to 7 nm. As pressure is increased in increments, one only gets information about wetted pore volume for a specific range, the reported values correspond to the median of these intervals. Also, it is important to keep in mind, that the pressure employed corresponds to the pressure necessary to access the specific pore *entry*. Thus, one actually does not get information on the respective pore diameter but rather the diameter of the narrowest entry to the pore. This can, in specific cases, lead to misinterpretation and a lack of consistency between results from porosimetry and observations from microscopic techniques. Furthermore, difficulty in interpretation arises for complex pore networks without well-defined pore geometries.

4.3.3 Scanning electron microscopy (SEM)

In order to get a better understanding of the electrode structure, images were taken with an electron microscope. The SEM images were taken by Ina Plock at DLR. An ULTRA plus electron microscope from Zeiss was used for that purpose. To make the distribution of different elements in the images visible, material contrast images were created by using an angle-specific backscatter detector, in which different shades of grey are recorded depending on the density of the material. By measuring the X-rays which the scanned area sends back due to the excitation by the electron beam and which are characteristic for the composition of the scanned area, exact information about the occurrence of different elements at this location can be made. This method is called energy dispersive X-ray spectroscopy (EDX) and was also used. Mapping this information over the whole evaluated surface allows to produce so-called element maps. The shading of the colors in these images represents the measured signal intensity for the respective elements.

4.3.4 X-ray Diffraction (XRD)

X-ray diffraction (XRD) analysis of the supported electrocatalyst powder and the electrodes was carried out using a Bruker D8 Advance diffractometer at 35 kV and 40 mA with a CuKα (λ= 0.154 nm) radiation source.

4.3.5 X-ray photoelectron spectroscopy (XPS)

X-ray photoelectron spectroscopy (XPS) is a surface sensitive characterization technique which gives information on the elemental and chemical composition of the sample surface. This is done by irradiating the sample of interest with a beam of electromagnetic X-ray radiation exciting electrons in the inner shell of the atom and deliberating them from the atom with a kinetic energy with which it is detected. The kinetic energy of the emitted electrons is characteristic for the atom it was detached from and its binding energy. The intensity of the signal which is proportional to the number of emitted electrons can be used to gain quantitative conclusions on the composition.

XPS was performed by Pawel Gazdzicki from the DLR using a Thermo ESCALAB 250 (Thermo Electron Corp.) ultra-high vacuum facility with a base pressure of $1 \cdot 10^{-9}$ mbar. Analysis was conducted using a nonmonochromated AlKa X-ray source (Thermo XR4) operated at 300 W in combination with a hemispherical six-channeltron electron energy analyzer operated in small area mode, i.e., on 0.8 mm^2

analyzed surface area. The atomic concentrations are quantified using sensitivity factors provided by Thermo Scientific using the Shirley algorithm for peak background correction.

4.3.6 Capacitance Measurements and Electrochemically Active Surface Area (ECSA)

The analysis of the double layer capacitance as measure of the surface area of the electrode in contact with liquid electrolyte is based on the fact that an electrochemical double layer is formed at the electrode-electrolyte interface as soon as an electrode is immersed in an electrolyte solution. It is characteristic for the material-electrolyte combination at given experimental conditions. When a defined material-electrolyte combination is used, the macroscopically measurable capacitance correlates linearly with the wetted surface area of the material. Although, the specific capacitance of a material is usually difficult to access, especially if an undefined and non-homogeneous surface exists, it can give a qualitative measure with which the electrochemically active surface area (ECSA) can be compared when the same material combination is used.

Capacitance analysis is conducted by performing consecutive cyclic voltammetry (CV) measurements at increasing scan rate (10, 20, 40, 60, 80, 100 mV/s) under open-circuit voltage (OCV) conditions. To obtain meaningful results, long enough breaks are necessary for the cell to reach equilibrium and the CV curves to reach stationary behavior. This is the case due to a partial withdrawal of electrolyte from the pore network and pronounced accumulation of reaction products. If this is not ensured, the curves strongly deviate from the horizontal double layer charging making a quantitative analysis impossible. Normally, a break of 20 min was sufficient. The starting point, direction and potential range for the CV scans were optimized with regard to what gave the best results. The CV scan was commonly started at OCV and the potential scanned in positive direction for 40 mV and back to OCV. The CV was repeated two times, before stepping directly to the next scan rate without intermediate break. For analysis, the oxidative current of the median potential during the third scan of each scan rate was chosen to achieve the best reproducibility. The procedure is described exemplary in chapter 5.2.1. To ensure robustness of the results, the possibility of the change of electrolyte composition over time having an effect on specific capacity of the material/electrolyte combination was examined by performing two consecutive capacitance measurements with different electrolyte composition (0.1 M after electrolysis and fresh 1.0 M $KHCO_3$). The obtained CV spectra did not show any difference.

4.4 Derivation of cost calculation

The reference electrolyzer for which a cost estimate is implemented herein is based on an exemplary commercial alkaline water electrolysis system which is adjusted to CO2RR operation according to the considerations described in chapter 7. The development of the model, its contributions, the most important concepts and assumptions are elaborated in said chapter. For better readability, a few calculations and the summary of the quantitative assumptions that went into the model together with the references (Table 4.1), are given in the method section herein. The total cost of the electrolysis system, C_{total}, in units of €/Ah_t is calculated as

$$C_{total} = \frac{C_{stack} + C_{operation}}{i \cdot FE} + C_{electricity} \cdot \frac{U_{0,cell}}{EE} \qquad 4.2$$

where C_{stack} is the depreciated investment cost associated with the electrolyzer stack (in units of $€\cdot m^{-2}\cdot h^{-1}$, see below), $C_{operation}$ is the operating cost excluding electricity (normalized on electrode area, $€\cdot m^{-2}\cdot h^{-1}$), i is the current density ($A\cdot m^{-2}$), FE is the Faraday efficiency (percentage of charge that goes into the desired product), $C_{electricity}$ is the cost of electricity ($€\cdot kWh^{-1}$), $U_{0,cell}$ is the standard voltage of the cell reaction (V), and EE is the energetic efficiency (percentage of electrical energy converted into chemical energy of desired product).

To distribute stack cost over the run time of the electrolyzer, a simple financial model is implemented, assuming fixed payment at equal intervals. Using an interest rate r of 5% on the capital investment and a loan term of 20 years, the annual cost can be calculated as fixed-rate mortgage [146] according to

$$C_{year} = C_0 \, \frac{(1+r)^{years} \cdot r}{(1+r)^{years} - 1}. \qquad 4.3$$

As annual run time, 5000 hours/year at average nominal load are assumed to be realistic for Germany to account for the availability of cheap renewable electricity and the flexibility of the process to adapt to the volatile electricity market [147] while ensuring a high enough utilization to facilitate an economic operation. Accordingly, when prices are low and excess electricity from wind and solar energy is available, the electrolysis is ramped up and down when prices are high (maintaining inside the flexibility range of the electrolyzer).

Table 4.2 Summary of assumptions and references that went into analysis model.

	unit	**value**	**Reference**
Investment cost of system (2030)	€/kW	580	[148]
Conversion factor betw. power and area	kW/m²	6	calc. from [149]
Stack share on investment cost	%	50	[148]
Installation factor	-	1.1	
Installed stack cost per area	€/m²	1,914	calc.
Maintenance	%	5	[148]
Financial model			
Run time per year	h/year	5000	[147]
Interest rate	%	5	[150]
Loan term	years	20	[150]
Stack cost incl. financial model	€/m²h	0.0307	calc.
Electrochemistry			
Standard cell voltage (base case)	V	1.12	$HCOO^-$ at pH14
Faradaic efficiency (base case)	%	80	target
Energetic efficiency	%	-	analysis variable
Electricity			
Electricity price (base case)	€/kWh	0.05	[151]

Chapter 5

Analysis of Electrode Properties

Prior to discussing the results of the electrochemical characterization during CO2RR in the upcoming chapters, a comprehensive investigation of the electrode properties is conducted and summarized herein. This is important to understand and classify the results of the electrochemical experiments and to get a better understanding on how the gas-diffusion electrode is constructed, how it works and how it behaves during the reaction. To this end, textural properties of the three-dimensional pore structure will be evaluated using porosimetry, physisorption and microscopic methods. Subsequently, wettability by the aqueous electrolyte, an important metric to assess the extent of the reaction zone, will be discussed. The more general description of the GDE properties in this chapter will be complemented by a more detailed and concluding assessment in the respective chapters discussing and explaining the electrochemical performance. Besides giving information on the GDE properties, the goal of this chapter is further to introduce the characterization methods important to this work for which meaningful examples have been chosen.

5.1 Investigation of the Electrode Texture

5.1.1 General description of the pore system

The gas-diffusion electrode is a porous system which is formed by its constituents during the preparation process. The porous three-dimensional network is determined by the type of carbon and the preparation method. It spans several orders of magnitude in pore diameter which can only be assessed by a combination of different characterization techniques. The typical methods for evaluation of porosity related properties are gas physisorption, most commonly with nitrogen, porosimetry by mercury intrusion as well as microscopic methods. Both physisorption and porosimetry have their respective limitations regarding the range of pore diameters which can be assessed and can therefore be considered complimentary. Physisorption is the method of choice for micro- ($d < 2$ nm) and mesoporous ($d < 50$ nm) materials and, depending on the pore structure, allows access to pores up to 100-150 nm before the saturation pressure of liquid nitrogen sets in, with a meaningful assessment suggested to be below 50 nm [152]. The intrusion of the non-wetting mercury, on the other hand, is dependent on the maximum applicable pressure of the measuring device. This normally restricts the wetting capability to pores above 5 nm, yet, up to several micrometers in size. The combination of both methods can give a very complete assessment of the porous structure of the electrode. As there is a certain overlap of pore diameters this can be used to validate the consistency of the methods. This is exemplary shown in Figure 5.1 on the left for the benchmark GDE (prepared from Acetylene Black, 35% PTFE and 5 mg/cm² commercial tin powder), in which the logarithmic pore size distributions of a GDE for both methods are included. As one can see, both methods demonstrate a good consistency in the measurements at hand. Furthermore, the same data is also plotted as cumulative pore volume (dashed black line), together with the linear pore distribution *dV/dD* in the inset on a linear x-scale in the range of interest. The meaning of the different types of plots is described further below.

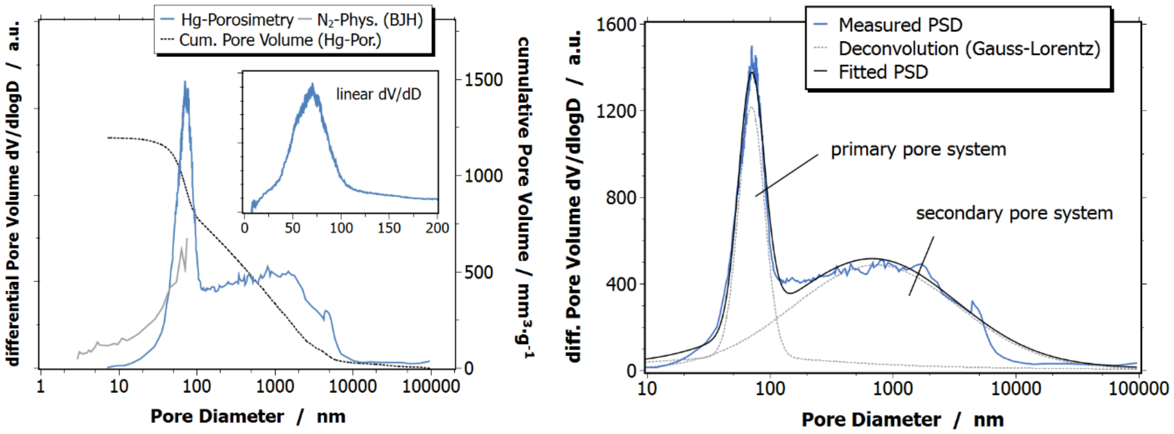

Figure 5.1 Logarithmic pore size distribution derived from N_2-physisorption (BJH) and Hg-porosimetry, cumulative pore volume and linear distribution (left), deconvolution of primary and secondary pore distribution (based on Gauss-Lorentz-distribution) employed on data from Hg-porosimetry (right), both AB35K

The pore distribution obtained *via* N_2-physisorption has been derived by applying the commonly employed BJH method (Barrett-Joyner-Halenda) onto the adsorption isotherm which is recommended for disordered and connected pore systems to avoid influence of pore-network and percolation effects [153]. The method is based on the modified Kelvin equation which describes the shift of the liquid-gas phase transition of the adsorbate inside a pore of certain radius due to wall-adsorbate interactions as compared to the transition in the bulk. It can be described by the macroscopically observable surface tension and contact angle between adsorbate and pore wall, thereby relating transition (condensation/evaporation) pressure to pore radius. Despite being a very widespread method and considering that it yields the expected result in the above example, one has to be aware of the limited universality and model assumptions that the BJH method is based on. Accordingly, it has to be exercised carefully if the real pore structure has to be reproduced as precise as possible. Especially in the range of small mesopores (d<15 nm) deviations from reality are to be expected [154] due to the macroscopic and thermodynamic concept of the underlying modified Kelvin equation. For the qualitative assessment and comparison of (rather macroporous) materials of a given class which is done here, it is suggested to be a simple and adequate solution.

Pore size distribution (PSD) *via* mercury porosimetry, on the other hand, relies on the application of the Laplace-Washburn equation (see experimental section), which correlates the applied pressure for intrusion of a non-wetting liquid with the pore radius by accounting for surface tension and contact angle. The interpretation of the data from porosimetry is not straightforward, which is why some explanations on the different type of plots are included here [152]. The *logarithmic* PSD (*dV/dlogD*, depicted on the left and the right) is a convenient choice for plotting the distribution when the pore network spans a broad range of diameters over several orders of magnitude and when a qualitative comparison of different materials over the whole pore range is of interest. However, its analysis does not allow for a direct *physical* interpretation of the pore nature and the respective pore volume over a discrete range of interest. This is because larger pores are strongly emphasized as a result of normalizing on the differential *logarithmic* pore diameter *dlogD*. Thus, their magnitude observable in the graph and the value on the y-axis does not reflect their actual contribution to the pore volume, as well summarized in [154]. A more unambiguous way of presentation is the *linear* distribution *dV/dD*, which is recommended by the IUPAC and given in the inset frame on the left. In this presentation, however, the large pores are not visible in the graph (therefore only limited x-range shown). Thus, compared to the share of pores below 100 nm, large pores are rather evanescent when depicted on a differential scale which resembles reality more intuitively. Both representations are mathematically related to each other by the coordinate transformation D → logD. However, a direct physical comparison of the data is not possible. The cumulative pore volume (dashed line) is less prone for misinterpretation, reveals information on the complete pore system, and is therefore included throughout this work (*e.g.* Figure 5.1, left, dashed line). Also, since the logarithmic scale on the x-axis can cause confusion in the correct assessment of the data in either type of graph, the inset showing *dV/dD* is given on a *linear* x-scale [154].

For all measured carbon black-based electrodes, a bimodal pore structure with one distinct maximum below 100 nm and a very broad distribution in the micrometer range is observed in the porosity measurements which can be ascribed to the characteristic structure of the carbon black support. As the SEM images in the following chapter will show, compared to activated carbon or graphite, carbon black has a very distinct structure made up of the spherical primary carbon particles which are intergrown into aggregates that form a three-dimensional porous network. The voids between the carbon particles inside of the agglomerates that are made up of the aggregates is known in literature as the primary pore system. It can be well recognized in the linear pore distribution *dV/dD* given in the inset in the graph as well as in the sudden change in the slope of the cumulative pore volume. The inter-agglomerate porosity formed due to the binder particles which spread during thermal treatment and leave larger voids in the µm-range constitutes the superordinate secondary pore volume. To illustrate this, in Figure 5.1 on the right, both pore modes are deconvoluted and fitted to a Gauss-Lorentz distribution.

Due to their respective measuring range, nitrogen physisorption and porosimetry both have their respective advantage in the assessment of each part of the pore system. In the following, nitrogen physisorption will be employed to evaluate the carbon-derived micro- and mesoporosity of the carbon and the resulting electrodes, *i.e*. the microstructure and the primary pore system of the GDE. Due to the above-mentioned limitation of the BJH-model, no pore size distribution will be evaluated on the basis of the adsorption isotherm. Instead, the PSD from Hg-porosimetry will be consulted for pores with d>5 nm. The secondary pore volume of the electrodes, which is not accessible *via* physisorption of liquid nitrogen, will be assessed using Hg-intrusion.

5.1.2 Visualization of Pore Structure by Scanning Electron Microscopy (SEM)

In the following some exemplary scanning electron microscopic (SEM) images are shown to elucidate important aspects of the GDE structure and to aid in the quantitative description in the subsequent chapters. Additional images will be shown in further chapters throughout this thesis where their information is valuable.

General assessment of the pore network

The SEM images of the GDE in Figure 5.2 and Figure 5.3 reveal the typical appearance of carbon black materials discussed above which are comprised of the spherical primary carbon particles with a diameter ranging between 20 and 40 nm. These particles form small colloidal aggregates during the synthesis of the material which in turn build larger agglomerates that form the backbone of the porous network (see theory section, chapter 2.5.1). One such agglomerate is shown in Figure 5.3 on the right. Further zooming out shows the inter-agglomerate void space between these agglomerates, already above 100 nm and up in the micrometer range (Figure 5.2 right and Figure 5.3 left), which is essential for gas passage through the electrode. The carbon black-based GDEs resemble each other to a large degree regarding their general texture and are mostly undistinguishable. Therefore, only the images of the AB-GDEs are shown. The activated carbon-based samples on the other hand, Norit GSX CAT and the pyrolyzed wood sample (produced in [141]) are substantially different in their morphology, as shown in Figure 5.4, with a more heterogeneous and disordered structure which is governed by the activated substrate.

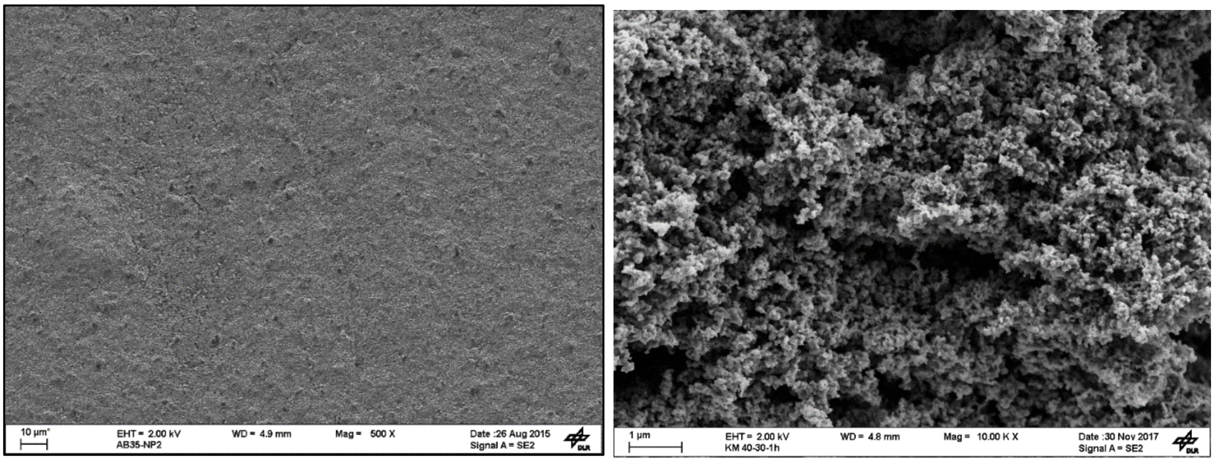

Figure 5.2 SEM image of AB35NP-GDE at 500x and 10.000x magnification.

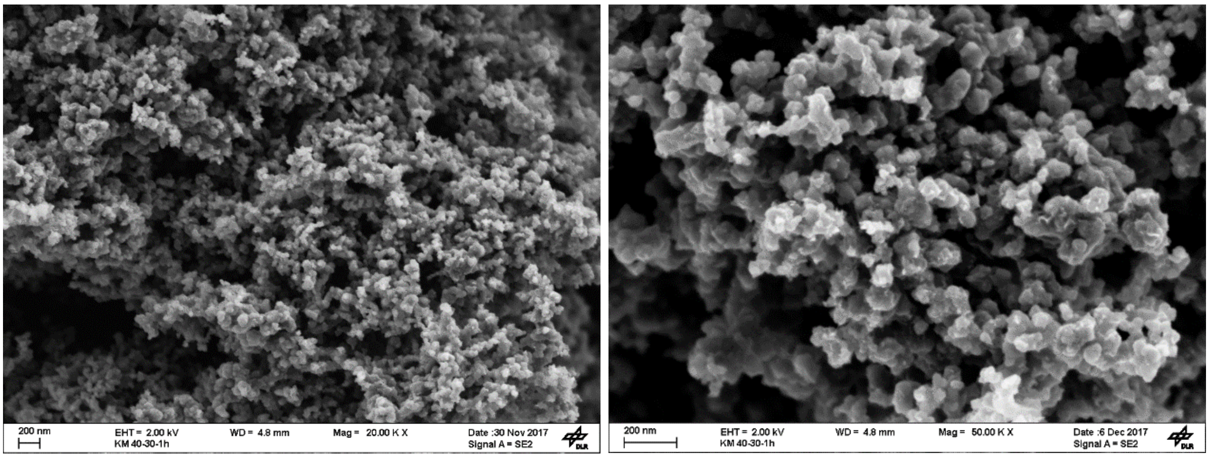

Figure 5.3 SEM image of AB35NP-GDE at 20.000x and 50.000x magnification.

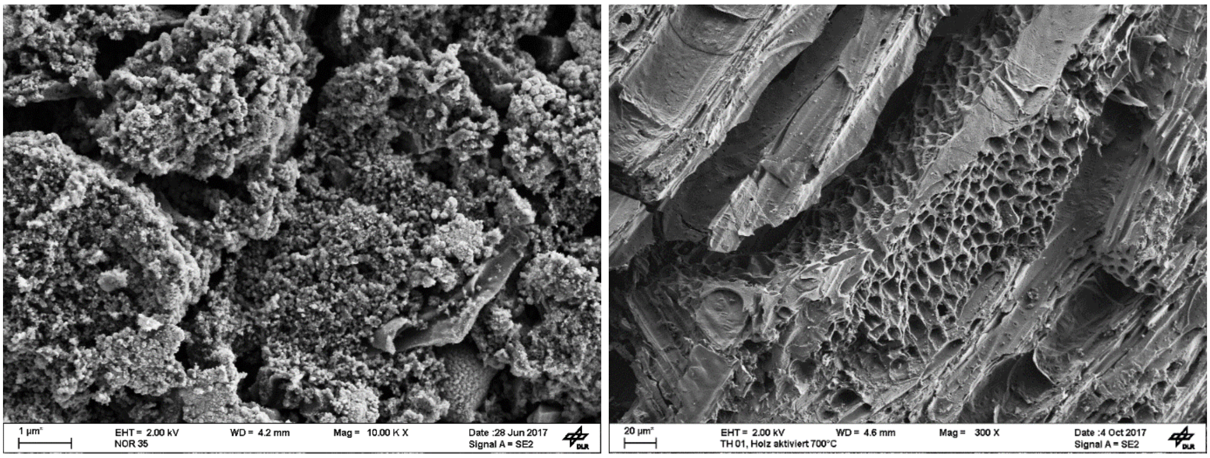

Figure 5.4 SEM image of the activated carbon-based GDEs, Norit (left) and the pyrolyzed wood sample (right) showing the irregular texture of the carbon material.

Distribution of PTFE and the Effect of Thermal Treatment

In order to keep the agglomerates together, the catalyzed carbon powder is mixed with the binding agent Polytetrafluoroethylene (PTFE) and undertaken a subsequent thermal treatment step at 340 °C after pressing. This treatment step turned out to be a crucial prerequisite for the electrolysis as it tremendously improves the mechanical stability of the electrodes and facilitates employing the electrodes at higher current densities. For the analysis, the slightly higher atomic mass of fluorine in the PTFE compared to the carbon, allows visualizing its distribution using an angle-selective backscattering detector which renders heavier atoms slightly brighter. This is shown in Figure 5.5 on the left for a GDE before the thermal treatment. The gray-colored PTFE particles between the black agglomerates can be seen by careful observation with their particle size around a few µm. This is consistent with the properties given by the manufacturer (average agglomerate size of 4 µm, primary particle size of 120 nm). The bright white particles are the agglomerates of the commercial tin powder from which a few also range up to several µm in size. Increasing the magnification in Figure 5.6, the PTFE filaments are visible which form during manufacturing of the electrode, *via* the shearing force in the knife mill during the mixing step and the high compacting pressure during pressing. This morphology is known from literature for electrodes prepared *via* dry deposition and suggested to play a pivotal role in supplying mechanical integrity [46].

After thermal treatment of the electrodes, the picture looks substantially different. As the treatment entails heating the GDE beyond the melting point of PTFE (327 °C), neither the filaments, nor the large particles can be observed (Figure 5.5, right). Zooming out in order to reveal the morphology of the surface, as done in Figure 5.7, one can see that the PTFE particles leave behind large pores on the order of several µm when melted; an observation that will be quantified in the following chapter.

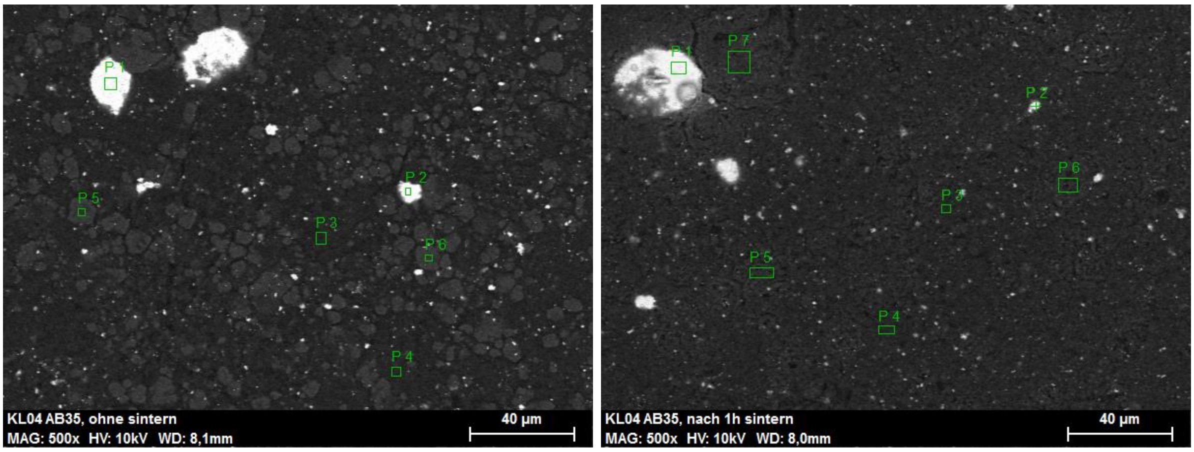

Figure 5.5. Material-contrast SEM images of GDE before (left) and after thermal treatment. Bright grey spots are PTFE particles, bright white is tin. Green square mark areas where EDX measurements were performed.

As it as originally intended, the PTFE is distributed more homogeneously over the surface, after thermal treatment. To make this more evident, EDX measurements before and after the treatment have been conducted. The corresponding weight concentration of the different atoms is given in Table 5.1 for the areas marked in green in Figure 5.5. In the pristine GDE, PTFE can mainly be found when analyzing the bright grey particles (P5+P6) while on the rest of the surface (P3+P4) the binder is absent. In contrast, it can be found throughout the electrode surface after the treatment with a concentration between 11% and 35%. It is important to note, that no further investigation on the heating conditions and their influence on GDE properties was performed although it is clear that the dispersion of the PTFE and its homogeneity leave room for improvement. As shown in [39], in which dispersion of PTFE and the resulting hydrophobicity is examined by optimizing heating temperature, this can indeed have an effect on the GDE performance and should be considered for the GDEs at hand in the future. The EDX analysis further reveals the elemental composition of the large tin/tin oxide particles, depicted in white in the SEM images. Whereas the particles were comprised mainly of metallic tin before the treatment (P1 and P2, in left image, >90% Sn), the oxygen content significantly increases thereafter resulting in a molar ratio of slightly above 2:1, indicative of a complete oxidation of tin to SnO_2 (measured wt.% of 21 and 70% for Sn and O corresponds to a molar ratio of 2.2:1). This is confirmed through further catalyst characterization using XRD and XPS in chapter 5.3.

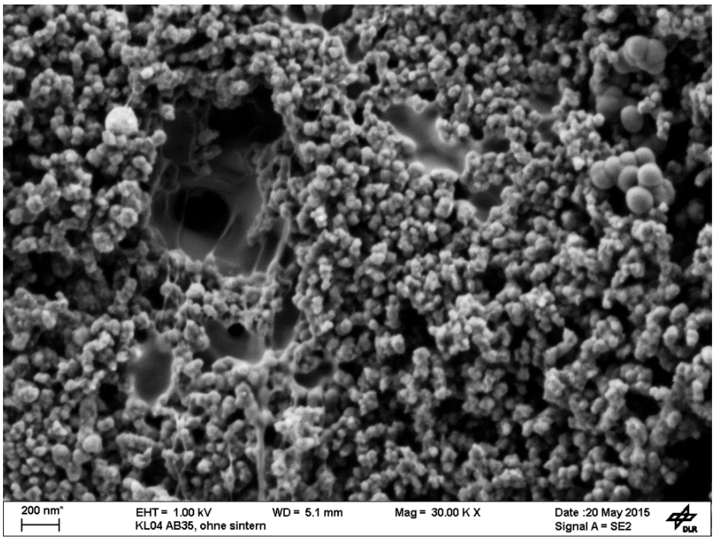

Figure 5.6 SEM image of GDE before thermal treatment showing the PTFE filaments.

Table 5.1. Elemental composition in weight percentage obtained from EDX analysis measured inside the green boxes (P1-P7) in Figure 5.5. Left is before, right after treatment

	C	O	F	Sn		C	O	F	Sn
P1	3.6	5.0	0.3	91.2	P1	2.7	21.3	4.6	71.5
P2	2.8	4.5	0.8	92.0	P2	4.7	21.0	5.2	69.1
P3	99.2	0.8	-	-	P3	85.4	-	11.4	3.1
P4	95.9	-	-	4.1	P4	87.9	-	11.5	0.5
P5	57.2	-	42.8	-	P5	80.1	-	18.6	1.2
P6	48.1	-	51.9	-	P6	76.4	-	21.6	2.0
					P7	63.9	-	35.0	1.1

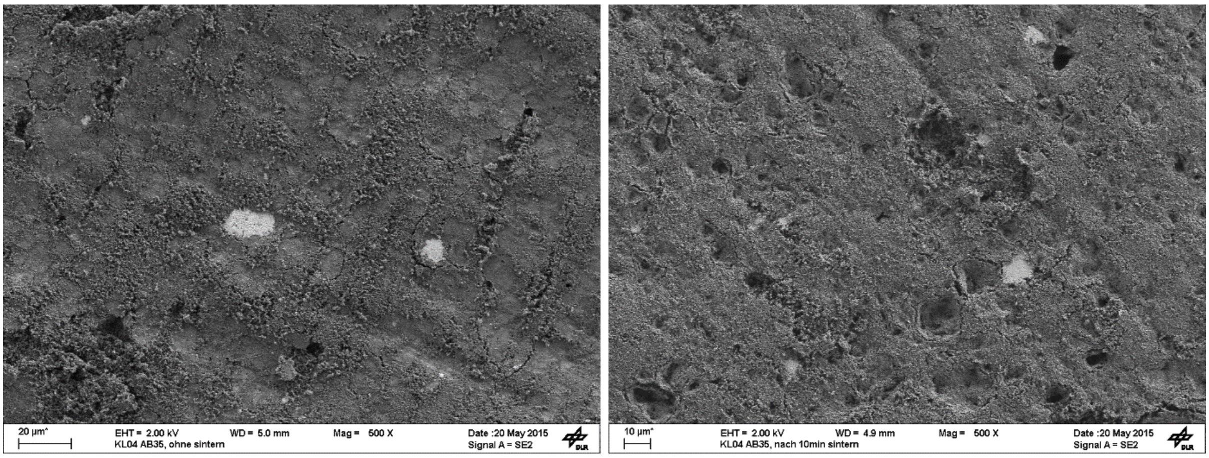

Figure 5.7 SEM image of surface morphology before (left) and after (right) melting of the PTFE particles during thermal treatment

5.1.3 Influence of Electrode Composition on Textural Properties

In the following. first. the textural properties of the carbon materials are assessed on the basis of physisorption data to allow for a first classification on the general difference of the materials. Subsequently. the analysis of the prepared GDEs is reported using both information from physisorption and porosimetry. This is done to determine the influence of the carbon support. PTFE content and the compacting pressure. It is attempted to obtain a quantitative assessment on how the GDE porosity is affected by its preparation parameters. separating the influence on primary (agglomerate). secondary (inter-agglomerate) porosity and its microstructure (accessible *via* physisorption). Such comprehensive investigation focusing on the understanding of how the porous GDE structure is assembled. how it is affected by preparation conditions and how it is operated have particularly been conducted in early studies on PTFE-bonded gas-diffusion electrodes for liquid electrolytes such as in [38.40.55].

Textural properties of the carbon materials

Within the frame of the project. various commercially available carbon materials have been tested with a wide range of different properties. as summarized in Table 5.2. Besides Norit GSX CAT (NOR) and the pyrolyzed wood samples which are activated carbons. all other examined materials are carbon blacks with a similar assembly of the porous network. as described in the theory section and as evidenced by the SEM images. The materials have been selected to cover a broad range of textural properties. As one can see in Table 5.2 and Figure 5.8. their porosity ranges from highly microporous such as Black Pearls 2000 (BP). to the mesoporous Ketjen Black (KB). types with intermediate surface area such as Vulcan XC72-R (in the following only called Vulcan or VXC) as well as the low-surface area and mostly macroporous Ensaco (ENS) and Acetylene Black (AB).

Table 5.2 Physisorption data of carbon materials employed in this work.
* surface area of pyr. wood determined by DFT (QSDFT model for cyl. pores. adsorption branch)

Carbon Material	**Abbr.**	**Type**	**BET** m²/g	**Micro** m²/g	**Micro** %
Acetylene Black	AB	Carbon Black	74	0	0
Vulcan XC72-R	VXC	Furnace Black	234	93	40
Ensaco 250	ENS	Carbon Black	78	0	0
BlackPearls 2000	BP	Carbon Black	1493	953	64
KetjenBlack EC600JD	KB	Carbon Black	1395	0	0
Norit GSX CAT	NOR	Act. Carbon	1580	875	55
Pyrolyzed Wood 700°C	PW7	Act. Carbon	1057*	986	93
Pyrolyzed Wood 900°C	PW9	Act. Carbon	1083*	1009	93

In the next paragraph. the classification is justified by the appearance of the adsorption isotherm. The surface area included in the above table was analyzed *via* the BET model with liquid nitrogen at 77 K. microporosity by the t-plot method using a non-porous carbon black as reference material to obtain the statistical thickness. In contrary to what is often the case in literature. total pore volume on the basis of physisorption is not evaluated herein. as no meaningful value exists in macroporous systems. This is evident by the absence of a plateau in the isotherm at high relative pressure [155]. Instead. total pore volume is assessed by Hg-porosimetry. Further. no additional distinction between meso- and macropores is undertaken. as the commonly employed BJH method for this purpose does not provide the robustness and universal applicability for meaningful and quantitative assessment of the differential pore volume while porosimetry is not fully reliable towards very small mesopores. In addition. in [154] it is pointed out that for the type of isotherm-shape that the carbon black-based GDEs exhibit (type H3 hysteresis). the BJH-derived pore distribution should be taken with caution. More sophisticated methods. such as DFT or Monte-Carlo are not applicable as no meaningful kernels exist for the materials at hand with a highly non-uniform pore system and heterogeneous surface chemistry.

In Figure 5.8. the adsorption isotherms of a selection of the employed carbon materials are depicted. As one can see. certain isotherms closely resemble each other in their appearance. namely the carbon blacks AB. VXC and BP. They can be classified type II isotherms according to the IUPAC classification. typical for macroporous adsorbates. The steep increase at very low p/p_0 before the inflection point is representative of micropore filling and indicates a large share of micropores (d<2nm) for BP which is responsible for its very high surface area (~1500 m²/g). The same accounts for the pyrolyzed wood sample. Starting at $p/p_0 \approx 0.2$ multilayer adsorption occurs together with capillary condensation in mesopores which translates into a continuous increase of the isotherm and is commonly accompanied by a hysteresis between ad- and desorption. which. for the above (AB. VXC. BP). can be observed only at high $p/p_0 > 0.8$. most closely resembling type H3 hysteresis. The absence of a plateau close to saturation pressure is also typical for macroporous materials for which no terminated pore-filling via liquid nitrogen exists. KB deviates from the other carbon blacks in that a pronounced hysteresis exists between ad- and desorption starting already at p/p_0=0.4. which has its origin in the presence of a substantial amount of small mesopores. This is verified by the high surface area of ~1400 m²/g but complete absence of microporosity. The pyrolyzed wood sample on the other hand. is almost exclusively comprised of micropores (93%) generated during chemical activation at high temperatures. The very horizontal plateau starting directly after the region of the micropore-filling indicates that the pore system is almost free of meso- and macropores accessible for liquid nitrogen. This corresponds to a perfect example of a Type I isotherm [156]. Due to its highly ultramicroporous nature (d<0.7 nm) for which N_2 physisorption is rather unsuitable. the results should be taken with caution. The most accurate way of determining the porous nature of such samples would be measurement of physisorption isotherms with CO_2 or He. The same accounts for the BET analysis model which is historically used but not the optimal choice for highly microporous samples. To come closer to reality. a more adequate DFT model particularly developed for microporous samples was employed herein to analyze the adsorption isotherms (QSDFT model for cylindrical pores. using the adsorption branch for analysis). Despite unclear accuracy of the results. the important takeaway here is that the pyrolyzed wood is extremely microporous and lacks the meso- and microporous pore network of the carbon blacks. which has substantial implications on the electrolysis. as will be discussed in the results section.

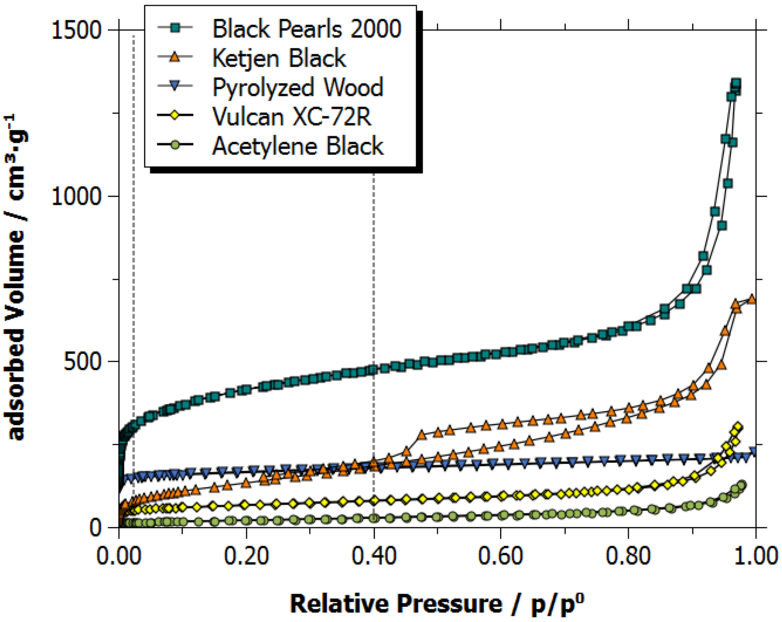

Figure 5.8 Excerpt of N_2 adsorption isotherms of employed carbon materials

Textural Properties of the GDEs

To get insight on what happens during manufacturing. the same analysis has been conducted for GDEs prepared with the above carbon materials. If not otherwise mentioned they are composed of 35% PTFE and 5 mg/cm² Sn-nanopowder. The GDEs are denoted with the PTFE-wt.% in relation to the matrix mass (PTFE + C) as number after the carbon type abbreviation (*i.e.* AB35 means Acetylene Black. 35% PTFE). The BET surface area and the micropore share for the GDEs with varying carbon types are given in Table 5.3. In addition. the surface area normalized on the carbon mass is also included to assess how the surface area of the carbon matrix changes due to the pressing. mixing with non-porous PTFE and its subsequent melting during thermal treatment. Unsurprisingly and despite normalization on carbon mass. the surface area of all the GDEs is significantly reduced during the preparation process. which is particularly pronounced for the high surface area samples and their microporosity. For the VXC-based GDE. the share of the latter dropped for example from 40% in the carbon powder to zero. As one can see. similar to the powder form. the difference between the GDEs prepared with various carbon supports is still considerable. with the AB35 having only a surface area of 22 m²/g compared to more than 500 m²/g for the BP- and KB-based GDE. The values for VXC35. ENS35 and AB35 are in close proximity. between 20 and 35 m²/g. On the basis of these findings. the GDEs can be classified in two categories with ENS. VXC and AB giving GDEs of very low BET surface and the ones with high surface area. BP. NOR and KB characterized by a pronounced share of micro- and small mesopores.

Table 5.3 Physisorption data of GDEs with different carbon type. BET$_{norm}$ denotes the surface area normalized on carbon mass

Composition	**BET** m²/g	**BET$_{norm}$** m²/g C	**Micro** m²/g	**Micro** %
AB35	22	36	0	-
VXC35	35	58	0	-
ENS35	25	42	0	-
BP35	539	898	193	36
KB35	507	844	0	-
NOR35	276	461	175	63

To assess the complete pore range. the same electrodes were examined via Hg-porosimetry. The data of interest from porosimetry measurements are porosity. pore size distribution (PSD) and pore volume. In Figure 5.9. the logarithmic pore size distribution *dV/dlogD* and the cumulative pore volume of the analyzed GDEs are depicted for different carbon types with 35% PTFE. To avoid misinterpretation induced by the logarithmic x-scale both graphs include an inset plotted on a linear x-scale. Furthermore. in the PSD plot the inset is given as *dV/dD* and zoomed into the primary pore region to facilitate physical interpretation of the PSD (see chapter 5.1.1 for explanation of the different type of plots).

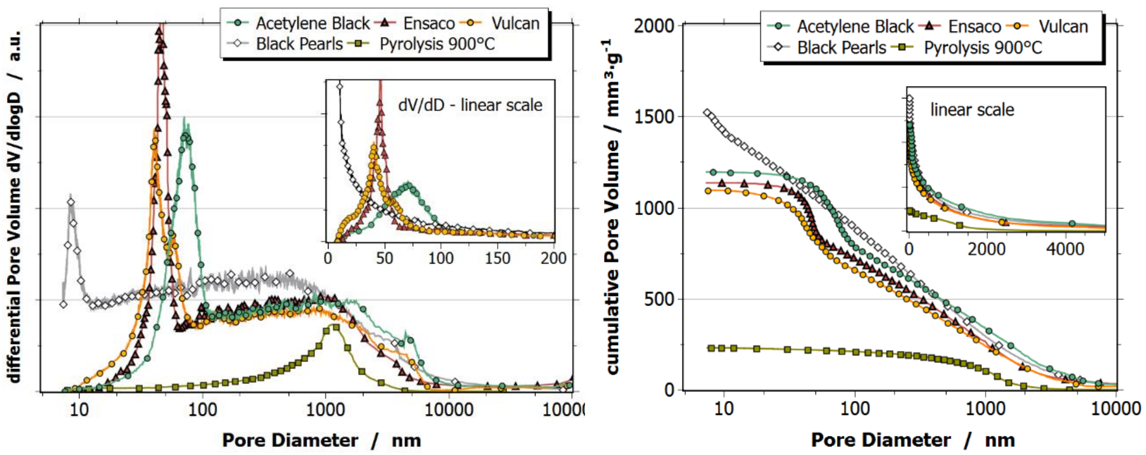

Figure 5.9 Differential logarithmic (left) and cumulative pore volume (right) of employed GDEs. with 35% PTFE. Inset on the right. zoom in agglomerate region using linear scale.

Examining Figure 5.9. the characteristic bimodal PSD of the carbon black-based GDEs can be seen for all GDEs shown here. except for the GDEs prepared from the activated carbon pyrolyzed from wood. The latter has a rather distinct pore diameter maximum at around 1 µm (also observable in the SEM images) but without additional features and. importantly. lacking the pronounced three-dimensional pore network of the carbon blacks. For the other GDEs. due to the appearance of the PSD and the knowledge of its assembly. the pore volume can further be divided into primary and secondary pore volume as discussed above. As one can see in the PSD of the GDEs with different carbon materials. each material has a very distinct transition between the primary porosity and the secondary pore system at which a sudden change in the slope of the pore volume is visible. Up to the steep increase. the progression of the secondary pore distribution in the differential graph is very similar for all the carbon-black GDEs. suggesting that the secondary pore structure is a result of the GDE preparation method. namely. the PTFE addition. its distribution after thermal treatment and the compacting pressure. The curves start to significantly deviate from each other at the pore diameter at which the primary pore system inside the aggregates sets in. This is governed by the pore structure of the carbon aggregates and their pore size distribution. characteristic of the carbon type. Whereas. for example. for the very macroporous AB this boundary is at ~120 nm. BP seems to have a very dense aggregate structure with pores below 15 nm diameter. To facilitate a quantitative assessment of both contributions to the total pore volume. the distributions would need to be deconvoluted with high precision. As the progression of the secondary pore distribution is masked by the porosity within the aggregates. a clear distinction is difficult and will not be performed quantitatively herein. Besides. during electrolysis the electrolyte intrusion does not differentiate between primary and secondary pore system. but is solely driven by the pore size. The distinction between both contributions would only be of academic value to characterize the pore system but. arguably. not give additional insights for the application of the GDEs. In contrary. the analysis of the maximum pore diameter of the primary pore system indicates an essential property of the porous structure related to the porosity of the aggregates and how dense they are. This value is given in Table 5.4 together with other information derived from these measurements. The assignment of being rather macroporous based on the surface area from physisorption data above is confirmed for VXC. AB and ENS by the data from porosimetry here. with the aggregate pore size ranging into to the macropore region (> 50 nm). Accordingly. based on the *dV/dD*-plot the AB-GDE has the most open aggregate pore structure. with a maximum in the primary distribution at 71 nm. followed by ENS and VXC. with pore diameter of 47 and 41 nm. respectively. In contrary. the primary pore volume accessible via porosimetry is significantly lower for BP35 (*e.g.* only one third of AB35) as the aggregates only comprise pores with diameter lower than 13 nm. with a maximum at 8 nm. For KB35. the aggregate porosity is not even accessible *via* porosimetry suggesting it starts at even lower pore diameters. In contrary to the other carbon blacks for which the cumulative pore volume becomes flat below 10 nm diameter. suggesting there is not much additional pore volume in this pore diameter region. the PSD of KB35 and BP35 indicate that the actual pore volume and agglomerate porosity cannot be assessed correctly *via* Hg-porosimetry. Still. the *accessible* pore volume is already very high for BP and KB which is ascribed to a very high secondary pore volume. particularly pronounced in the mesopore range (between 10 and 30 nm) formed between the aggregates. In this range. the macroporous carbons exhibit very low differential pore volume (or a plateau in the cumulative distribution. compared to the linear rise for BP35 on the logarithmic scale). which would further fall into the primary porosity inside the aggregates.

Table 5.4 Textural properties of GDEs obtained from Hg-porosimetry

GDE	**Porosity** %	$V_{P.total}$ mm³/g	**Boundary** nm	$d_{max.\ prim}$ nm
AB35	71.24	1195	123	70.7
VXC35	68.73	1095	89	40.5
ENS35	65.27	1134	70	46.5
BP35	70.11	1524	13	8.3
KB35	70.10	1577	-	-

Influence of PTFE and thermal treatment

To understand how the porous nature of the GDE is influenced by the presence of the PTFE and the preparation method. GDEs with different PTFE contents have been prepared and analyzed. Although. the effect of PTFE content on the electrochemical performance has not been studied extensively herein. the investigation of the physical properties aids in deriving a better understanding on how texture of the GDE is influenced by preparation conditions.

In Figure 5.10. the BET surface area of GDE made from VXC and AB are exemplary depicted as a function of PTFE content. VXC is chosen as an additional example as it exhibits a certain amount of microporosity. thereby. giving better information on how the micropores are affected during preparation. Naturally. mixing the porous carbon with the non-porous PTFE decreases the surface area *per gram of* *the electrode*. To make the comparison more meaningful. the surface area has also been normalized to the amount of carbon in the electrode to compensate for this effect (open symbols).

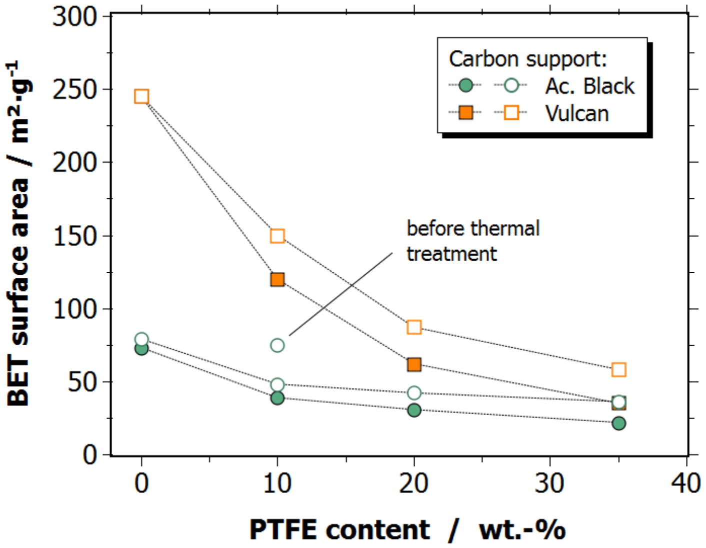

Figure 5.10 BET surface area normalized on electrode (filled) and carbon (open) mass as function of PTFE content

The first important observation that can be made is that by simply mixing the components and pressing the electrode. the porosity of the carbon matrix does not undergo significant changes. This is shown by comparing the specific surface area of AB10 before thermal treatment normalized on the carbon amount (m^2/g_C) with bare AB powder and the GDE pressed in the absence of PTFE. Only after the thermal treatment at 340 °C slightly above the melting point of the PTFE. the surface area is significantly affected. decreasing from 78 m^2/g_C to 48 m^2/g_C. This is due to the melting of the PTFE particles which intrude the aggregates by capillary forces forming a thin layer coating the pore walls and clogging parts of the pore network. Increasing PTFE content affects the higher surface area carbon VXC disproportionally as especially microporosity responsible for the higher BET values of the Vulcan-based GDE is affected. Microporosity decreases from 93 m^2/g_C (40% of surface area) for pure Vulcan to 30 m^2/g_C (20%) already at 10% PTFE and to zero when going higher. For both carbon types. the increase of PTFE content continuously decreases all properties related to the carbon texture. *i.e*. surface area and microporosity.

To get a better understanding on how the PTFE affects the pore distribution. Hg-porosimetry was conducted on GDEs with AB and 20% PTFE before and after thermal treatment. The corresponding pore size distribution is visualized in Figure 5.11. As one can see. the observation from the SEM images in the previous chapter can be verified also quantitatively when comparing the untreated and thermally treated GDE. Indeed. the pore volume significantly increases in the region between around 200 nm to 10 µm as the PTFE particles of this size range melt and leave large pores in the same order of magnitude behind. This pore region has a negligible effect on the measured BET surface area by physisorption. Pores below 100 nm are shifted in size to lower values which. in turn. can be ascribed to the PTFE film which forms after melting. covering the pore walls and decreasing the pore diameter. The maximum in the agglomerate PSD is 74 and 58 nm. respectively. The distribution inside the aggregate region shifts by around 16 nm with the smaller diameters less affected. This suggests an average film thickness of around 8 nm. The influence on the aggregate porosity is observable in the BET measurements and responsible for the decrease of surface area after thermal treatment. Solely looking at the effect on porosity. this shift could be disadvantageous as it makes the wetted agglomerates more compact impeding transport of involved species. However. the main impact the treatment has on the effectiveness of the GDE is to facilitate more uniform and pronounced hydrophobicity as well as rendering mechanical integrity towards the GDE. It is important to keep in mind that a uniform film of PTFE fully covering the internal structure of the GDE is unlikely. as otherwise also the active sites would be blocked and the reaction impeded significantly or even completely. That is why it is assumed that particularly in the primary pore region a distinct part of the pore area should be free of PTFE. either due to inhomogeneous distribution or by decomposition of excess PTFE on the electrode surface during polarization.

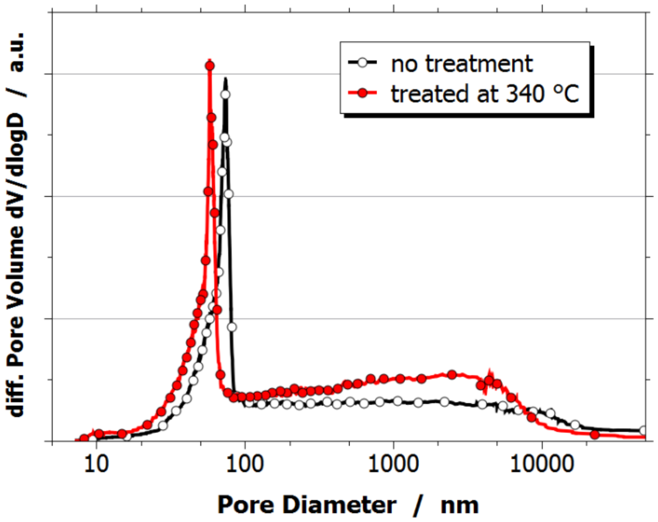

Figure 5.11 Pore size distribution of GDE with 20% PTFE before and after thermal treatment at 340 °C (derived from two pieces of the same GDE).

Table 5.5 Data from Physisorption and Porosimetry for the AB-based GDEs

GDE	**BET**	**norm.**	**Micro**	**Porosity**	**$V_{p.total}$**	**$d_{max.\ prim}$**	**$V_{p.prim}$**	**$V_{p.second}$**
	m^2/g	**m^2/g_C**	**%**	**%**	**mm^3/g_c**	**nm**	**mm^3/g_c**	**mm^3/g_c**
AB10	39	48	0	75	1921	60	523	1398
AB20	31	42	0	76	2033	63	570	1463
AB35	22	36	0	72	1912	71	558	1354
AB50	15	32	0	63	1662	100	642	1020

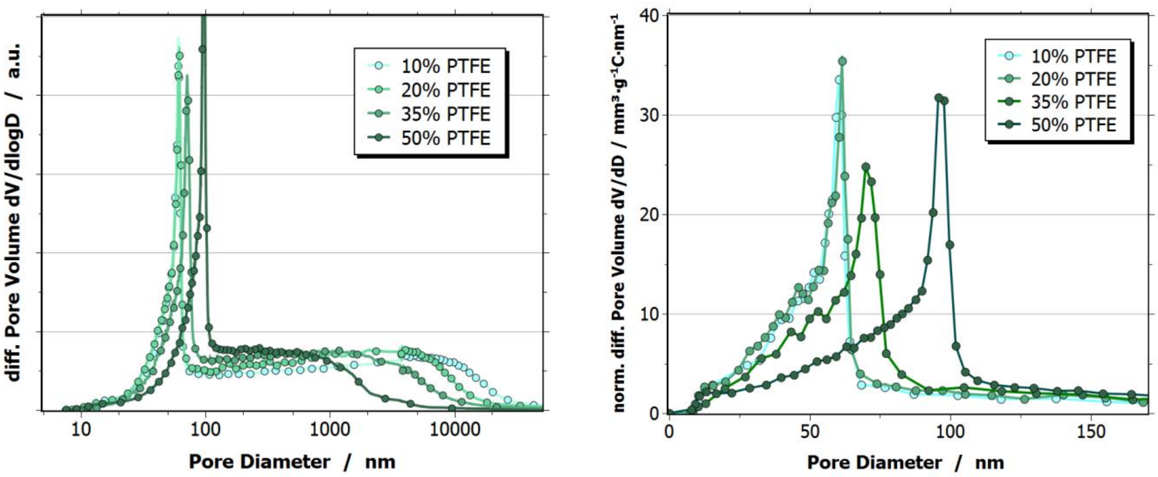

Figure 5.12 Differential logarithmic pore distribution of AB-GDEs with different PTFE content (left) and zoom into agglomerate porosity region (right. linear dV/dD scale). both normalized on carbon mass.

To study the effect on the superordinate pore structure. the GDEs with varying PTFE content are further characterized *via* Hg-porosimetry. The results are shown in Figure 5.12 and summarized in Table 5.5. Again. the data has been normalized on carbon content to better understand the effect on the porosity of the porous matrix. While the complete pore distribution is significantly affected by the addition of PTFE. the interpretation is not as straightforward. Besides the effect of bringing the non-porous PTFE into the system. the compacting behavior during manufacturing is affected and the pore structure changes with thermal treatment. In the intermediate secondary pore region between 100 nm and a few µm. one can see that the differential pore volume increases with an increase of PTFE content. This is the region in which the PTFE particles leave behind large pores during thermal treatment as discussed above. If the GDE contains more PTFE. there is more pore volume in this region created. At the same time. at higher pore sizes. the opposite observation can be made: the maximum pore size is shifted drastically to higher values and clearly when going to lower PTFE amounts. This might have to do with how the powder mixtures behaves during pressing as this is also the region affected by variation of the compacting pressure as described in chapter 6.2.3. The excess PTFE amount between the agglomerates could make the pore structure more ductile and facilitate a more pronounced compression of the GDE. Also. there is less pore volume into which the PTFE can penetrate during melting as the PTFE:carbon ratio increases. which should also play a role for the PTFE distribution after pressing and melting. The primary porosity is substantially affected as well by the addition of PTFE. except for 10 and 20% PTFE which are essentially the same. While the total agglomerate pore volume remains similar (the slightly higher volume for 50% could be due the pore size of the agglomerates ranging further into the secondary pore range. impeding clear distinction). the distribution is shifted towards larger pore sizes. At the same time at lower pore sizes. the differential pore volume decreases. The latter can be explained by the PTFE clogging and partially filling the pores inside the agglomerates during melting as shown above. Yet. the fact that the differential pore size is not only decreased but in addition significantly shifted towards higher pore sizes. suggests that the PTFE is not only penetrating the pores and leaving the matrix unchanged. but that it changes the agglomerate structure itself. That could be ascribed to what happens during pressing in which PTFE becomes mobile due to the high forces. pressed into the agglomerates and widening them up. During melting. the PTFE penetrates deeper into the pore system and leaves behind the pores which were widened during pressing. It is difficult to validate this hypothesis just by studying the PSD. Instead. graphical reconstruction of the pore system *via* CT or FIB-SEM could help to understand what is happening more clearly. If this becomes more interesting in the near future. this could be an option to get additional insights.

5.2 Wetting behavior and hydrophobicity

Besides porosity. a property shown in this work to have a substantial effect on the operation of the GDE. is its wetting behavior which is characterized by the intrusion of electrolyte and the establishment of the triple-phase boundary during the reaction. Understanding how the wetting proceeds. by which parameters it is affected. how it evolves with time and as function of the electrode preparation parameters is essential to explain and understand the electrochemical behavior of the electrode [22.55]. The goal of this chapter is to generate the basis for these discussions. To this end. the capacitance as measure of the extent of the electrochemical double layer and the analysis of the intrusion depth *via* element mapping will be introduced.

Although evaluation of the contact angle is known to be not very meaningful to give a decisive assessment of hydrophobicity of *porous* materials [157]. it can give a first qualitative impression on the property of the GDE and how it evolves during preparation and electrolysis. Figure 5.13 depicts a sessile drop of water on the GDE after pressing. after thermal treatment and after electrolysis. As one can see. the GDE before the thermal treatment is highly hydrophobic. exhibiting a contact angle >90°. This is due to the high hydrophobicity of the carbon support (here: Acetylene Black) [36] as well as the addition of the hydrophobic PTFE. The subsequent thermal treatment further increases hydrophobicity with a resulting contact angle well above 90°. This is due to the melting of the PTFE and formation of a thin layer coating on the surface of the electrode. Initially. when placed into the electrolyte. a film of air covers the GDE surface. During the experiment. as soon as a polarization begins. the electrolyte starts to penetrate the pore system; a process driven by capillary forces and a result of a change in the surface tension induced by the applied potential (see below). Further. excessive PTFE covering the GDE surface is decomposed by the electrochemical stress. as shown by Wagner et al. for alkaline fuel cells [46]. This makes the GDE accessible to electrolyte. and more hydrophilic as shown for the contact angle after electrolysis.

Figure 5.13 Contact angle measurements using a sessile drop of water. from left to right on: fresh AB35-GDE taken out of the press. after thermal treatment and spent GDE after electrolysis

Although this method is very simple in its execution and analysis. thus. sometimes employed in literature. the informative value is rather limited for the system at hand and more of qualitative value. This is due to the porous nature of the GDE and its high surface roughness. making this method unsuitable for a more quantitative evaluation [157].

5.2.1 Analysis of Electrode Capacitance

Wettability of the GDEs is strongly influenced by the electrode composition. preparation procedure and the reaction environment. To facilitate the discussion on how this relationship is constituted. a method to quantify the wetting of the GDE needs to be introduced. The so-called electrochemical surface area (ECSA) of an electrode in contact with electrolyte can be assessed with a variety of methods which are adequate for different applications and systems [158]. For the studies at hand. the method needs to be applicable *in situ* during the experimental sequence and. preferably. allow the assessment of the wetting without changing the course of the experiment. The measurement of the electrochemical double layer capacitance is a convenient method for this purpose. The capacitance C in general is an important property in electronics correlating the charge Q stored on a capacitor at a given voltage U according to

$$Q = C \cdot U \tag{5.1}$$

This concept is utilized in electrochemistry where charge is stored at the electrode | electrolyte interface through the development of the electrochemical double layer on both sides of the interface (electrode surface and solution). by the alignment of ions and electrons. As the specific capacitance for a given electrode | electrolyte system is a material constant. the macroscopically measured capacitance can be approximated as a linear function of the surface area over which the double layer spans. thus. for a GDE. the surface area in contact with electrolyte. Although. the specific capacitance of a material is usually hardly accessible. *e.g.* because. as in the case at hand. a relatively undefined and non-homogeneous surface exists. it can give at least a qualitative measure with which the electrochemical surface area (ECSA) of porous electrodes [158] can be compared when the same material is used. If a reference value for the specific capacitance of the material is known. the real ECSA can be estimated.

There are different techniques to assess the capacitance. such as Electrochemical Impedance Spectroscopy (EIS) or the recording of cyclic voltammetry (CV) at different scan rates from which the latter was chosen here due to its simple and straightforward implementation into the experimental sequence. However. in the future. it is reasonable to validate via EIS and leverage the additional insights that can be derived from it. According to equation 5.1. the capacitance correlates the applied voltage and the corresponding charge Q stored in the double layer. While the actual charge of the double layer is not directly accessible. its change can be assessed in the form of the current I passed when the voltage is changed:

$$\frac{dQ}{dt} = I = C \cdot \frac{dU}{dt} \tag{5.2}$$

This correlation holds only true. when the charge is solely employed to charge the double layer in the absence of any Faradaic process and can be evaluated to obtain C when CVs are performed at different scan rates (dU/dt). Consequently. the anodic/cathodic current in the middle of the potential window is plotted over the scan rate. Assuming an ideal capacitor as model yields a straight line with its slope constituting the capacitance. as given by equation 5.2 and extracted by linear regression [159].

The procedure is illustrated in Figure 5.14 for a representative type of experiment. On the left. the appearance of the CV scans is shown from which the capacitance is derived. In the right graph. the relation between current and scan rate is shown for three distinct measurements. In this set of experiments. the GDE was stressed potentiostatically at three different electrode potentials for one hour. after which the capacitance was evaluated. Accordingly. increasing the electrode potential from -1.3 V vs. Hg|HgO to -1.5 V leads to an increase of the capacitance and. thus. wetted surface area. by a factor of 5. indicated by the respective slope.

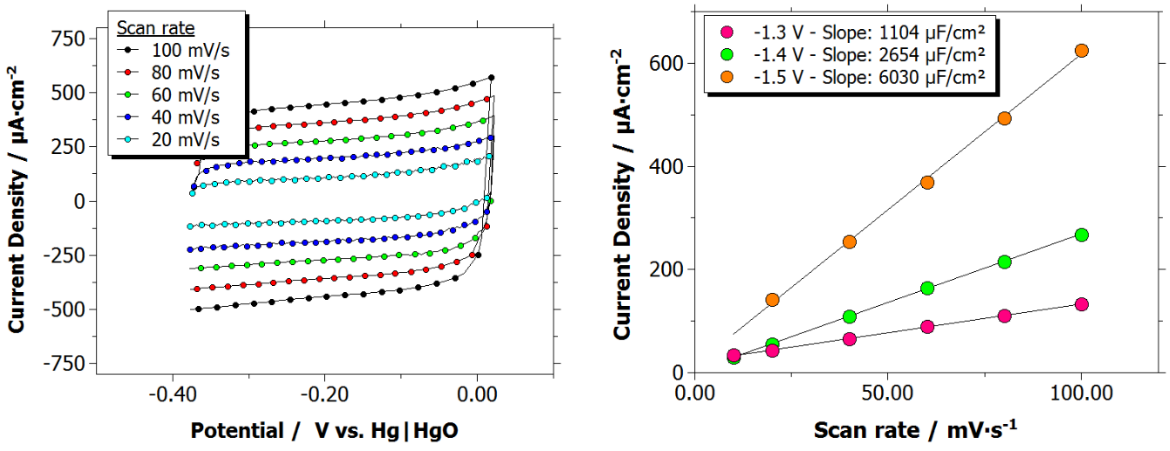

Figure 5.14 Exemplary measurement of CV scans at different scan rates to derive double layer capacitance (left). current density at potential in the middle of the scans over corresponding scan rate for one GDE stressed at different potentials over one hour (right)

While the GDEs employed in this work are highly hydrophobic. wetting only proceeds as soon as the experiment is started and the electrode polarized. This effect. the dependence of the contact angle θ on the electrode potential. is known from literature and called electrocapillarity or electrowetting [160.161]. In its simplest form. it is mathematically described by an extension of the Young equation. relating the surface tension γ between the participating phases (liquid. gas. solid) to the contact angle θ. according to

$$cos\theta = \frac{\gamma_{SG} + \gamma_{SL}}{\gamma_{LG}}. \qquad 5.3$$

To account for the contribution of the electrode potential *E*. the surface energy of the liquid-solid interface γ_{LG} is corrected for the electrostatic energy (*$CE^2/2$*). stored in the capacitance *C* of the double layer and induced by the electric field [161]. giving

$$cos\theta = cos\theta^0 + \frac{CE^2}{2\gamma_{LG}}. \qquad 5.4$$

The cause for this effect is that a deviation from the potential of zero charge (pzc). for which the contact angle goes through a maximum. leads to a charging of the electrode surface (either excess or deficiency of electrons) and an increase of its polarity. As a result. the surface tension and the contact angle decrease. at some point rendering the surface hydrophilic. Thereby. this causes a wetting of the pore system despite the surface being hydrophobic in the absence of polarization [162]. In [163] it is reported for example that the pzc of a Pt/C electrode lies at a potential of -0.13 V vs. Hg|HgO in dilute KOH electrolyte while tin was reported to be around -0.4 V vs. SHE [164]. Accordingly. by polarizing the electrode beyond this value. the more negative the potential. the lower the contact angle should become and the stronger the wetting of the pore system by capillary forces should prevail. This is verified by the data at hand and throughout this work.

In order to get insight into how the wetting proceeds in the system at hand. the capacitance was measured throughout a potentiostatic experiment at -1.4 V in a time-resolved manner. To this end. each 10 min. the experiment was interrupted and the capacitance measured after which the potential was re-applied. The results are shown in Figure 5.15 for a Vulcan and Acetylene Black-based GDE. The capacitance increases linearly with time for both. with the VXC35 having a higher capacitance than AB35 by one order of magnitude. Besides having slightly higher surface area (35 to 22 m²/g). more importantly. Vulcan is known to be only moderately hydrophobic compared to the highly hydrophobic AB [165] which is reflected in a significantly more pronounced wetting. Furthermore. keeping a constant potential. it is evident that the electrolyte continuously and steadily penetrates the pore system of the GDE without decelerating in the frame of this experiment.

As the evaluation of the capacitance turns out be an efficient and convenient tool for the interpretation of the electrochemical results throughout this work. it will be consistently employed throughout chapter 6 where it is utilized to gain information on the interplay between GDE properties. reaction conditions and the electrochemical performance.

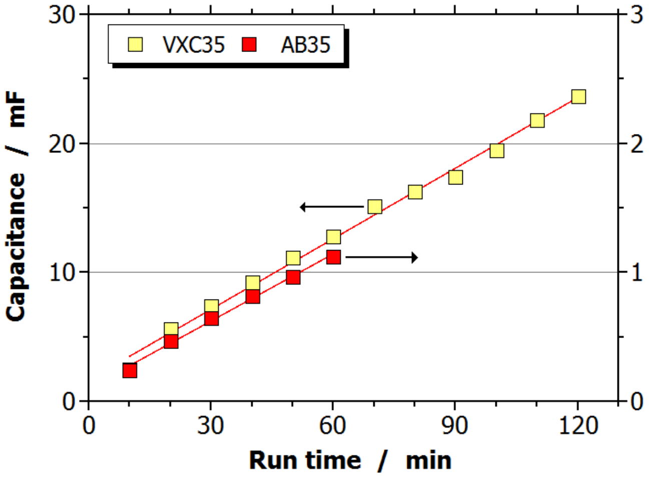

Figure 5.15. Capacitance of AB35 and VXC35 determined by interrupting potentiostatic experiment each 10 min and performing CV measurements at various scan rates.

5.2.2 Intrusion depth

Evaluation of the double layer capacitance gives information on the overall extent of wetted surface area but not about its distribution over the electrode volume. As no experience exists with such type of electrodes in this reaction. it was regarded as an important aim to get a better understanding on the way the GDE works and how the wetting actually proceeds. Therefore. some of the above electrodes have been analyzed via scanning-electron microscopy of their cross-section and studied with EDX to evaluate the spatial elemental distribution. Accordingly. the elements can be highlighted in different colors according to their prevalence which is particularly interesting for tin (green) and potassium (blue). The latter facilitates reproducing the occurrence of electrolyte ($KHCO_3$) inside the GDE during electrolysis. This general assessment is introduced in the following and further elaborated in chapter 6.3.3. In Figure 5.16. this approach is exemplary shown for two GDEs made from Vulcan with 35% (VXC35) and 20% PTFE (VXC20). both exposed to 400 mA/cm^2 for 1h. The occurrence of potassium is highlighted in blue. The images clearly visualize a “front of electrolyte” close to the electrolyte side of the electrode (top). Furthermore. from the images it is clearly visible that only a small electrode volume was at all in contact with electrolyte. what is in accordance with the results from capacitance which will be correlated with wetted surface below.

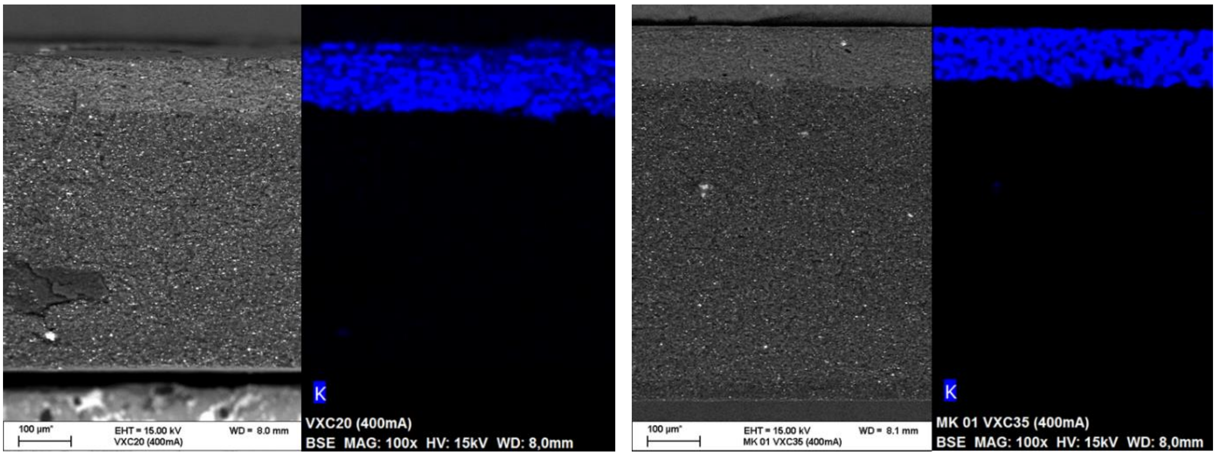

Figure 5.16. Material contrast and element mapping image of a spent VXC20 (left) and VCX35-GDE (right). 1h at 400 mA/cm². Occurrence of Potassium is depicted in blue

For a quantitative assessment. the images were analyzed with an image analysis software (*imageJ*). The varying brightness of the color is not considered as it has no clear physical meaning but is rather an artefact of the measurement and image processing. Furthermore. the actual wetted surface area is not accessible by this method. as the resolution of the method is too low (~1µm) in relation to the pore sizes of relevance. As a result. a rather macroscopic assessment of elemental distribution is obtained which means that a differentiation of wetted and non-wetted pores inside the electrolyte front is not possible. However. the macroscopic average intrusion depth over the electrode cross-section can be studied and consequently compared to the wetted surface area from capacitance. As an example. the cross-sections of the VXC35-GDEs at 200 mA/cm² and 400 mA/cm² as well as VXC20 with lower PTFE content at 400 mA/cm² have been analyzed and the corresponding results. namely. the intrusion depth and the measured capacitance are summarized in Table 5.6. In addition. the cross-section element maps of the 400 mA/cm² experiments are shown in Figure 5.16. The analysis confirms that the electrolyte only wets a small volume of the GDE and that this depends on reaction conditions and GDE properties.

Table 5.6 Information on wettability-related properties of Vulcan-based GDEs. stressed at different conditions.

		VXC35	**VXC35**	**VXC20**
Thickness	µm	740	730	630
Current density	mA/cm²	200	400	400
avg. intrusion depth	µm	85	107	130
Capacitance	mF	12.5	18.4	45
Electrode potential (average)	V vs. Hg|HgO	-1.67	-1.89	-1.87

As expected. a clear *qualitative* trend is visible. that is that the wetting increases with increasing polarization (which increases with current density) and decreasing PTFE content. For the first example. the intrusion depth increases from 85 µm to 107 µm and the capacitance from 12.5 mF to 18.4 mF after 1 h when the current density is increased from 200 mA/cm² to 400 mA/cm² and the electrode potential from -1.67 V to -1.89 V correspondingly. Also. decreasing the PTFE content from 35% to 20% with Vulcan as carbon support at 400 mA/cm² leads to a more pronounced wetting. Especially the capacitance is strongly enhanced by more than a factor of two from 18.4 to 45 mF. while the intrusion depth increases to 130 µm. This can be well explained by the increase of hydrophobicity at higher PTFE content but also by the lower surface area. Regarding the latter. surface area of VXC20 is 87 m²/g vs. 58 m²/g for VXC35 (both normalized on carbon mass to allow better comparison). VXC20 is further comprised of a higher share of smaller pores which should become more easily wetted due to stronger capillary forces. Also the electrode potential will have a strong influence. However. in this particular case. the average electrode potential over the course of the experiment is almost identical. This is because the lower polarization at the beginning of the experiment for the more thoroughly wetted VXC20 GDE (more catalyst in contact with electrolyte) is compensated by a drift towards more negative potentials due to an increasing HER with time. similar as in Figure 6.38. From all three measurements which are supposed to give a first. preliminary idea on the system behavior. it is evident that the ratio between capacitance and the intrusion depth. which can be considered proportional to the wetting degree inside the macroscopically wetted electrode volume. does not remain constant but is highly dependent on electrolysis conditions and electrode properties. Accordingly. the combination of intrusion depth and capacitance can give valuable insight into how wetted area and gas-filled pores are distributed in the electrolyte-filled electrode volume from which the front is traveling through the GDE cross-section.

5.2.3 Estimation of Electrochemical Surface Area and wetting degree

To obtain a quantitative estimate for the wetted surface area. the so-called *Electrochemical Surface Area* (ECSA) is the metric of interest. It can be estimated by using literature values for the specific double layer capacitance. *i.e.* capacitance per surface area for the material of interest. and setting it in relation to the measured capacitance. A typical value for carbon black given in [27] is 8 µF/cm² (cm² BET area). dependent on the type of carbon (amount and type of surface functional groups) [166]. while [167] gives a value of 10-16 µF/cm² for carbon black electrodes containing a binder. Depending on what value inside of this range is chosen. the obtained ECSA will be higher. for lower specific capacitance. and vice-versa. To account for the tin oxide which has a higher specific capacitance than the carbon ([158] gives a typical value of around 60 µF/cm² for metal oxides) but also contributes a substantially lower surface area compared to the carbon support. a conservative value of 15 µF/cm² is assumed herein.

In all the experiments for both Vulcan and AB-based GDEs and even for high electrochemical stress. the degree of wetting normalized to the total surface area of the GDE is very low. On the one hand. this is because the GDEs are highly hydrophobic and stressed for very short times (at most. a few hours). Thus. the run time must more realistically be regarded as wetting-in or induction period. On the other hand. normalizing on the total surface area. one has to bear in mind that only a layer with small thickness close to the electrolyte side of the GDE is macroscopically wetted as shown above. A large part of the

GDE remains completely dry. To get a first impression. this estimation is performed for the GDEs from the capacitance measurements that have been conducted over time in 5.2.1 at potentiostatic polarization. The AB35 and VXC35 were mildly stressed at -1.4 V for one hour (with CV measurements every 10 min) which resulted in a current density of around 15 mA/cm² and 40 mA/cm². respectively. at the end of the experiment. The measured capacitance of 1 mF and 12.5 mF correspond to a wetted surface area of 67 cm² and 833 cm² respectively. The BET surface area of 22 and 35 m²/g translates to a total BET surface area of 1.32 m² and 2.28 m² for a GDE with 1 cm² geometric surface area. Combining both gives a wetting of 0.5% and 3.7% of the BET area of the GDE. which is in line with the proposed hydrophobicity of the material and the very limited intrusion (compared to the large GDE thickness) at such short runtime and low electrochemical stress (indicated by the low current density). For 1 h at -1.5 V and AB35 for example. a capacitance of 6 mF was measured and the wetted percentage increases to 3% by a factor of 6. For high electrochemical stress the percentage of wetting increases correspondingly. *e.g.* to 9.7% (45 mF) for VXC20 at 400 mA/cm² over 1 h. 5.5% for VXC35 at the same conditions or 16 mF and 7% for AB20 after 500 mA/cm² for 5 h. These results. amongst others. show that AB is considerably more hydrophobic than VXC as electrode support and that for lower PTFE content. the share of wetted pore area increases for the same conditions.

As the above percentage values are normalized on the total BET surface area of the GDE with the majority of the GDE volume opposing the electrolyte side remaining completely dry. the above values do not give insights into fundamental functioning of the GDE and constitution of the triple-phase boundary (TPB) during electrolysis. Increasing or decreasing the thickness of the GDE would in fact significantly change the percentage values. however. only produced by a change of the large dry volume which does not participate in the reaction at these conditions as later shown in chapter 6. In contrary. normalizing on the macroscopically wetted volume is a significantly more meaningful metric which can be examined for the experiments in which intrusion depth was analyzed. To this end. the wetted surface area reived from capacitance measurements is set in relation to the total surface area inside the macroscopically wetted volume. The latter is given by correcting the total BET surface area of the GDE with the ratio of intrusion depth and total thickness. The corresponding wetting-ratio is given in the last row of Table 5.7 together with the other data required for this calculation.

Table 5.7 Information on wettability-related properties GDEs with varying composition and stressed at different conditions.

		VXC35	VXC35	VXC20	AB35NP
		200 mA/cm²	400 mA/cm²	400 mA/cm²	500 mA/cm²
avg. intrusion depth	µm	85	107	130	102
Capacitance	mF	12.5	18.4	45	5.5
ECSA	cm^2_{ECSA}	833	1227	3000	367
Percentage of BET	$\%_{ECSA}$	3.7	5.5	9.7	2.4
Wetting ratio*	-	0.33	0.37	0.47	0.22

* ratio of wetted surface area from capacitance to BET surface area inside macroscopically wetted volume

As the data shows. when accounting only for the volume into which the electrolyte intruded. the wetting degree is much higher: depending on the GDE and reaction conditions. this value ranges between about 20% and 50%. As a comparison. in [163] a wetting degree between 15% and 30% was found during so-called wetting-in studies of VXC-based GDEs for ORR in alkaline fuel cell cathodes which uses comparable GDEs and is one of the few studies where such an assessment was performed. They could show that wetting increases with time. potential and current density. In contrast to the investigation at hand. these results are based on the weight of intruded electrolyte and. hence. give information on wetted volume instead of surface area. Assuming that pores above certain diameters are rather wetted by a thin film instead of being completely filled and considering that small pores are wetted preferentially. thus. contributing stronger to surface area than to pore volume. the wetting degree based on wetted volume is naturally lower. Still. this example from literature suggests that the obtained values in this work are in a realistic range. Furthermore. and importantly. the analysis at hand. reveals that increasing the conditions beneficial for wetting. *i.e.* higher current density and lower PTFE content. use of more hydrophilic VXC instead of highly hydrophobic AB. not only results in a deeper intrusion of electrolyte into the GDE volume. but also into a more pronounced wetting inside the macroscopically wetted volume. This is not surprising. as the capillary forces inside the pore in contact with electrolyte increase for a surface less hydrophobic due to lower surface tension and contact angle. Higher current density implies a more negative electrode potential and. therefore. also a decrease of surface tension according to equation 5.4.

These results aim to introduce the concept and give the basis for understanding the wetting properties of the GDEs studied in the system at hand. It will later be elaborated in chapter 6.3.3 in which investigation of the time behavior of the electrolyte intrusion in the transport limited region is conducted and related to the ability of the GDE to operate at high current density. Besides that. although of very high value. a more comprehensive and systematic analysis of the relationship between intrusion depth and capacitance as function of current density and electrode composition could not be performed in the frame of this work. To fully understand how the GDE operates and how its properties relate to its performance said investigations are highly recommended to allow for the establishment of a more sophisticated and knowledge-based optimization of the system.

5.3 Characterization of the Electrocatalyst

The goal of the characterization studies in the following is to obtain information on the chemical nature of the electrocatalyst. Therefore. X-ray diffraction (XRD) and X-ray photoelectron spectroscopy (XPS) were performed to reveal its *initial* bulk nature and surface composition. respectively. Naturally. this does not give information on the conditions during the reaction which would require utilization of *operando* techniques. Results from such studies are discussed in the theory section 3.2 and. together with the significance of the obtained information from this work. summarized at the end of this chapter.

X-Ray diffraction

XRD gives information on the existence and distribution of crystalline phases in the analyzed sample. Their occurrence produces distinct diffraction patterns which can be assigned to certain phases using simulated patterns from a library. Diffractograms of the investigated electrodes. namely. with the commercial tin nanopowder. both before and after thermal treatment (35% PTFE. AB. 5 mg/cm² Sn). and with the precipitated SnO_x/C-nanoparticles (35% PTFE. 1 mg/cm²). as well as from the supported SnO_x/C-particles in powder form. are shown in Figure 5.17. Due to the high metal loading and relatively large particles of up to 150 nm. the reflexes of tin species in the diffractogram of the GDEs with commercial particles are clearly visible. Before the thermal treatment. mainly metallic tin is observed whereas although a thin native oxide layer should prevail. no corresponding reflexes can be assigned which can be explained by the low thickness of the layer. After the thermal treatment of the GDE. the metallic tin particles are completely oxidized to SnO_2 and the reflexes characteristic for Sn^0 vanish. This suggests that although the thermal treatment has been conducted under inert nitrogen atmosphere it is not unlikely that small concentrations of oxygen diffuse into the muffle oven used or that the nitrogen gas coming from the grid supply of the university could possess oxygen impurities. with both suggestions argued to be reasonable. In addition. distinct reflexes for the highly crystalline PTFE and graphitic phases in the carbon black can be found in the pattern. Carbon blacks are known to exhibit a certain degree of graphitization which is pivotal for its high conductivity [49].

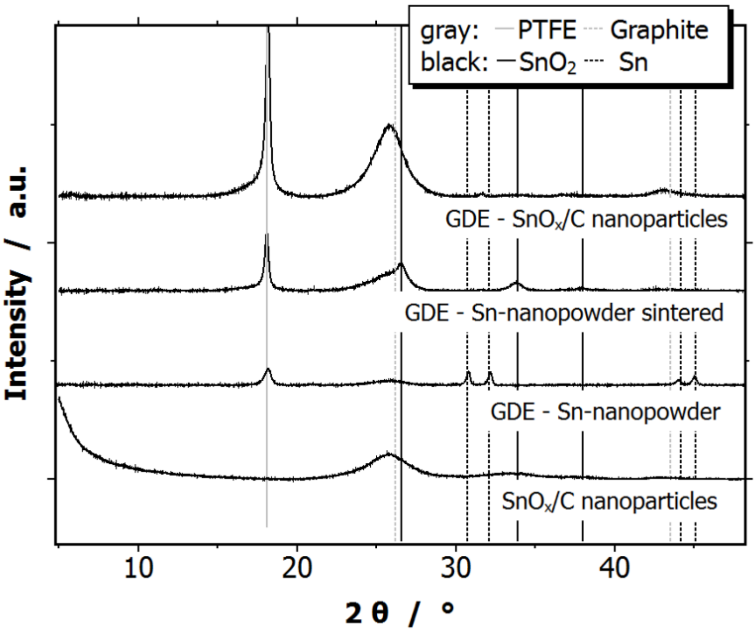

Figure 5.17 XRD pattern of (from bottom to top) SnOx nanoparticles supported on AB (~9 wt.-%). GDEs with tin nanopowder (5 mg/cm²) before and after thermal treatment. with SnOx-nanoparticles (1 mg/cm²). all GDEs with 35% PTFE and Acetylene Black.

Due to the low loading combined with the small particle size (crystallites below an average size of 5 nm. see chapter 6.2.2). XRD fails to show any Sn-specific reflexes for the SnO_x/C-GDE. However. the sample with the supported particles on the carbon when analyzed as powder (not as GDE) and with five times higher metal concentration than the one used in the GDE. shows the characteristic but relatively broad reflexes for the SnO_2 phase. While the reflex around 26° is clearly observable the other two at higher θ are relatively hard to spot due to strong broadening and low intensity which is commonly more pronounced at high 2θ-values [168]. The general broadening of the peaks compared to the other samples is in line with the nano-sized crystallite dimensions resulting in significant broadening of the reflexes. Evidently. the XRD analysis demonstrates that the initial bulk composition of both the commercial and the precipitated tin catalyst employed in the GDE is of fully oxidized nature. In contrary. the former is fully oxidized during the thermal treatment of the electrode. the synthesized tin nanoparticles supported on the carbon are already precipitated as tin oxide.

X-ray photoelectron spectroscopy

In contrast. to XRD which allows assessment of *bulk* crystalline phases. XPS is a surface sensitive characterization technique which gives information on the elemental and chemical composition of the sample surface. The intention of this investigation was to obtain information on the prevalence and ratio between metallic Sn^0 and tin oxide (either Sn(II) or Sn(IV)) surface species (with much higher sensitivity as XRD) and the total elemental composition of the GDE surface. Therefore. the ability of the technique to probe the local bonding environment of the atom is utilized which leads to a characteristic shift of the binding energy according to the binding to its neighboring atom. Here. this would correspond to the oxidation state of tin. The XPS spectrum obtained is depicted in Figure 5.18 with the in-lay zoomed into the region in which the tin related signal for Sn3d is expected. Indeed. two characteristic peaks are prevalent at 487 eV and 495.8 eV which can be ascribed to Sn(IV) (Sn3d$_{5/2}$ and Sn3d$_{3/2}$. respectively). according to [169]. Peaks indicating the presence of metallic tin are completely absent. This supports what has been suggested by XRD. but extended to the surface composition and with much higher precision. The latter is important. as the sensitivity of XRD has been shown to be very low in this case due to low loading and particle size. evidenced by low signal/noise-ratio and pronounced broadening of the reflexes. XPS on the other hand. has a significantly higher resolution and detection limit which makes the absence of Sn^0 on the surface very reliable. However. there is no clear distinction between the partially oxidized tin with intermediate binding state (SnO) and the fully oxidized form possible as the difference in the chemical shift for both species is not resolvable by the device [169]. If a discrimination would be important. it could be realized by checking the Sn:O ratio. however. due to the oxygen content in the functional groups of the carbon black surface which is unknown. this is not possible in this sample. Despite the absence of any evidence of SnO in the XRD analysis. its presence cannot be completely excluded on the basis of the data at hand. at least in low quantity.

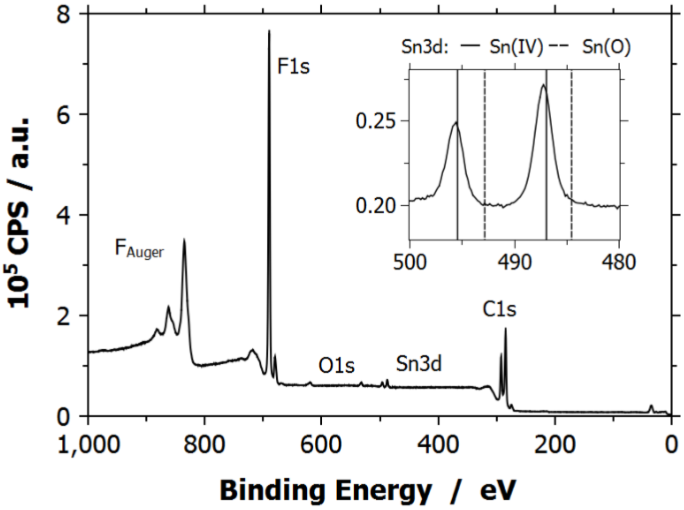

Figure 5.18 XPS survey spectrum of AB35NP-GDE with in-lay showing binding energy range of Sn3d-region.

Summary

While the depicted characterization results confirm that tin is completely oxidized. both on the surface and in the bulk. this does not give information on the active species during electrolysis. Naturally. it cannot be excluded that the oxide is at least partially reduced at the negative potentials necessary for CO2RR which are more negative than the thermodynamic standard potential of the Sn/SnOx redox-couple (-0.66 V vs SHE at pH10. see chapter 6.3.2). For that purpose. the use of *operando* characterization would be valuable to gain information on the catalyst properties during the reaction. As discussed in chapter 3.3. using such methods. it has indeed recently been shown. that a metastable oxide layer which withstands the reducing environment not only participates in the reaction but is pivotal for obtaining reasonable performance [94.101]. Furthermore. the occurrence of differences in the oxide layer thickness and oxide-metal ratio is argued to be responsible for substantial differences in literature studies regarding the FE towards formate when working under the same conditions and – at least presumed – the same tin catalyst (as described in chapter 3.3). Although the derivation of a robust oxide layer is merely a side-effect of the GDE preparation method in this work. it explains the high formate selectivity already at low current densities [93] which is superior to most studies from literature using tin as catalyst. It would be interesting and potentially support this argumentation. when tin with tailored oxide layer thickness or metallic tin could be incorporated into the GDEs employed in this work. *e.g.* by avoiding (or mitigating) their oxidation during thermal treatment or intentionally reducing them before use. However. more detailed catalyst studies were not in the scope of this work. but left open for further investigation.

Chapter 6

Electrochemical Characterization of Gas-Diffusion Electrodes

The core of this work was the electrochemical characterization of the GDE and the evaluation of the interplay between its preparation. properties and electrochemical performance. In the following chapter. this will be systematically discussed along the various parameters governing the GDE performance. The goal is to establish a clear guide for a more rational tailoring of the GDE properties based on a more fundamental understanding on the influence of the preparation parameters. The chapter starts with a short description of the system and how the experiments with GDEs are conducted. their performance assessed and compared. The chapter continues with the investigation of the effect of metal loading and dispersion. a screening of different carbon materials and the influence of the PTFE content. Following the obtained information from these experiments. a more targeted investigation of the electrode properties is pursued to elucidate the decisive parameters for the electrochemical behavior. The studied properties include the hydrophobicity and porosity. evaluated by oxidizing the carbon carrier. use of pore-forming agents and varying compacting pressure. electrode thickness and the operational mode. It has to be noted that in the course of these investigations. the benchmark GDE onto which adjustments have been made. was not always the same with regard to the carbon support what might lead to confusion when comparing results beyond chapters. The same accounts for the electrolyte composition which changed from 0.1 M to 1 M $KHCO_3$ in the course of this work.

As a starting point for this work. the sketch in Figure 6.1 illustrates the interplay of the GDE preparation parameters and what properties they influence. The employed GDEs are carbon-based. catalyzed by tin/ tin oxide and bound together by PTFE (polytetrafluoroethylene) as binding agent which besides supplying mechanical integrity renders the pore system hydrophobic. The main contributions which influence how efficient the reaction proceeds can be divided into contributions given by the electrocatalyst. mainly the kinetics. participating catalyst surface area and accessibility. the wettability of the pore system determining the extent of the reaction zone and the porous structure. All of the above parameters control the mass transfer from gas phase to the triple-phase boundary. as well as mass transport of dissolved CO_2 to the active site and of the charged products to the bulk electrolyte. These aspects will be elaborated in the next chapters.

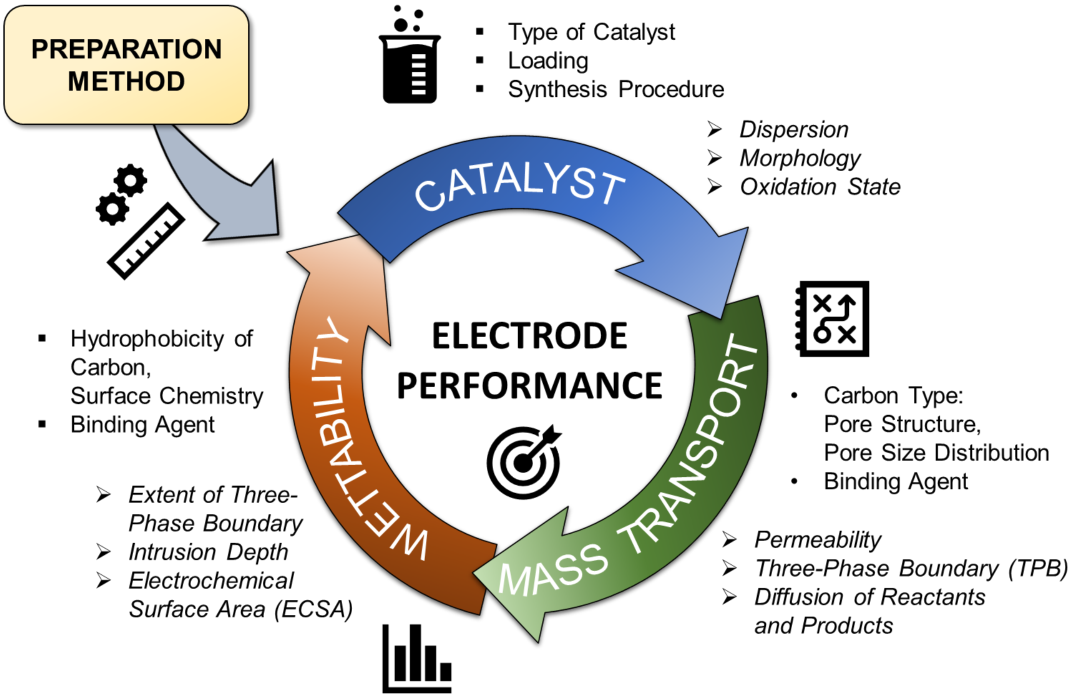

Figure 6.1 Illustration of parameters determining electrode performance

The important performance figures which are addressed in this work are the following:

- Achievable current density. Working at high current density is advantageous as it directly relates to the space-time yield of the electrolyzer. However. at some point. the reaction becomes mass transport limited. *i.e.* a further increase beyond this limiting current density only translates in an enhancement of hydrogen evolution.
- Activity. given by the potential-current relationship or the polarization curve. which correlates with the reaction rate according to the Butler-Volmer equation (eq. 2.15). The driving force for the reaction is the electrode potential. Working as close as possible at the thermodynamic optimum given by the Nernst equation (eq. 2.10) is desirable.
- Stability. with respect to activity and product distribution over time. For technical realization thousands of hours are desired. Naturally. an investigation on these time scales is unrealistic and not the scope of this work. The screening and comparison of different electrodes has in most cases been done in one-hour experiments due to the limitation in the semi-batch experiments regarding the change in the electrolyte composition with time. whereas the experiments in the continuous mode were extended to several hours. Furthermore. a discussion of the transient behavior in these short time intervals and the progressing wetting behavior with time during the initial phase will be discussed.

6.1 Development of GDEs and their electrochemical behavior

6.1.1 Electrochemical Reduction of CO_2 on Planar Tin Foil

In this work. tin was chosen as active cathode material due to its promising ability to convert CO_2 to formate at Faradaic Efficiency (FE) above 80% at moderate overpotential as suggested in a variety of studies summarized in chapter 3. Furthermore. it is inexpensive and neither toxic nor problematic for the environment as it is the case for the other formate-producing catalysts such as Hg. In. Pb and Cd which makes it attractive for technical application of the process.

To get a general understanding of the electro-reduction of CO_2 in the system at hand with tin/ tin oxide as active component. preliminary experiments were conducted using bare tin foil as working electrode. The foil was pre-treated to clean-off contaminants by mechanical polishing and washing with diluted HNO_3 solution. It was further undertaken the same thermal treatment at 340 °C as for the GDEs reported in the following chapters to obtain comparable surface properties. As a starting point for the work in this thesis. cyclic voltammetry (CV) measurements have been performed in the 0.1 M $KHCO_3$ benchmark electrolyte. both. saturated with CO_2 (pH 6.82) and degassed with N_2 (pH 9.2) to assess its behavior in the presence and absence of CO_2. Thereby. the participating redox reactions can be ascribed to distinct potentials and the potential range. in which the experiments in this work have to be conducted. can be assessed. The results of the scans are depicted in Figure 6.2. plotted on the RHE scale (reversible hydrogen electrode. $E_{RHE} = E_{SHE} - 0.059 \cdot pH$) to compensate for the different pH values in both solutions and the according difference in standard potentials. Furthermore. to set the results into relation. the scan in the degassed solution was also performed with a Pt rod. which is known to be one of the most active metals for hydrogen evolution (HER) [29].

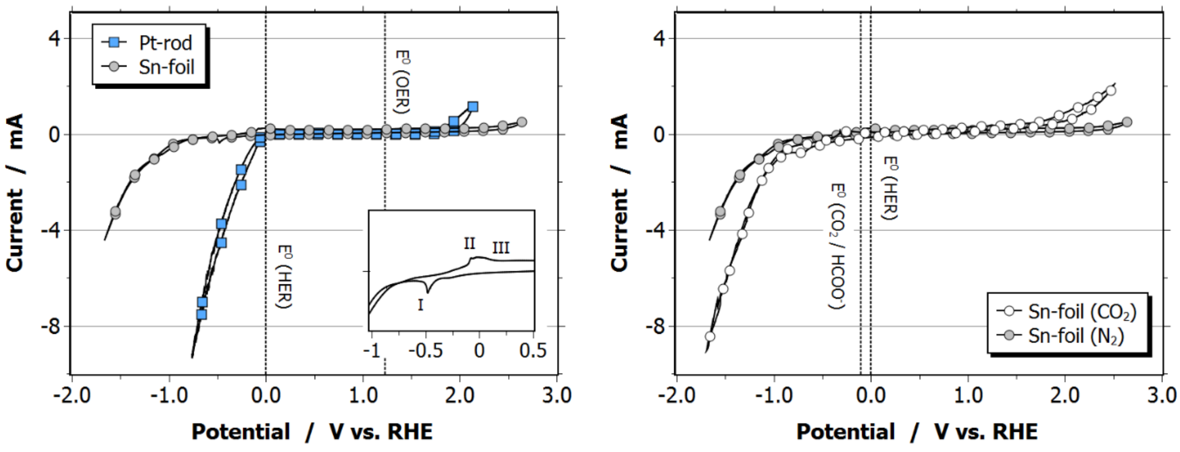

Figure 6.2 Cyclic voltammetry scans (scan rate 10 mV/s) in degassed electrolyte (CO_2-free 0.1 M $KHCO_3$. pH 9.2) using tin foil and Pt rod as comparison (left. inset shows redox-behavior of tin surface). Electrochemical behavior of tin foil in degassed and CO_2 saturated electrolyte (pH 6.82) (right). standard potentials of relevant reactions indicated with dashed vertical lines

In the absence of CO_2 (left figure). hydrogen evolution can be observed as the steep exponential rise of the cathodic (negative) current when the electrode is polarized in negative direction. Comparing the standard potential included in the graph as dashed line with the onset of the reaction. the assessment of Pt above is confirmed. indeed exhibiting negligible overpotential for HER. On the other hand. tin shows quite a remarkable overpotential towards HER which is in line with the requirements outlined in the theory section for suitable CO2RR electrocatalysts. Accordingly. HER is strongly suppressed on its surface in the potential region of CO2RR which is important as both reactions are competing for active sites. For completeness. also the anodic branch of the CV is included which was scanned into the potential region of OER. evidenced by a slow rise of anodic (positive) current at potentials beyond $E^0 = 1.23$ V. Since OER is the significantly more complex reaction. overpotentials are much higher than for HER. rendering even a rather active catalyst such as Pt with high overpotentials.

For the tin foil three peaks can be observed. shown in the inset of the left graph. They can be assigned to the redox-behavior of the tin oxide film on its surface. two of them with a pronounced plateau up to the start of OER being oxidative and the other of reductive nature. The reduction peak is always present in the literature on CO2RR on tin surfaces and is commonly ascribed to the partial reduction of the oxide film (of whatever nature) to metallic tin; partial because a metastable oxide film maintains in the presence of CO_2 despite the negative potential. see 3.3. Its exact position. here at -0.47 V. is largely dependent on the history of the sample. its pre-treatment. electrolyte composition and the conditions of CV (scan rate. limits) with the peak position ranging approx. between -0.1 V and -0.5 V vs. RHE at different anodic scan limits. according to [170] in slightly alkaline media. For the oxidation peaks. the picture is not as clear but according to more fundamental electrochemical studies on the tin oxide surface they can be associated with the hydroxylation of the metallic tin surface and its oxidation to $Sn(OH)_2$ or SnO (i.e. Sn(II). peak III). followed by the progressive passivation to $Sn(OH)_4$ or hydrated SnO_2 at more positive potentials. evidenced by the pronounced anodic plateau beyond peak III.

In Figure 6.2 on the right. the scan in the CO_2 saturated electrolyte is plotted together with the one in the CO_2-free solution. both for the tin foil. It is clearly visible that the presence of CO_2 changes the onset and the magnitude of the cathodic current (also in the RHE-scale. *i.e.* even when the change of pH is accounted for) when scanning in the negative direction. suggesting that in the presence of CO_2 an additional process proceeds starting at lower polarization of the electrode than HER in the absence of CO_2. This feature accelerating at around -0.8 V vs. RHE (-1.2 V vs. SHE) but slowly setting in already at more positive potentials is associated with CO2RR. Naturally. it is not clear by these experiments alone what this current exactly corresponds to and how the current is distributed between CO2RR and HER. As pointed out by Hori [62]. the current assigned to CO2RR is not simply the difference between the current in degassed and saturated solution as the presence of CO_2 in solution. besides changing electrolyte composition and proton concentration. directly affects HER and the active sites on which it proceeds. *e.g.* by competitive adsorption. Furthermore. also a clear assignment to an exact onset overpotential is difficult as. evidently. different reactions are overlapping in this potential region (HER. CO2RR to different products and SnO_x reduction). However. these simple experiments already demonstrate that the presence of CO_2 significantly changes the electrochemistry of the system. because additional current arises by the reduction of CO_2 which will be quantified in the following chapters. Furthermore. it is clearly shown that the use of planar electrodes only facilitates electrolysis at small current densities. In the above case. ~10 mA/cm² can only be achieved at an overpotential of about 2 V which is at least one order of magnitude below what is considered viable for technical realization [19].

6.1.2 Preparation of Gas-diffusion electrodes

The above discussion showed that using flat electrode architectures severely suffer from low achievable current densities. This is not so relevant when new types of materials are evaluated. or mechanistic investigations are performed. however. for technical realization of the process. current densities on the order of several hundreds of mA/cm² are indispensable which makes the use of GDEs essential as elaborately discussed in chapter 3.4.3. Choosing an appropriate method for the preparation of GDEs is important as besides governing the electrochemical performance it also determines how economically feasible the process is. It is surprising that there is no profound investigation on the influence of preparation method. as it is the case for other applications such as fuel cells or water electrolysis for which numerous studies have been published [128.171.172]. For technical realization. certain requirements are placed on the preparation method that have to be met: Besides being cost-efficient. exhibiting high reproducibility and low environmental impact. the method has to be suitable for scale-up. preferably in an automated and continuous manner. In the frame of the project. the goal was to develop a solvent-free dry deposition method for lab-scale investigations. The general advantage of dry methods is that avoiding solvent use leads to lower cost. less waste and the possibility of continuous operation without additional time for drying. Furthermore. in case of wet techniques. the reproducible formulation of the catalytic ink. its storage and the stability of the dispersion are difficult challenges for scale-up purposes. which is avoided when powder mixtures are deposited [173].

Based on the work by A. Inan [174] in which the general procedure of the electrode preparation was introduced and the key features implemented. this process was refined and the preparation conditions optimized. The initial goal was to produce mechanically stable electrodes with the desired composition in an efficient and. importantly. reproducible manner. The method is a dry pressing method developed for fast and simple evaluation of GDE preparation and electrolysis conditions in a lab-environment. The method comes with certain advantages over *e.g.* solvent-based wet deposition methods. such as hand-painting or air-brushing usually employed for electrodes in CO_2 reduction research (see chapter 3.4.2). The method is very simple and straightforward. includes very few production steps with few parameters to be optimized and has very low excess material input. A sketch of the process steps is given in Figure 6.3. the exact conditions are described in the experimental section. In short. after thoroughly mixing the powders in a knife mill. a certain amount is given in a cylindrical mask and pressed with a hydraulic press at defined pressure for 1 h. The chosen mass determines the thickness of the layer while the compacting pressure also influences porosity. Both paramezers will be evaluated later. In a last and decisive step. the electrode is undertaken a thermal treatment (in literature often misleadingly termed ‘sintering’) in an oven at 340 °C slightly above the melting point of PTFE (327 °C) to obtain a homogeneous distribution of PTFE as thin film over the interior electrode structure. PTFE was chosen as binder. instead of Nafion which is commonly employed as binder and ionomer in wet-deposition methods for CO2RR (see 3.4.2) inspired by PEMFC research. The choice for PTFE was made to produce *hydrophobic* GDEs with coexisting aggregates wetted by the liquid electrolyte and dry gas channels distributed throughout the active layer to maximize gas dissolving sites and the TPB. This approach is suggested to be advantageous herein. as the benefit of Nafion as proton-transport ionomer is questionable for CO2RR and in alkaline media in general. and would lead to a flooding of the whole catalyst layer due to its hydrophilic nature. This can be desired in the case of thin-film catalyst layers and multi-layer assemblies. yet. is not the case in this work where the deposition method intrinsically produces thicker single-layer electrode structures.

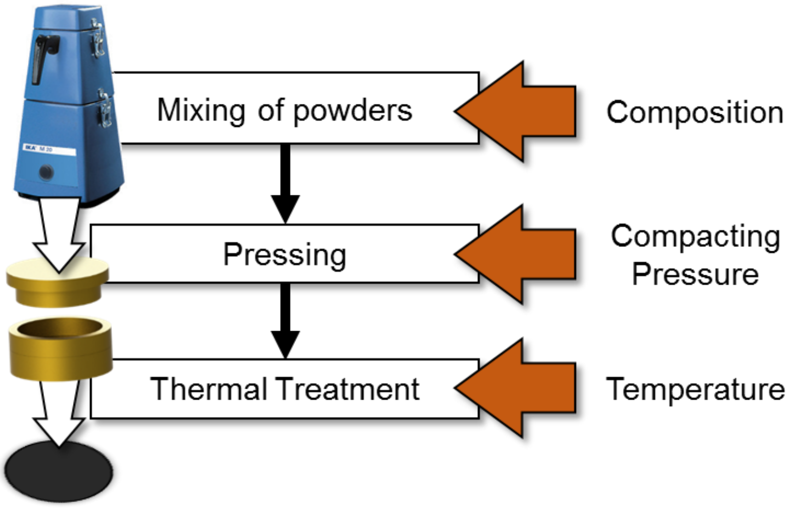

Figure 6.3 Production steps during GDE preparation and respective parameters to optimize

To demonstrate the reproducibility of the preparation method regarding the catalyst layer thickness. several thickness measurements have been performed over various positions of the same electrode to evaluate uniformity and at different electrodes. This has been done for GDEs with different overall mass from 100% to 50% and 30% for which variation of the thickness was targeted. The results are summarized in Table 6.1 showing the good reproducibility and uniformity of the GDEs with the standard deviation of the thickness increasing slightly from 1% to 6% when going towards smaller thickness whereas the reproducibility maintains stable between 2% and 4%. The reproducibility regarding electrochemical performance will be discussed later.

Table 6.1 Thickness of GDEs with different electrode mass. uniformity and reproducibility (standard deviation inside GDE and between GDEs)

Electrode Mass	**Thickness** **µm**	**Uniformity** **µm / %**	**Reproducibility** **µm / %**
100%	829	±12 / ±1.5	±21 / ±2.6
50%	427	±10 / ±2.4	±16 / ±3.8
30%	281	±19 / ±6.4	±7 / ±2.5

It is clear that the developed method that produces one electrode at a time cannot be simply transferred into larger-scale in an industrial environment. That said. this was not the purpose but rather to set a benchmark for the scientific investigation and to allow a systematic optimization of the electrode properties. Further development would include the transfer of this knowledge into a continuous dry deposition of GDEs with larger dimensions (5x5 or even 10x10 cm²). Also. the derivation of thinner layers would be beneficial to minimize ohmic losses and ionic transport limitation as would be the deposition of the layer onto a support such as a current collector or a macroporous carbon substrate to minimize contact resistances. Possible technologies for technical realization are dry-spraying [173] or the direct rolling of the homogenized powder mixture onto a support/ metal net. *i.e.* roll compaction or calandering how it is already in place for certain applications. such as gas diffusion layers for fuel cell application or oxygen-depolarized cathodes for the chlor-alkali synthesis [47].

6.1.3 Relationship between potential. current density and product distribution

Prior to the in-depth investigation of the GDE behavior as function of its properties in the subsequent chapters. the discussion will start with an exemplary description and interpretation of the commonly conducted experiments to introduce how the performance of the electrodes and catalysts are assessed. This comprises the assessment of activity. *i.e.* the recording of the potential-current relationship or so-called polarization curves. the influence of the potential and current density on product distribution and a description on how the galvanostatic experiments (at fixed current density) are evaluated to compare electrodes with different properties. To clearly demonstrate the importance and the benefits of using a GDE for this reaction. the voltammetry scans from the previous section on planar electrodes have been repeated. both with nitrogen and CO_2. Instead of pre-saturating or degassing the electrolyte. both experiments were conducted in the same electrolyte but with CO_2 and N_2 flowing on the gas side of the GDE. This is reasonable. as the dissolved CO_2 in pre-saturated electrolyte will give negligible contribution to the expected current density for GDEs due to its low solubility and constant supply of gaseous CO_2 from the back. After pre-conditioning the GDE (here: Acetylene Black. 35% PTFE. 5 mg/cm² commercial tin powder) at -1.5 V vs Hg|HgO for 1 h. Linear Sweep Voltammetry Scans (LSV) have been conducted in which the potential is scanned with a fixed scan rate (here 5 mV/s) over a given range. As the name suggests. in contrary to a cyclic voltammetry scan. in an LSV only the forward sweep is performed during the measurement. While for kinetic studies commonly the CV is the measurement type of choice as it gives more valuable information. herein due to the significant change of the catalyst environment at the high current densities due to product accumulation as well as partial reduction of the catalyst itself. an LSV is considered more practical. In addition. a pre-conditioning step was shown to be necessary to facilitate a reproducible wetting of the hydrophobic GDE. thus. a prerequisite to perform LSVs in the first place. The result is shown in Figure 6.4. As expected. tin as electrocatalyst exhibits a high overpotential towards hydrogen evolution. with an on set overpotential of around 600 mV (-1.2 V vs. SHE at 1 mA/cm². E^0_{HER} = -0.59 V) at these conditions (compared to a few mV for Pt. see above). Furthermore. in the presence of CO_2. the current is significantly increased which suggests that reduction of CO_2 proceeds and that it is strongly favored over HER. Whereas. current density at -1.6 V which corresponds to an overpotential of 1 V ($E^0_{CO2/HCOO}$ = -0.6 V at pH10) is as high as 185 mA/cm² under CO_2 flow. it decreases to only 15 mA/cm² in its absence. Such LSV scans were regularly performed in this work to assess activity of electrode and catalyst. The graph it produces is also often referred to as polarization curve or E-i curve and depicts the potential-current relationship of an electrode system at specific electrolysis conditions.

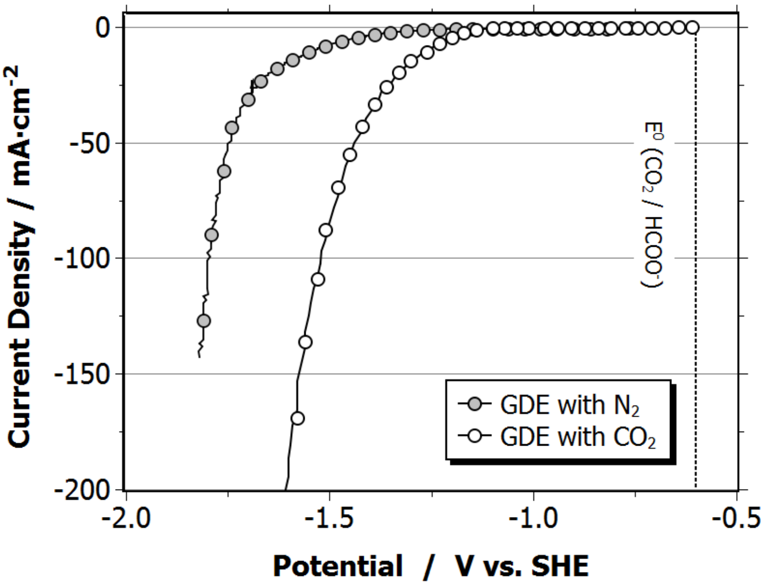

Figure 6.4 Polarization curves of GDE (AB35. 5 mg/cm² Sn) with CO_2 and N_2 flowing on the gas side in 0.1 M $KHCO_3$ at pH10.

To obtain information on product distribution. most of the experiments were conducted under galvanostatic control. which means that the current was fixed and the potential measured over time while the product distribution was evaluated. The latter was done on-line *via* gas chromatography to measure the gas phase distribution while the volumetric flow-rate at the outlet of the half-cell was monitored continuously. Furthermore. after each experiment a liquid sample was taken to evaluate liquid phase products and components (formate and dissolved CO_2 in the form of (bi)carbonate. the latter to close the carbon balance). Since one of the main goals of this work was the optimization of the electrode properties to facilitate efficient mass transport and achieve high current density. the behavior at high current density is regarded as particularly important. Thus. the current density was stepwise increased between each experiment and the product distribution analyzed. Plotting the FE towards the products over the current density. as further below. allows the comparison of the different electrodes regarding their ability to work at high product yield. Figure 6.5 shows the course of such a galvanostatic experiment for different current densities.

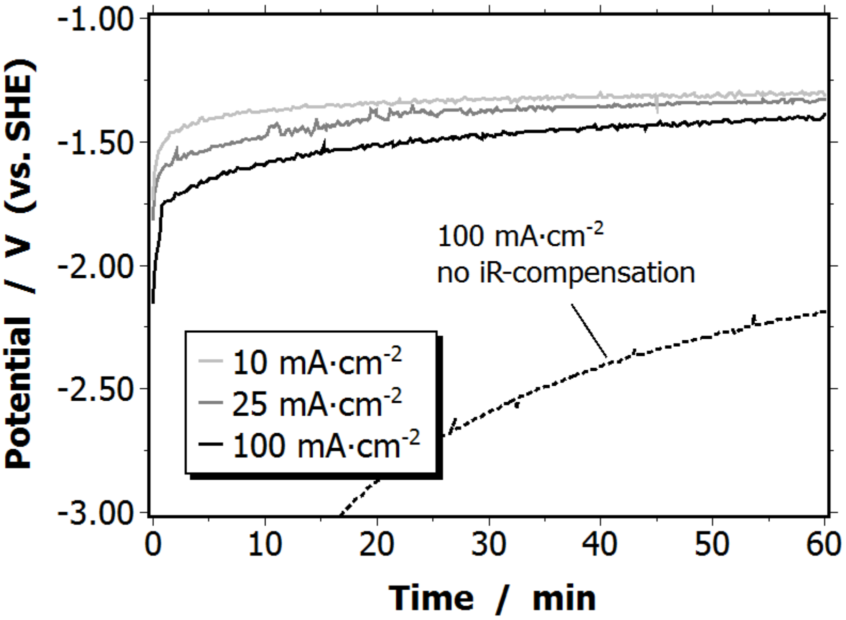

Figure 6.5 Exemplary development of electrode potential over time at different current densities. dashed line: without iR-compensation (AB35 with 10% graphite. 5mg/cm² Sn. in 0.1M $KHCO_3$. see [175]).

As one can see. the potential becomes more negative as the current density is increased due to a higher electrode polarization. Also included is the course of the potential without *iR-compensation* with a dashed line. iR-compensation is an important technique to compensate for the ohmic voltage drop between working and reference electrode owing to the limited ionic conductivity of the electrolyte. The higher the current. the higher the distance and the lower the conductivity of the electrolyte. the higher the deviation between measured and actual electrode potential. Here. it is particularly high. because the preliminary experiments were all conducted with $KHCO_3$ of a very low concentration 0.1 M which is translating into low conductivity of 9.7 mS/cm (compared *e.g.* to 170 mS/cm of 1 M KOH). The difference between actual and non-compensated potential becomes less pronounced with time due to the accumulation of product $HCOO^-$ and OH^- as well as diffusion of K^+ as charge carrier from the anode to cathode chamber. This results in a steady rise of conductivity. for example to ~30 mS/cm after 1 h at 50 mA/cm². Only by subtracting this contribution. a meaningful assessment of the actual potential is possible without influence of reactor geometry and placement of the reference electrode. In this work. the so-called *Current-Interrupt* technique was employed for this purpose which is automatically performed by the potentiostat software in the background of the experimental sequence. In the following if not otherwise mentioned all the potentials are iR-compensated. The iR-compensated curves still show a decrease of polarization with time which can be explained by the continuous wetting of the electrode with time which puts more catalyst in contact with electrolyte and thus lowers the local current density when the macroscopic current density remains constant.

The changing electrode polarization influences the different participating reactions to different degrees as each reaction proceeds *via* different pathway which has its own potential dependence. The product distribution as function of current density and average potential during the experiment is depicted in Figure 6.6. The graph was obtained by stepwise increasing the current density from 10 to 250 mA/cm² in consecutive experiments and plotting the FE of the products over the average potential during the experiment (as product distribution is also averaged). The employed GDE was made from a mixture of 35% PTFE. with an Acetylene Black : Graphite ratio of 9:1 and a tin loading of 5 mg/cm². In these preliminary experiments. graphite was added to the GDE mixture to facilitate mechanical stability which constituted a problem at the very beginning of this work but could be alleviated in the course of optimizing the preparation procedure in the next chapters. As one can see. HER is mostly suppressed for all potentials in the presence of CO_2. Only when going to very low negative potentials there is a slight increase of HER observable. This trend is in agreement with literature in which the FE towards CO2RR linearly increases from the onset potential towards more negative potentials. However. the observation that CO2RR makes up more than 80% and HER is mostly suppressed over the whole investigated potential range. even at potentials close to onset was rather uncommon at the time this study was performed. Surveying the broad discrepancies of results when using tin-based metals in literature. it is evident that the outcome is highly sensitive to experimental conditions and the exact catalyst properties that result from the synthesis and pre-treatment. Indeed. it has been show that the ratio between CO2RR and HER is a strong function of subsurface oxygen content [93]. which can readily explain the desirable outcome herein with the fully oxidized tin oxide catalyst (see chapter 5.3). The suppression of HER proceeds up to the current density for which transport limitation sets in. here at 200 mA/cm². beyond which HER increases rapidly. Furthermore. the ratio between CO_2 reduction into formate and CO is clearly affected by the electrode potential as shown in Figure 6.6. At low negative potentials. the distribution of the CO_2 products is slightly shifted towards CO with a FE close to 20% and 80% to formate at -1.2 vs. SHE whereas at high overpotentials the ratio shifts in favor of formate increasing to over 90%. This potential dependent variation in the CO_2 reduction product spectrum has been observed in literature before [88]. It is not surprising as formate and CO go through different mechanisms which show different dependence on the electrode potential (see chapter 3.2). The same effect of the competition between CO and formate production as function of the potential can be observed throughout this work. independent of where the effect on the electrode potential comes from (higher metal loading. better wettability of electrode or increased wetting with time). Also shown in Figure 6.6 is the sum of the FEs which does not go above 3% deviation from 100% and maintains at 100% ± 5% throughout this work.

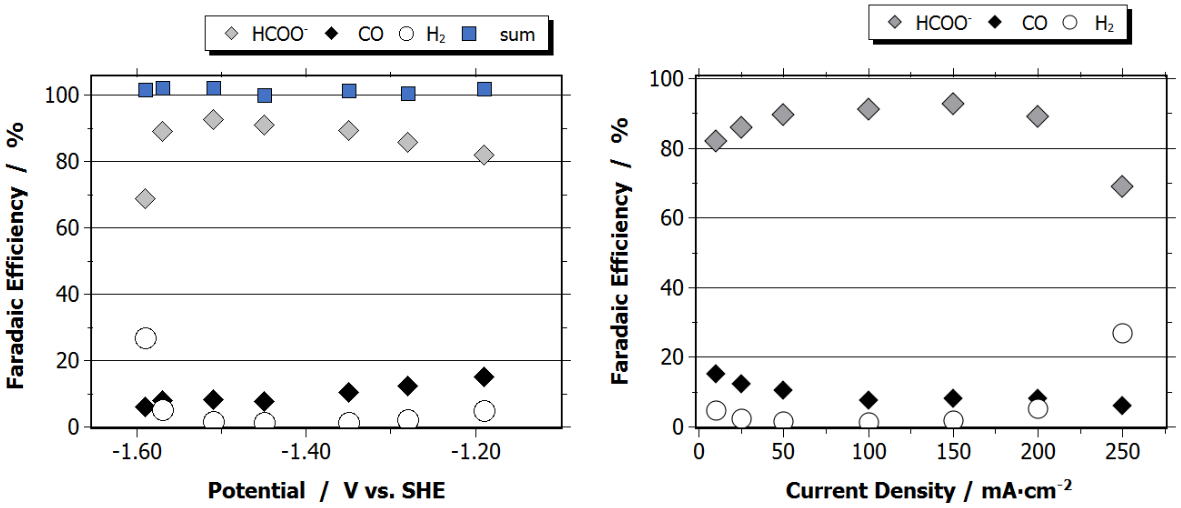

Figure 6.6 Product distribution and sum of FE as function of electrode potential (left) and current density (right). both depicting the same data (AB35 with 10% graphite. 5mg/cm² Sn. in 0.1M $KHCO_3$).

Finally. on the right of Figure 6.6 the product distribution as function of the current density is depicted. It shows the results from the same experiments but instead of the resulting potential. the set current density is plotted on the x-axis. While both graphs in principle show the same results. depending on the question asked. either of the diagrams yields the desired information. Whereas the potential gives information on the intrinsic properties of the electrocatalyst which produces different product mixture depending on its polarization. the current density is better suited for evaluating the electrode performance from an application point of view. as it is possible to assess the current density window. one can work in to get a product of desired yield. In the depicted case. one can see that at very low current densities below 50 mA/cm². which corresponds to low electrode polarization. formate selectivity is slightly lower due to an increased CO generation than in the CD window between 50 and 200 mA/cm² for which formate FE is around 90%. Beyond that. transport limitation sets in. clearly visible by an acceleration of HER. For the following experiments. the current density plot will be shown almost exclusively as one major goal was to assess achievable current densities.

6.1.4 The Wetted Surface Area and its Influence on Activity

The extent of the triple-phase boundary where catalyst. gas phase and electrolyte meet and the surface area of wetted electrocatalyst in this reaction zone are the governing variables that determine activity. *i.e.* how much CO_2 can be converted at a given electrode potential. To have an idea of the magnitude of this reaction zone and where it is situated inside the GDE is of pivotal interest. As discussed in chapter 5. the actual participating electrode surface is. indeed. extremely low compared to the total GDE surface area. Even when only the macroscopically wetted electrolyte front is taken into account. a large portion of this volume remains dry. which is suggested to be beneficial for gas transport throughout the GDE and accessibility of the wetted regions by reactant. On the other hand. for a given current density. low wettability increases the electrode polarization. due to higher *local* current densities. For a better understanding of this effect. targeted experiments have been conducted to examine the time evolution at constant potential and establish the relationship between the wetting of the electrode structure and the electrode activity for different electrodes. The experiments are conducted at low polarization to maintain in the kinetically limited region far away from transport limitations. In contrast. the behavior in the transport limited region is investigated in 6.2.3.

Change of wetting with time

As mentioned. the GDE becomes increasingly active with time. as the electrolyte continuously penetrates into the pore system of the GDE. This can be readily observed in potentiostatic experiments at constant electrode potential. To correlate the effect of increasing activity and electrode wetting with time. a one-hour experiment was interrupted in equal intervals of 10 min. the double layer capacitance measured. and the run resumed. As one can see in Figure 6.7. the activity increases for each 10 min run with the same slope. However. surprisingly. the consequent runs do not pick up where they ended before but at a slightly lower activity. This becomes clear when running the experiment for 60 min without interruption to measure the capacitance: without the breaks the final current density is three times higher than in the sequence with the breaks. The datapoints in Figure 6.7 on the right are the measured current densities at the end of the consecutive 10 min runs. whereas the red line is from the experiment without breaks. It is important to note that the activity decrease is not caused by the capacitance measurements as it also occurs to the same extent when the current is just switched off for the same period of time. understanding of the system was obtained. as discussed in the following.

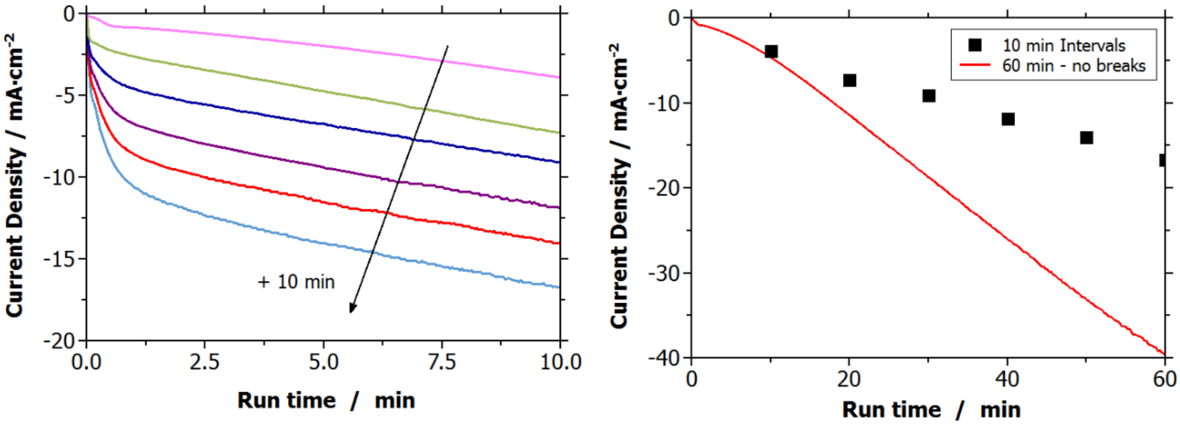

Figure 6.7. Current density over time for consecutive 10 min experiments with the same GDE (left) and comparison with an experiment running for 60 min without breaks (right). each at -1.4 V

First. it was hypothesized that the intrinsic activity of the catalyst is affected by switching off the current. such as that a reduction of the tin oxide surface occurs or the catalyst is leached. Evaluating the capacitance after each step and comparing it to the 1 h experiment. as depicted in Figure 6.8. gives another explanation. The lighter red datapoint at 2.5 mF gives the capacitance of the GDE which ran for 60 min without break. The much higher capacitance suggests that interrupting the experiment has an effect on the wetting behavior. Accordingly. the current density before the break is plotted against the corresponding capacitance in the break on the right figure. Evidently. a direct relationship can be drawn between the wetted surface area and the activity which increases linearly with wetting and time. Moreover. the GDE without the breaks lies on the same straight line relating current density and capacitance as do the other two reproducibility tests. The higher activity can thereby be readily explained by a higher wetting degree which in turn suggests that the reason for the decrease in activity with each break is due to an apparent retreat of electrolyte as soon as the potential is switched off. As soon as the potential is applied again. the progressive wetting continues but starts from a slightly lower initial point. This can be ascribed by the influence of the electrode potential on the surface tension between liquid and the pore surface. as described in chapter 5 [162]. When a negative potential is applied. the surface tension decreases. and the pore system becomes partially hydrophilic. The pores become wetted through capillary forces. When switching off the current. the electrode potential slowly returns to the open circuit potential. the surface becomes hydrophobic again and the electrolyte partially retracts.

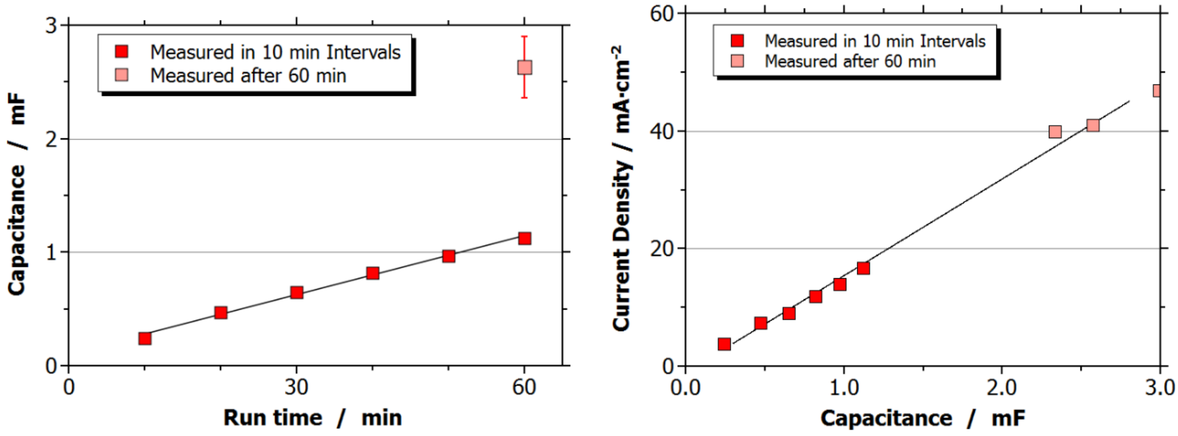

Figure 6.8. Development of capacitance over time at -1.4 V (left). current density as function of corresponding capacitance (right).

Influence of electrode composition on wettability and activity

In principle. wettability should directly correlate with hydrophobicity of the pore system and. accordingly. be influenced by the PTFE content of the GDE and the employed carbon type. In the following both activity and capacitance of GDEs with different PTFE content ranging from 10 to 50% have been evaluated. The GDEs have been pre-conditioned at -1.4 V for one hour. the capacitance measured and. finally. activity assessed *via* an LSV measurement. The results are shown in Figure 6.9. The activity (left figure) increases with decreasing PTFE content. From the knowledge obtained so far. this can be ascribed to an increasing wettability of the electrode due to less hydrophobic PTFE in the electrode matrix. rendering more catalyst in contact with electrolyte. Evaluating the capacitance clearly verifies this hypothesis. Indeed. a striking linear correlation between wetted surface area. given by the capacitance. and activity can be observed. when the current density at the end of the run is plotted versus the measured capacitance. Together with the results from the time-resolved measurements in the previous subsection. this clearly indicates the wetted surface area to be the governing parameter for activity at low to moderate current densities and that this can be qualitatively assessed via double layer capacitance measurements.

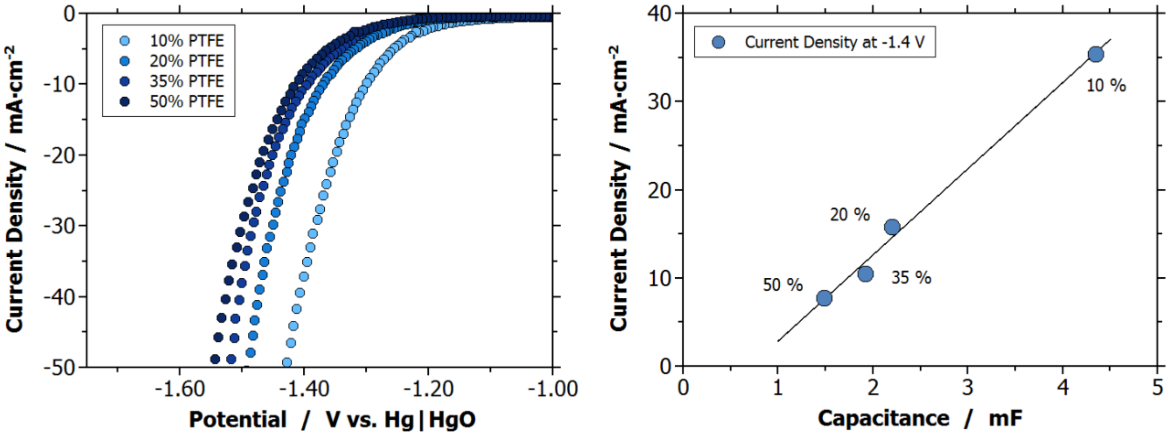

Figure 6.9. Polarization curves of GDEs with different PTFE content after one hour at -1.4 V. scan rate 5 mV/s. Relation between current density and measured capacitance for GDEs with different PTFE content after 1 hour at -1.4 V.

6.2 The Influence of electrode properties on electrochemical behavior

The operation of a GDE is determined by a complex interplay of different contributions and phenomena governed by the employed materials and the preparation conditions. In the following. the experiments and results examining their influence on the electrochemical performance are described and interpreted. Namely. the influence of carbon support and electrocatalyst is investigated. as well as the effect of porosity and wettability.

6.2.1 Screening of a suitable Carbon Support

The carbon material of choice is usually a type of carbon black. Carbon blacks such as most prominently Vulcan XC-72R or Acetylene Black exhibit moderate to high surface area values (yet. inferior compared to activated carbon). a micro-. meso- and macroporous structure and a very high electric conductivity due to their partially crystalline structure formed by graphitic layers that build near-spherical particles which in turn form the aggregates. see chapter 2.5 [176]. Most widely used carbons have been the highly hydrophobic acetylene black and the more moderately hydrophobic oil furnace (*e.g*. Vulcan) carbon blacks [165.177]. However. different groups have found different carbon materials to be superior for the same application suggesting that the actual choice is highly dependent on electrode preparation procedure. reaction parameters and the goal of the investigation (activity. catalyst dispersion. stability). Therefore. it is inevitable to investigate and empirically compare the different carbons for each application and system on its own.

In order to have a solid basis to draw conclusions on the influence of carbon type. different carbon materials with a wide range of different properties have been evaluated. For this reason. the most prevalent carbon black materials in similar applications (e.g. fuel cells. batteries) have been tested. namely. Acetylene Black (AB). Vulcan (VXC). Ensaco (ENS). Black Pearls (BP) and Ketjen Black (KB). Furthermore. as an example for an activated carbon Norit GSX CAT (NOR) was chosen. A detailed overview of the properties of the carbons are given in chapter 5.1. In short. it can be said. that while BP and NOR are highly microporous materials with very high surface area. the latter is also true for KB which. however. is free of micropores but made up of small mesopores. ENS and AB are rather macroporous carbon blacks with low surface area of below 80 m²/g whereas VXC. the most prevalently used commercial carbon black for electrochemical applications. ranges in between those materials. with a moderate surface area of 230 m²/g and certain share of micropores (40% of surface area). The GDEs were prepared with commercial tin powder (5 mg/cm²) and 35% PTFE. the experiments conducted in 0.1 M $KHCO_3$ at pH 10 with the aim to assess ability to work at high current densities before transport limitation sets in. Commercial tin powder was used to avoid influence of metal loading. its dispersion and particle size which is suggested to differ strongly given the high difference in surface area when it is deposited *via* wet chemical routes onto the carbon. It is also important to note that the given values are average values over the one-hour experiment and that in these first screening experiments. the experiments started at room temperature and were conducted non-isothermal. The effect of this will be discussed in chapter 6.3.1.

As Figure 6.10 clearly shows. the materials strongly deviate in their performance when employed as catalyst support. As an indicator of the ability to allow for efficient mass transport. the FE towards H_2 is depicted over the CD. as it will be done throughout this work. The remainder accounts for formate and CO. the ratio of which is solely a function of potential (see above). The first observation that can be made. is that the carbons with high surface area fail at achieving even moderate current densities. Accordingly. transport limitation for KB. NOR and BP already sets in below 50 mA/cm² evidenced by a substantial share of HER. On the other hand. the three macroporous carbon blacks with low surface area but a rather open pore structure show relatively similar results with achievable current densities between 300 and 500 mA/cm² which is already in the range of what is aimed for (see chapter 7.2). Naturally. obtaining information on the decisive properties of the GDE simply by changing the carbon material falls short in such a complex system. as the carbons types differ from each other in several characteristics. such as surface area. pore size distribution and surface functionality. The latter together with the texture leads to different wettability. It is evident that the carbons which exhibit a high share of small pores (micro- and meso) which translates into the observable high surface cannot facilitate electrolysis at reasonable rates when compared to the more macroporous samples. This seems reasonable. as no matter the limiting transport mode. the microporous nature of the pore system seems to entail a severe transport resistance for reactants or products through the pore system. This can include transport of gaseous CO_2 to the triple-phase boundary (TPB). diffusion of dissolved CO_2 to the active site or the diffusion of the liquid products out of the pore system into the bulk electrolyte. A closer look into the potential rate-limiting transport mode is done in chapter 6.2.3

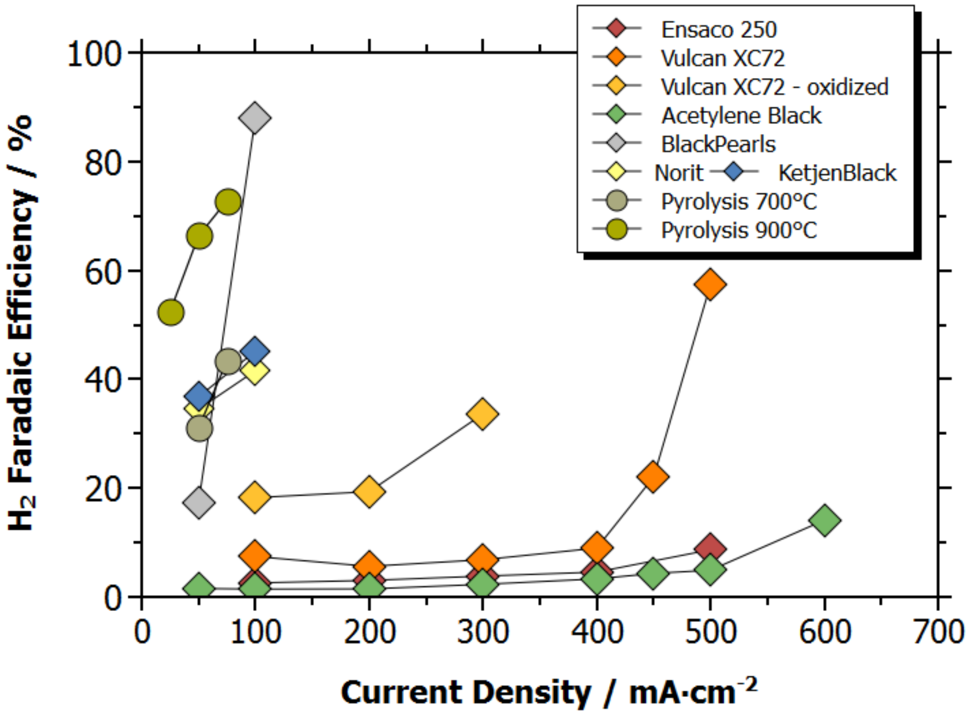

Figure 6.10 Faradaic Efficiency for H_2 over current density for various carbon supports (PTFE content 35%. 5 mg/cm² Sn in 0.1M $KHCO_3$. pH 10).

Besides the transport characteristics and pore structure. it is clear that wettability must play a key role as well for achievable current densities. This is because it determines the magnitude of the triple-phase-boundary and the length of the diffusion path for the dissolved CO_2 to the active sites and the products to reach the bulk electrolyte. According to literature. AB and ENS are highly hydrophobic. the activated carbon NOR and BP are hydrophilic while KB and VXC are moderately hydrophobic [178]. This qualitative assessment which is consistent with achievable current densities could also points towards hydrophobicity being an as important characteristic. Unfortunately. a more meaningful and quantitative analysis of hydrophobicity of the carbon materials requires development of sophisticated methods and was not in the scope of this study despite being of high interest to obtain a better understanding of relationship between GDE properties and performance. A measure which can give a hint on wettability and. indirectly. to hydrophobicity is the measurement of the double layer capacitance. as described in chapter 5.2.1. For the three GDEs which facilitate high current densities. VXC. ENS and AB. the capacitance is depicted over current density in Figure 6.11. Indeed. the above assessment can be verified with VXC exhibiting a higher wetting degree as the highly hydrophobic carbon blacks which are very similar. One has to be aware. that the surface area of VXC35 is higher than AB35 and ENS35 by a factor of 1.6 and 1.4. respectively. While this can contribute accordingly to the increased double layer capacitance of VXC35. it cannot explain completely the difference in capacitance which is more than twice as high.

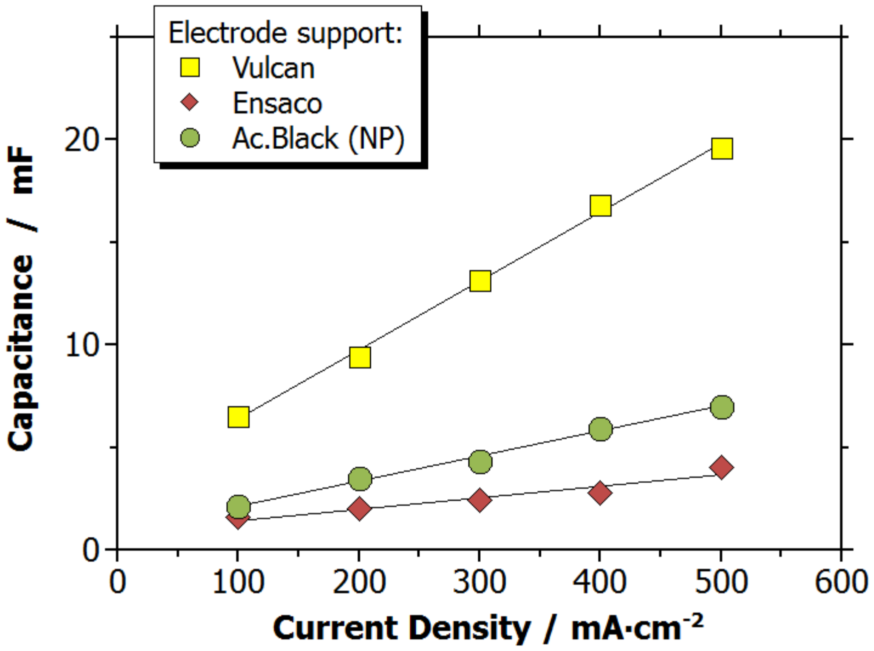

Figure 6.11 Electrochemical double layer capacitance as function of current density for GDEs with different carbon support and 35% PTFE.

With regard to the achievable current densities. a definite answer on a single decisive factor. if existent. or which factor prevails cannot be made with the above results but will be investigated in the subsequent chapters. In the following. in most cases Acetylene Black will be further investigated as reference material as it gave the most promising results here. In some cases. Vulcan is chosen to produce GDEs with moderate performance and lower limiting current density to ensure that limiting current density is not reached due to non-GDE related reasons. such as reactor- or electrolyte-specific reasons.

6.2.2 The effect of loading and dispersion of electrocatalyst

Besides its intrinsic activity and selectivity. an important factor describing electrocatalyst influence on electrochemical behavior is its accessibility in the porous system which in turn is determined by its loading and dispersion. Both are investigated in the following chapter. For the establishment of the GDE preparation method and most preliminary experiments. commercial tin powder was employed but later changed to tin oxide nanoparticles synthesized by homogeneous precipitation.

Influence of metal loading

Although catalyst cost is not a critical factor in this case. as tin is rather inexpensive. this work started with an investigation of the influence of the metal loading on activity and product distribution to choose a reasonable loading for the following studies. For formate generation. there are only a few studies which examined the effect of catalyst amount on the GDE operation. The results presented herein were published in [175] and were one of only a few examples in literature [131.137] at the time of publication.

Due to a different type of electrode structure used. literature examples are not directly transferable. as will be discussed below. To gain insight into how catalyst loading influences the reaction. electrodes with different amounts of tin powder ranging from 0 mg/cm^2 to 15 mg/cm^2 have been prepared and activity as well as product distribution analyzed. The activity was assessed via LSV measurements (scan rate 5 mV/s) for which three exemplary results are shown in Figure 6.12.

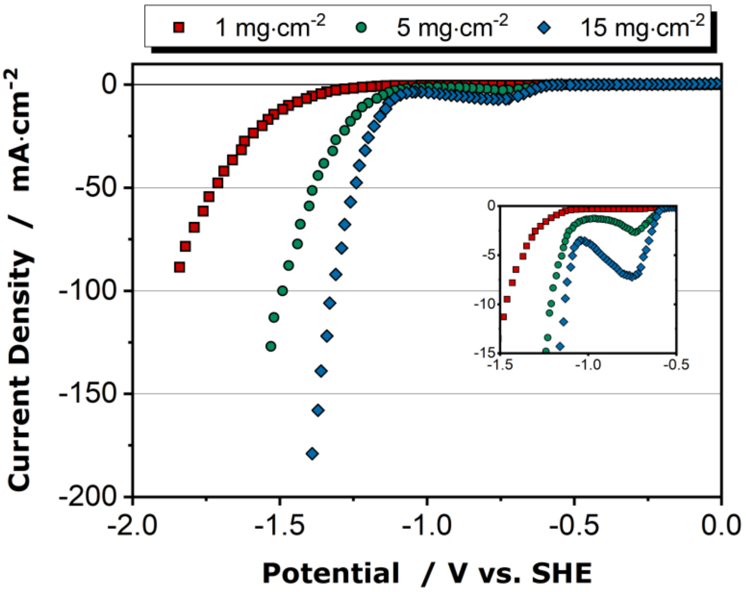

Figure 6.12 Polarization curves of GDEs prepared with varying metal loading

The small peak observed around −0.75 V can be attributed to the partial reduction of tin oxide on the surface of the particles [96]. It becomes increasingly pronounced at higher loadings at which more metal is reduced. as can be seen in the magnification. Independent of the loading. the onset of the reaction is around a potential of −1.0 V vs. SHE. This value is consistent with literature although variations therein are quite pronounced. This is because the reaction is highly sensitive to the surface structure. morphology and chemical environment. At more negative potentials. the current density rises significantly faster for higher loadings. Unsurprisingly. increasing metal loading leads to an enhancement of the macroscopically observable activity due to an increase of active sites wetted by electrolyte and participating in the reaction. However. when normalizing on the metal loading one can observe that activity does not simply scale with the concentration of metal on the carbon support. At -1.3 V for example. the current density is 2. 26 and 85 mA/cm^2 for the GDE with 1. 5 and 15 mg/cm^2. respectively. and 6. 56. 191 mA/cm^2 at -1.4 V. While the activity of the 5 and 15 mg/cm^2 loaded GDE is similar when normalized on the loading. particularly the GDE with lower loading shows a strong deviation. One hypothesis is that the hydrophilic nature of the metal / metal oxide leads to a more pronounced wetting and. thus. more wetted electrode surface. While. unfortunately. capacitance measurements were not conducted at this stage of the study. the amount of wetted catalyst surface can be estimated by integrating the tin oxide reduction peak between -0.5 V and -1.0 V. assuming the same extent of reduction during the potentiodynamic scan.

To evaluate the amount of electrochemically active surface area. the polarization curve was deconvoluted by curve fitting of an exponential function and a Gauss distribution describing CO_2 reduction with an onset at -1 V and the tin oxide reduction at ~ -0.7 V. respectively. The result is depicted in Figure 6.13 for the GDE with 5 mg/cm^2 loading. Although the two functions can nicely fit a large range of the experimental curve. it is visible for all the curves. that the tin oxide reduction does not follow a distinct Gauss distribution throughout the scan but exhibits pronounced tailing which merging into the exponential curve. This suggests that the tin oxide reduction is kinetically limited and not fully completed at the sweep-rate at hand. As the sweep-rate. the morphology of the catalyst and its environment is the same in all cases. it is reasonable to assume that the change of the shape of the reduction peak is comparable and that the obtained area when integrating the fitted gaussian distribution allows a comparison of the relative increase of wetted surface area when increasing the metal loading. Following this argument. it is estimated that the electrochemically active surface area increases by a factor of 6.78 and 17.8. when going from 1 mg/cm^2 to 5 and 15 mg/cm^2. respectively. Particularly in the very low current density region (potential > -1.25V). there is a striking consistency of the curves when normalizing to the area of the tin reduction peak as shown in Figure 6.13 on the right. At moderate current density. particularly the GDE with low loading slowly shifts towards more negative potentials. arguably induced by an increasing share of overpotential from transport limitation (longer diffusion paths for dissolved CO_2 to reach active site) and increased HER production. As in chapter 6.1.4. this analysis again validates what is expected: that the amount of wetted catalyst surface is the sole GDE parameter determining the activity in the kinetically-limited region. It is important to note. that the amount of wetted catalyst surface can only be analyzed *qualitatively* by this technique as it is not clear what percentage of tin oxide is reduced during the sweep. This is because according to literature [101] a metastable share of oxide species remains on the surface during the reduction despite the potential being more negative than the reduction potential. Here. it is assumed that the share of active sites reduced during one sweep remains constant when the same conditions are applied.

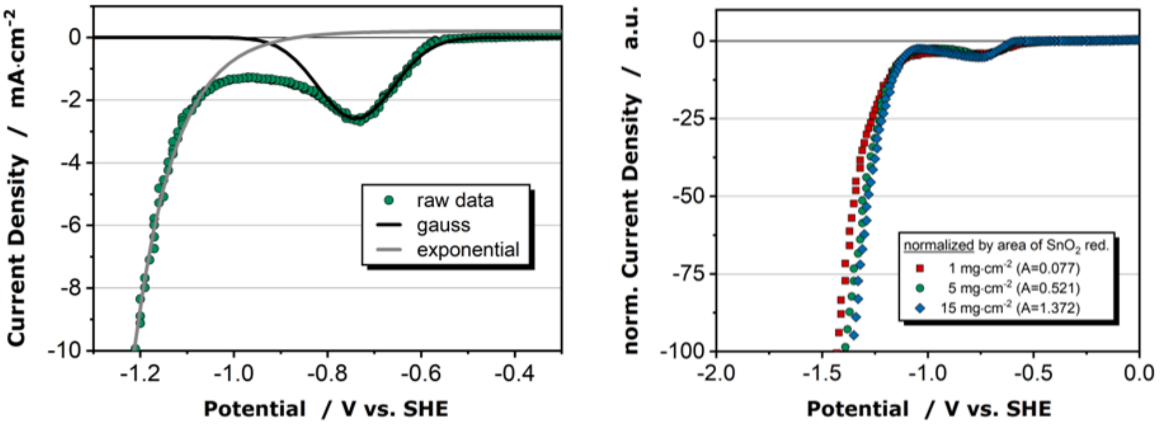

Figure 6.13 Deconvolution of polarization curve of GDE with 5 mg/cm^2 metal loading (right) and polarization curves of GDEs with varying metal loading normalized on area of Gaussian distribution characterizing SnO_2 reduction.

To evaluate the effect of metal loading on the product distribution. galvanostatic experiments were conducted at a moderate current density of 50 mA/cm² as well as in the transport limited region. The latter is discussed below together with the effect of dispersion. The assessment at rather low current density of 50 mA/cm² was conducted at a relatively early stage of the GDE investigation with the aim to get a better understanding on how the system behaves when the composition is changed. The corresponding product distribution is given in Figure 6.14 as a function of the metal loading. As can be seen. already in the absence of catalyst. CO_2 reduction is observed with an FE of approximately 35 % towards formate and 2 % to CO. whereas the remainder accounts for HER. Electrochemical activation of CO_2 in the absence of metal catalyst on pure carbon (without intentional doping of heteroatoms) has already been observed before and could be ascribed to metal contamination of the pristine carbon [118]. For a current density of 50 mA/cm^2. a loading as low as 0.2 mg/cm^2 (~1.5 wt.-% on carbon) was enough to substantially suppress HER and increase FE to formate to 93 %. This is due to the high overpotential of tin oxide towards HER. effectively suppressing HER while promoting CO_2 reduction. It must be noted. that the minimum amount of metal necessary to suppress HER depends on applied current density. For a current density of 200 mA/cm^2. which is close to transport limitation for this type of GDE. a loading of 0.2 mg/cm^2 for example. still yields a FE to hydrogen of 22 %. At this rate. a loading of at least 1 mg/cm^2 is necessary to suppress HER below 5 %. At 50 mA/cm^2 and loadings up to 5 mg/cm^2. the FE for formate remained at ~ 90 %. 10 % for CO and 3 % for H_2. Beyond this loading. FE to formate was found to decline; to 82 % at 10 mg/cm^2 and 80 % at 15 mg/cm^2. Analysis of the product distribution shows that HER is still mostly suppressed. and that the decline of formate selectivity goes in favor of CO production which increases accordingly.

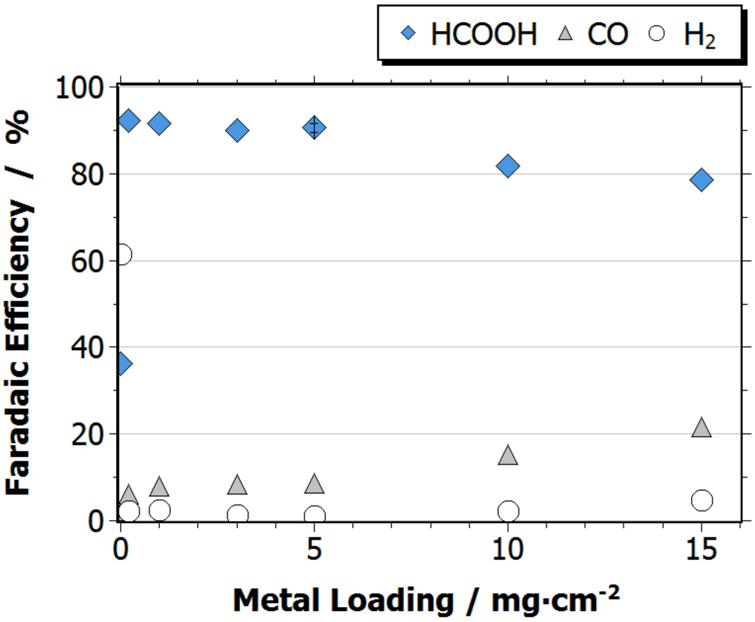

Figure 6.14 Product distribution as function of the metal loading at 50 mA/cm².

This shift in product distribution from formate to CO can be attributed to the different electrode potentials under galvanostatic conditions. as described in chapter 6.1.3. As shown in Figure 6.12. the metal loading has a significant influence on the resulting overpotential at a given current density due to the availability of active sites. The difference at 50 mA/cm^2 between 1 mg/cm^2 and 15 mg/cm^2 *e.g.* is as high as 0.4 V (–1.3 V vs. –1.7 V). Accordingly. the partial current density for different reactions are influenced by the electrode potential to varying degrees yielding the potential dependence of the FE shown in Figure 6.6 [179]. The same trend can also be seen for experiments at low current density and in the time behavior of the product distribution which steadily shifts from formate to CO as activity increases and potential becomes less negative due to an increase of wetting. The influence of the loading at high current densities as well as a comparison with literature is discussed below together with the influence of dispersion.

Influence of metal dispersion

The commercial tin powder was employed merely as the starting point for this investigation. The manufacturer of the powder gives a mean particle size <150 nm which already leaves room for improvement. However. evaluating SEM images of the GDE shows that the mechanical mixing of the powder mixture in the knife mill does not facilitate breaking down the powder agglomerates into primary particles. Instead the catalyst agglomerates inside the GDE structure remains in the µm-range in size. as shown in Figure 6.15. It is obvious that in general increasing the dispersion of the catalyst should increase the accessibility of active sites for dissolved CO_2 and its electrochemically active surface area. This has already been demonstrated by Zhang et al. who prepared nanoparticulate tin with different particle size via a hydrothermal method on a carbon black support [96]. Although they did not use a GDE. they could show a pronounced effect of particle size on product distribution and activity. Accordingly. it is very likely that a similar approach will be beneficial when utilized in a GDE for the same reasons. Due to a straightforward implementation and the possibility to deposit particles with a very fine dispersion. a homogeneous precipitation method was chosen to precipitate tin oxide nanoparticles on the carbon black support. The synthesis is based on [142] in which nanoparticulate tin oxide agglomerates with high surface area were synthesized in substance for the use in gas sensors. In this work. the precipitation was performed directly onto the carbon black support using the same conditions which yielded the highest surface area powder in the above study. The result can be seen in the SEM images in Figure 6.15. The weight percentage of the carbon-supported tin oxide was 1.81 % with respect to tin. the metal loading of the prepared GDEs was 0.87 mg/cm^2. A higher tin loading on the carbon support resulted in more pronounced agglomeration on the low surface area Acetylene Black (75 m^2/g). Therefore. a low metal loading on the carbon was chosen for the investigation. even though increasing loading proved to be beneficial for both activity (more active sites) and mass transport (lower diffusion length). as shown further below. As one can see. at such low Sn loading the obtained dispersion is remarkably homogeneous without noticeable agglomeration observable. Particle size seems to be below 20 nm. yet. this is very difficult to judge from the SEM images alone. For that reason. further TEM images were taken which are shown in Figure 6.16. Zooming in. it becomes evident that the supposed particles are actually agglomerates of even smaller nanoparticles that go down in crystallite size to as small as 2 nm diameter.

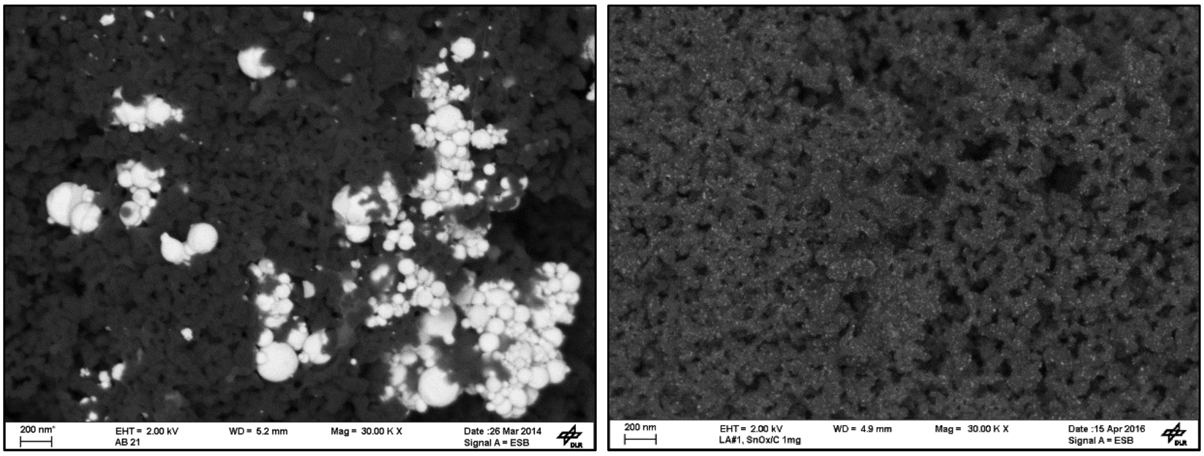

Figure 6.15 SEM images evaluating Sn/SnO_2 dispersion on a physical mixture of AB and the commercial tin nanopowder (left) and of the precipitated SnO_2/C (right) catalyst (5mg/cm² and 0.81 mg/cm²)

In a few publications it has been reported. that going towards nanoparticulate structures besides increasing accessible active sites through a higher catalytic surface area. might also change intrinsic activity of the active sites [78.180]. This is said to be facilitated by stabilization of intermediates or decreasing activation barrier of the rate-determining step (RDS) due to higher share of undercoordinated edge or kink sites. If this were the case. it should be reflected in a lower on set potential or a change in the Tafel slope when the RDS is changed. However. in the case at hand. this did not hold true as evidenced by comparing polarization curves for GDEs with commercial and synthesized nanoparticles given in Figure 6.17. Although. catalytic activity was considerably increased. the onset potential did not change substantially (all between 1.25 and 1.15 V). as shown in the semi-logarithmic zoom.

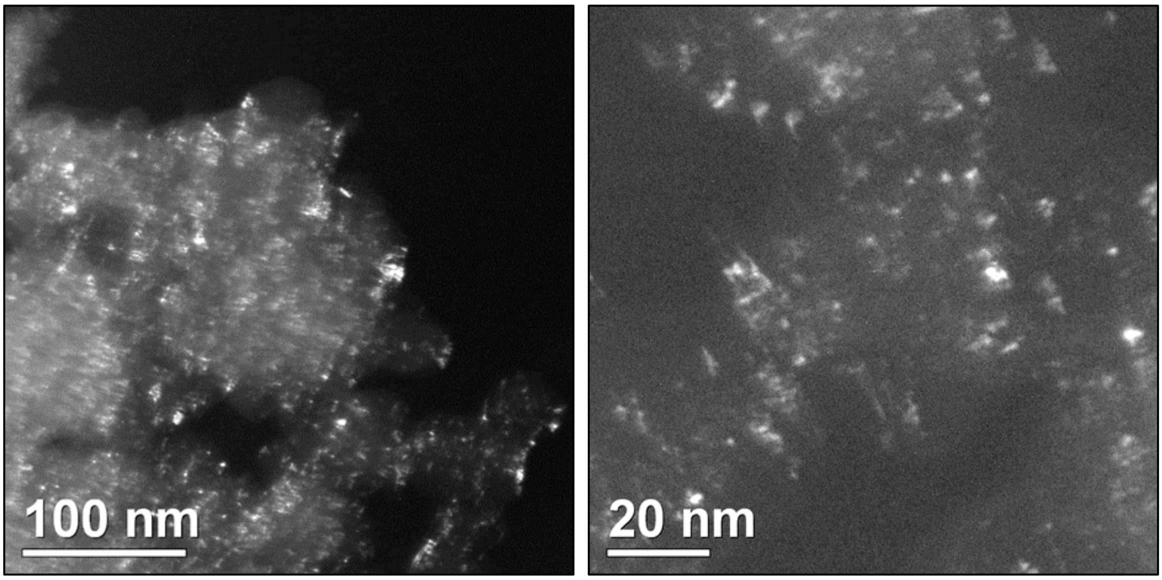

Figure 6.16 TEM-images of SnO_2 precipitated on AB powder with GDE tin loading of ~1 mg/cm²

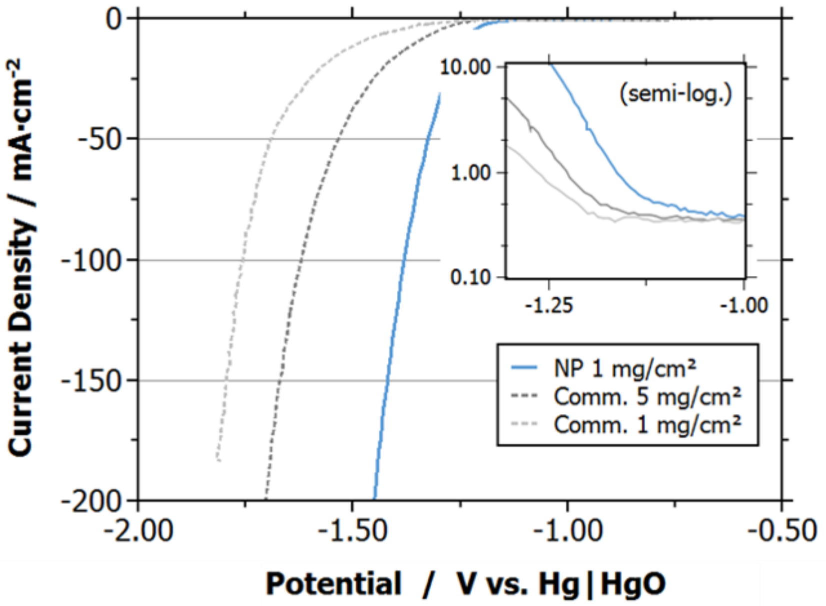

Figure 6.17. U-I curves of GDEs with commercial and precipitated tin oxide catalyst (denoted *NP* for nanoparticle in the graph).

The GDE with the precipitated SnO_2 catalyst proved to be even more active than the GDE based on a physical mixture of commercial tin nanopowder and AB powder at 5 times higher loading. This can be ascribed to the substantially increased SnO_2 surface area due to higher dispersion. However. as the latter also influences wettability due to the hydrophilic nature of the metal oxide surface [181] and. therefore. the amount of participating electrode volume. a deconvolution of both effects is not possible without evaluating the wetting extent during the experiments. The latter has not been done at this stage of the studies as the methodology was not introduced yet. At the studied conditions. a low loading seemed to be advantageous regarding the selectivity to formate due to the effect of potential. However. lower metal loading (at the same dispersion) also means that CO_2 has to travel longer distances after dissolving at the TPB to reach the active site since metal occupation on the carbon surface is lower. The same accounts for a lower dispersion at constant loading. This situation will have an effect on the achievable current density for which reactant diffusion becomes the decisive factor. To demonstrate that this holds true. GDEs with different loadings for both commercial and precipitated catalyst were further tested at a stepwise increase of the current density in galvanostatic experiments to see at what current density transport limitation sets in. In a first step. GDEs with commercial and precipitated Sn/SnO_2 catalyst at a loading of 1 mg/cm² were examined. As shown in Figure 6.18. going from the physically-mixed to the supported nanoparticles could tremendously increase the current density at which transport limitation and HER sets in. In this case. current density at which FE to formate dropped below 80% more than doubled. from 200 to 500 mA/cm² which at the time was one of the highest reported values in literature for this reaction [138.182]. In addition. it can be observed that at low current densities <100 mA/cm² FE to $HCOO^-$ is lower for the GDE with the supported nanoparticles with ~80% vs. 90%. As discussed above. this is ascribed to the higher activity. thus. lower electrode potential for the same applied current density. This increases the ratio between CO and $HCOO^-$.

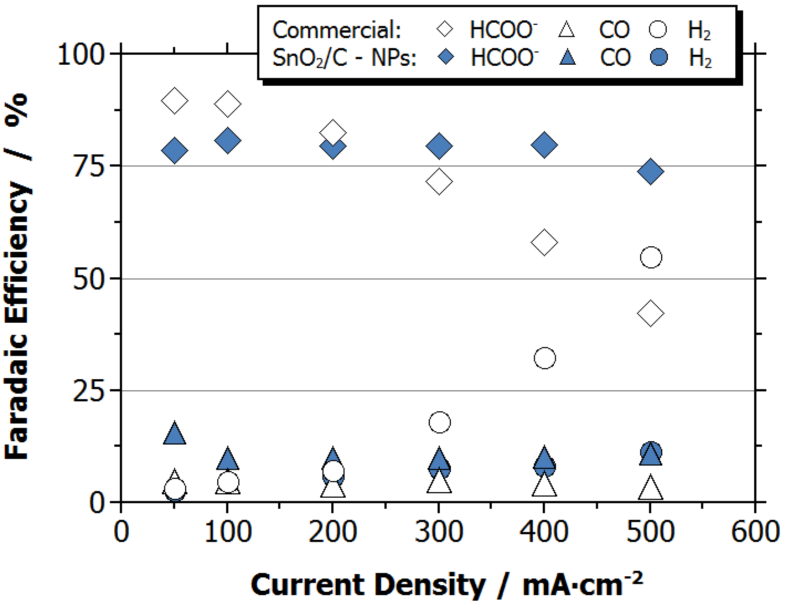

Figure 6.18. Comparison of product distribution between GDEs with commercial tin nanoparticles and precipitated SnO_2/C. both with 1 mg/cm² catalyst loading.

To further stress the effect of dispersion and diffusion length of dissolved CO_2 on the limiting current density. in Figure 6.19. HER is plotted for GDEs with different catalyst dispersion *and* loading. namely 1 and 5 mg/cm² of commercial and 1 and 2.5 mg/cm² of highly dispersed carbon supported SnO_2. as function of current density. Again. the results clearly demonstrate the importance of offering highly dispersed catalyst not only for activity but also for enhancing the limiting current density for CO2RR. This strongly suggests diffusion of dissolved CO_2 to the active site as limiting process.

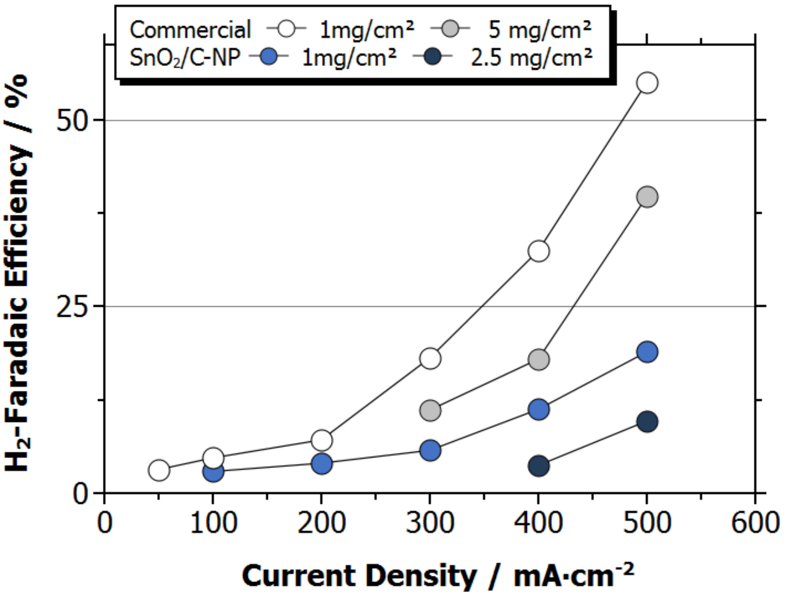

Figure 6.19. HER as function of current density for GDEs with different catalyst dispersion and loading.

The limiting current density i_L can be described by Fick's Diffusion as

$$i_{L.diff} = z\,F\,\dot{n}_{i.diff} \tag{6.1}$$

$$\dot{n}_{i.diff} = D_{i.eff}\,\frac{\Delta c_i}{d} \tag{6.2}$$

with the limiting species flux $\dot{n}_{i.diff}$ and the diffusion distance d. The lower the diffusion distance. the higher the limiting current density.

In literature. the effect of metal loading on formate production has been investigated by Wu et al. and Sen et al. [137.138]. Both came to the same conclusion that there exists an optimum of catalyst loading beyond which an increase leads to a decrease of performance. It is important to understand that a direct comparison to the results at hand is difficult as the type of GDE is different. In the mentioned studies. an increase of loading translates into the deposition of a thicker catalytic layer onto the substrate which at some point leads to an increase of transport limitation and decline of activity. In contrary. herein. the metal loading is increased by adjusting the carbon-to-metal ratio while keeping the mass of the other components in the GDE constant. Total mass loading of the GDE only slightly increased by that and thickness remained basically the same as additional Sn/SnO_2 is located inside the pore system of the carbon matrix. While the 1 mg/cm² sample of the supported SnO_2 exhibited a very homogeneous dispersion. increasing metal loading on the carbon led to more pronounced agglomeration and. thus. to lower catalyst utilization. That is why in the following. 1 mg/cm² was chosen as reference loading for the GDEs with supported SnO_2 and 5 mg/cm² for the one with commercial tin nanopowder.

6.2.3 Influence of electrode porosity

As the diffusion through the pore system. both for the reactants and the products. plays a pivotal role in achieving high current density. a manifest next step for the optimization of the GDE is to improve diffusion characteristics inside of the pore system. Maintaining the reaction conditions (electrolyte composition and temperature) and wettability. this can be done by modifying the pore system in order to adjust the effective diffusion coefficient $D_{i.eff} = D_i\,\frac{\varepsilon}{\tau}$ with ε the porosity and τ the tortuosity of the porous network in which transport proceeds. Two methods have been evaluated. that are the use of pore-forming agents and adjusting the compacting pressure during the GDE preparation. which are both described in the following. It could be shown that there is no effect of the electrode thickness on the performance characteristics of the GDE when going from the reference GDEs with ~800 µm thickness down to 300 µm which was the thinnest GDE with adequate mechanical integrity fabricable by the pressing method. This is demonstrated in Figure 6.20 in which the FE towards HER at 500 mA/cm² and the corresponding capacitance at the end of the 1h experiment is shown for GDEs with varying powder mass employed during the pressing step. The respective GDE thickness was 829±21. 430±16 and 280±7 µm (see chapter 6.1.2).

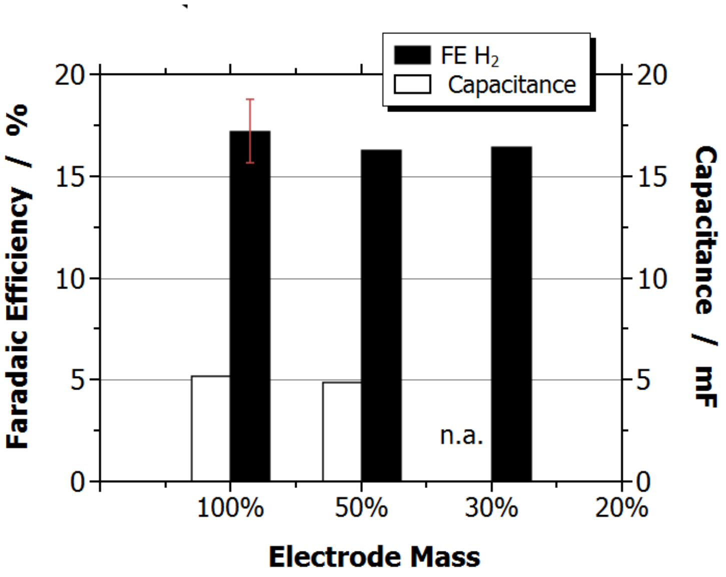

Figure 6.20. Faradaic Efficiency towards H_2 and capacitance after 1 h at 500 mA/cm² of AB35-GDEs prepared with different powder weight. SnO_2 loading on carbon support such that metal loading equals 1 mg/cm² for 100% electrode mass

The observation that the amount of H_2 generation as proxy for transport limitation is basically the same. suggests that gas transport through the dry pore volume does not play a role in determining the achievable current density as long as the thickness is larger than the macroscopically wetted thickness. Otherwise. the significantly different dry pore volume that needs to be traversed from the gas channels on the gas side of the GDE to the TPB inside the GDE would clearly affect the achievable current density. In contrary. as the following chapters will show. the electrochemical behavior is governed by the electrode characteristics in the macroscopically wetted volume such as liquid-phase diffusion of reactants and products as well as the distribution and contact area of dry and wetted pores in this region. These characteristics remain unchanged here as evidenced by the measured capacitance. All of this is not surprising in light of the orders of magnitude higher diffusion coefficients of gaseous compared to dissolved CO_2 as well as the high excess of CO_2 and its low conversion.

Use of pore-forming agents

To increase the porosity. one possibility is to use pore-forming agents during GDE preparation and ensure their decomposition before the GDE is used. Ammonium oxalate was chosen because its use has already been demonstrated in the literature to be beneficial for other applications [183] and because it is decomposed at temperatures below the temperature of the thermal treatment step during GDE preparation. Accordingly. no additional step is required when it is added in powder form during the mixing of the powder components. The oxalate particles are decomposed to N_2 and CO_2. and leave behind pores in the range of several micrometers. This is evidenced by means of thermogravimetric analysis (TGA) demonstrating the complete decomposition of oxalate up to 280 °C in a pristine GDE. If the same GDE is exposed to an additional heat-treatment. it shows the exact same course of the TGA-measurement as a standard GDE (without oxalate) with no additional mass loss in the characteristic region suggesting that there is no remainder of oxalate after the first heat treatment. Furthermore. CHN-analysis showed no occurrence of nitrogen beyond the traces associated to residues already observable in the carbon black. The SEM images in Figure 6.21 and Figure 6.22 clearly show that the desired result was obtained. Rather large pores in the range between a few µm up to around 100 µm were created with an increase of their prevalence with increasing concentration from 10% to 40%. For this study. VXC35-GDEs with 5 mg/cm² commercial tin powder were employed as benchmark to which the oxalate was added.

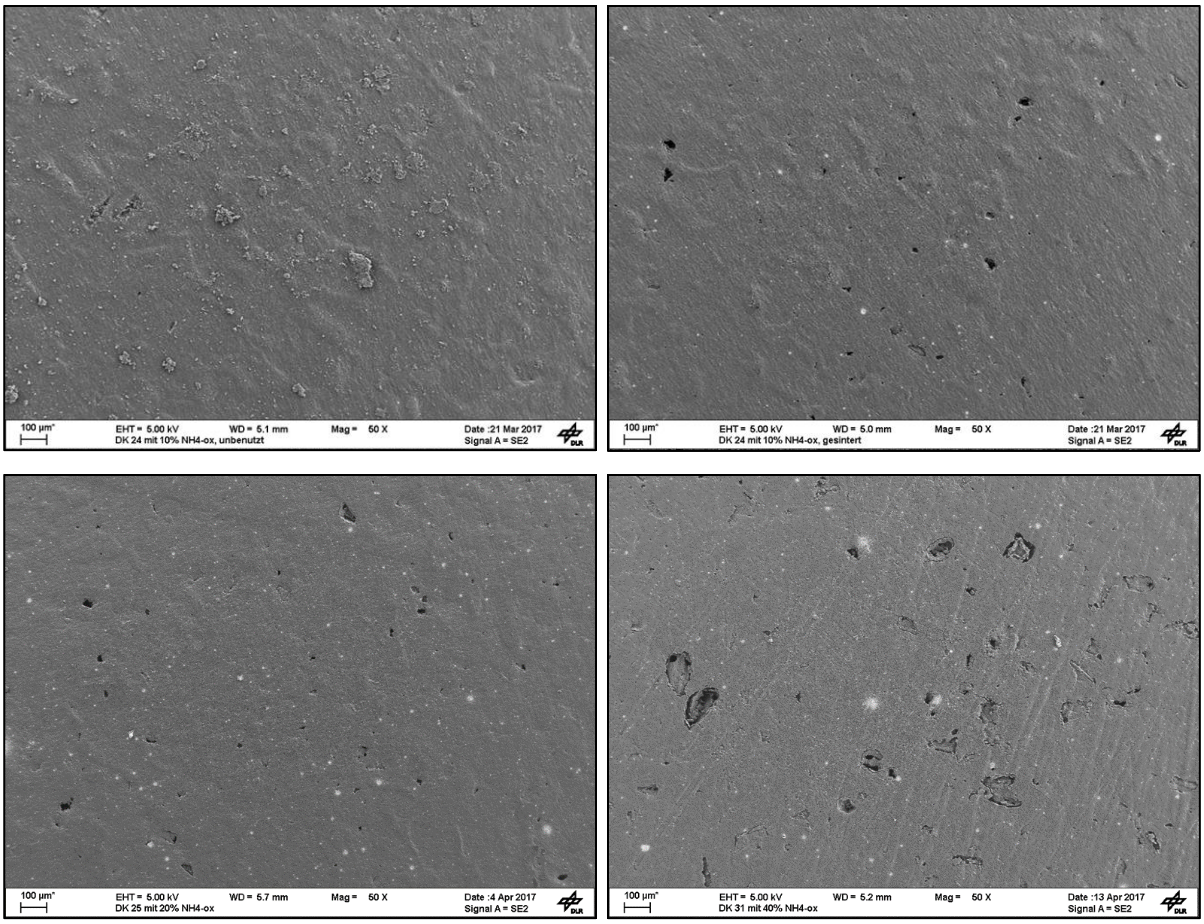

Figure 6.21. SEM images of GDE with b) 10% c) 20% d) 40% NH4-oxalate after and with a) 10% oxalate before thermal treatment.

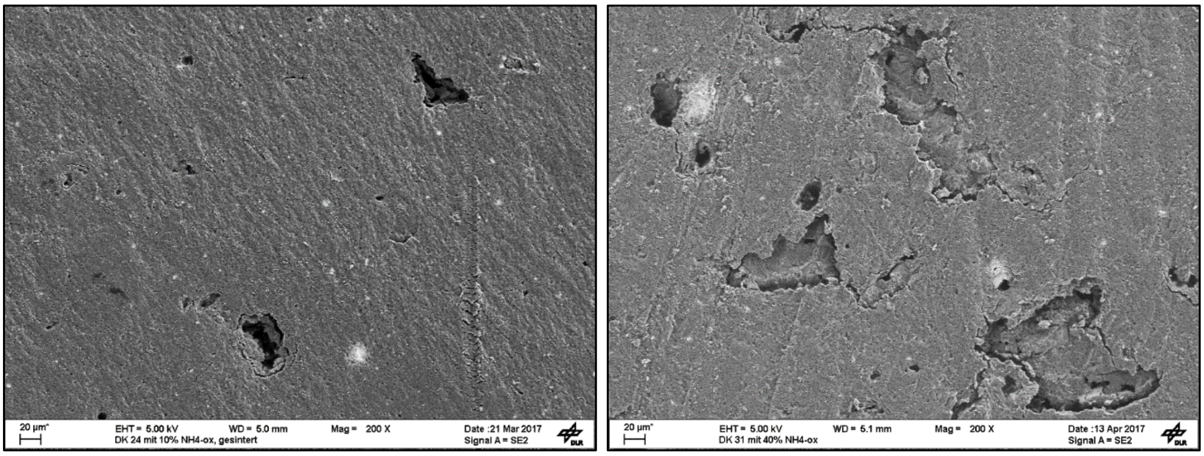

Figure 6.22. Closer look at formed pores after decomposition of NH4-oxalat.
Right: 10%. left: 40%

To see if the obtained pores in this range have a beneficial influence on the GDE performance. the prepared GDEs were evaluated in their ability to facilitate CO2RR at high current densities. The outcome of these experiments is shown in Figure 6.24. in which FE of HER is depicted as function of the current density. Working at moderate current densities below 300 mA/cm². away from transport limitation. there is no significant change of HER which remains at around 10%. except for the GDE with 40% oxalate for which limitation already sets in at 200 mA/cm². Increasing current density. HER rises continuously for all samples. demonstrating the onset of transport limitation. Surprisingly. this limitation becomes more pronounced when adding the pore-forming agent at increasing amounts. At 450 mA/cm² FE towards HER rises from 10% to 12%. 22% and 30% when increasing content from 0% to 10%. 20% and 40%. respectively. It is evident from this investigation that the use of the oxalate does not hold up to its expectation and. conversely. is even detrimental to the GDE performance which was highly unexpected.

A first approach to understand this behavior is to examine the textural properties of the GDEs. To this end. pore size distribution has been measured by Hg-porosimetry. In Figure 6.25. the data is depicted and the pore volume deconvoluted into primary and secondary pores according to the procedure described in chapter 5.1.3. As it is already suggested from the SEM images. the additional pores have mainly been formed in the secondary pore region. with the primary pore volume staying relatively constant. This is not surprising as *via* the dry mixing. the pore formers are not expected to intrude the powder agglomerates of the carbon. Also. BET surface area which is a good measure of the microstructure of the aggregate porosity in the GDE stays within experimental uncertainty around 30-35 m²/g. According to the size of the new formed pores and the understanding of how the GDE works it is suggested that the addition of the pore formers leads to an increase of dry pore volume in which gas transport proceeds (capillary forces in large pores too small to facilitate wetting). Evidently. increasing secondary pore volume does not lead to an improvement of the transport properties but is negatively affecting the reaction. One hypothesis to explain this behavior could be the additional barrier towards liquid phase diffusion of the dissolved products that is generated by the existence of the additional large and non-wetted pores. This is visualized schematically in Figure 6.23 for better understanding. The disturbed connection between the partially wetted aggregates by the large and dry pores leads to a longer diffusion pathway for the products to be transported from TPB to bulk electrolyte. This corresponds to an increase of the tortuosity factor of the wetted pore network. The hypothesis of product diffusion limitation to which this points to is further elaborated in chapter 6.3.4

One might argue that the existence of the large pores leads to less active phase inside the macroscopically wetted pore volume. However. the evaluation of the capacitance depicted in Figure 6.24 on the right shows that the electrochemically active surface area rather increases than decreases suggesting that the wetted electrolyte volume spreads deeper into the GDE. This increase which is fairly consistent with the rise in HER can be well ascribed to the drifting of the potential towards less negative potentials as result of the shift of product distribution towards HER as encountered several times in this work.

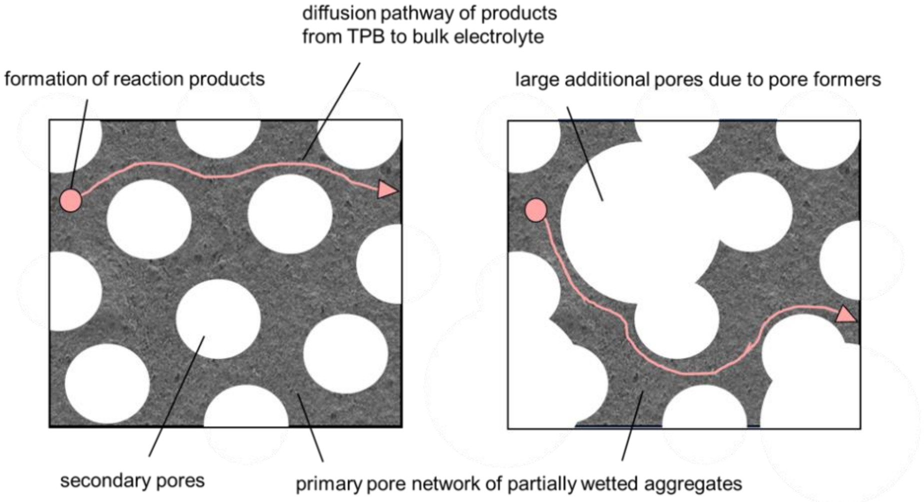

Figure 6.23 Schematic depicting the disturbance of the diffusion pathway of dissolved reaction products from TPB to bulk electrolyte induced by the formation of additional large pores (right)

While the hypothesis of how the pore formers influence the electrochemical behavior is in line with the overall framework established in this thesis on how the GDE works. a conclusive explanation on the effect could not be developed in the frame of this work. Clearly. it could help in obtaining a better understanding of how the GDE works and what the limiting factors for operation are. Therefore. a more elaborate and systematic investigation of this is highly encouraged. Three-dimensional reconstruction of the pore structure via FIB-SEM or computer tomography (CT) could aid in getting quantitative assessment and better understanding of these phenomena.

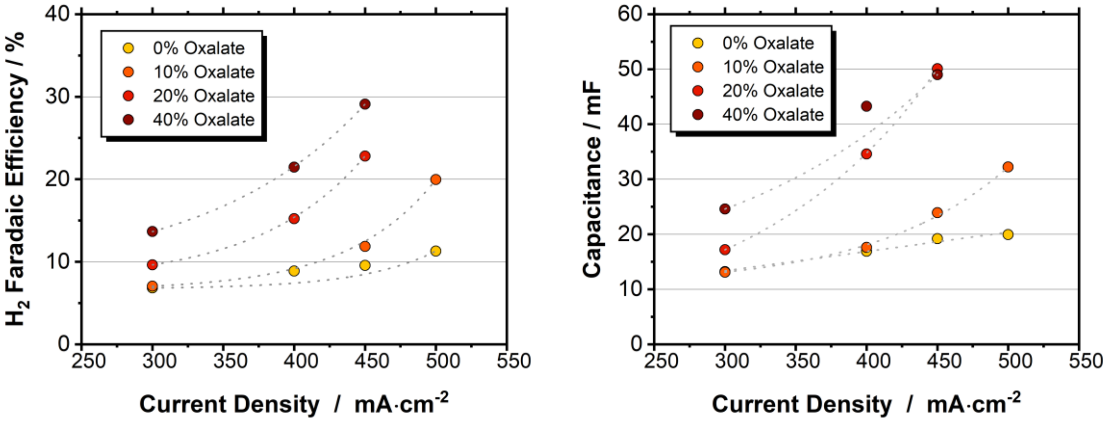

Figure 6.24 Left: FE towards HER over current density. for VXC35-GDEs (5 mg/cm²) with various NH_4-oxalate content. obtained in first generation experimental set-up (non-isothermal). right: corresponding capacitance measured at the end of experiment (the dashed lines are for guiding the eye)

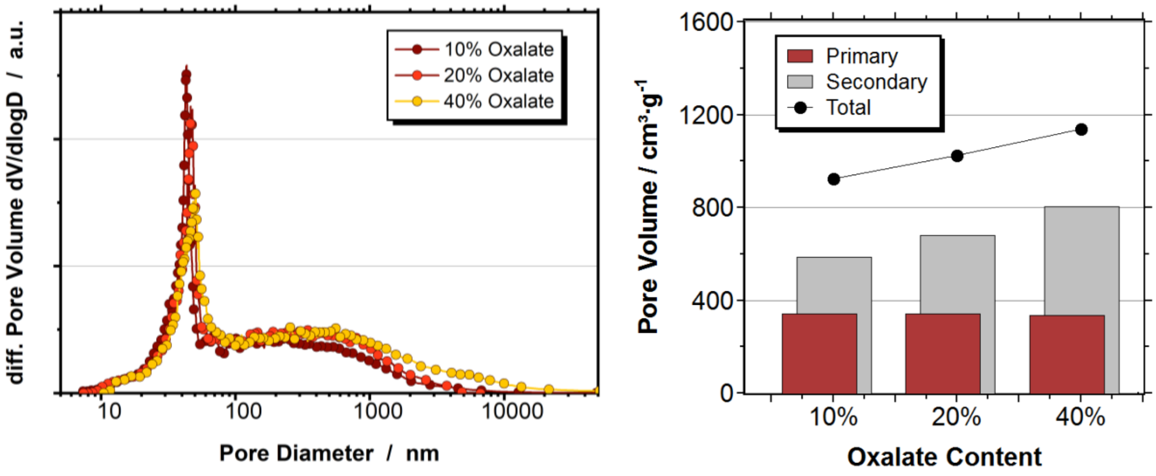

Figure 6.25 Cumulative pore volume for GDEs (VXC35) with different NH4-oxalate content after decomposition. left data from right separated by primary and secondary pore volume

Adjustment of porosity by compacting pressure

With these results in mind. an alternative was chosen with which also the primary pore system. can be adjusted. That is. by decreasing compacting pressure the GDE should be made less compact throughout the whole pore range. To evaluate if this hypothesis holds true. the compacting pressure was decreased from 17.7 kN/cm² to 14.2 kN/cm² and 10.6 kN/cm² for a AB35-GDE with SnO_2 nanoparticles. The GDEs were employed in the transport limited region at 500 mA/cm² in the CSTR mode. as later explained. Although only very little experiments were conducted for this study. the results in Figure 6.26 clearly show that indeed the extent of the transport limitation indicated by a shift towards HER could be substantially decreased from 35% to 15% after 1 h with a flatter slope of the performance degradation.

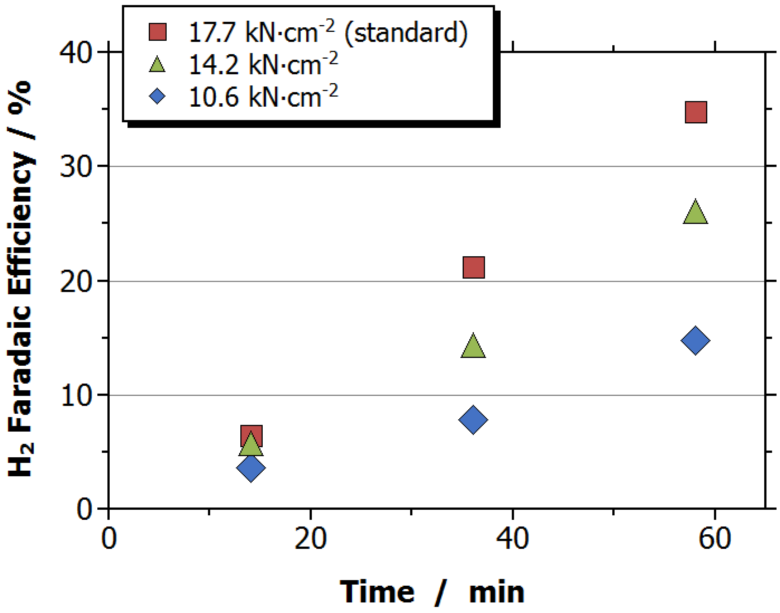

Figure 6.26. Increase of HER over time for GDEs prepared with different compacting pressure at 500 mA/cm².

To obtain a palpable explanation for this. again both physisorption and porosimetry were performed to examine the texture of the electrodes. As one can see in Figure 6.27 in which the differential and cumulative pore volume from porosimetry are plotted. and as it is expected. the overall pore volume decreases when higher pressures are applied. making the pore system of the GDE more dense and compact. This effect can be seen in both. the secondary pore volume. especially in the range between 10 µm to 1 µm. and in the primary pore distribution. Applying higher pressure shifts the pore distribution inside the agglomerates to lower diameters as it is very clearly shown in the inset of the graph. As summarized in Table 6.2. both the boundary diameter between agglomerate and superordinate pore structure as well as the maximum in the agglomerate distribution is slightly decreased. which is in agreement to the expectation that higher pressures make the pore system more compact. The slight increase of the BET surface area at higher compacting pressure can probably be explained by the shift of the average pore diameter in the agglomerates to smaller values which exhibit a higher surface to volume ratio.

Table 6.2 Textural properties obtained from N_2-physisorption and Hg-porosimetry of AB35NP-GDEs at varying compacting pressure

pressure	**BET m^2/g**	**Porosity %**	**$V_{P.overall}$ mm^3/g**	**$V_{P.primary}$ mm^3/g**	**$V_{P.secondary}$ mm^3/g**	**Boundary nm**	**$d_{prim.max}$ nm**
75kN	22.7	73.58	1405	415	990	85	78
100kN	23.3	73.95	1301	407	894	81	74
125kN	25.4	71.75	1243	373	870	79	71

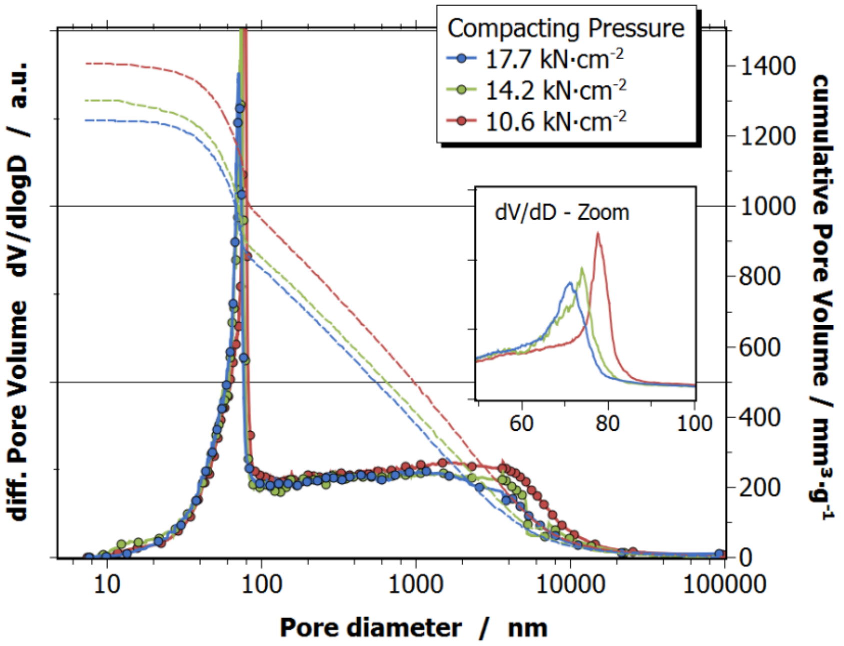

Figure 6.27 Pore size distribution (logarithmic. linear and cumulative) of AB35 prepared with different compacting pressure

As hydrophobicity of the pore system remains unchanged and gas transport through the secondary pore system has been shown to have no influence on achievable current density by the variation of electrode thickness (see Figure 6.20). this strongly suggests that the change in the agglomerate porosity should be responsible for the improvement of the performance. This could be either due to reactant diffusion to the active site or the transport of the products from TPB to the electrolyte bulk being alleviated. However. also the influence of these effects on catalyst stability could play a decisive role. This is discussed in more detail in section 6.3.4 in which all the results from this work are gathered and it is attempted to draw a thorough conclusion.

6.2.4 Influence of carbon wettability

During the course of this work. electrodes with significantly different hydrophobicities have been tested. Naturally. the influence of the wetting behavior is difficult to examine since along with the hydrophobicity. other properties like the pore size distribution are changing as well when modifying the composition. Thus. for understanding how the GDE works it is crucial to separate the influence of hydrophobicity from these other properties. Tailoring surface chemistry which determines the interaction between the liquid and the pore system can in principle facilitate modifying the wettability without changing textural properties. The latter can be ensured by a mild oxidation of the carbon surface by an adequate oxidation agent. In this work. hydrogen peroxide and nitric acid were chosen to obtain a mild and moderately strong oxidation of the carbon support. respectively. Two different set of experiments were performed to make the outcome of the experiments robust and meaningful.

First. Vulcan-based electrodes. for which the reference GDEs showed moderate hydrophobicity and intermediate performance were prepared with pristine and oxidized carbon substrate. The commercial tin nanopowder was chosen to avoid the potential influence of catalyst dispersion as function of surface functionalities. Hydrogen peroxide has indeed been shown to allow for a mild oxidation leaving the microstructure of the carbon intact whereas the oxidation by nitric acid slightly decreased the porosity of the carbon carrier. Accordingly. the BET surface area of 234 m²/g for unmodified VXC powder changed to 240 m²/g and 216 m²/g. respectively. This observation is consistent with literature where H_2O_2 is described as particularly mild oxidant compared to other oxidizing agents. Due to the oxidation of the surface and the corresponding creation of polar functional groups (*e.g.* -OH. -COOH). the pore system becomes more hydrophilic compared to the carbon-terminated unpolar π-bonding [144]. That said. wetting should proceed more rapidly as soon as the electrode is polarized. The so-prepared GDE was consequently compared to the reference GDE regarding the extent of wetting and its performance at moderate and high current density. namely. at 300 and 500 mA/cm^2. As shown in Figure 6.28. the wetting could be clearly increased by oxidation with H_2O_2 and even further when using nitric acid with its higher oxidation capability. This is shown for 300 mA/cm² while for higher current densities. the CV curves after electrolysis did not show a prolonged plateau for an accurate determination of the capacitance. This was consistently observed for GDEs with higher surface area at current densities where transport limitation sets in. For moderate current density. the GDE oxidized with H_2O_2 does not show significant changes in the HER; both GDEs work outside the transport-limited regime. However. when increasing current density. HER is clearly enhanced from slightly above 20 to almost 40% at 500 mA/cm². For the GDE modified in nitric acid. this effect is even more pronounced. However. here also the pore system was slightly affected by the treatment which makes the assessment less clear. Still. the above finding is surprising. considering that often a balanced hydrophobicity is argued to be important for GDEs to allow for sufficient wetting and to establish an extended TPB [31.128]. Evidently. this is not the case for the Vulcan-based GDE. at least when maximizing achievable current density is the target. On the other hand. as Vulcan is only moderately hydrophobic. it could still be the case that it is already beyond the point of optimal hydrophobicity and in the range where further decrease of hydrophobicity already leads to a decline in performance. To investigate if this holds true. Acetylene Black which showed the highest hydrophobicity of the carbon substrates in this work was also undertaken the same procedure with H_2O_2 as oxidizing agent. This time. the oxidized carbon was subsequently loaded with the SnO_2 nanoparticles *via* the homogeneous precipitation method. This was done to investigate the limiting factor for transport limitation with the state-of-the-art GDE in this work.

Although not as pronounced. the results point in the same direction. With a slight increase of capacitance at both current densities. also the amount of HER increases. particularly at 500 mA/cm². This indicates that the importance of a highly hydrophobic GDE is universal for the applied GDE type developed herein for achieving high current densities. Note. that this argumentation holds only true when achieving high current density is the sole objective. Naturally. high hydrophobicity comes with the drawback of low catalyst utilization and. thus. higher polarization for the same current density. As it will later be shown. this increased polarization can contribute to decreased catalyst stability which to a certain degree counteracts the benefits and might explain why the effect shown here is not as pronounced as expected from the VXC-GDEs.

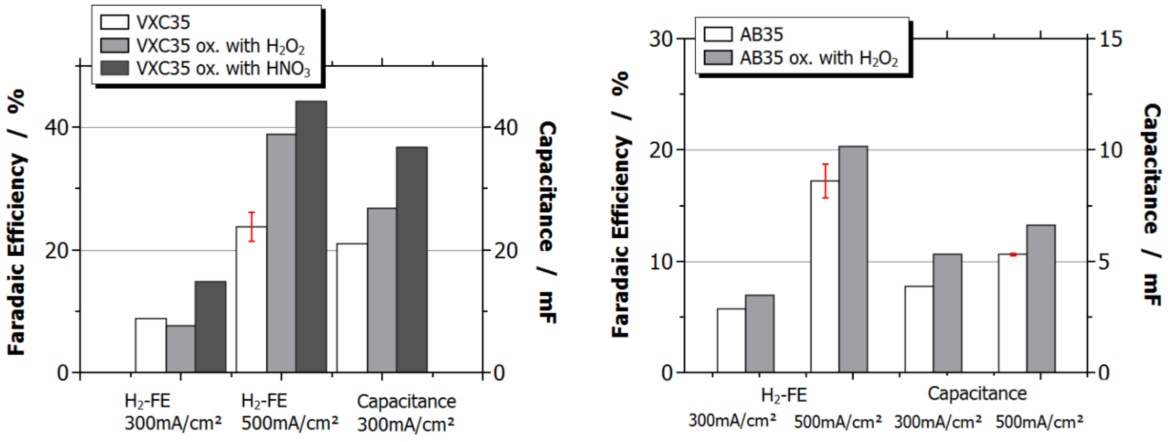

Figure 6.28. Capacitance and FE to H_2 at 200 mA/cm² and 500 mA/cm² for AB35NP and GDE with same composition but oxidized carbon carrier

6.3 Achievable current density and decisive electrode properties

While the activity. *i.e*. the potential-current characteristic. is determined by the active catalyst phase (amount and dispersion) and the extent of GDE wetting. regarding the limiting current density. the picture is more complex and one has to consider the sequence of steps from CO_2 in the gas-phase to the liquid product in the bulk electrolyte. Accordingly. one has to consider

i. the gas-phase diffusion and pressure-gradient driven viscous flow of CO_2 through the pores of the carbon matrix to the triple-phase boundary (TPB).
ii. its dissolution and subsequent diffusion of $CO_{2.aq}$ through an electrolyte film into the flooded carbon black agglomerates to the active site.
iii. Furthermore. one important step which is often neglected is the transport of the produced ions (here: formate and OH^- or (bi)carbonate) from the active sites at the TPB through the wetted agglomerates into the bulk electrolyte. The driving force in this case can be both the electric field (migration) and the concentration gradient (diffusion) to different degrees depending on the reaction conditions. This last step is important to close the electric circuit and maintain charge-neutrality.

The limiting current density depends on the transport rate of the slowest step – the limiting transport mode – in this sequence according to

$$i_L = z \cdot F \cdot \dot{n}_{i.L} \qquad 6.3$$

Which transport process is predominant is not easily predictable and depends on the reaction conditions. current densities. operating time and the properties of the electrode. Also. the different steps are not independent but interact with each other. For example. when limitation in the gas-phase arises. CO_2 is depleted at the TPB which influences the equilibrium concentration in the electrolyte according to Henry's Law. Within the frame of this thesis. it was attempted to get a better understanding of each step and its influence on the limitation by investigating the electrode behaviour in the limiting region (500 mA/cm². as discussed in the next chapter) and varying the electrode properties and experimental conditions.

6.3.1 Time behavior in the transport limited current density region

Prior to discussing the influence of electrode properties on the achievable current density. it is important to first have a closer look on how the electrodes behave when the proposed transport limitation sets in. This is because it was found for all situations that the limitation seems to set in slowly but steadily with time. observable by a continuous rise in HER. It seems evident that understanding this time behaviour will help in understanding how the limitation is influenced by the properties of the GDE. As an example. the time behaviour of the FE towards HER is depicted in Figure 6.29 for AB35NP and AB10NP at 500 mA/cm². For both GDEs transport limitation sets in while for the AB10NP. the effect is less pronounced. On the right side. the time behaviour of the outlet flow-rate is shown which indicates the rise of HER (or its absence) with time for GDEs with different carbon substrate to different degrees. While these are exemplary graphs. the general appearance of the experiments is similar for all cases when limitation sets in. It should be noted. that the experiments in the right graph in contrary to the ones on the left were performed at non-isothermal conditions. which is why the observable behaviour is different in both cases.

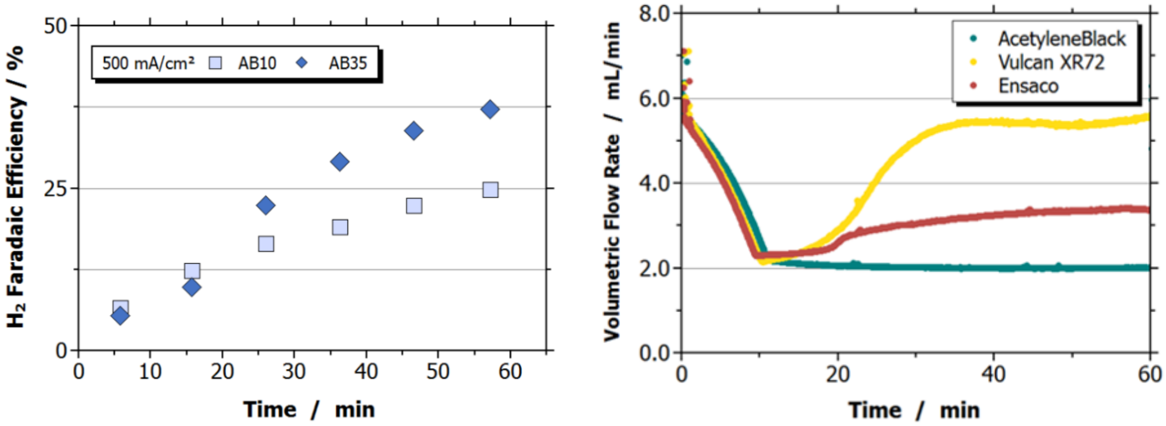

Figure 6.29 Time behavior of FE towards H_2 (left) and volumetric outlet flow rate (right) in the transport limited region (500 mA/cm² and 400 mA/cm². respectively) for different GDEs. On the left. AB-GDEs with two different PTFE content. on the right. GDEs with 35% PTFE and different carbon substrates were used (non-isothermal conditions).

Evidently. the GDEs manage the delivery of the set current into the desired product in the first minutes but increasingly lose their capability to do so at these high rates. The decrease in performance is irreversible and a reused GDE sets in approximately where it has been stopped in the experiment before. The suggested mechanisms which could play a role can be grouped into phenomena specific to the reaction environment.

i) temperature rise due to ohmic losses and reaction enthalpy.
ii) changes in electrolyte composition

and such which are electrode-dependent:

iii) catalyst deactivation. *e.g.* by leaching of active components or change of oxidation state.
iv) loss of hydrophobicity.

These mechanisms will be discussed in the following chapters.

Heat dissipation and influence on product distribution

Due to ohmic losses which are dissipated into heat and the reaction enthalpy. a significant amount of heat is produced during one experiment [27]. Although the investigation of the temperature influence was not the scope of this work. in order to be able to critically assess the performance of the different electrodes. isothermality is an important requirement of the experimental procedure. especially to assess the time behavior and to obtain meaningful information on the electrode performance. To illustrate how strong the temperature rise during the reaction is. the temperature in the cathode chamber has been recorded at different current densities over the course of an experiment. The outcome of these experiments. namely the evolution of the temperature over time and dT as function of current density is depicted in Figure 6.30. It can be seen that especially at high current densities. the temperature rise is substantial. *e.g.* around 50 K after 1 h at 500 mA/cm². To account for that. an integrated cooling system was implemented which continuously pumps the electrolyte through a cooling bath of set temperature. Thereby isothermality inside of the cell can be ensured and the temperature maintained at 25 °C ± 3 K for all experiments. Comparing the results from the isothermal experiment with the uncontrolled system. shows a considerable difference in the product distribution. particularly at high current densities where the temperature increase is more pronounced. As Figure 6.31 shows. higher temperatures are clearly advantageous. in that the current density at which transport limitation sets in is shifted to higher values: whereas under isothermal conditions. FE towards H_2 already rises above 10% at 400 mA/cm². the same value is reached not until about 600 mA/cm² when there is no cooling applied.

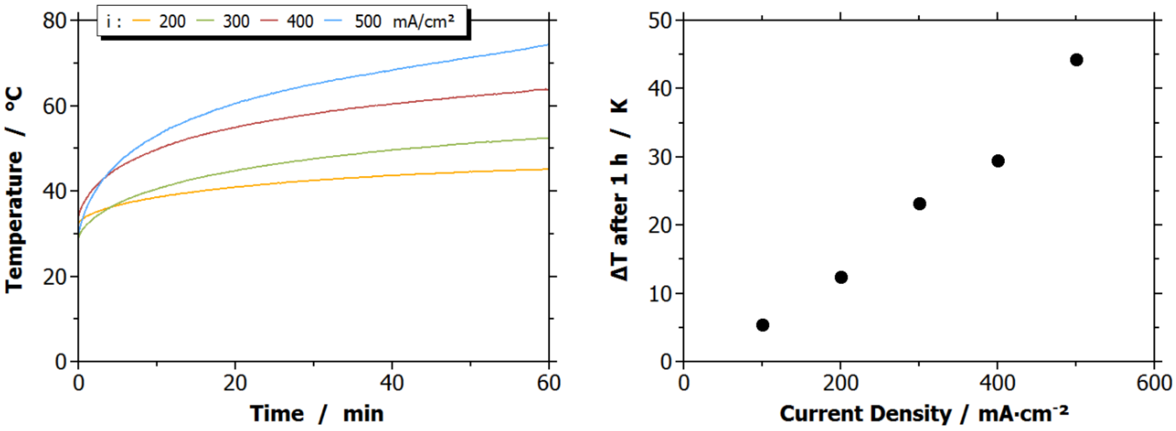

Figure 6.30 Evolution of bulk temperature in the cathode chamber during experiment at different current densities (left). temperature increase after 1 h as function of current density.

The beneficial effect of elevated temperatures is ascribed to accelerated diffusion rates and more facile kinetics. However. a more profound analysis and discussion on this trend. is not done here. as the experimental basis is by far not sufficient. Still it is possible to exclude temperature effects to be responsible for the observed time behaviour. In contrary. the temperature rise counteracts the rise in HER by improving mass transport in the range investigated and is shifting the limiting current density to higher values.

Change of electrolyte composition

A general issue when conducting semi-batch experiments is that they are intrinsically non-stationary. With proceeding time product accumulates. pH changes and CO_2 dissolves into the electrolyte. In the experiments at hand (500 mA/cm². isothermal). formate concentration reaches 0.22 mol/L at the end of the experiment while OH^- from $HCOO^-$. CO and H_2 generation reacts with CO_2 to HCO_3^- which generates 0.012 mol additional bicarbonate corresponding to a total concentration of 0.39 mol/L. Furthermore. one ion K^+ crosses the membrane from anode to cathode for each electron transferred [184]. To investigate if this change is responsible for the observed time behaviour. the semi-batch cell was modified to allow for a continuous flow of electrolyte through the reactor. As fresh electrolyte is replenished in the cell volume and the same flow-rate leaving the reactor. a stationary electrolyte composition should be developed after some time. provided the product distribution stays constant. However. Figure 6.32 shows. that although in CSTR-mode with continuously replenished fresh electrolyte. there is still a constantly rising generation of HER. Although this cannot explain the degradation of performance with time in the transport-limited region. one can see a slight difference in the development of H_2-FE.

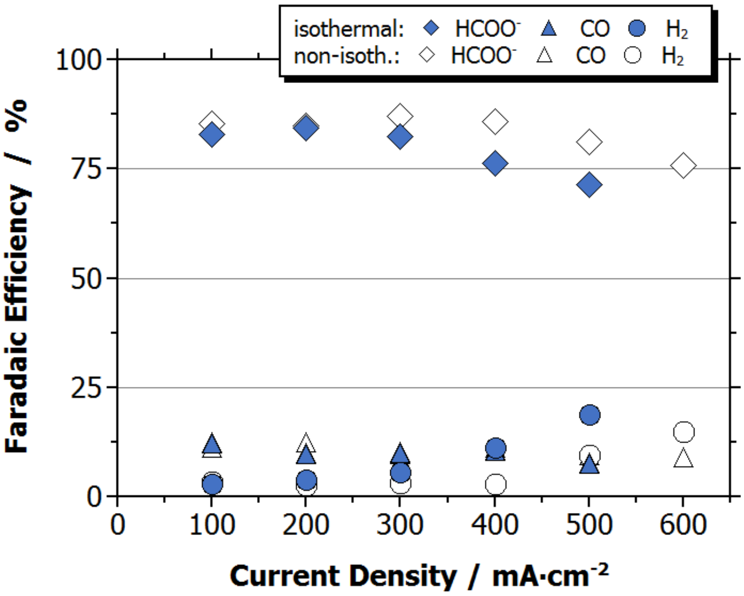

Figure 6.31 Product distribution of galvanostatic experiments under isothermal conditions and uncontrolled electrolyte temperature using AB35NP.

While the difference at a low flow-rate of 1 mL/min. corresponding to a residence time τ of ~30 min is close to experimental uncertainty (see error bar of two experiments). further decreasing τ to 3 min. indeed induces a slight change of performance. That is the FE towards H_2 decreases from 37% to 29% after 1 h. Residence time influences the electrochemistry mainly by determining the average composition in the cathode chamber and the accumulation of product in the bulk electrolyte. Thereby it should also have an effect on the diffusion characteristics. as the concentration gradient between TPB and bulk electrolye is changed. More rigorously replenishing the electrolyte. *i.e.* drastically decreasing τ. the average concentration gradient remains closer to the initial value. thereby ensuring efficient product diffusion to the bulk. In contrary. in semi-batch mode. bulk concentration rises with time slowly approaching concentration at the TPB.

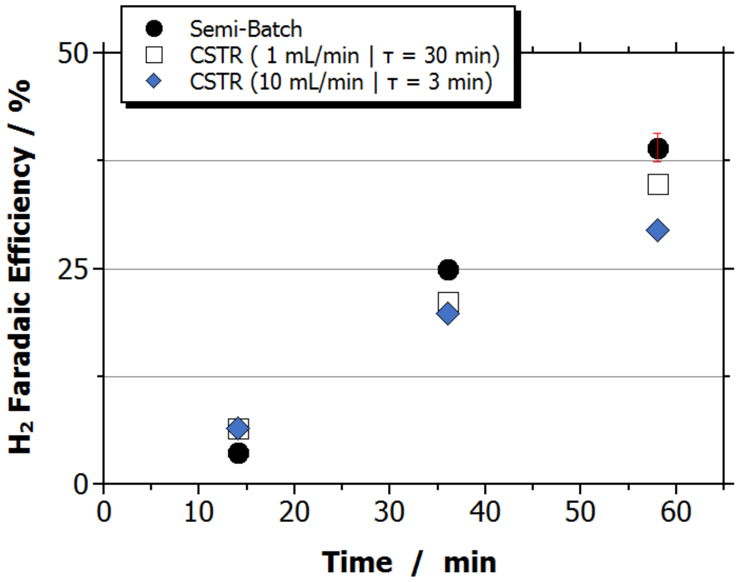

Figure 6.32. FE towards H_2 over time in modified half-cell operated in CSTR-mode.

To quantitatively capture this effect. the concentration profile has been simulated *via* Python using the experimental product distribution and the mass balance equations of the semi-batch reactor and a continuously-stirred tank reactor (CSTR) according to [185]:

$$V_R \frac{dc_i}{dt} = \dot{V}\,(c_{in} - c_{out}) + V_R \cdot \upsilon_i r_i \qquad 6.4$$

In the equation. V_R is the cathode chamber volume. c_i is the concentration of the respective species and r the reaction rate with the stoichiometric coefficient υ_i. The reaction rate is defined by Faraday's Law. For the semi-batch configuration. the flow rate $\dot{V}$ equals zero and the change in concentration is solely ascribed to the reaction. The simulation is based on the measured FE towards hydrogen over time from the above experiments. CO was assumed to be constant at 8% (the average FE for the semi-batch experiment at 500 mA/cm^2). which is justified as for these conditions changes in CO FE are not very pronounced. As the time evolution of the FE towards formate is not known. it is derived by assuming all products together amount to 100% which is a robust assumption considering current selectivity usually closes within ±5%. Produced OH^- is assumed to be converted quantitatively with CO_2 towards HCO_3^-. The evolution of formate and HCO_3^- over the course of the experiments is depicted in Figure 6.33.

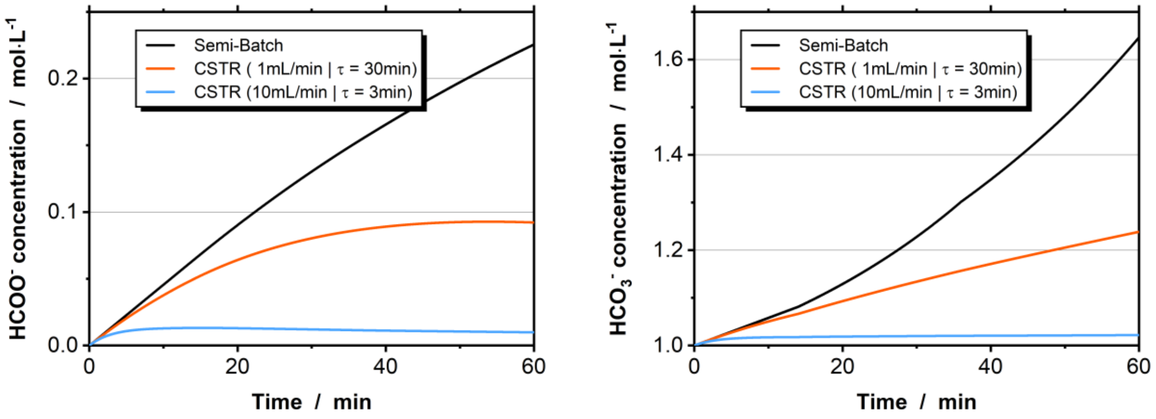

Figure 6.33 Simulated formate and bicarbonate concentration profile over time for different reactor configurations based on measured evolution of HER and assuming all generated OH^- is converted to HCO_3^-

Indeed. the picture strongly differs between the different conditions. Whereas in the semi-batch mode. concentration of both formate and bicarbonate continuously increase. formate concentration reaches a stationary value in the CSTR after a certain initial phase. In contrary. bicarbonate concentration continues to rise as product distribution steadily shifts towards H_2 which produces twice the amount of OH^- compared to formate. Still. the bulk electrolyte composition maintains close to the initial conditions for the low residence time experiment. As this does not significantly change the outcome of the experiment. it can be argued from this. that the electrolyte evolution might have an influence but cannot be the main driver for the time behaviour. It should be noted that this discussion focused on the bulk composition of the electrolyte whereas the composition inside the GDE and close to the TPB is not revealed. Particularly the pH value in the reaction zone is known to rise significantly at such high current densities due to the generation of OH^- as elaborated by Burdyny and Smith [21] reaching values well above 12 at high current densities. Such high alkalinity can have a detrimental influence on catalyst stability. as it will be shown in the following chapter. If this is the case. this could give an explanation on the influence of residence time on stability of operation: as the concentration gradient between bulk electrolyte and TPB is determined by the residence time as outlined above. replenishing the electrolyte decreases bulk concentration and by that increases the diffusion flux of products. Accordingly. the rise of the local pH on the catalyst surface and corresponding stability issues can be compensated to a certain degree. For future work. a comprehensive analysis of electrolyte composition. pH and equilibria *inside the GDE* as well as in the bulk is of high interest to progress towards better understanding of the reaction. The issue of catalyst stability is elaborated in the following.

6.3.2 Investigation of catalyst deactivation

A likely scenario for the observed deactivation behaviour could be related to catalyst deactivation. *i.e.* agglomeration. leaching or change of oxidation state of the SnOx nanoparticles.

As first step. potential leaching of the active phase was studied by examination of the electrolyte after the experiments *via* elemental analysis (ICP-OES) for a handful of different electrodes and reaction conditions. For example. for a VXC35-GDE stressed at 400 mA/cm² which already shows substantial increase of HER during the one hour reaction (see 5.2.2). almost negligible amount of around 0.07% of the *total* amount of tin in the GDE could be found in the electrolyte. Estimating the wetted surface area as described in 5.2.3 and assuming homogeneous distribution within the GDE. this corresponds to a loss of 1.33% of the tin in contact with electrolyte. This suggests that the actual loss of active phase from the electrode surface is rather unlikely responsible for the progressive and substantial deactivation of GDEs in this work. The same analysis has been done for other GDEs and reaction conditions as well. and for none. the loss exceeds 3% unless the GDE starts to mechanically deteriorate.

As pointed out in recent work by Bienen et al.. tin distribution cannot be evaluated accurately *via post-mortem* element mapping of the GDE cross-section [186]. This is because the potassium signal overlaps with the tin signal in the EDX measurements. thereby pretending redistribution of the tin particles. as suggested when looking at Figure 6.34. Accordingly. it is not possible to differentiate between actual loss of tin and artefact of the analytical method. However. in the above study by switching the electrolyte cation from potassium to sodium it could be clearly shown that loss of active tin species takes place.

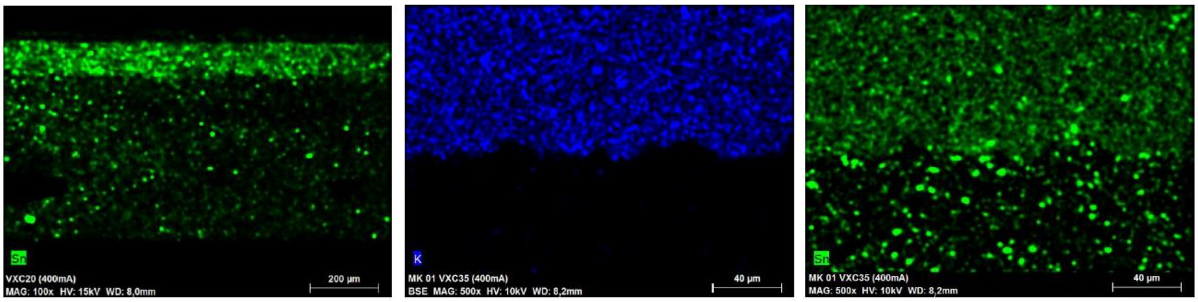

Figure 6.34. Element map for Sn (green) and potassium (blue). Top part is wetted region (as evidenced by potassium distribution). middle and right image is zoomed in to interface between wetted and non-wetted region.

Loss of tin species from the carbon surface can take place *via* the cathodic dissolution according to equation 6.6 at the negative potentials at hand [187] or even chemical dissolution due to the highly alkaline conditions inside the porous structure during reaction (eq. 6.5). Figure 6.35 shows the Pourbaix-diagram of the tin water system in which the predominating species in thermodynamic equilibrium are depicted as function of pH and potential. As one can see. beyond pH 12. soluble Sn(IV) stannate species are formed. according to equation 6.5 independent on the potential. whereas at less alkaline pH. SnO_2 is electrochemically reduced to aqueous $HSnO_2^-$ (eq. 6.6). This dissolved species can be further reduced and deposited onto the electrode surface to metallic tin (eq. 6.7). In addition. the dissolved species could also be precipitated as potassium stannate during drying of the electrode after disassembly of the cell and before *post-mortem* analysis. Although it is argued that in the presence of CO_2 a metastable oxide layer is kinetically stable even beyond the thermodynamic reduction potential of -0.66 V or -0.72 V vs

SHE at pH10 and pH12. respectively (calculated with thermodynamic data from [188]). it is reasonable to take into account that at least a certain share can be reduced when the potential becomes negative enough. Thereby. soluble Sn^{2+} species can be produced that can be redeposited when further reduction to metallic tin takes place.

$SnO_2 + 2\ OH^- \rightleftharpoons SnO_3^{2-}\ (aq.) + H_2O$ 6.5
$SnO_2 + 2e^- + H_2O \rightleftharpoons HSnO_2^- + OH^-$ 6.6
$HSnO_2^- + 2e^- + H_2O \rightleftharpoons Sn + 3\ OH^-$ 6.7

Both the presence of metallic tin as well as the loss of active tin oxide species will result in an increase of HER and could readily explain the observed phenomena in this work. Literature supports this finding as well. For example. Dutta et al. [101] could observe a significant decrease of tin oxide species during electrolysis using operando Raman spectroscopy at substantially more negative cathode potentials than the thermodynamic stability region. According to their studies. at pH10 this takes place beyond ~ -1.5 V vs. SHE. a potential region which is indeed surpassed at high enough current densities in this work. Particularly. when HER sets in. the cathode potential shifts to increasingly negative potentials which in turn further favours reduction of tin oxide and HER over CO2RR.

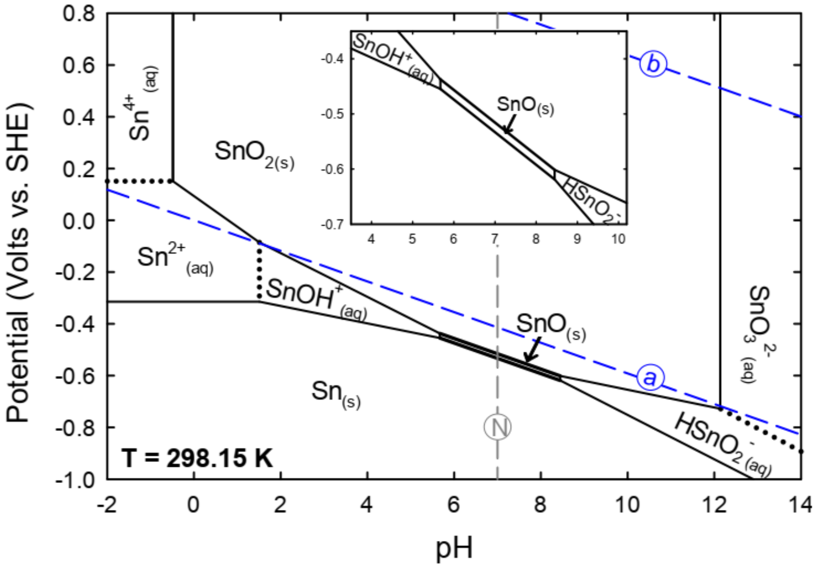

Figure 6.35. Pourbaix diagram of the tin-water system showing prevalent species as function of electrodes potential and pH value [188].

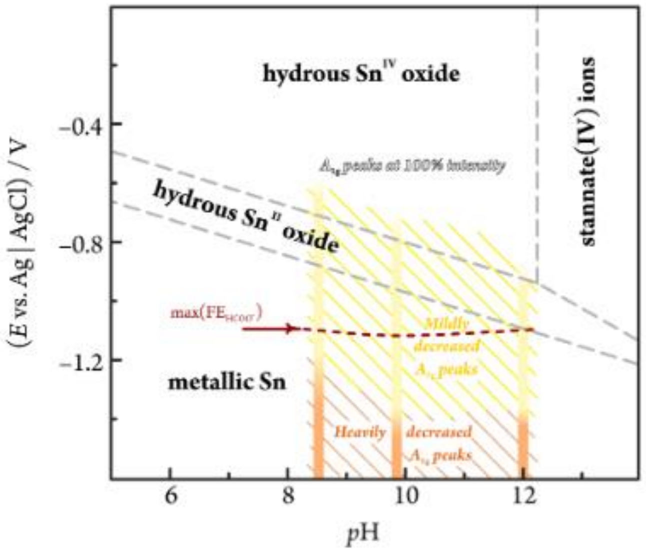

Figure 6.36. Pourbaix diagram of the tin-tin oxide system in water and intensity of SnO_2-related Raman signal during CO_2 electrolysis [101].

The corresponding Pourbaix diagram for the tin/tin oxide system from the above study is depicted in Figure 6.36 together with the region in which they found the signal of the oxide species to decrease (heavily). Ultimately. they could correlate the decrease of $HCOO^-$ production with the gradual reduction of tin oxide species over time. In the case at hand. this supports the hypothesis from above that during electrolysis the Sn(IV) oxide species become reduced when potentials are negative enough. dissolved and likely redeposited as metallic tin on the electrode surface. The latter could explain why active material is not washed out and found in the electrolyte in significant amounts. The above argumentation suggests that this phenomenon is likely to play a decisive role in the observed deactivation behaviour and needs to be further investigated in a systematic manner.

6.3.3 Evaluation of wetting behavior with time

As discussed in chapter 5.2. wetting proceeds *via* two processes: traveling of the electrolyte front from electrolyte to gas side and wetting of the pore system inside of this front. In order to get an idea on how the evolution of wetting proceeds during electrolysis and how this affects behavior in the transport-limited region. *post-mortem* analysis for evaluation of electrolyte intrusion *via* element mapping of the cross-section is linked with capacitance measurements during the electrolysis. The measurements were conducted with electrodes stressed at 500 mA/cm² after 30 min (at which the rise in HER just appears). 1 h and 2 h. As shown in the right graph of Figure 6.38 in which the FE to H_2 is given. the results from the experiments are consistent and reproducible with H_2 generation continuously increasing from 4% after 30 min to ~30% and ~40% after 1 h and 2 h. respectively. The electrode potential continuously shifts towards more negative values despite progressive wetting which is ascribed to the increase of HER which exhibits higher overpotential than CO2RR on this catalyst. The intrusion depth was evaluated for the three element maps depicted in Figure 6.37. as described in chapter 5.2.2. showing an evolution of intrusion depth from 91 µm after 30 min to 160 µm after 2 h. The same trend is observable when the capacitance is measured for the GDEs; both together is given in Figure 6.38. demonstrating the progressive intrusion of electrolyte under high electrochemical load. One important question that can be answered with these results. is. how the wetting proceeds inside the electrolyte front. *i.e.* if the share between wetted and non-wetted pores changes in the course of the experiment or if it maintains constant. The latter would mean that the increase of capacitance is solely due to the progressive intrusion of electrolyte towards gas-phase side of the GDE and the ratio between the two values should stay constant with time. Using a specific capacitance of 15 µF/cm² to calculate the ECSA and setting this into relation with the BET surface area of the wetted GDE volume obtained from the element mapping yields an estimate of the wetting ratio inside of the electrolyte front (cf. chapter 5.2.3). The results of this are given in Table 6.3.

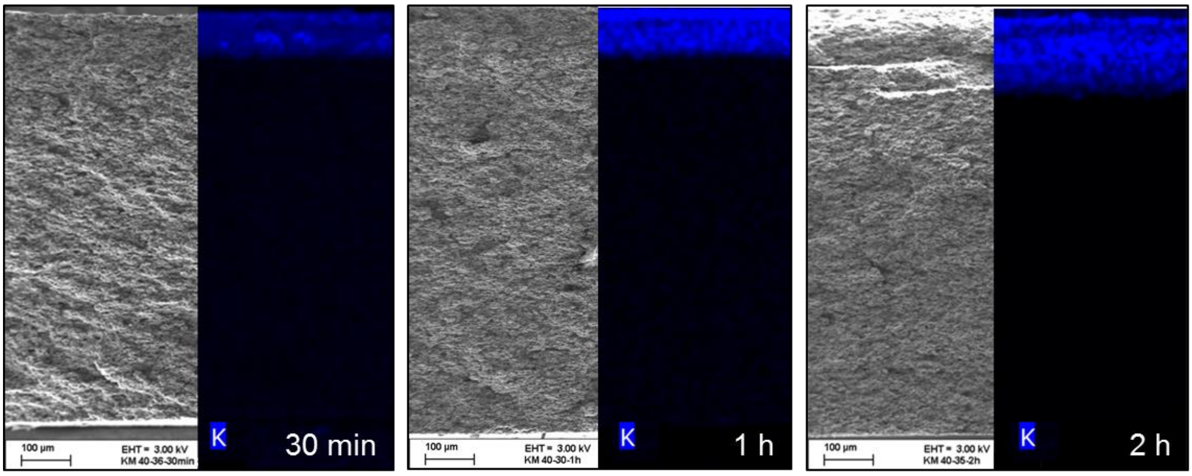

Figure 6.37 Element mapping (potassium occurrence is colored blue) along SEM image of the cross-section of AB35NP. stressed at 500 mA/cm² for 30min. 1h and 2h.

Table 6.3 Wetting data of AB35NP stressed at 500 mA/cm² after defined time intervals

		30 min	**1 h**	**2 h**
Capacitance	mF	4.2	5.5	9.9
ECSA (15 µF/cm²)	cm²	280	367	660
Intrusion depth	µm	91	102	160
Wetting-ratio*	% BET	18	22	24

* ratio of wetted surface area calculated from ECSA and BET surface area inside macroscopically wetted GDE volume

From the data it is evident that not only does the wetting increase due to an electrolyte front moving from electrolyte to gas side. but also inside of this front. the share of wetted surface area increases. from 18% to 24% after 30 min and 2 h. This means that as the intrusion depth of the electrolyte increases also larger pores become wetted (assuming constant porosity over electrode cross-section). In the transport-limited region. this can be explained by the electrode potential becoming increasingly negative with time which decreases the surface tension. This effect called electrowetting was discussed in chapter 5.2.1. Furthermore. as the results from oxidation of the carbon surface have demonstrated. a decrease in hydrophobicity and the corresponding increase of wetting degree of the GDE has a negative impact on transport limitation which should further accelerate HER. On the other hand. also catalyst reduction / dissolution is favored at increasingly negative potential. Both phenomena contribute to a self-inducing acceleration of HER generation with time. It is not clear to this point. which phenomenon contributes how much to GDE deterioration and which is more decisive for long-term performance. Unfortunately. it was not possible. to elaborate these very interesting findings regarding the progress of wetting as function of reaction conditions. electrode composition and time. and to build a more extensive basis for further discussion. Therefore. this can only serve as a starting point for a more comprehensive investigation. which should give important insight into long-term stability and how it is affected by the above. Particularly. it would be valuable to study how fast this wetting proceeds as function of the current density. if a stationary value is reached. and what this means for the performance of the GDE. If a stationary wetting degree translated into constant performance. this would suggest that catalyst deactivation could be excluded as being responsible for electrode deterioration under these conditions.

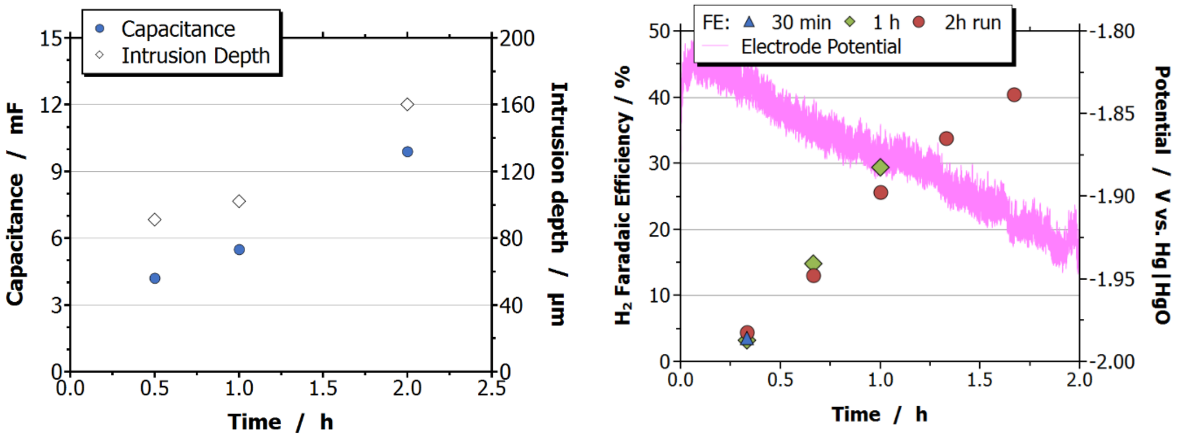

Figure 6.38 Development of wetting (intrusion depth and capacitance. left) and performance (electrode potential and HER. right) with time for AB35NP operated at 500 mA/cm²

6.3.4 Discussion on the rate-limiting process and decisive electrode property for achieving high current densities

Due to the complexity of the different phenomena taking place during reaction and how they are influenced by the electrode properties. it is difficult to explicitly nail down one single rate-limiting step and respective electrode parameter being responsible for the observed limiting current density. This holds particularly true. as the influence of electrode properties on performance is strongly masked by the proposed catalyst deactivation which. in turn. is a function of the electrode properties itself. That said. when varying the electrode properties. it is difficult to assess how much of the observed effect is due to the actual change in the properties and what is associated to the influence the change has on the deactivation of the catalyst.

A good example is the influence of catalyst dispersion and loading on achieving high current densities. The first and simple explanation of why higher loading and dispersion increases achievable current density would be that it is ascribed to the diffusion length of dissolved CO_2 from dissolution site at the TPB to the active site of the catalyst. The higher the dispersion. the lower is the average diffusion length and as a result. the higher the limiting current density according to equation 6.2. This would translate into a simple reactant diffusion limitation. On the other hand. it could still be the case. that reactant diffusion is not limiting but instead what is observed. is simply the effect of different degrees of catalyst deactivation. The deactivation described herein. is mainly affected by the electrode potential and local chemical environment. mainly the pH value. Increasing electrochemically active surface area (either by dispersion or loading) enhances the activity of the electrode. thus. lowers polarization as clearly shown in chapter 6.2.2. This will decrease the extent of catalyst reduction and deactivation in case reductive dissolution is the prevailing mode of deactivation. Even more complexity arises considering that wettability is different for the hydrophilic metal oxide and the hydrophobic carbon surface. Increasing dispersion and loading would lead to an increase of electrochemically active surface area. lower local current densities and. therefore. lower local pH values due to less OH^- generation. This would result in less deactivation if chemical dissolution at high pH values ($pH > 12$) is the prevailing dissolution process. Thus. this could point to the situation that the increased dispersion or amount of catalyst simply leads to less deactivation. Ultimately. one can say that the results from catalyst studies alone do not allow drawing a clear conclusion on how dispersion and loading contribute to enhancing current density as their influence is masked by its deactivation. To obtain a better understanding of the GDE behavior. it is crucial to address this stability issue first. *e.g.* by switching to a more stable catalyst.

In contrary. the conclusion from the wettability studies remains valid despite the significant influence deactivation has. For a given current density. both pH value und electrode potential are strongly influenced by wettability and wetted surface area. The extent of electrocatalyst in contact with electrolyte determines the local current density and therefore concentration of reactants and products (incl. OH^-) adjacent to the active sites. In particular. lower wettability leads to higher local pH value and higher polarization. both due to higher local current density. According to Dutta et al. [101] and Figure 6.36. both effects make the catalyst less stable. This observation strengthens the arguments made herein regarding the influence of wettability as the corresponding deactivation actually counteracts the observed trend: increased wettability decreases polarization and local pH. both lowering extent of deactivation. Still. the GDE performs worse when wettability is higher. Accordingly. taking catalyst deactivation out of the equation would most probably lead to an even more pronounced effect.

Bringing together all the information obtained in this work allows drawing some robust but still preliminary conclusions which need to be elaborated in upcoming work. preferably supported by modeling and simulation and more advanced *operando*-characterization.

i. Electrode wettability
The experiments describing the oxidation of the carbon carrier while maintaining its microstructure clearly show that the high hydrophobicity of the GDEs is the most critical feature when aiming for high current densities. The results suggest that. just aiming for high current density. there is not an optimum for wettability as expected. but instead maximizing hydrophobicity is always advantageous. However. for technical realization of course a compromise has to be found between shifting transport limitations to high current densities and adequate wetting to decrease overpotential and ohmic losses.

ii. Electrode porosity
The second property which shows substantial influence on achievable current density is the texture of the electrode which is determined by the carbon carrier and electrode manufacturing. This is not surprising as it strongly influences mass transport of both reactants and products. By increasing the compacting pressure. the porous network becomes more compact in the whole pore range and mass transport of all species involved in CO2RR becomes impeded. leading to a shift towards HER in the limiting current density region.

iii. Product vs. reactant diffusion limitation
A surprising finding is that increasing porosity *via* pore-forming agents is detrimental to performance. Considering gas-phase diffusion does not play a role for limiting current density (as evidenced by the independence on electrode thickness) and that porosity is only enhanced in the pore size region where gas phase transport prevails while the primary porosity remains unchanged. one should expect that the effect of pore-forming agents should be negligible. However. the opposite is the case. The observations suggest that two things are taking place: i) the wetted pore network becomes strongly disturbed owing to the large pores formed by the decomposed salt. Accordingly. the tortuosity for liquid phase diffusion from TPB to bulk increases. ii) the electrolyte front moves deeper into the GDE evidenced by an increasing capacitance despite less surface area per electrode volume (due to the large pores formed). Considering that the primary pore system is unchanged and the fact that in the limiting current density regime dissolved CO_2 is completely converted adjacent to the dissolving site and not diffusing into the aggregates. it is unlikely that CO_2 diffusion to the active site is the decisive factor here. Instead the observation points towards a product diffusion limitation by the combined

effect of an increase of tortuosity in the wetted pore network connecting flooded aggregates and bulk electrolyte. and the longer diffusion distance by a deeper penetration depth.

Mathematically. the liquid-phase diffusion of the products can be described in the simplest form by Fick's Law in a porous system according to equation 6.2 with $D_{i.eff}$ being the effective diffusion coefficient. The latter accounts for the properties of the pore system. *i.e*. for its porosity ε and the tortuosity factor τ. according to

$$D_{i.eff} = D_i \frac{\varepsilon}{\tau} \qquad 6.8$$

It is evident how the porous properties of the carbon matrix greatly influence the diffusion rate and. accordingly. the limiting current density. In addition. also the wetting degree plays into this as τ only accounts for the wetted pore region. The diffusion of the negatively charged products into the bulk is necessary to close the charge balance. At the TPB. the produced OH^- undergoes reaction with dissolved CO_2 and is sequestered into the carbonate equilibrium under alkaline conditions [184] according to

$$CO_2 + OH^- \rightleftharpoons HCO_3^- \qquad 6.9$$

In common applications for GDEs. mainly ORR. limitation by product diffusion is usually not pronounced. as OH^- is the only product for which diffusion is very fast as it follows the Grotthuis mechanism and since catalyst layers in such applications are very thin and highly optimized. However. in older publications it is possible to find examples where the diffusion / migration of product ions in the liquid-phase is indeed rate-determining. For example. Striebel et al. reported OH^- transport out of the catalyst layer to be the limiting factor in PTFE-bonded oxygen cathode electrodes in K_2CO_3 electrolyte [189]. Using an adjusted flooded agglomerate-model. they estimated that OH^- concentration close to the gas-phase side is 132 times higher than in the bulk at 100 mA/cm² leading to a doubling of the Tafel slope at high current densities. As a result. they propose an increase of porosity and decrease of thickness of catalyst layer (they used a layer with 120 µm. a similar length as the wetted GDE part in this work) to mitigate this effect. In comparison to OH^-. CO_3^{2-}. which is the predominant form when pH > 10. exhibits much slower diffusion with a diffusion coefficient of $D_{CO3} = 0.8 \cdot 10^{-9}$ m²/s at 25 °C [190]. Formate diffusion is slightly faster with $D_{HCOO} = 1.45 \cdot 10^{-9}$ m²/s [191] suggesting that if product diffusion is limiting it should be associated with bicarbonate or carbonate. In light of the pronounced accumulation of products inside the GDE. one result of the slow transport of carbonate could be its precipitation inside the pore system. This would lead to a clogging of pores and thereby further deterioration of performance. Although during HER. twice the amount of carbonate is produced (2 OH^- per H_2). HER is not restricted to the TPB the same way as CO2RR but instead can be produced close to the bulk side of the GDE where diffusion length is much lower. Accordingly. transport limitation by product diffusion is not an issue for HER in the investigated region and will compensate for CO2RR at high current densities.

Although it could not be conclusively proven during the work at hand. this argumentation is in line with the observed behavior of the GDE throughout this work. It can explain the inferior performance of microporous carbon carriers (although wettability certainly plays a role there too). temperature dependence (which can also point to reactant diffusion limitation). the positive influence of less compact agglomerate porosity but – at the same time – detrimental effect of pore-formers as well as the influence of the operation mode. The latter can be rationalized by the same argument that was employed to correlate operation mode and catalyst deactivation: by continuously replenishing the electrolyte. the driving force for diffusion $\Delta c/d$ is maintained by a close to stationary bulk composition whereas in semi-batch mode the products continuously accumulate in the bulk. As discussed. the impeded transport of products away from the TPB can i) lead to more severe deactivation of the catalyst by increasing pH at the TPB or ii) it can intensify product transport limitation. both leading to more pronounced shift towards HER with time.

Chapter 7

Cost analysis of CO_2 electrolysis

To derive a quantitative description on why the use and optimization of GDEs is crucial for commercialization of CO_2 electrolysis. a cost analysis is developed and employed to describe the cost of producing formic acid (not potassium formate. see below) in the system at hand. It is described in the following chapter and subsequently employed to demonstrate how current density as decisive parameter significantly influences the cost of electrolysis up to a certain point. By employing the model. one obtains an impression on what the critical factors for rentability of such a system are and how the costs are affected by the different input parameters of the model. such as stack cost or Faradaic Efficiency. Part of this. was published in generalized form in [192].

7.1 Derivation of the model

Recently. a few analysis models have been published on CO_2 electrolysis (CO2EL) systems focusing on different aspects of the process. *e.g.* the evaluation of the economic competitiveness of different product routes [14] or establishing quantitative targets for technical realization [150.193]. Among the published models. none explicitly describes the influence of operating conditions for the production of formate or formic acid in the system at hand. that is using an alkaline electrolyzer as basis. In the following. the most important concepts and assumptions that went into the model will be discussed. For further details it is referred to the method section 4.4. Although the actual product at the commonly employed electrolyte condition is potassium formate. the calculation will be conducted using the molar mass of formic acid as this is the desired end product of the overall process for which the electrolysis step is considered herein. This allows direct comparison of the electrolysis cost to the market price (€/t).

The reference system

As no commercial electrolyzer technology exists for CO_2 reduction and therefore the important information regarding investment and operating cost are missing. the model is based on the cost structure of commercial water electrolysis systems for which reliable and comprehensive data on the techno-economics can be found in literature. The reference system herein is a state-of-the-art alkaline water electrolyzer (AEL) for which a sketch is given in Figure 7.1. This technology was chosen over polymer-electrolyte membrane (PEM) electrolysis as with the liquid buffer electrolyte and the alkaline conditions it resembles more closely the conditions employed herein and what is state-of-the-art. The most obvious difference between the reference AEL and the actual system is the electrode architecture on the cathode side and the supply of reactant. A cost breakdown of the different contributions to the total stack cost given in [194] assumes a cathode share of around 25% in AEL. in which nickel-based electrodes are commonly employed. To account for the more costly manufacturing of the GDE used in CO2EL and the additional gas feed as well as other deviations and uncertainties in the stack cost. a sensitivity analysis on the investment cost is included and discussed below to investigate what influence the difference has on the outcome of the analysis.

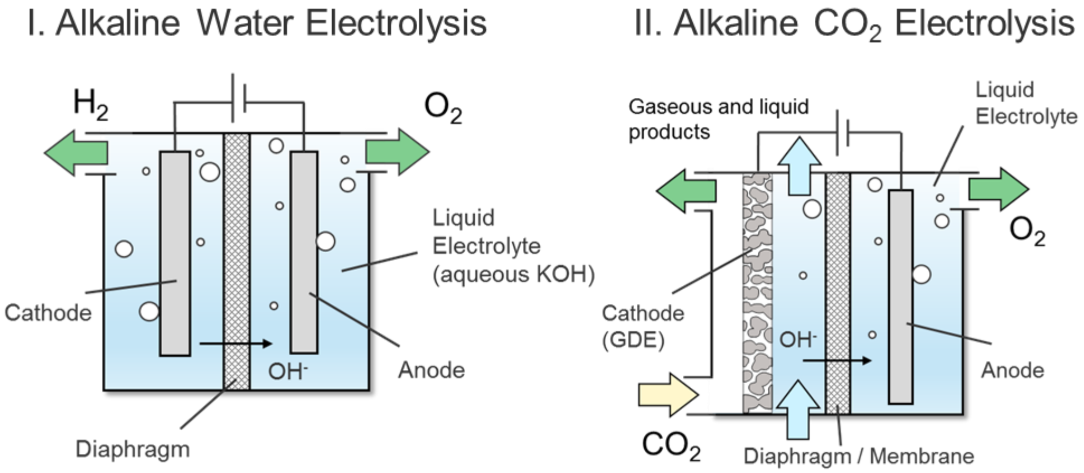

Figure 7.1 Sketches of reference system alkaline water electrolysis (left) and actual alkaline CO_2 electrolysis system.

Investment Cost

The investment cost for the manufacturing of the components and assembly of the stack is based on a study of the Fuel Cells and Hydrogen Joint Undertaking (FCH JU) and the values projected by its members [148]. Therein. a cost range between 800 €·kW^{-1} and 370 €·kW^{-1} in 2030 is predicted for an AEL system. for which the stack accounts for 50% of the cost. As the non-stack contributions (including the whole periphery of the facility. e.g. feed preparation. thermal management. power supply. etc.) are difficult to be translated directly from water to CO_2 electrolysis without making unnecessary assumptions. only the stack itself is accounted for (see also method section). To make the investment cost sensitive to the current density in which it operates (the input variable of the model). the nominal power of the stack must be converted into the employed electrode area. thus. the cost from €·kW^{-1} to €·m^{-2}. Therefore. the relationship between nominal power and electrode area has to be known. Using Faraday's Law (with 100% FE towards H_2). the electrode area for a typical state-of-the-art water electrolyzer can be estimated by its product yield (given by the manufacturer) and a common current density of 300-400 mA/cm² for commercial AEL systems. Something similar has been done in [14] however. just for *one* exemplary electrolyzer. To account for the different operating conditions and stack properties of different manufacturers and models. and to put the input parameters on a more solid basis. the data herein is based on the market survey of Buttler and Spliethoff from 2017 [149]. Accordingly. using reported product yield and nominal power for the reported 15 commercial AEL systems. one obtains an average conversion factor of 6 kW/m² (ranging between 5-8 kW/m²). Including an installation factor of 10%. this gives an average price of around 2.300 €/m² which is consistent to the one obtained in [195] for alkaline CO_2EL (1221 to 4884 €/m²). The depreciation of the investment is assumed to follow a simple fixed-mortgage financial model (fixed rate over loan term. see method section). Dividing by the current density and applying Faraday's Law. this gives the final specific investment cost of product-yield in €/mol/h as function of the current density. According to that. with increasing current density. the required electrode area for desired product output and as a result the investment cost decrease.

Operating cost

The operating cost of the electrolyzer can be divided into electricity dependent part resulting from the electrochemistry of the system. cost of feedstock and auxiliaries as well as the maintenance cost to keep the electrolyzer running. For water electrolysis. non-electricity operating cost is commonly given as percentage on the initial investment cost. as it usually scales directly with the size of the electrolyzer similar to the investment cost. Amongst others. this share contains replacement of electrode and electrocatalyst. replenishment of electrolyte and actual maintenance of the system. According to [148] it ranges between 2 and 5%. depending on the size of the electrolyzer. As CO_2 electrolysis is not as mature as water electrolysis and long-term stability of electrode materials has yet to be demonstrated. a conservative value of 5% was chosen as base case. In a more detailed techno-economic study. it would be required to develop the balance of material and energy fluxes to explicitly evaluate requirements for thermal management and the input of auxiliary streams (electrolyte. water) which. however. goes beyond the scope of this assessment. Also. CO_2 cost or credit is not accounted for as price development is difficult to project at the moment (projected price of CO_2 separation in the mid-term is assumed ~40 €/t [196]) as it will strongly depend on the legislative framework to be established in the next years. It would in any case not change the outcome of the analysis but just account for an additional contribution on top of the estimated cost: for the production of potassium formate and CO at 80% and 10% FE. respectively. and the remainder being H_2. this equals 0.59 kg CO_2 per kg HCOOK (and 42 g CO). Assuming. in alkaline conditions CO_2 additionally reacts with produced OH^- (one OH^- per HCOOK and two for CO and H_2) to potassium bicarbonate. this value rises to 1.375 kg CO_2. With CO_2 separation cost of 40 €/t. this amounts to 55 €/t HCOOK or 97 €/t HCOOH.

Electricity Cost

The cost of electricity is reflected in the cost of specific energy input which describes the electric energy required to produce a given amount of the desired product. It is defined as

$$Specific\ energy\ input = \frac{U_{cell} \cdot I}{\dot{n}_{prod}} = \frac{U_{cell} \cdot I \cdot z \cdot F}{I \cdot FE}. \qquad 7.1$$

and accounts for the cell voltage during operation and lost charge due to parasitic side reactions. The cell voltage U_{cell} depends on the energetic efficiency *EE* as operating variable of the model and on the standard cell potential U_0 of the overall reaction. It is 1.12 V with anodic oxygen evolution (anode and cathode at pH 14). The energetic efficiency is defined as

$$EE = \frac{U_0}{U_{cell}} FE \, . \tag{7.2}$$

For the electricity cost. a value of 0.05 €/kWh is used. following reported wholesale electricity prices in the European Union 2018[151]. Electricity cost can of course be lower when production is shifted towards regions with abundant renewable energy availability or when only excess electricity is to be used. Accordingly. often an optimistic value of 0.02 €/kWh is chosen in certain scenarios [193]. However. it is not the goal herein. to generate the most optimistic outcome but to give a realistic assessment. In addition. for an electrolyzer to be economically viable. maximization of full load hours is crucial to obtain low production cost and focusing on excess electricity not constructive.

7.2 Analysis

In the following. the developed model will be employed to analyze the different contributions to the electrolysis cost for the generation of potassium formate and to show how the production cost is affected by the operating conditions.

7.2.1 Base case scenario

First. for the base case scenario (values given in Table 4.2). the influence of current density and energetic efficiency (EE) on the total electrolysis cost is evaluated and depicted in Figure 7.2. As one will see in the following. the general appearance of the graph remains the same independent on the input parameters. It is determined by the combined effect of stack and electricity cost which in turn are governed by current density and EE. respectively. That is. at low current densities below 100 mA/cm². total cost rises significantly. while for increasing current density it levels off at around 300 mA/cm². The final cost largely depends on the energetic efficiency. *i.e.* cell voltage. and electricity cost whereas the current density at which this happens is determined by the stack cost.

This can be understood when looking at the cost breakdown given in Figure 7.3 in which the cumulative cost of the three contributions investment. operating and electricity cost is shown over current density for the base case scenario and a high investment cost scenario. For the latter. the input parameters that determine investment and electricity cost are chosen such that the outcome is highly unfavorable towards investment cost but favorable for electricity cost both maintain in a realistic range. The scenario is described below in more detail in the scenario analysis.

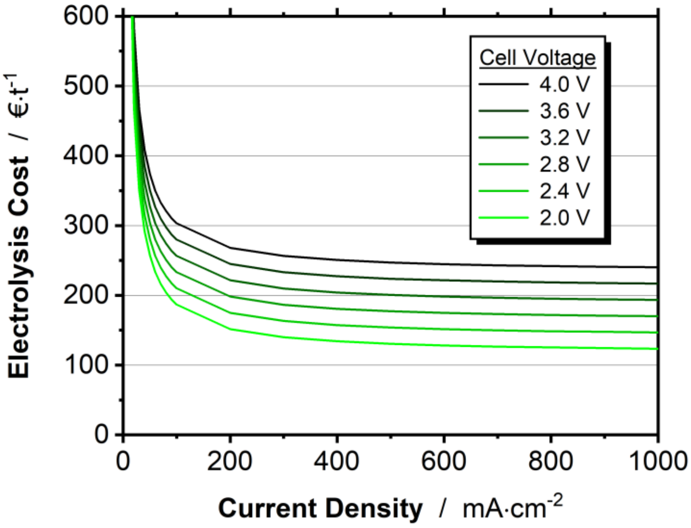

Figure 7.2 Cost of formic acid production as function of current density and cell voltage calculated with base case parameters (see Table 4.2).

The observation that electricity cost (normalized on ton of formic acid) is independent on current density is not surprising as it is only determined by the price of electricity and the specific energy input which in turn is given by the cell voltage. Since electricity cost is a linear function of the latter its influence on total cost is quite considerable. On the other hand. investment and operating cost which are inversely proportional to current density. are substantial at low current densities but drop drastically in the range up to 200 mA/cm². Beyond that. its contribution levels off before becoming mostly independent on current density. This is in agreement with the results from the techno-economic analysis done by Jouny et al. who investigated the effect of various input parameters to the net present value of different reduction products. In their sensitivity analysis for the current density. they concluded that increasing current density from their base case of 300 mA/cm² to an “optimistic value” of 500 mA/cm² has a negligible effect on total cost compared to other contributions (in contrary to decreasing it down to 100 mA/cm² as “pessimistic case”). Evidently. using a GDE or any other approach to facilitate working at high current density is indispensable. For the base case and 3 V cell voltage. increasing current density from 10 mA/cm² characteristic to conventional electrode architectures to 100 mA/cm² decreases investment cost from ~450 €/t to 45 €/t. *i.e*. by 405 €/t. whereas a further increase to 500 mA/cm² leads to investment cost of around 9 €/t. thus. savings of only 36 €/t. With electricity cost constant. this effect becomes even more pronounced when looking at the total cost: for 3 V. it drops by a factor of 3.6 (~875 to ~250 €/t) for the first case but only by 1.3 or 1.4 when increasing current density further to 500 mA/cm² or 1000 mA/cm². respectively.

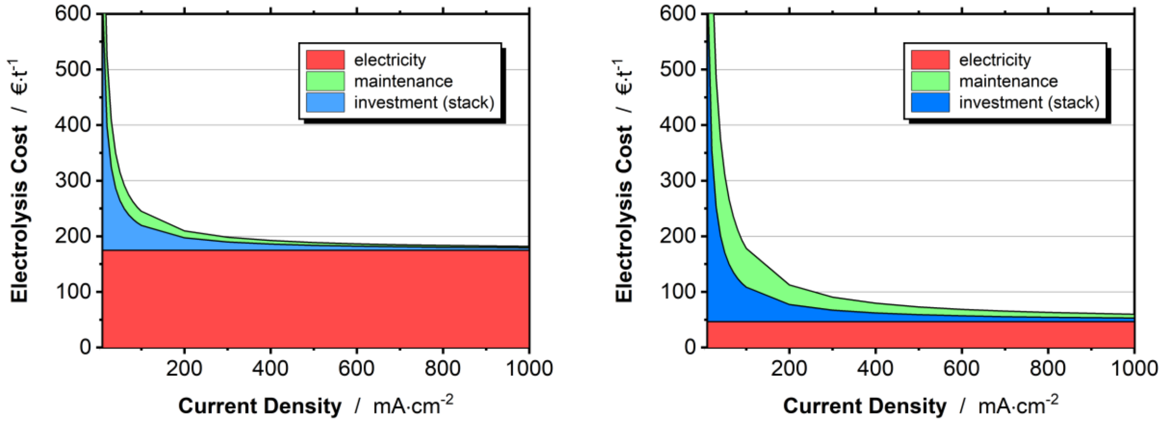

Figure 7.3 Cost breakdown over current density for base case (a. 3 V cell voltage) and high investment/low electricity cost scenario (b. 2 V cell voltage).

Although this is just very simple math ($c_{invest} \sim 1/i$). the practical implications of this are considerable. Accordingly. while the first 90 mA/cm² increase is crucial for application. the benefit-cost analysis becomes increasingly unfavorable. especially beyond 300 mA/cm².

In reality. this effect is even more severe considering that current density and cell voltage are not independent variables. To demonstrate this. a U-I curve representative of a full CO_2 electrolysis cell has been fitted from literature data [20] in Figure 7.4. Here. the kinetic polarization and the ohmic losses are separated which together yield the total cell voltage. As one can see. in the high current density region. the cell voltage is largely determined by ohmic losses which scale linearly with i and lead to a significant increase of cell voltage. As a result. EE will decline rapidly. and the resulting electricity cost will rise in the same manner. This makes working at such high current densities less favorable. Similarly. in the low current density region. the investment cost are decisive due to large electrode areas required for a given production output.

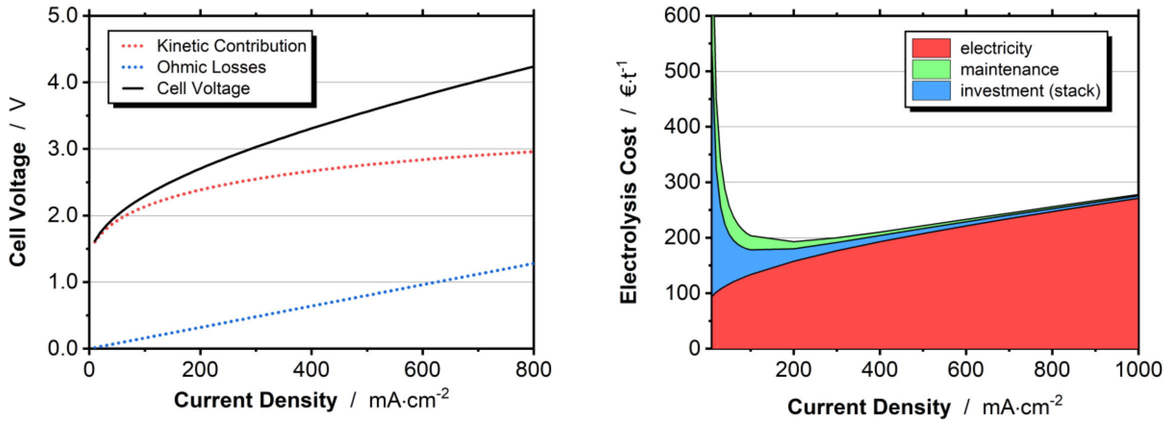

Figure 7.4 Representative U-i curve for a potential full cell with anodic OER (fitted from literature data. left) and corresponding cost breakdown of electrolysis cost (right)

As the discussion as well as intuition suggests. the electrolyzer comes with an optimum operating point at intermediate current densities at which cost goes through a minimum. In this particular case. which is based on realistic assumptions. this operating point is located around 200 mA/cm²; a typical operating point of commercial alkaline electrolyzers.

7.2.2 Sensitivity analysis

To show the limitation of the analysis with regard to its quantitative outcome and to check if the trends obtained are general enough to draw a conclusion from. the uncertainty of the model has been assessed. This is done by sampling the input parameters in a realistic range characteristic of different best case and worst case scenarios. To evaluate the effect of electricity and stack-related cost separately. scenarios assuming high and low cost for investment and electricity (including the related variables). respectively. as well as a combination of both (low/high investment *and* electricity cost). yielding maximum and minimum total cost are considered. Furthermore. scenarios are considered in which electricity cost is low *and* investment cost high. and vice versa. to check if the trends from above are still valid.

To derive the upper and lower limit of stack-related cost. the range of suggested investment cost for the electrolyzer system is taken in accordance to the projected cost range for 2030 from above. that is 380 to 800 €/kW. Maintenance cost was increased to 10% of the investment cost per year to account for less stable electrodes and less mature technology in the worst-case scenario. The electricity price was increased by 50% around the base case of 0.05 €/kWh to 0.075 €/kWh and decreased to 2 ct/kWh to simulate what is often considered a long-term favorable electricity price for electrification characteristic of regions with high abundance of cheap renewable energy [193].

Table 7.1 Input parameters for scenarios used in sensitivity analysis

	unit	**worst case**	**base case**	**best case**
Investment cost of system (2030)	€/kW	800	580	380
Maintenance cost	%	10	5	5
Electricity cost	€/kWh	0.075	0.05	0.02
Cell voltage	V	3.5	3	2

The outcome of this scenario analysis is shown in Figure 7.5. The scenarios which give the highest and lowest total cost are herein given as boundary conditions in gray. It can be clearly seen that the uncertainty is very high which can be ascribed to the wide range of electricity price and the respective cell voltages assumed as summarized in Table 7.1. The high current density limit yields 50 and 320 €/t in these cases. From the above cost breakdown as well as from the electricity cost variation in Figure 7.5 on the left. this can be clearly attributed to the effect of electricity cost being the main external parameter determining the economics of the system. The offset to the cost limit is due to the cell voltage which is varied in addition. As expected from above as well. the effect of investment cost on total cost is especially pronounced for low current densities. however. the curves for the stack cost variation gradually approach the cost of the base case scenario at >300 mA/cm^2 making the actual stack cost insignificant in this region. Varying the stack-related cost shows. however. that although the general trend prevails. stack-cost can play a role when high in comparison to the electricity cost as depicted in green on the right graph. Accordingly. current density which needs to be reached for leveling off of electrolysis cost is gradually shifted to higher values (here 500 mA/cm^2). This shows that the cost of the electrolyzer system cannot be neglected and needs further development.

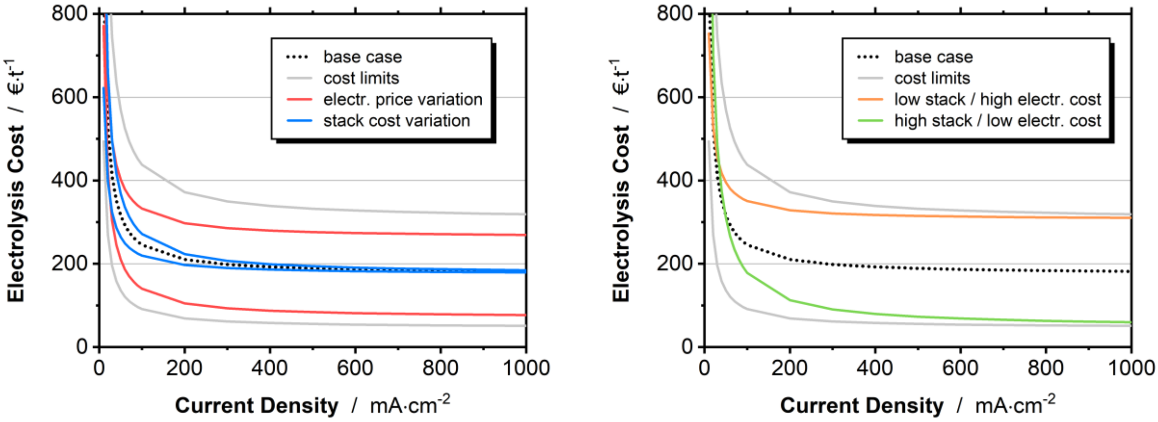

Figure 7.5 Sensitivity analysis performed around the base case scenario with different combinations of electricity and stack costs

Still. independent on the specific input parameters. all curves exhibit the same trend. The difference is limited to the current density of the inclination point after which the cost becomes saturated. and the exact value of the total cost that the total electrolysis levels off to. While the inclination point is determined by the stack cost. electricity cost is determined by Faraday’s Law and cell voltage. thus. constant for given EE. For the base case scenario. electrolysis cost for a realistic target of 3 V and current density of several hundred mA·cm^{-2} levels of at around 180 €/t. It is important to keep in mind. that the investment cost in this analysis is only comprised of the stack cost. not including peripheral elements that add to the cost of the whole electrolyzer system. When including these. investment cost would double if the cost structure of water electrolysis is assumed. The influence at high current densities. however. is not significant as shown in the sensitivity analysis above. A further assumption was that assuming the cost structure of AEL to obtain a meaningful assessment of cost for alkaline CO$_2$ electrolysis is a valid simplification. Accounting for gaseous feed supply and GDEs instead of nickel-plates would influence both stack and maintenance cost. If the cathode cost which accounts for 25% of the cost stack would *e.g.* increase by a factor of 10. total stack cost would roughly triple (cathode cost was 25% of stack cost). As a result. electrolysis cost for formic acid production would increase from 190 to 220 €/t for the base case scenario at 3 V and 500 mA/cm^2 which is in the range of the uncertainty expected from this cost assessment. Importantly. it is comprehensible from this analysis why the availability of cheap and abundant renewable energy is a decisive factor for profitability of electrolyzer systems. as stressed for example by [193]

7.2.3 Discussion

In general. the sensitivity analysis shows that it is possible to use this assessment to draw conclusions about the effect of operating conditions on profitability of the process. First. it can be clearly shown that the working hypothesis of this work. that is the importance of current density. can be validated. In particular. increasing current density to several hundreds of mA/cm² is crucial and can be enabled by using optimized GDE structures. On the other hand. the outcome shows that at some point. further increase does not give a decisive improvement of electrolysis cost and that electricity cost becomes the determining factor at high current densities. Thus. cell voltage overtakes as the main contributor above 300 mA/cm². This is particularly important when taking into account that in a real system current density and cell voltage are not independent variables but are coupled by the current-dependence of the overpotentials and ohmic losses. Due to the linear relation. the latter becomes significant at high current densities. so further increase of current density. although being facilitated by the GDE structure. comes with a considerable voltage penalty. Accordingly. the operating point might in reality be chosen far from what the GDE is able to achieve with regard to transport limitation. In turn. for the development activities. this implies that improving achievable current densities is important but that the corresponding overpotentials should not be neglected and that minimizing losses both from kinetics but also from an engineering point of view (electrolyte. cell design) is needed. Although not subject of this work. this needs further systematic investigation to obtain the optimum form a system point of view.

Ultimately. it was argued that the generation of formic acid (not formate. see below) being a high-value product would be a reasonable route for technology introduction of CO_2 electrolysis and could drive cost down for other less costly products with higher market volume and therefore higher impact. Indeed. the market volume of formic acid is rather small (950 $kt \cdot a^{-1}$ production in 2014 [197]) due to its use in niche applications such as in the leather and tanning industry. as reactant in the pharmaceutical and chemical industry. as well as to control pH in silage. animal feed or the textile industry. As a matter of fact. the market price of formic acid is with 600 €/t [14] clearly higher than the estimated electrolysis cost herein showing that in principle electrochemical production from CO_2 might be competitive against conventional production. This has also been suggested by [14.150]. Even in the most unfavorable case of combined high investment *and* electricity cost. with around 320 €/t cost remains below market price. However. cost of separation which was not accounted for herein will most arguably challenge profitability considerably. especially considering low concentration of formate in the product stream and an additional required protonation step to obtain the desired formic acid. Achieving high product concentration on the order of several mol/L is of utmost importance as well as finding a way to produce formic acid in its non-dissociated form as has been achieved by Yang et al. [198]. Although CO_2 electrolysis is almost exclusively reported in neutral to alkaline electrolyte and acidic conditions suggested to come with significant performance penalty. it is not fully clear why this argument prevails. It has been shown in several studies [21] that pH value close to the reaction zone increases dramatically due to the generation of OH^-. Accordingly. even in bulk acidic conditions. the pH value inside the GDE should reach more alkaline conditions favorable for CO2RR. This is a pathway which should be investigated more extensively including modelling activities to understand the role of pH inside the GDE. Formate itself instead of formic acid can only be regarded as promising product when a pathway for an energy storage cycle is established with formate as hydrogen storage chemical or as fuel for direct-liquid fuel cells as suggested by Bienen et al. [199] to create a market of interest.

Chapter 8

Summary and Conclusion

In the course of this work. carbon-based and PTFE-bound gas-diffusion electrodes (GDE) have been developed and investigated for the electrochemical reduction of CO_2 (CO2RR) to potassium formate at high current densities and Faradaic efficiencies (FE) in an industrially relevant environment (*i.e.* besides targeting high space-time yield. the use of aqueous electrolyte and inexpensive materials where possible). Their ability to facilitate the reaction at such conditions is determined by a complex interplay of different kinetic phenomena which leads to a non-trivial optimization approach that can hardly be conducted on a sole empirical methodology and needs thorough understanding of the system. It could be shown that the electrochemical behavior is strongly influenced by the parameters employed during electrode manufacturing (*i.e*. composition. compacting pressure and post-treatment). the resulting GDE properties (mainly texture and wettability) and the reaction conditions (electrolyte. temperature. electrode potential). As such the goal of this work. that is. getting a thorough understanding of how the GDE works and separating the different contributions on the electrochemical behavior is strongly complicated by the interactive nature of these variables. Thus. an elaborate and systematic investigation of the relationship between said variables and the electrochemical performance was conducted to establish a starting point for a more targeted optimization of the GDE in future work.

From an application point of view. GDEs were developed with highly promising performance characteristics combining a newly developed simple and scalable dry deposition technique for the manufacturing of the GDEs with a homogeneous precipitation method to obtain fine dispersion of the tin oxide electrocatalyst on the carbon substrate. Optimizing electrode properties yielded GDEs that allowed for operation at current densities >500 mA/cm² while maintaining FE towards formate >80%. While these are striking values and already in the range of what is targeted for technical application. long-term stability evidenced by a continuously increasing rise of hydrogen evolution over time is far from suitable from a technical point of view. By investigating the effect of the GDE properties – that are the composition (carbon type. PTFE content. electrocatalyst content). texture (adjusted via pore-forming agents and compacting pressure) as well as hydrophobicity (function of carbon substrate and adjusted by its oxidation) – and evaluating the time behavior. it could be shown that working at high current densities is determined by i) reactant and product transport. ii) wettability and iii) catalyst accessibility. To address the first point. it could be demonstrated that an open pore structure (evaluated by Hg-porosimetry) which can be tailored by the employed carbon type and compacting pressure improves transport characteristics of the GDE. This allows for an increase of the achievable current density by as much as a factor of 10. from 50 mA/cm² to 500 mA/cm² simply by choosing the most suitable carbon black carrier. It has to be noted that in this case in contrary to the sole adjusting of compacting pressure. the different wettability of the carbon blacks will also strongly affect the suitability of the GDE. That said. wettability has a more ambiguous way of affecting the GDE functionality. On the one hand. the activity of the electrode at moderate polarization. is solely determined by the wetted catalyst surface as demonstrated by the clear relationship between double layer capacitance and current density for given electrode potential. This not surprising correlation was substantiated by experiments elucidating the influence of PTFE content. carbon wettability and the respective increase of macroscopically observable current density with time at constant polarization due to continuous wetting of the pore system. On the other hand. this work points towards a detrimental effect of increased wetting with regard to achievable current density in the system at hand and with the type of hydrophobic GDEs used herein. This striking correlation could be evaluated by adjusting the functional groups of the carbon carrier by surface oxidation. Increasing the wettability while maintaining the carbon microstructure led to a clear shift of transport limitation to lower current densities.

To get a better understanding of how the wetting proceeds and how it is affected by both the GDE properties and reaction conditions. a novel methodology was established herein combining capacitance measurements and intrusion depth analysis by *post-mortem* element mapping of the cross-section. Whereas the latter allows for a macroscopic assessment of how deep the electrolyte front has penetrated from electrolyte towards gas side of the GDE. the capacitance is a qualitative measure of the wetted surface area inside this electrolyte front. As a first example of what this methodology is capable of. it could be quantitatively shown that the extent of wetting inside the electrolyte front is a strong function of the electrode properties and experimental conditions. Switching from low (highly hydrophobic Acetylene Black. 35% PTFE) to high wetting conditions (Vulcan. 20% PTFE) causes the degree of wetting to increase from 22% to 47% after 1 h. Leveraging this methodology to its full extent with systematic experimental studies in the future will allow for an assessment of long-term stability. degradation mode and can reveal how the wetting process is determined by applied potential and electrode hydrophobicity. *Operando* techniques such as nano-CT as well as microstructurally-resolved modelling of the electrode structure and the processes occurring during electrolysis can aid in getting a clearer understanding of the limiting factors and how the GDE can be further improved [200]. This is crucial. as studies on the influence of wettability are still one of the most open scientific directions for further investigation of the process and therefore highly recommended. Although consistent with other observations in this work. the hypothesis that increased wetting with time also contributes to the GDE degradation by shifting the triple-phase boundary deeper into the GDE structure. thereby. impeding transport of products back into the bulk cannot be fully validated at this stage of research. This is because at the same time. one of the main findings of this work was the observation that stability issues of the electrocatalyst encountered herein due to the high pH value in the reaction zone and the high cathodic polarization tend to mask the real electrode behavior and made clear conclusions difficult. As a result. it could be shown that although often claimed to be metastable at the conditions at hand. significant loss of active species can be observed. most arguably by reductive dissolution and consequent redeposition as metallic tin which is active towards the undesired hydrogen evolution (HER). This effect has been found to prevail throughout the different studies herein. partially masking the real electrode behavior and influence of its properties. It is thus questionable. if tin oxide is a reasonable electrocatalyst for this reaction and future work should either consider switching to more stable catalysts such as bismuth which is active for CO2RR also in metallic form or find solutions to stabilize tin oxide. Only if this stability issue is under control. a more robust assessment of GDE operation can facilitate conclusions on the decisive parameters and most suitable optimization routes. After all. for technical realization of the process. the GDE needs to exhibit durability of several thousands of hours.

Ultimately. the cost analysis conducted herein can give a good estimate on reasonable targets for optimization of CO_2 reduction technology. Facilitating high enough current density is decisive as shown by the quantitative outcome proving the working hypothesis and the motivation of this work highly relevant. When this work started. state-of-the-art systems were not able to facilitate such rates encouraging the efforts conducted herein to develop such electrode systems. However. in the last years. current densities of several 100 mA/cm^2 using GDEs have become state-of-the-art demonstrating that as soon as long-term stability is ensured. electrode performance is not the limiting factor anymore. Going one step further and keeping in mind that cost levels off drastically beyond 300 mA/cm^2 while the influence of cell voltage maintains decisive. it might not be reasonable to push current density too far towards high values. At such high current densities. cell voltage is mainly determined by the ohmic losses of the cell which scale linearly with current density. Thus. the increasingly less pronounced benefit of increasing current density would come with the considerable disadvantage of increasing cell voltage with a high impact on total production cost. Accordingly. to derive the desired operating point with maximum profitability for the actual system. obviously. one needs to establish the electrolysis cost with the actual *U-I* characteristic of the cell. The resulting optimum point of operation would then be a compromise of high current density (investment cost) and low cell voltage (electricity cost) as well as long-term stability of the electrode. Regarding the cell voltage. the focus for further optimization is an engineering one. shifting the emphasis of future development in the direction of cell design and operating conditions. CO_2 electrolysis is currently indeed at the stage where this becomes an increasingly important topic and increased efforts to couple the electrochemical research with the work of mechanical and process engineering become visible. ultimately. paving the way towards commercialization and defossilation of the chemical industry.

9 References

[1] E. Byers. M. Gidden. D. Leclere. et al.. Global exposure and vulnerability to multi-sector development and climate change hotspots. Environ. Res. Lett. 13 (2018) 055012. https://doi.org/10.1088/1748-9326/aabf45.

[2] COP26 special report on climate change and health. The health argument for climate action . 2021. https://reliefweb.int/sites/reliefweb.int/files/resources/9789240036727-eng.pdf (accessed February 16. 2022).

[3] UNFCCC. Conference of the Parties. Adoption of the Paris Agreement. in: Paris. 2015.

[4] Intergovernmental Panel on Climate Change. Intergovernmental Panel on Climate Change. Global warming of 1.5° C: an IPCC special report on the impacts of global warming of 1.5° C above pre-industrial levels and related global greenhouse gas emission pathways. in the context of strengthening. 2018.

[5] Detlef Drosihn. Übersicht zur Entwicklung der energiebedingten Emissionen und Brennstoffeinsätze in Deutschland 1990 – 2019. 2021.

[6] H. Ritchie. M. Roser. CO_2 and Greenhouse Gas Emissions. OurWorldInData.Org. (2020).

[7] Z.J. Schiffer. K. Manthiram. Electrification and Decarbonization of the Chemical Industry. Joule. 1 (2017) 10–14. https://doi.org/10.1016/j.joule.2017.07.008.

[8] R. Geres. A. Kohn. S. Lenz. F. Ausfelder. A. Bazzanella. A. Möller. Roadmap Chemie 2050 - Auf dem Weg zu einer treibhausgasneutralen chemischen Industrie in Deutschland. 2019.

[9] World Greenhouse Gas Emissions: 2018 (Data Visualization). (2021). https://www.wri.org/data/world-greenhouse-gas-emissions-2018 (accessed February 17. 2022).

[10] F. Seitz. Raw Material Change in the Chemical Industry and the Role of Biomass.. in: Catal. Convers. Biomass Its Deriv.. Max-Planck-Gesellschaft zur Förderung der Wissenschaften. Berlin. 2013.

[11] G. Centi. S. Perathoner. Opportunities and prospects in the chemical recycling of carbon dioxide to fuels. Catal. Today. 148 (2009) 191–205. https://doi.org/10.1016/j.cattod.2009.07.075.

[12] A. Rafiee. K. Rajab Khalilpour. D. Milani. M. Panahi. Trends in CO2 conversion and utilization: A review from process systems perspective. J. Environ. Chem. Eng. 6 (2018) 5771–5794. https://doi.org/10.1016/j.jece.2018.08.065.

[13] A. ElMekawy. H.M. Hegab. G. Mohanakrishna. A.F. Elbaz. M. Bulut. D. Pant. Technological advances in CO2 conversion electro-biorefinery: A step toward commercialization. Bioresour. Technol. 215 (2016) 357–370. https://doi.org/10.1016/j.biortech.2016.03.023.

[14] M. Jouny. W.W. Luc. F. Jiao. A General Techno-Economic Analysis of CO2 Electrolysis Systems. Ind. Eng. Chem. Res. (2018) acs.iecr.7b03514. https://doi.org/10.1021/acs.iecr.7b03514.

[15] Y.Y. Birdja. E. Pérez-Gallent. M.C. Figueiredo. A.J. Göttle. F. Calle-Vallejo. M.T.M. Koper. Advances and challenges in understanding the electrocatalytic conversion of carbon dioxide to fuels. Nat. Energy. 4 (2019) 732–745. https://doi.org/10.1038/s41560-019-0450-y.

[16] W. Zhang. Y. Hu. L. Ma. G. Zhu. Y. Wang. X. Xue. R. Chen. S. Yang. Z. Jin. Progress and Perspective of Electrocatalytic CO 2 Reduction for Renewable Carbonaceous Fuels and Chemicals. Adv. Sci. 5 (2018) 1700275. https://doi.org/10.1002/advs.201700275.

[17] O.G. Sánchez. Y.Y. Birdja. M. Bulut. J. Vaes. T. Breugelmans. D. Pant. Recent advances in industrial CO2 electroreduction. Curr. Opin. Green Sustain. Chem. (2019). https://doi.org/10.1016/J.COGSC.2019.01.005.

[18] D.M. Weekes. D.A. Salvatore. A. Reyes. A. Huang. C.P. Berlinguette. Electrolytic CO2 Reduction in a Flow Cell. Acc. Chem. Res. 51 (2018) 910–918. https://doi.org/10.1021/acs.accounts.8b00010.

[19] R. Krause. D. Reinisch. C. Reller. H. Eckert. D. Hartmann. D. Taroata. K. Wiesner-Fleischer. A. Bulan. A. Lueken. G. Schmid. Industrial Application Aspects of the Electrochemical Reduction of CO2 to CO in Aqueous Electrolyte. Chemie Ing. Tech. 92 (2020) 53–61. https://doi.org/10.1002/cite.201900092.

[20] A.J. Martín. G.O. Larrazábal. J. Pérez-Ramírez. Towards sustainable fuels and chemicals through the electrochemical reduction of CO2: Lessons from water electrolysis. Green Chem. 17 (2015) 5114–5130. https://doi.org/10.1039/c5gc01893e.

[21] T. Burdyny. W.A. Smith. CO2 reduction on gas-diffusion electrodes and why catalytic performance must be assessed at commercially-relevant conditions. Energy Environ. Sci. 12 (2019) 1442–1453. https://doi.org/10.1039/c8ee03134g.

[22] M. Li. M.N. Idros. Y. Wu. T. Burdyny. S. Garg. X.S. Zhao. G. Wang. T.E. Rufford. The role of electrode wettability in electrochemical reduction of carbon dioxide. J. Mater. Chem. A. 9 (2021) 19369–19409. https://doi.org/10.1039/D1TA03636J.

[23] S. Dieckhöfer. D. Öhl. J.R.C. Junqueira. T. Quast. T. Turek. W. Schuhmann. Probing the Local Reaction Environment During High Turnover Carbon Dioxide Reduction with Ag-Based Gas Diffusion Electrodes. Chem. – A Eur. J. 27 (2021) 5906–5912. https://doi.org/10.1002/chem.202100387.

[24] V.M. Schmidt. Elektrochemische Verfahrenstechnik. Wiley-VCH Verlag GmbH & Co. KGaA. Weinheim. FRG. 2003. https://doi.org/10.1002/3527602143.

[25] Modern Electrochemistry 2A. Kluwer Academic Publishers. 2002. https://doi.org/10.1007/b113922.

[26] C.H. Hamann. W. Vielstich. Elektrochemie. 4.. vollst. Wiley-VCH Verlag. Weinheim. 2005.

[27] V.M. Schmidt. Elektrochemische Verfahrenstechnik : Grundlagen. Reaktionstechnik. Prozessoptimierung. Wiley-VCH. 2003.

[28] W. Schmickler. E. Santos. Interfacial Electrochemistry. Springer Berlin Heidelberg. Berlin.

Heidelberg. 2010. https://doi.org/10.1007/978-3-642-04937-8.

[29] Z.W. She. J. Kibsgaard. C.F. Dickens. I. Chorkendorff. J.K. Nørskov. T.F. Jaramillo. Combining theory and experiment in electrocatalysis: Insights into materials design. Science (80-85). 355 (2017). https://doi.org/10.1126/science.aad4998.

[30] J. Greeley. T.F. Jaramillo. J. Bonde. I. Chorkendorff. J.K. Nørskov. Computational high-throughput screening of electrocatalytic materials for hydrogen evolution. Nat. Mater. 5 (2006) 909–913. https://doi.org/10.1038/nmat1752.

[31] F. Bidault. D.J.L. Brett. P.H. Middleton. N.P. Brandon. Review of gas diffusion cathodes for alkaline fuel cells. J. Power Sources. 187 (2009) 39–48. https://doi.org/10.1016/j.jpowsour.2008.10.106.

[32] T. Danner. B. Horstmann. D. Wittmaier. N. Wagner. W.G. Bessler. Reaction and transport in Ag/Ag2O gas diffusion electrodes of aqueous Li–O2 batteries: Experiments and modeling. J. Power Sources. 264 (2014) 320–332. https://doi.org/10.1016/J.JPOWSOUR.2014.03.149.

[33] D. Franzen. B. Ellendorff. M.C. Paulisch. A. Hilger. M. Osenberg. I. Manke. T. Turek. Influence of binder content in silver-based gas diffusion electrodes on pore system and electrochemical performance. J. Appl. Electrochem. (2019) 1–9. https://doi.org/10.1007/s10800-019-01311-4.

[34] D.C. Higgins. C. Hahn. C. Xiang. T.F. Jaramillo. A.Z. Weber. Gas-Diffusion Electrodes for Carbon-Dioxide Reduction: A New Paradigm. (2018). https://doi.org/10.1021/acsenergylett.8b02035.

[35] H. Li. Y. Tang. Z. Wang. Z. Shi. S. Wu. D. Song. J. Zhang. K. Fatih. J. Zhang. H. Wang. Z. Liu. R. Abouatallah. A. Mazza. A review of water flooding issues in the proton exchange membrane fuel cell. J. Power Sources. 178 (2008) 103–117. https://doi.org/10.1016/j.jpowsour.2007.12.068.

[36] M. Maja. C. Orecchia. M. Strano. P. Tosco. M. Vanni. Effect of structure of the electrical performance of gas diffusion electrodes for metal air batteries. Electrochim. Acta. 46 (2000) 423–432. https://doi.org/10.1016/S0013-4686(00)00601-0.

[37] A. Eftekhari. B. Ramanujam. C. Liu. P. Phillips. P. Yasaei. A. Behranginia. P. Zapol. R.F. Klie. L.A. Curtiss. A. Salehi-Khojin. X. Lepró. R. Ovalle-Robles. R.H. Baughman. K. Kang. K. Amine. L.A. Curtiss. Q. Yan. L.A. Curtiss. K. Amine. In pursuit of catalytic cathodes for lithium–oxygen batteries. J. Mater. Chem. A. 5 (2017) 7710–7731. https://doi.org/10.1039/C7TA01124E.

[38] N. Giordano. E. Passalacqua. V. Alderucci. P. Staiti. L. Pino. H. Mirzaian. E.J. Taylor. G. Wilemski. Morphological characteristics of PTFE bonded gas diffusion electrodes. Electrochim. Acta. 36 (1991) 1049–1055. https://doi.org/10.1016/0013-4686(91)85314-W.

[39] D.S. Chan. C.C. Wan. Influence of PTFE dispersion in the catalyst layer of porous gas-diffusion electrodes for phosphoric acid fuel cells. J. Power Sources. 50 (1994) 163–176.

https://doi.org/10.1016/0378-7753(94)01897-9.

[40] M. Uchida. Y. Aoyama. N. Eda. A. Ohta. Investigation of the Microstructure in the Catalyst Layer and Effects of Both Perfluorosulfonate Ionomer and PTFE-Loaded Carbon on the Catalyst Layer of Polymer Electrolyte Fuel Cells. J. Electrochem. Soc. 142 (1995) 4143–4149. https://doi.org/10.1149/1.2048477.

[41] M. V. Williams. E. Begg. L. Bonville. H.R. Kunz. J.M. Fenton. Characterization of Gas Diffusion Layers for PEMFC. J. Electrochem. Soc. 151 (2004) A1173. https://doi.org/10.1149/1.1764779.

[42] A. Verma. S. Basu. Direct alkaline fuel cell for multiple liquid fuels: Anode electrode studies. J. Power Sources. 174 (2007) 180–185. https://doi.org/10.1016/j.jpowsour.2007.07.077.

[43] E. Antolini. E.R. Gonzalez. Alkaline direct alcohol fuel cells. J. Power Sources. 195 (2010) 3431–3450. https://doi.org/10.1016/j.jpowsour.2009.11.145.

[44] F.R. Brushett. M.S. Naughton. J.W.D. Ng. L. Yin. P.J.A. Kenis. Analysis of Pt/C electrode performance in a flowing-electrolyte alkaline fuel cell. Int. J. Hydrogen Energy. 37 (2012) 2559–2570. https://doi.org/10.1016/j.ijhydene.2011.10.078.

[45] D. Wittmaier. S. Aisenbrey. N. Wagner. K.A. Friedrich. Bifunctional. Carbon-Free Nickel/Cobalt-Oxide Cathodes for Lithium-Air Batteries with an Aqueous Alkaline Electrolyte. Electrochim. Acta. 149 (2014) 355–363. https://doi.org/10.1016/J.ELECTACTA.2014.10.088.

[46] N. Wagner. M. Schulze. E. Gülzow. Long term investigations of silver cathodes for alkaline fuel cells. J. Power Sources. 127 (2004) 264–272. https://doi.org/10.1016/j.jpowsour.2003.09.022.

[47] J. Kintrup. M. Millaruelo. V. Trieu. A. Bulan. E.S. Mojica. Gas Diffusion Electrodes for Efficient Manufacturing of Chlorine and Other Chemicals. Electrochem. Soc. Interface. 26 (2017) 73–76. https://doi.org/10.1149/2.F07172if.

[48] M. Kluüppel. A. Schroüder. G. Heinrich. Carbon Black. in: Phys. Prop. Polym. Handb.. Springer New York. New York. NY. 2007: pp. 539–550. https://doi.org/10.1007/978-0-387-69002-5_31.

[49] J.B. Donnet. R.C. Bansal. M.-J. Wang. Carbon black: Science and technology. 2nd ed.. Marcel Dekker. New York. 1993. https://books.google.com/books?id=SPpx6MkRYwMC&pgis=1

[50] M. Uchida. Y. Fukuoka. Y. Sugawara. N. Eda. A. Ohta. Effects of Microstructure of Carbon Support in the Catalyst Layer on the Performance of Polymer-Electrolyte Fuel Cells. J. Electrochem. Soc. 143 (1996) 2245–2252. https://doi.org/10.1149/1.1836988.

[51] J. Liu. C. Yang. C. Liu. F. Wang. Y. Song. Design of Pore Structure in Gas Diffusion Layers for Oxygen Depolarized Cathode and Their Effect on Activity for Oxygen Reduction Reaction. Ind. Eng. Chem. Res. 53 (2014) 5866–5872. https://doi.org/10.1021/ie403975r.

[52] K. Tomantschger. K. V. Kordesch. Structural analysis of alkaline fuel cell electrodes and electrode materials. J. Power Sources. 25 (1989) 195–214. https://doi.org/10.1016/0378-

7753(89)80004-7.

[53] H. Schmidt. 129Xe-NMR-spektroskopische Untersuchungen an Carbon Black und Graphit. University of Duisburg. 2003.

[54] T. Soboleva. X. Zhao. K. Malek. Z. Xie. T. Navessin. S. Holdcroft. On the Micro-. Meso-. and Macroporous Structures of Polymer Electrolyte Membrane Fuel Cell Catalyst Layers. ACS Appl. Mater. Interfaces. 2 (2010) 375–384. https://doi.org/10.1021/am900600y.

[55] M. Watanabe. M. Tomikawa. S. Motoo. Experimental analysis of the reaction layer structure in a gas diffusion electrode. J. Electroanal. Chem. Interfacial Electrochem. 195 (1985) 81–93. https://doi.org/10.1016/0022-0728(85)80007-3.

[56] M.L. Perry. J. Newman. E.J. Cairns. Mass Transport in Gas-Diffusion Electrodes: A Diagnostic Tool for Fuel-Cell Cathodes. J. Electrochem. Soc. 145 (1998) 5–15. https://doi.org/10.1149/1.1838202.

[57] S.M. Hassanizadeh. W.G. Gray. Thermodynamic basis of capillary pressure in porous media. Water Resour. Res. 29 (1993) 3389–3405. https://doi.org/10.1029/93WR01495.

[58] M. Royer. Reduction de l’acide carbonique en acid formique. Compt. Rend. (1870) 731–732.

[59] K.P. Kuhl. E.R. Cave. D.N. Abram. T.F. Jaramillo. New insights into the electrochemical reduction of carbon dioxide on metallic copper surfaces. Energy Environ. Sci. 5 (2012) 7050. https://doi.org/10.1039/c2ee21234j.

[60] J.. I. Bard. A.; Parsons. R.; Jordan. Standard potentials in aqueous solution. Marcel Dekker. Inc.. 1985.

[61] K. Zeng. D. Zhang. Recent progress in alkaline water electrolysis for hydrogen production and applications. Prog. Energy Combust. Sci. 36 (2010) 307–326. https://doi.org/10.1016/j.pecs.2009.11.002.

[62] Y. Hori. Electrochemical CO2 Reduction on Metal Electrodes. in: Mod. Asp. Electrochem.. Springer New York. New York. NY. 2008: pp. 89–189. https://doi.org/10.1007/978-0-387-49489-0_3.

[63] Y. Hori. A. Murata. R. Takahashi. Formation of hydrocarbons in the electrochemical reduction of carbon dioxide at a copper electrode in aqueous solution. J. Chem. Soc. 85 (1989) 2309. https://doi.org/10.1039/f19898502309.

[64] M. Azuma. K. Hashimoto. M. Hiramoto. M. Watanabe. T. Sakata. Electrochemical Reduction of Carbon Dioxide on Various Metal Electrodes in Low-Temperature Aqueous KHCO3 Media. J. Electrochem. Soc. 137 (1990) 1772–1778. https://doi.org/10.1149/1.2086796.

[65] Y. Hori. K. Kikuchi. S. Suzuki. Production of CO and CH4 in electrochemical reduction of CO2 at metal electrodes in aqueous hydrogencarbonate solution. Chem. Lett. 14 (1985) 1695–1698. https://doi.org/10.1246/cl.1985.1695.

[66] Y. Hori. S. Suzuki. Electrolytic Reduction of Carbon Dioxide at Mercury Electrode in Aqueous Solution. Bull. Chem. Soc. Jpn. 55 (1982) 660–665. https://doi.org/10.1246/bcsj.55.660.

[67] H. Noda. S. Ikeda. Y. Oda. K. Imai. M. Maeda. K. Ito. Electrochemical Reduction of Carbon Dioxide at Various Metal Electrodes in Aqueous Potassium Hydrogen Carbonate Solution. Bull. Chem. Soc. Jpn. 63 (1990) 2459–2462. https://doi.org/10.1246/bcsj.63.2459.

[68] A. Bagger. W. Ju. A.S. Varela. P. Strasser. J. Rossmeisl. Electrochemical CO2 Reduction: A Classification Problem. ChemPhysChem. 18 (2017) 3266–3273. https://doi.org/10.1002/cphc.201700736.

[69] A.S. Varela. M. Kroschel. T. Reier. P. Strasser. Controlling the selectivity of CO2 electroreduction on copper: The effect of the electrolyte concentration and the importance of the local pH. Catal. Today. 260 (2016) 8–13. https://doi.org/10.1016/j.cattod.2015.06.009.

[70] R. Reske. M. Duca. M. Oezaslan. K.J.P. Schouten. M.T.M. Koper. P. Strasser. Controlling Catalytic Selectivities during CO2 Electroreduction on Thin Cu Metal Overlayers. J. Phys. Chem. Lett. 4 (2013) 2410–2413. https://doi.org/10.1021/jz401087q.

[71] H. Mistry. A.S. Varela. S. Kühl. P. Strasser. B.R. Cuenya. Nanostructured electrocatalysts with tunable activity and selectivity. Nat. Rev. Mater. 1 (2016) 16009. https://doi.org/10.1038/natrevmats.2016.9.

[72] B. Kumar. M. Asadi. D. Pisasale. S. Sinha-Ray. B.A. Rosen. R. Haasch. J. Abiade. A.L. Yarin. A. Salehi-Khojin. Renewable and metal-free carbon nanofibre catalysts for carbon dioxide reduction. Nat. Commun. 4 (2013) 2819. https://doi.org/10.1038/ncomms3819.

[73] X. Duan. J. Xu. Z. Wei. J. Ma. S. Guo. S. Wang. H. Liu. S. Dou. Metal-Free Carbon Materials for CO2 Electrochemical Reduction. Adv. Mater. 29 (2017) 1701784. https://doi.org/10.1002/adma.201701784.

[74] X. Sun. X. Kang. Q. Zhu. J. Ma. G. Yang. Z. Liu. B. Han. Very highly efficient reduction of CO2 to CH using metal-free N-doped carbon electrodes. Chem. Sci. 7 (2016) 2883–2887. https://doi.org/10.1039/C5SC04158A.

[75] W. Li. M. Seredych. E. Rodríguez-Castellón. T.J. Bandosz. Metal-free Nanoporous Carbon as a Catalyst for Electrochemical Reduction of CO2 to CO and CH4. ChemSusChem. 9 (2016) 606–616. https://doi.org/10.1002/cssc.201501575.

[76] S. Zhang. P. Kang. S. Ubnoske. M.K. Brennaman. N. Song. R.L. House. J.T. Glass. T.J. Meyer. Polyethylenimine-Enhanced Electrocatalytic Reduction of CO2 to Formate at Nitrogen-Doped Carbon Nanomaterials. J. Am. Chem. Soc. 136 (2014) 7845–7848. https://doi.org/10.1021/ja5031529.

[77] M.S. Jee. H.S. Jeon. C. Kim. H. Lee. J.H. Koh. J. Cho. B.K. Min. Y.J. Hwang. Enhancement in carbon dioxide activity and stability on nanostructured silver electrode and the role of oxygen. Appl. Catal. B Environ. 180 (2016) 372–378. https://doi.org/10.1016/j.apcatb.2015.06.046.

[78] Q. Lu. J. Rosen. Y. Zhou. G.S. Hutchings. Y.C. Kimmel. J.G. Chen. F. Jiao. A selective and efficient electrocatalyst for carbon dioxide reduction. Nat. Commun. 5 (2014) 3242. https://doi.org/10.1038/ncomms4242.

[79] S.K. Kim. Y.-J. Zhang. H. Bergstrom. R. Michalsky. A. Peterson. Understanding the Low-Overpotential Production of CH4 from CO2 on Mo2C Catalysts. ACS Catal. 6 (2016) 2003–2013. https://doi.org/10.1021/acscatal.5b02424.

[80] K.P. Kuhl. T. Hatsukade. E.R. Cave. D.N. Abram. J. Kibsgaard. T.F. Jaramillo. Electrocatalytic Conversion of Carbon Dioxide to Methane and Methanol on Transition Metal Surfaces. J. Am. Chem. Soc. 136 (2014) 14107–14113. https://doi.org/10.1021/ja505791r.

[81] S. Zhao. S. Guo. C. Zhu. J. Gao. H. Li. H. Huang. Y. Liu. Z. Kang. Achieving electroreduction of CO2 to CH3OH with high selectivity using a pyrite–nickel sulfide nanocomposite. RSC Adv. 7 (2017) 1376–1381. https://doi.org/10.1039/C6RA26868D.

[82] M. Jitaru. D.A. Lowy. M. Toma. B.C. Toma. L. Oniciu. Electrochemical reduction of carbon dioxide on flat metallic cathodes. J. Appl. Electrochem. 27 (1997) 875–889. https://doi.org/10.1023/A:1018441316386.

[83] C. Cui. J. Han. X. Zhu. X. Liu. H. Wang. D. Mei. Q. Ge. Promotional effect of surface hydroxyls on electrochemical reduction of CO2 over SnOx/Sn electrode. J. Catal. 343 (2016) 257–265. https://doi.org/10.1016/j.jcat.2015.12.001.

[84] J.E. Pander. M.F. Baruch. A.B. Bocarsly. Probing the Mechanism of Aqueous CO2 Reduction on Post-Transition-Metal Electrodes using ATR-IR Spectroelectrochemistry. ACS Catal. 6 (2016) 7824–7833. https://doi.org/10.1021/acscatal.6b01879.

[85] C.W. Lee. N.H. Cho. K.D. Yang. K.T. Nam. Reaction Mechanisms of the Electrochemical Conversion of Carbon Dioxide to Formic Acid on Tin Oxide Electrodes. ChemElectroChem. 4 (2017) 2130–2136. https://doi.org/10.1002/celc.201700335.

[86] Y. Zhang. L. Chen. F. Li. C.D. Easton. J. Li. A.M. Bond. J. Zhang. Direct Detection of Electron Transfer Reactions Underpinning the Tin-Catalyzed Electrochemical Reduction of CO2 using Fourier-Transformed ac Voltammetry. ACS Catal. 7 (2017) 4846–4853. https://doi.org/10.1021/acscatal.7b01305.

[87] H. Zhong. K. Fujii. Y. Nakano. F. Jin. Effect of CO2 Bubbling into Aqueous Solutions Used for Electrochemical Reduction of CO2 for Energy Conversion and Storage. J. Phys. Chem. C. 119 (2015) 55–61. https://doi.org/10.1021/jp509043h.

[88] J.T. Feaster. C. Shi. E.R. Cave. T. Hatsukade. D.N. Abram. K.P. Kuhl. C. Hahn. J.K. Nørskov. T.F. Jaramillo. Understanding Selectivity for the Electrochemical Reduction of Carbon Dioxide to Formic Acid and Carbon Monoxide on Metal Electrodes. ACS Catal. 7 (2017) 4822–4827. https://doi.org/10.1021/acscatal.7b00687.

[89] R. Kortlever. J. Shen. K.J.P. Schouten. F. Calle-Vallejo. M.T.M. Koper. Catalysts and Reaction Pathways for the Electrochemical Reduction of Carbon Dioxide. J. Phys. Chem. Lett. 6 (2015) 4073–4082. https://doi.org/10.1021/acs.jpclett.5b01559.

[90] B. Schmid. C. Reller. S. Neubauer. M. Fleischer. R. Dorta. G. Schmid. Reactivity of Copper Electrodes towards Functional Groups and Small Molecules in the Context of CO2 Electro-

Reductions. Catalysts. 7 (2017) 161. https://doi.org/10.3390/catal7050161.

[91] T.-T. Zhuang. Y. Pang. Z.-Q. Liang. Z. Wang. Y. Li. C.-S. Tan. J. Li. C.T. Dinh. P. De Luna. P.-L. Hsieh. T. Burdyny. H.-H. Li. M. Liu. Y. Wang. F. Li. A. Proppe. A. Johnston. D.-H. Nam. Z.-Y. Wu. Y.-R. Zheng. A.H. Ip. H. Tan. L.-J. Chen. S.-H. Yu. S.O. Kelley. D. Sinton. E.H. Sargent. Copper nanocavities confine intermediates for efficient electrosynthesis of C3 alcohol fuels from carbon monoxide. Nat. Catal. 1 (2018) 946–951. https://doi.org/10.1038/s41929-018-0168-4.

[92] Y. Hori. H. Wakebe. T. Tsukamoto. O. Koga. Electrocatalytic process of CO selectivity in electrochemical reduction of CO2 at metal electrodes in aqueous media. Electrochim. Acta. 39 (1994) 1833–1839. https://doi.org/10.1016/0013-4686(94)85172-7.

[93] D.H. Won. C.H. Choi. J. Chung. M.W. Chung. E.H. Kim. S.I. Woo. Rational Design of a Hierarchical Tin Dendrite Electrode for Efficient Electrochemical Reduction of CO2. ChemSusChem. 8 (2015) 3092–3098. https://doi.org/10.1002/cssc.201500694.

[94] Y. Chen. M.W. Kanan. Tin Oxide Dependence of the CO2 Reduction Efficiency on Tin Electrodes and Enhanced Activity for Tin/Tin Oxide Thin-Film Catalysts. J. Am. Chem. Soc. 134 (2012) 1986–1989. https://doi.org/10.1021/ja2108799.

[95] F. Li. L. Chen. G.P. Knowles. D.R. MacFarlane. J. Zhang. Hierarchical Mesoporous SnO2 Nanosheets on Carbon Cloth: A Robust and Flexible Electrocatalyst for CO2 Reduction with High Efficiency and Selectivity. Angew. Chemie. 129 (2017) 520–524. https://doi.org/10.1002/ange.201608279.

[96] S. Zhang. P. Kang. T.J. Meyer. Nanostructured Tin Catalysts for Selective Electrochemical Reduction of Carbon Dioxide to Formate. J. Am. Chem. Soc. 136 (2014) 1734–1737. https://doi.org/10.1021/ja4113885.

[97] M.F. Baruch. J.E. Pander. J.L. White. A.B. Bocarsly. Mechanistic Insights into the Reduction of CO2 on Tin Electrodes using in Situ ATR-IR Spectroscopy. ACS Catal. 5 (2015) 3148–3156. https://doi.org/10.1021/acscatal.5b00402.

[98] D.H. Won. C.H. Choi. J. Chung. M.W. Chung. E.-H. Kim. S.I. Woo. Rational Design of a Hierarchical Tin Dendrite Electrode for Efficient Electrochemical Reduction of CO2. ChemSusChem. 8 (2015) 3092–3098. https://doi.org/10.1002/cssc.201500694.

[99] C.H. Lee. M.W. Kanan. Controlling H+ vs CO2 Reduction Selectivity on Pb Electrodes. ACS Catal. 5 (2015) 465–469. https://doi.org/10.1021/cs5017672.

[100] R. Díaz Delgado. J.R. Morante i Lleonart. F. Sanz Carrasco. Universitat de Barcelona. Departament de Química Física.. Tin oxide gas sensors an electrochemical approach. Universitat de Barcelona. 2002.

[101] A. Dutta. A. Kuzume. M. Rahaman. S. Vesztergom. P. Broekmann. Monitoring the Chemical State of Catalysts for CO2 Electroreduction: An In Operando Study. ACS Catal. 5 (2015) 7498–7502. https://doi.org/10.1021/acscatal.5b02322.

[102] D.T. Whipple. E.C. Finke. P.J.A. Kenis. Microfluidic Reactor for the Electrochemical Reduction of Carbon Dioxide: The Effect of pH. Electrochem. Solid-State Lett. 13 (2010) B109. https://doi.org/10.1149/1.3456590.

[103] M.N. Mahmood. D. Masheder. C.J. Harty. Use of gas-diffusion electrodes for high-rate electrochemical reduction of carbon dioxide. I. Reduction at lead. indium- and tin-impregnated electrodes. J. Appl. Electrochem. 17 (1987) 1159–1170. https://doi.org/10.1007/BF01023599.

[104] D. Bohra. J.H. Chaudhry. T. Burdyny. E.A. Pidko. W.A. Smith. Modeling the electrical double layer to understand the reaction environment in a CO2 electrocatalytic system. Energy Environ. Sci. 12 (2019) 3380–3389. https://doi.org/10.1039/C9EE02485A.

[105] B. Kumar. J.P. Brian. V. Atla. S. Kumari. K.A. Bertram. R.T. White. J.M. Spurgeon. New trends in the development of heterogeneous catalysts for electrochemical CO2 reduction. Catal. Today. 270 (2016) 19–30. https://doi.org/10.1016/j.cattod.2016.02.006.

[106] Q. Lu. J. Rosen. F. Jiao. Nanostructured Metallic Electrocatalysts for Carbon Dioxide Reduction. ChemCatChem. 7 (2015) 38–47. https://doi.org/10.1002/cctc.201402669.

[107] D.D. Zhu. J.L. Liu. S.Z. Qiao. Recent Advances in Inorganic Heterogeneous Electrocatalysts for Reduction of Carbon Dioxide. Adv. Mater. 28 (2016) 3423–3452. https://doi.org/10.1002/adma.201504766.

[108] Y. Li. Q. Sun. Recent Advances in Breaking Scaling Relations for Effective Electrochemical Conversion of CO2. Adv. Energy Mater. 6 (2016) 1600463. https://doi.org/10.1002/aenm.201600463.

[109] S. Verma. Y. Hamasaki. C. Kim. W. Huang. S. Lu. H.-R.M. Jhong. A.A. Gewirth. T. Fujigaya. N. Nakashima. P.J.A. Kenis. Insights into the Low Overpotential Electroreduction of CO2 to CO on a Supported Gold Catalyst in an Alkaline Flow Electrolyzer. ACS Energy Lett. 3 (2018) 193–198. https://doi.org/10.1021/acsenergylett.7b01096.

[110] B.A. Rosen. A. Salehi-Khojin. M.R. Thorson. W. Zhu. D.T. Whipple. P.J.A. Kenis. R.I. Masel. Ionic Liquid–Mediated Selective Conversion of CO2 to CO at Low Overpotentials. Science (80-85). 334 (2011) 643–644. https://doi.org/10.1126/science.1209786.

[111] B. Kumar. V. Atla. J.P. Brian. S. Kumari. T.Q. Nguyen. M. Sunkara. J.M. Spurgeon. Reduced SnO2 Porous Nanowires with a High Density of Grain Boundaries as Catalysts for Efficient Electrochemical CO2-into-HCOOH Conversion. Angew. Chemie. 129 (2017) 3699–3703. https://doi.org/10.1002/ange.201612194.

[112] D. Li. J. Wu. T. Liu. J. Liu. Z. Yan. L. Zhen. Y. Feng. Tuning the pore structure of porous tin foam electrodes for enhanced electrochemical reduction of carbon dioxide to formate. Chem. Eng. J. 375 (2019) 122024. https://doi.org/10.1016/j.cej.2019.122024.

[113] X. Feng. K. Jiang. S. Fan. M.W. Kanan. Grain-Boundary-Dependent CO2 Electroreduction Activity. J. Am. Chem. Soc. 137 (2015) 4606–4609. https://doi.org/10.1021/ja5130513.

[114] A. Verdaguer-Casadevall. C.W. Li. T.P. Johansson. S.B. Scott. J.T. McKeown. M. Kumar.

I.E.L. Stephens. M.W. Kanan. I. Chorkendorff. Probing the Active Surface Sites for CO Reduction on Oxide-Derived Copper Electrocatalysts. J. Am. Chem. Soc. 137 (2015) 9808–9811. https://doi.org/10.1021/jacs.5b06227.

[115] S. Gao. Y. Lin. X. Jiao. Y. Sun. Q. Luo. W. Zhang. D. Li. J. Yang. Y. Xie. Partially oxidized atomic cobalt layers for carbon dioxide electroreduction to liquid fuel. Nature. 529 (2016) 68–71. https://doi.org/10.1038/nature16455.

[116] A. Tamimi. E.B. Rinker. O.C. Sandall. Diffusion Coefficients for Hydrogen Sulfide. Carbon Dioxide. and Nitrous Oxide in Water over the Temperature Range 293-368 K. J. Chem. Eng. Data. 39 (1994) 330–332. https://doi.org/10.1021/je00014a031.

[117] L. Zhang. Z. Wang. N. Mehio. X. Jin. S. Dai. Thickness- and Particle-Size-Dependent Electrochemical Reduction of Carbon Dioxide on Thin-Layer Porous Silver Electrodes. ChemSusChem. 9 (2016) 428–432. https://doi.org/10.1002/cssc.201501637.

[118] K. Hara. A. Kudo. T. Sakata. Electrochemical reduction of carbon dioxide under high pressure on various electrodes in an aqueous electrolyte. J. Electroanal. Chem. 391 (1995) 141–147. https://doi.org/10.1016/0022-0728(95)03935-A.

[119] H. Li. C. Oloman. Development of a continuous reactor for the electro-reduction of carbon dioxide to formate – Part 2: Scale-up. J. Appl. Electrochem. 37 (2007) 1107–1117. https://doi.org/10.1007/s10800-007-9371-8.

[120] C. Oloman. Trickle Bed Electrochemical Reactors. J. Electrochem. Soc. 126 (1979) 1885–1892. https://doi.org/10.1149/1.2128820.

[121] F. Köleli. T. Atilan. N. Palamut. A.M. Gizir. R. Aydin. C.H. Hamann. Electrochemical reduction of CO2 at Pb- and Sn-electrodes in a fixed-bed reactor in aqueous K2CO3 and KHCO3 media. J. Appl. Electrochem. 33 (2003) 447–450. https://doi.org/10.1023/A:1024471513136.

[122] A.S. Agarwal. Y. Zhai. D. Hill. N. Sridhar. The electrochemical reduction of carbon dioxide to formate/formic acid: Engineering and economic feasibility. ChemSusChem. 4 (2011) 1301–1310. https://doi.org/10.1002/cssc.201100220.

[123] M. Schwartz. R.L. Cook. V.M. Kehoe. R.C. MacDuff. J. Patel. A.F. Sammells. Carbon Dioxide Reduction to Alcohols using Perovskite-Type Electrocatalysts. J. Electrochem. Soc. 140 (1993) 614–618. https://doi.org/10.1149/1.2056131.

[124] R.L. Cook. R.C. MacDuff. A.F. Sammells. High Rate Gas Phase CO2 Reduction to Ethylene and Methane Using Gas Diffusion Electrodes. J. Electrochem. Soc. 137 (1990) 607–608. https://doi.org/10.1149/1.2086515.

[125] C. Delacourt. P.L. Ridgway. J.B. Kerr. J. Newman. Design of an Electrochemical Cell Making Syngas (CO+H2) from CO2 and H2O Reduction at Room Temperature. J. Electrochem. Soc. 155 (2008) B42. https://doi.org/10.1149/1.2801871.

[126] N. Furuya. T. Yamazaki. M. Shibata. High performance Ru/Pd catalysts for CO2 reduction at

gas-diffusion electrodes. J. Electroanal. Chem. 431 (1997) 39–41. https://doi.org/10.1016/S0022-0728(97)00159-9.

[127] H.R.Q. Jhong. F.R. Brushett. P.J.A.A. Kenis. The effects of catalyst layer deposition methodology on electrode performance. Adv. Energy Mater. 3 (2013) 589–599. https://doi.org/10.1002/aenm.201200759.

[128] M.S. Naughton. G.H. Gu. A.A. Moradia. P.J.A. Kenis. Tailoring electrode hydrophobicity to improve anode performance in alkaline media. J. Power Sources. 242 (2013) 581–588. https://doi.org/10.1016/j.jpowsour.2013.05.054.

[129] M.S. Wilson. S. Gottesfeld. Thin-film catalyst layers for polymer electrolyte fuel cell electrodes. J. Appl. Electrochem. 22 (1992) 1–7. https://doi.org/10.1007/BF01093004.

[130] B. Kim. F. Hillman. M. Ariyoshi. S. Fujikawa. P.J.A. Kenis. Effects of composition of the micro porous layer and the substrate on performance in the electrochemical reduction of CO2 to CO. J. Power Sources. 312 (2016) 192–198. https://doi.org/10.1016/j.jpowsour.2016.02.043.

[131] S. Ma. Y. Lan. G.M.J. Perez. S. Moniri. P.J.A. Kenis. Silver Supported on Titania as an Active Catalyst for Electrochemical Carbon Dioxide Reduction. ChemSusChem. 7 (2014) 866–874. https://doi.org/10.1002/cssc.201300934.

[132] S. Ma. J. Liu. K. Sasaki. S.M. Lyth. P.J.A. Kenis. Carbon Foam Decorated with Silver Nanoparticles for Electrochemical CO2 Conversion. Energy Technol. 5 (2017) 861–863. https://doi.org/10.1002/ente.201600576.

[133] S. Ma. R. Luo. J.I. Gold. A.Z. Yu. B. Kim. P.J.A. Kenis. Carbon nanotube containing Ag catalyst layers for efficient and selective reduction of carbon dioxide. J. Mater. Chem. A. 4 (2016) 8573–8578. https://doi.org/10.1039/C6TA00427J.

[134] C.E. Tornow. M.R. Thorson. S. Ma. A.A. Gewirth. P.J.A. Kenis. Nitrogen-Based Catalysts for the Electrochemical Reduction of CO2 to CO. J. Am. Chem. Soc. 134 (2012) 19520–19523. https://doi.org/10.1021/ja308217w.

[135] A. Salehi-Khojin. H.-R.M. Jhong. B.A. Rosen. W. Zhu. S. Ma. P.J.A. Kenis. R.I. Masel. Nanoparticle Silver Catalysts That Show Enhanced Activity for Carbon Dioxide Electrolysis. J. Phys. Chem. C. 117 (2013) 1627–1632. https://doi.org/10.1021/jp310509z.

[136] A. Del Castillo. M. Alvarez-Guerra. J. Solla-Gullón. A. Sáez. V. Montiel. A. Irabien. Sn nanoparticles on gas diffusion electrodes: Synthesis. characterization and use for continuous CO2 electroreduction to formate. J. CO2 Util. 18 (2017) 222–228. https://doi.org/10.1016/j.jcou.2017.01.021.

[137] J. Wu. P.P. Sharma. B.H. Harris. X.-D. Zhou. Electrochemical reduction of carbon dioxide: IV dependence of the Faradaic efficiency and current density on the microstructure and thickness of tin electrode. J. Power Sources. 258 (2014) 189–194. https://doi.org/10.1016/j.jpowsour.2014.02.014.

[138] S. Sen. B. Skinn. T. Hall. M. Inman. E.J. Taylor. F.R. Brushett. Pulsed Electrodeposition of Tin

Electrocatalysts onto Gas Diffusion Layers for Carbon Dioxide Reduction to Formate. MRS Adv. 2 (2017) 451–458. https://doi.org/10.1557/adv.2016.652.

[139] Q. Wang. H. Dong. H. Yu. H. Yu. Enhanced performance of gas diffusion electrode for electrochemical reduction of carbon dioxide to formate by adding polytetrafluoroethylene into catalyst layer. J. Power Sources. 279 (2015) 1–5. https://doi.org/10.1016/j.jpowsour.2014.12.118.

[140] P. Jeanty. C. Scherer. E. Magori. K. Wiesner-Fleischer. O. Hinrichsen. M. Fleischer. Upscaling and continuous operation of electrochemical CO2 to CO conversion in aqueous solutions on silver gas diffusion electrodes. J. CO2 Util. 24 (2018) 454–462. https://doi.org/10.1016/J.JCOU.2018.01.011.

[141] T. Hierlemann. Synthesis of Carbon-Based Electrodes from Biomass and Application in CO2 Conversion to Formate. University of Stuttgart. 2018.

[142] K.C. Song. Y. Kang. Preparation of high surface area tin oxide powders by a homogeneous precipitation method. Mater. Lett. 42 (2000) 283–289. https://doi.org/10.1016/S0167-577X(99)00199-8.

[143] L. Li. S. Liu. J. Liu. Surface modification of coconut shell based activated carbon for the improvement of hydrophobic VOC removal. J. Hazard. Mater. 192 (2011) 683–690. https://doi.org/10.1016/j.jhazmat.2011.05.069.

[144] V. Gomezserrano. M. Acedoramos. A. Lopezpeinado. C. Valenzuelacalahorro. Oxidation of activated carbon by hydrogen peroxide. Study of surface functional groups by FT-IR. Fuel. 73 (1994) 387–395. https://doi.org/10.1016/0016-2361(94)90092-2.

[145] A. Trunschke. Surface area and pore size determination. Mod. Methods Ind Heterog. Catal. Res. (2007). http://www.fhi-berlin.mpg.de/acnew/department/pages/teaching/pages/teaching__wintersemester__2007_2008/trunschke_surface_area_pores_191007.pdf.

[146] T. Schuster. L. Rüdt von Collenberg. Investitionsrechnung: Kapitalwert. Zinsfuß. Annuität. Amortisation. Springer Berlin Heidelberg. Berlin. Heidelberg. 2017. https://doi.org/10.1007/978-3-662-47799-1.

[147] A. Bazzanella. F. Ausfelder. Low carbon energy and feedstock for the European chemical industry. Technology Study. 2017.

[148] F.C. and H.J. Undertaking. Fuel Cells and Hydrogen Joint Undertaking (FCH JU) - Commercialisation of Energy Storage in Europe: Final Report. 2015. http://www.fch.europa.eu/sites/default/files/CommercializationofEnergyStorageFinal_3.pdf.

[149] A. Buttler. H. Spliethoff. Current status of water electrolysis for energy storage. grid balancing and sector coupling via power-to-gas and power-to-liquids: A review. Renew. Sustain. Energy Rev. 82 (2018) 2440–2454. https://doi.org/10.1016/j.rser.2017.09.003.

[150] S. Verma. B. Kim. H.R.M. Jhong. S. Ma. P.J.A. Kenis. A gross-margin model for defining

technoeconomic benchmarks in the electroreduction of CO2. ChemSusChem. 9 (2016) 1972–1979. https://doi.org/10.1002/cssc.201600394.

[151] DG Energy. Quarterly Report on European Electricity Markets. Mark. Obs. Energy. 11 (2018). https://ec.europa.eu/energy/sites/ener/files/documents/quarterly_report_on_european_electricity_markets_q1_2018.pdf.

[152] K. Meyer. P. Klobes. Comparison between different presentations of pore size distribution in porous materials. Fresenius. J. Anal. Chem. 363 (1999) 174–178. https://doi.org/10.1007/s002160051166.

[153] J.C. Groen. L.A.. Peffer. J. Pérez-Ramírez. Pore size determination in modified micro- and mesoporous materials. Pitfalls and limitations in gas adsorption data analysis. Microporous Mesoporous Mater. 60 (2003) 1–17. https://doi.org/10.1016/S1387-1811(03)00339-1.

[154] M. Thommes. Physical Adsorption Characterization of Nanoporous Materials. Chemie Ing. Tech. 82 (2010) 1059–1073. https://doi.org/10.1002/cite.201000064.

[155] M. Thommes. K.A. Cychosz. Physical adsorption characterization of nanoporous materials: progress and challenges. Adsorption. 20 (2014) 233–250. https://doi.org/10.1007/s10450-014-9606-z.

[156] S. Lowell. J.E. Shields. M.A. Thomas. M. Thommes. Characterization of Porous Solids and Powders: Surface Area. Pore Size and Density. Springer Netherlands. Dordrecht. 2004. https://doi.org/10.1007/978-1-4020-2303-3.

[157] F. Schüth. K.S.W. Sing. J. Weitkamp. eds.. Handbook of Porous Solids. Wiley. 2002. https://doi.org/10.1002/9783527618286.

[158] S. Trasatti. O.A. Petrii. Real surface area measurements in electrochemistry. Pure Appl. Chem. 63 (1991) 711–734. https://doi.org/10.1351/pac199163050711.

[159] D.M. Morales. M. Risch. Seven steps to reliable cyclic voltammetry measurements for the determination of double layer capacitance. J. Phys. Energy. 3 (2021) 034013. https://doi.org/10.1088/2515-7655/abee33.

[160] R. Sedev. Electrowetting: Electrocapillarity. saturation. and dynamics. Eur. Phys. J. Spec. Top. 197 (2011) 307–319. https://doi.org/10.1140/epjst/e2011-01473-4.

[161] V. Peykov. A. Quinn. J. Ralston. Electrowetting: a model for contact-angle saturation. Colloid Polym. Sci. 278 (2000) 789–793. https://doi.org/10.1007/s003960000333.

[162] A.J. Bard. L.R. Faulkner. Electrochemical Methods: Fundamentals and Applications. 2nd ed.. 2nd editio. John Wiley & Sons. Ltd. New York. 2000. https://doi.org/10.1023/A:1021637209564.

[163] A. Lundblad. P. Björnbom. Wetting-in Studies on Alkaline-Fuel-Cell Cathodes Using a Potentiostatic-Galvanostatic Experimental Design. J. Electrochem. Soc. 141 (1994) 1503–1508. https://doi.org/10.1149/1.2054953.

[164] S. Trasatti. E. Lust. The Potential of Zero Charge. in: Mod. Asp. Electrochem.. Kluwer

Academic Publishers. Boston. n.d.: pp. 1–215. https://doi.org/10.1007/0-306-46917-0_1.

[165] M. Sakaguchi. K. Uematsu. A. Sakata. Y. Sato. M. Sato. Correlation between wettability of carbon carriers and activity of porous electrodes. Electrochim. Acta. 34 (1989) 625–630. https://doi.org/10.1016/0013-4686(89)85005-4.

[166] A.G. Pandolfo. A.F. Hollenkamp. Carbon properties and their role in supercapacitors. J. Power Sources. 157 (2006) 11–27. https://doi.org/10.1016/j.jpowsour.2006.02.065.

[167] E. Frackowiak. F. Béguin. Carbon materials for the electrochemical storage of energy in capacitors. Carbon N. Y. 39 (2001) 937–950. https://doi.org/10.1016/S0008-6223(00)00183-4.

[168] M. Che. J.C. Védrine. eds.. Characterization of Solid Materials and Heterogeneous Catalysts. Wiley-VCH Verlag GmbH & Co. KGaA. Weinheim. Germany. 2012. https://doi.org/10.1002/9783527645329.

[169] A.W.C. Lin. N.R. Armstrong. T. Kuwana. X-ray photoelectron/Auger electron spectroscopic studies of tin and indium metal foils and oxides. Anal. Chem. 49 (1977) 1228–1235. https://doi.org/10.1021/ac50016a042.

[170] R. Díaz. I. Díez-Pérez. P. Gorostiza. F. Sanz. J.R. Morante. An electrochemical study of tin oxide thin film in borate buffer solutions. J. Braz. Chem. Soc. 14 (2003) 523–529. https://doi.org/10.1590/S0103-50532003000400006.

[171] M. Sabharwal. L.M. Pant. A. Putz. D. Susac. J. Jankovic. M. Secanell. Analysis of Catalyst Layer Microstructures: From Imaging to Performance. Fuel Cells. 16 (2016) 734–753. https://doi.org/10.1002/fuce.201600008.

[172] B. Bladergroen. H. Su. S. Pasupathi. V. Linkov. Overview of Membrane Electrode Assembly Preparation Methods for Solid Polymer Electrolyte Electrolyzer. in: Electrolysis. InTech. 2012. https://doi.org/10.5772/52947.

[173] E. Gülzow. T. Kaz. New results of PEFC electrodes produced by the DLR dry preparation technique. J. Power Sources. 106 (2002) 122–125. https://doi.org/10.1016/S0378-7753(01)01030-8.

[174] A. Inan. Experimentelle Untersuchungen zur technischen Machbarkeit der elektrochemischen CO2 Reduktion. Universität Stuttgart. 2019.

[175] D. Kopljar. A. Inan. P. Vindayer. N. Wagner. E. Klemm. Electrochemical reduction of CO2 to formate at high current density using gas diffusion electrodes. J. Appl. Electrochem. 44 (2014) 1107–1116. https://doi.org/10.1007/s10800-014-0731-x.

[176] E. Antolini. Carbon supports for low-temperature fuel cell catalysts. Appl. Catal. B Environ. 88 (2009) 1–24. https://doi.org/10.1016/j.apcatb.2008.09.030.

[177] A.L. Dicks. The role of carbon in fuel cells. J. Power Sources. 156 (2006) 128–141. https://doi.org/10.1016/j.jpowsour.2006.02.054.

[178] A.S. Arico’. V. Antonucci. M. Minutoli. N. Giordano. The influence of functional groups on the surface acid-base characteristics of carbon blacks. Carbon N. Y. 27 (1989) 337–347.

https://doi.org/10.1016/0008-6223(89)90065-1.

[179] M. Todoroki. K. Hara. A. Kudo. T. Sakata. Electrochemical reduction of high pressure CO2 at Pb. Hg and In electrodes in an aqueous KHCO3 solution. J. Electroanal. Chem. 394 (1995) 199–203. https://doi.org/10.1016/0022-0728(95)04010-L.

[180] Y. Chen. C.W. Li. M.W. Kanan. Aqueous CO2 Reduction at Very Low Overpotential on Oxide-Derived Au Nanoparticles. J. Am. Chem. Soc. 134 (2012) 19969–19972. https://doi.org/10.1021/ja309317u.

[181] J. Bae. I.A. Samek. P.C. Stair. R.Q. Snurr. Investigation of the Hydrophobic Nature of Metal Oxide Surfaces Created by Atomic Layer Deposition. Langmuir. 35 (2019) 5762–5769. https://doi.org/10.1021/acs.langmuir.9b00577.

[182] D. Kopljar. N. Wagner. E. Klemm. Transferring Electrochemical CO2 Reduction from Semi-Batch into Continuous Operation Mode Using Gas Diffusion Electrodes. Chem. Eng. Technol. 39 (2016) 2042–2050. https://doi.org/10.1002/ceat.201600198.

[183] C. Pan. Q. Li. J.O. Jensen. R. He. L.N. Cleemann. M.S. Nilsson. N.J. Bjerrum. Q. Zeng. Preparation and operation of gas diffusion electrodes for high-temperature proton exchange membrane fuel cells. J. Power Sources. 172 (2007) 278–286. https://doi.org/10.1016/j.jpowsour.2007.07.019.

[184] M.J.W. Blom. W.P.M. van Swaaij. G. Mul. S.R.A. Kersten. Overall mass balance evaluation of electrochemical reactors: The case of CO2 reduction. Electrochim. Acta. 333 (2020) 135460. https://doi.org/10.1016/j.electacta.2019.135460.

[185] K. Hertwig. L. Martens. C. Hamel. Chemische Verfahrenstechnik. De Gruyter. 2018. https://doi.org/10.1515/9783110501025.

[186] F. Bienen. A. Löwe. J. Hildebrand. S. Hertle. D. Schonvogel. D. Kopljar. N. Wagner. E. Klemm. K.A. Friedrich. Degradation study on tin- and bismuth-based gas-diffusion electrodes during electrochemical CO2 reduction in highly alkaline media. J. Energy Chem. 62 (2021) 367–376. https://doi.org/10.1016/j.jechem.2021.03.050.

[187] S. Geiger. O. Kasian. A.M. Mingers. K.J.J. Mayrhofer. S. Cherevko. Stability limits of tin-based electrocatalyst supports. Sci. Rep. 7 (2017) 4595. https://doi.org/10.1038/s41598-017-04079-9.

[188] O. Palazhchenko. Pourbaix Diagrams at elevated temperatures - a study of Zn and Sn. University of Ontario. 2012.

[189] K.A. Striebel. F.R. McLarnon. E.J. Cairns. Steady-state model for an oxygen fuel cell electrode with an aqueous carbonate electrolyte. Ind. Eng. Chem. Res. 34 (1995) 3632–3639. https://doi.org/10.1021/ie00037a052.

[190] R.E. Zeebe. On the molecular diffusion coefficients of dissolved . and and their dependence on isotopic mass. Geochim. Cosmochim. Acta. 75 (2011) 2483–2498. https://doi.org/10.1016/j.gca.2011.02.010.

[191] P. Vanýsek. Ionic conductivities and diffusion at infinite dilution. in: Handb. Chem. Phys.. CRC Press. Boca Raton. 1992: pp. 5–111.

[192] N.J. Claassens. C.A.R. Cotton. D. Kopljar. A. Bar-Even. Making quantitative sense of electromicrobial production. Nat. Catal. 2 (2019) 437–447. https://doi.org/10.1038/s41929-019-0272-0.

[193] P. De Luna. C. Hahn. D. Higgins. S.A. Jaffer. T.F. Jaramillo. E.H. Sargent. What would it take for renewably powered electrosynthesis to displace petrochemical processes?. Science (80-.). 364 (2019). https://doi.org/10.1126/science.aav3506.

[194] Bertuccioli. L.. A. Chan. D. Hart. F. Lehner. B. Madden. E. Standen. Development of Water Electrolysis in the European Union. 2016.

[195] X. Li. P. Anderson. H.-R.M. Jhong. M. Paster. J.F. Stubbins. P.J.A. Kenis. Greenhouse Gas Emissions. Energy Efficiency. and Cost of Synthetic Fuel Production Using Electrochemical CO2 Conversion and the Fischer–Tropsch Process. Energy & Fuels. 30 (2016) 5980–5989. https://doi.org/10.1021/acs.energyfuels.6b00665.

[196] A. Raksajati. M.T. Ho. D.E. Wiley. Reducing the Cost of CO2 Capture from Flue Gases Using Aqueous Chemical Absorption. Ind. Eng. Chem. Res. 52 (2013) 16887–16901. https://doi.org/10.1021/ie402185h.

[197] Hietala. Formic Acid. Ullmann’s Encycl. Ind. Chem. (2016) 1–22.

[198] H. Yang. J.J. Kaczur. S.D. Sajjad. R.I. Masel. Electrochemical conversion of CO2 to formic acid utilizing Sustainion^{TM} membranes. J. CO2 Util. 20 (2017) 208–217. https://doi.org/10.1016/j.jcou.2017.04.011.

[199] F. Bienen. D. Kopljar. A. Löwe. P. Aßmann. M. Stoll. P. Rößner. N. Wagner. A. Friedrich. E. Klemm. Utilizing Formate as an Energy Carrier by Coupling CO2 Electrolysis with Fuel Cell Devices. Chemie-Ingenieur-Technik. 91 (2019) 872–882. https://doi.org/10.1002/cite.201800212.

[200] P. Kunz. M. Paulisch. M. Osenberg. B. Bischof. I. Manke. U. Nieken. Prediction of Electrolyte Distribution in Technical Gas Diffusion Electrodes: From Imaging to SPH Simulations. Transp. Porous Media. 132 (2020) 381–403. https://doi.org/10.1007/s11242-020-01396-y.

10 List of figures

11 List of tables